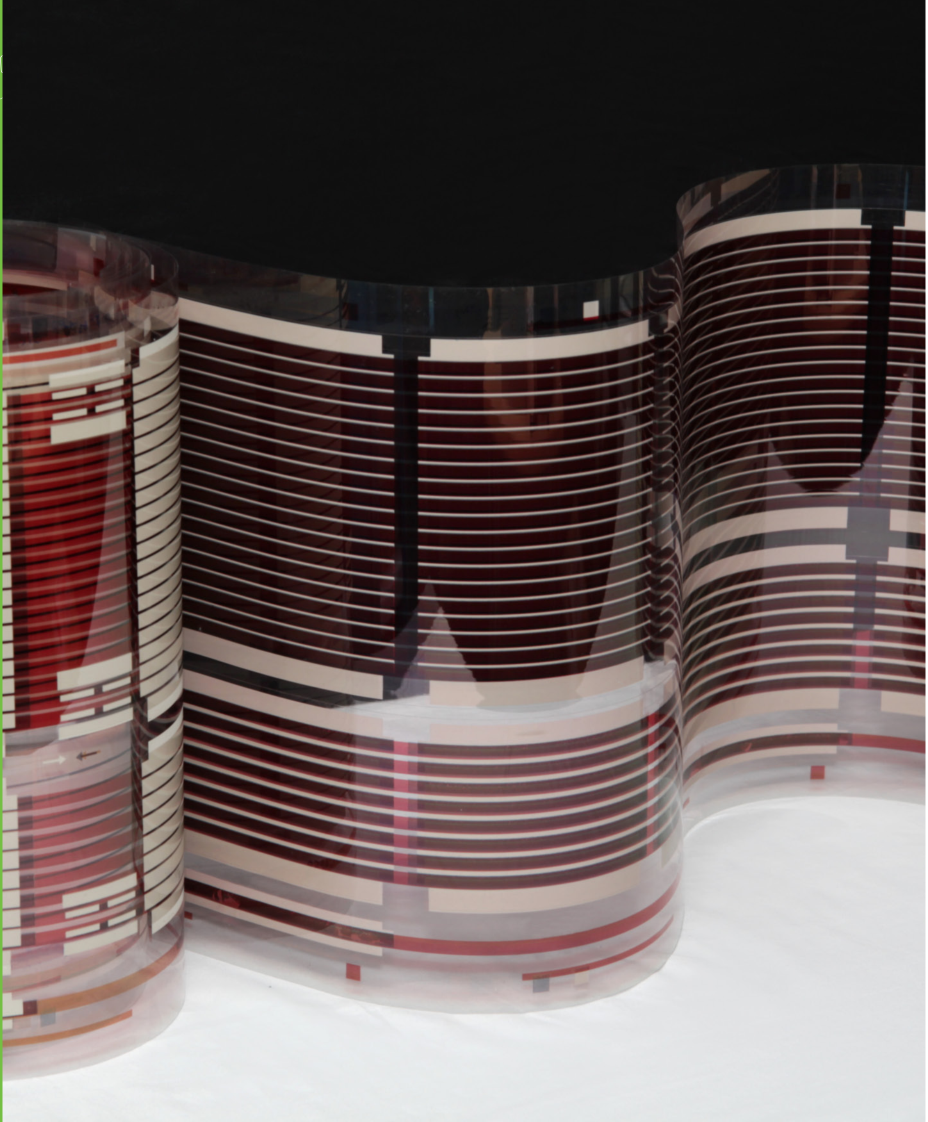

•SCIENCE•TECHNOLOGY•RESEARCH HIGHLIGHTS•VISIONS

Dissertation

101

Roll-to-roll printing of organic photovoltaic cells and modules

Pälvi Apilo

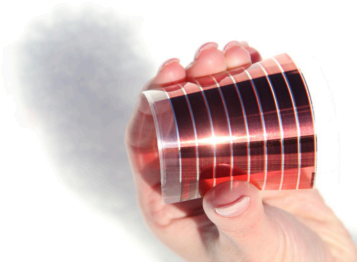

VTT SCIENCE 101

Roll-to-roll printing of organic photovoltaic cells and modules

Pälvi Apilo (formerly Kopola)

VTT Technical Research Centre of Finland Ltd

Thesis for the degree of Doctor of Science in Technology to be presented with due permission for public examination and criticism in Auditorium L10, at the University of Oulu, on the 4th of September, at 12 o'clock noon.

ISBN 978-951-38-8328-7 (Soft back ed.)
ISBN 978-951-38-8329-4 (URL: http://www.vttresearch.com/impact/publications)

VTT Science 101

ISSN-L 2242-119X
ISSN 2242-119X (Print)
ISSN 2242-1203 (Online)

JULKAISIJA – UTGIVARE – PUBLISHER

Teknologian tutkimuskeskus VTT Oy
PL 1000 (Tekniikantie 4 A, Espoo)
02044 VTT
Puh. 020 722 111, faksi 020 722 7001

Teknologiska forskningscentralen VTT Ab
PB 1000 (Teknikvägen 4 A, Esbo)
FI-02044 VTT
Tfn +358 20 722 111, telefax +358 20 722 7001

VTT Technical Research Centre of Finland Ltd
P.O. Box 1000 (Tekniikantie 4 A, Espoo)
FI-02044 VTT, Finland
Tel. +358 20 722 111, fax +358 20 722 7001

Cover image: Antti Veijola

Juvenes Print, Tampere 2015

Preface

This Thesis is based on the research carried out at VTT Technical Research Centre of Finland Ltd and The Fraunhofer Institute for Solar Energy Systems (ISE), Germany during the years 2008–2015. The research has been mainly performed in the research projects FACESS (EU), AUTOSYS (Tekes – the Finnish Funding Agency for Innovation), a customer funded project and few VTT self-financed projects.

First of all I would like to express my sincere gratitude to supervisors, Emeritus Professor Risto Myllylä and Research Professor Jukka Hast. I would like to thank Prof. Myllylä for encouraging my research and pushing me always forward to reach the final goal. I would like to thank Prof. Hast for giving continuous support and guidance during my PhD studies. Prof. Hast has been besides Dr. Sanna Rousu the most important persons for applying funding for OPV research. I would also like to thank Dr. Sanna Rousu for being tremendous mentor for me.

I greatly acknowledge Professor Reinhard Baumann (Technische Universität Chemnitz) and Professor Ronald Österbacka (Åbo Akademi University) for comprehensive peer-reviewing of the Thesis manuscript.

I am grateful to Dr. Uli Würfel and Dr. Birger Zimmermann for giving me the opportunity to work one year at Fraunhofer ISE under their excellent supervision. I would also thank all the great co-workers at Fraunhofer ISE to do research with, Jens, Hans-Frieder, Aleksander, Clemens, Deepak, Thomas, Jakob, Helene, Baste, Felix, Babu, Sebastian, Chegnui, Markus, Katharina, Chris, Olena, Patrick, Nikolas, Martin, Timo, Biljana, Jan and Klara. Thank you also for teaching the German way of living.

I would like to forward my special thanks to Marja Välimäki who has been one of the most important persons of our success in R2R printing of OPV modules. She has been actively brainstorming with me to solve the processing issues related to OPVs and given invaluable insight and expertise to thin film printing. My sincere gratitude goes to Dr. Jussi Hiltunen who is always enthusiastic to discuss about research and willing to share his excellent ideas.

I would like to thank the team who has worked hard to transfer the OPV process from laboratory to pilot environment, in particular, Marja Välimäki, Anne Peltoniemi, Antti Veijola, Mikko Hietala, Mari Ylikunnari, Dr. Marja Vilkman, Elina Jansson and Pentti Korhonen. Also, I would like to acknowledge Dr. Riccardo Po, Dr. Andrea Bernardi and Dr. Gianni Corso from ENI S.p.A for their expertise. I would also be indepted to all of my co-workers at VTT who have supported me during the PhD studies.

I would like to thank Dr. Arto Maaninen and Professor Harri Kopola for insightful comments to improve the first draft of my PhD Thesis.

I would like to acknowledge the financial support for the thesis from Emil Aaltonen Foundation, Finnish Foundation for Technology Promotion (Tekniikan Edistämissäätiö, TES), Seppo Säynäjäkangas Science Foundation and Tauno Tönning Foundation.

I would like to thank my parents, my siblings, parents-in law and friends for their love and support.

Finally, I would like to acknowledge the two most important persons in my life – my husband Olli and my little daughter Ada – for their love. Additionally, I would like to thank Olli for supporting me in my time-consuming free time projects. First when I played semi-professionally floorball and then with the PhD studies. I would like to thank Ada for her adorable smile which helps me to forget work and studies.

Oulu, June 2015

Pälvi Apilo

Academic dissertation

Supervisors	Professor Emeritus Risto Myllylä Optoelectronics and Measurement Techniques Laboratory Faculty of Information Technology and Electrical Engineering University of Oulu, Finland
	Research Professor Jukka Hast Printed and hybrid functionalities VTT Technical Research Centre of Finland Ltd, Finland
Advisor	Doctor Sanna Rousu Printed Optoelectronic Systems Printed and hybrid functionalities VTT Technical Research Centre of Finland Ltd, Finland
Reviewers	Professor Reinhard R. Baumann Department of Digital Printing and Imaging Technology Institute for Print and Media Technology Technische Universität Chemnitz, Germany
	Professor Ronald Österbacka Organic Electronics Department of Natural Sciences Åbo Akademi University, Finland
Opponents	Professor Reinhard R. Baumann Department of Digital Printing and Imaging Technology Institute for Print and Media Technology Technische Universität Chemnitz, Germany
	Professor Donald Lupo Organic and Nanoelectronics Group Department of Electronics and Communications Engineering Tampere University of Technology, Finland

List of publications

This thesis is based on the following original articles, which are referred to in the text as articles I–VI. The publications are reproduced with kind permission from the publishers.

I **Kopola P**, Aernouts T, Guillerez S, Jin H, Tuomikoski M, Maaninen A, Hast J (2010) High efficient plastic solar cells fabricated with a high-throughput gravure printing method. Solar Energy Materials & Solar Cells 94:1673–1680.

II **Kopola P**, Aernouts T, Sliz R, Guillerez S, Ylikunnari M, Cheyns D, Välimäki M, Tuomikoski M, Hast J, Jabbour G, Myllylä R, Maaninen A (2011) Gravure printed flexible organic photovoltaic modules. Solar Energy Materials & Solar Cells 95:1344–1347.

III **Apilo P**, Hiltunen J, Välimäki M, Heinilehto S, Sliz R, Hast J (2015) Roll-to-Roll Gravure Printing of Organic Photovoltaic Modules – Insulation of Processing Defects by an Interfacial Layer. Progress in Photovoltaics: Research and Applications 23:918-928.

IV Välimäki M, **Apilo P**, Po R, Jansson E, Bernardi A, Ylikunnari M, Vilkman M, Corso G, Puustinen J, Tuominen J, Hast J (2015) R2R-printed inverted OPV modules – towards arbitrary patterned designs. Nanoscale 7:9570–9580.

V **Kopola P**, Zimmermann B, Filipovic A, Schleiermacher H-F, Greulich J, Rousu S, Hast J, Myllylä R, Würfel U (2012) Aerosol jet printed grid for ITO-free inverted organic solar cells. Solar Energy Materials & Solar Cells 107:252–258.

VI Reinhardt J, **Apilo P**, Zimmermann B, Rousu S, Würfel U (2015) Determining the photocurrent of individual cells within an organic solar module by LBIC and the filtering approach: Experiments and simulations. Solar Energy Materials & Solar Cells 134:157–164.

Author's contributions

I	The author defined the research plan, conducted the gravure printing experiments and processed the gravure-printed solar cells. The author analysed the results, prepared the literature review, wrote the first version of the manuscript, and produced the final paper.
II	The author planned the experiments, prepared the gravure-printed modules and conducted the electrical measurements at University of Oulu together with Rafal Sliz. The author carried out the literature review, wrote the first version of the manuscript and prepared the final paper.
III	The author prepared the research plan and processed the laboratory-scale modules. The author conducted the R2R experiments with Marja Välimäki. The author performed the electrical measurements at VTT and more accurate measurements together with Rafal Sliz at the University of Oulu. The equivalent circuit models and lithographic samples were prepared together with Jussi Hiltunen. X-ray photoelectron spectroscopy measurements and analysis were performed by Santtu Heinilehto and surface energy measurements by Marja Välimäki. The author carried out the literature review, wrote the first version of the manuscript and prepared the final paper.
IV	The author participated in preparation of the research plan and performed the R2R pilot runs together with the corresponding author Marja Välimäki. The author prepared the electrical measurements together with the corresponding author and analysed the results. Marja Välimäki prepared the alignment and dimensional accuracy analysis. Elina Jansson made the measurements and analysis for the rheological characterization. Jarkko Tuominen and Jarkko Puustinen prepared the surface roughness characterisation. The author wrote the electrical measurement part of the manuscript, carried out the literature

	review related to R2R printing and coating and helped to review the entire paper.
V	The author planned the experiments, prepared the samples, carried out the measurements and analysed the results. Aerosol printing was conducted together with co-author Aleksander Filipovic. The author carried out the literature review, wrote the first version of the manuscript and prepared the final paper.
VI	The author defined the research plan together with the co-authors. The author prepared the DLIT, EL and LBIC measurements together with the corresponding author Jens Reinhardt. The author conducted the pre-filtering studies of the modules. The author carried out the literature review and wrote the introduction part of the paper. The author helped to review the entire paper.

Contents

Appendices

Articles I–VI

Abstract

Tiivistelmä

List of abbreviations and symbols

acceptor	electron accepting material
AM1.5G	air mass 1.5 global, reference solar spectrum
a-Si	amorphous silicon
ASTM	American Society for Testing and Materials
CD	cross directional
CdTe	cadmium telluride
CF	chloroform
CIGS	copper-indium-gallium-diselenide
c-Si	crystalline silicon
DLIT	dark lock-in thermography
donor	electron donating material
DSSC	dye sensitized solar cell
EL	electroluminescence
EQE	external quantum efficiency
ETL	electron transport layer
G	gravure printing
HOMO	highest occupied molecular orbital
HTL	hole transport layer
IEC	International Electrotechnical Commission
IPA	2-propanol (iso-propanol)
IQE	internal quantum efficiency
IR	infrared

ISOS	International Summit on OPV Stability
ITO	indium tin oxide
LBIC	laser beam induced current
LED	light-emitting diode
LiF	lithium fluoride
LUMO	lowest unoccupied molecular orbital
M	mismatch factor
o-DCB	1,2-dichlorobenzene
OLED	organic light-emitting diode
OPV	organic photovoltaics
OTFT	organic thin-film transistor
PCBM	methanofullerene [6,6]-phenyl C_{61}-butyric acid methyl ester
PCE	power conversion efficiency
PEDOT:PSS	poly(3,4-ethylenedioxythiophene)-poly(styrenesulfonate)
PET	polyethylene terephthalate film
PTB7	poly[[4,8-bis[(2-ethylhexyl)oxy]benzo[1,2-b:4,5-b′]dithiophene-2,6-diyl][3-fluoro-2-[(2-ethylhexyl)carbonyl]thieno[3,4–b]thiophenediyl]]
PV	photovoltaic
P3HT	poly(3-hexylthiophene-2,5-diyl)
R	reflectance
RS	rotary screen printing
R2R	roll-to-roll
Si-CCD	silicon charge coupled device
TiOx	titanium oxide
ZnO	zinc oxide
d	layer thickness
D	diode
e	elementary charge, $1.60217657 \times 10^{-19}$ C

E_{REF} (λ)	reference spectral irradiance
E_{S} (λ)	source spectral irradiance
eV	electronvolt, ~1.6×10^{-19} J
FF	fill factor
f_{fr}	frame rate of IR camera
$f_{lock\text{-}in}$	lock-in frequency
g m^{-2}	gram per metre squared; unit for active solid weight on cylinder surface
I–V	current-voltage characteristics of a solar cell
I_{SC}	short-circuit current
I_{MPP}	current at maximum power point
I_{PH}	photocurrent source
I_{0}	reverse bias saturation current
J_{sc}	short-circuit current density
k_{B}	Boltzmann's constant, $1.3806488 \times 10^{-23}$ J K^{-1}
l cm^{-1}	lines per centimetre; unit for line density
L inch^{-1}	lines per inch; unit of screen mesh
mg ml^{-1}	milligram per millilitre; unit for concentration
m min^{-1}	metres per minute; unit for printing speed
ml m^{-2}	millilitres per square metre; unit for cell volume
mN m^{-1}	millinewton per metre; unit for surface tension/surface energy
mPa·s	millipascal-second; unit for viscosity
n	diode ideality factor
n_{F}	number of frames (samples) per lock-in period
Ω·cm	ohms centimetre; unit for resistivity
Ω sq^{-1}	ohms per square; unit for sheet resistance
P_{IN}	input power
P_{MPP}	maximum power point
R_{a}	average surface roughness

rpm	rounds per minute; unit for spin coating speed
R_S	series resistance
R_{S_LIF}	series resistance of LiF layer
$R_{S\_CONTACT}$	sum of series resistance of ITO, PEDOT:PSS and Ca/Ag
R_{SH}	shunt resistance
R_{SH_LIF}	shunt resistance of LiF layer
S_R (λ)	spectral response of the reference cell
S_T (λ)	spectral response of the cell under measurement
$S^{0°}$	in-phase image
$S^{-90°}$	quadrature image
T	absolute temperature
V_{MPP}	voltage at maximum power point
V_{OC}	open-circuit voltage
W m^{-2}	watts per square metre; unit for irradiance
γ_{SV}	surface energy of the solid (substrate)
γ_{SL}	interfacial tension between solid (substrate) and liquid (ink)
γ_{LV}	surface tension of the liquid (ink)
η_{abs}	absorption efficiency
η_{CC}	charge collection efficiency
η_{CT}	charge transfer efficiency
$\eta_{exharvest}$	exciton harvesting efficiency
η_{GS}	geminate separation efficiency
ϴ	contact angle

1. Introduction

1.1 Background and research environment

Solar energy has unlimited potential – the amount of energy hitting the earth's surface in an hour is roughly equal to the entire energy consumption of all human activity in a year. Sunlight can be directly converted into electrical energy via photovoltaic (PV) technology. However, solar energy currently accounts for only ~1.3% of the gross electricity generated by renewable energy sources [1]. Light energy is abundantly available both outdoors and indoors and could be utilized to a much greater extent than at present. PV technologies can be categorized into three main groups: wafer-based crystalline silicon (c-Si) (1st generation), thin films (2nd generation) and emerging and novel PV technologies (3rd generation). Today, c-Si and thin films dominate the energy market. Crystalline silicon covers 85–90% of the PV market, with the remainder represented by thin-film technologies including amorphous silicon (a-Si), cadmium-telluride (CdTe) and copper-indium-gallium-diselenide (CIGS) [2]. Organic photovoltaics (OPV), as investigated in this thesis, is one of the emerging and novel PV technologies. OPV can be divided into three key technologies: polymer-based solar cells, small-molecule-based solar cells and dye-sensitized solar cells (DSSC). The main difference between polymer-based and small-molecule-based solar cells is the processing method; polymer-based solar cells are typically solution processed and small-molecule-based solar cells vacuum deposited. In DSSCs, the light absorption and charge carrier transport functions are separated [3]. Hereafter, the term "OPV technology" refers to polymer-based solar cells. In OPV technology several thin layers (electrodes, interfacial layers and the photoactive layer itself) of thickness ranging from tens of nanometres to a few micrometres are stacked on top of each other. All of these layers can be processed from solutions on low-temperature flexible substrates using high-volume production technologies such as roll-to-roll (R2R) printing and coating, which can potentially lead to cost-efficient industrial production [4]–[7]. The high optical absorption coefficient of photoactive materials enable active layer thicknesses in the range of 100–300 nm for efficient absorption [8]. In addition to potentially highly cost-efficient manufacturing, OPV technology has other benefits. Low energy input during manufacturing due to low processing temperatures gives a clear advantage over other technologies. Additionally, the flexibility, light weight and adjustable absorption region of photoactive materials are desirable characteristics for many application areas, while transparent/semitransparent OPVs are of interest in window applications [9], [10]. The potential of OPV technology has been forecasted in several market reports. For instance, IDTechEx valued the OPV market at $4.6 million in 2012, rising to $630 million by 2022 [11].

The first bilayer organic solar cell was discovered by Tang in 1986. This breakthrough device consisted of two organic layers of copper phthalocyanine and a perylene tetracarboxylic derivative deposited between electrodes [12]. Since this discovery, extensive research has been focused on improving the power conversion efficiency (PCE) beyond 10% [13], which is considered a threshold level for wider market penetration of OPV. Currently, the highest reported polymer-based organic solar cell has exhibited 10.6 % [14]. A major reason for this progress has been the rapid development of more efficient photoactive polymers. Further improvements are expected [15], but so far these record levels have been achieved with small-area cells processed with non-scalable techniques, such as spin coating or vacuum evaporation on glass under inert conditions. It was recently demonstrated by Hosoya et al. that it is in principle possible to obtain comparable results (9.0%) with small-scale (25 cm^2) modules and single cells (10.3%) prepared in inert atmosphere using a R2R compatible coating method [16]. Although novel high-performing polymers exceeding the 10% efficiency threshold have been developed, the most extensively studied polymer-fullerene system for upscaling the OPV process has been poly(3-hexylthiophene-2,5-diyl) (P3HT): methanofullerene [6,6]-phenyl C_{61}-butyric acid methyl ester (PCBM). Slot die coating has been the main processing approach for upscaling polymer-fullerene solar cells. Prof. F.C. Krebs and his team from the Danish Technical University and the US company Konarka (founded 2001, company filed in bankruptcy protection in 2012) have largely dominated OPV research in the field of R2R slot die coating. The key advantage of slot die coating is that there are no strict limitations on the properties of the coating inks. Inks with a wide viscosity and solids content range can be successfully coated [17]. In 2009, Blankenburg et al. reported on cells with a R2R slot die coated bilayer of poly(3,4-ethylenedioxythiophene)-poly(styrenesulfonate) (PEDOT:PSS) and P3HT:PCBM followed by thermal evaporation of aluminium. A maximum efficiency of 1.7% was achieved with an active area of 0.25 cm^2. The team focussed on testing several ink compositions and processing parameters such as coating speed, flow rate and coating width for both layers [17]. Concurrently, Krebs reported partly R2R-processed OPV modules with a structure of indium tin oxide(ITO)/zinc oxide(ZnO)/P3HT:PCBM/PEDOT:PSS/Ag. All layers except the batch screen printed Ag were R2R slot die coated. With modules having a total active area of 120 cm^2 built from 8 cells, a typical efficiency of 1.78% was reached [18]. In 2010 the first demonstration of fully R2R-processed OPV modules was reported by Krebs et al. They investigated the effect of increased active area on module performance. They also experimentally optimized the ITO width and gap. With this approach, a mean efficiency of 1.79±0.09% for 96 cm^2 modules and 1.18±0.13% for 360 cm^2 modules were attained. The maximum efficiencies were 2.00% and 1.69% for the module sizes of 96 cm^2 and 360 cm^2, respectively [19]. A larger batch of modules (totally ~2000 modules) having the same device configuration as previously described was fabricated. The active area of each module was 35.5 cm^2. A mean efficiency of 1.96±0.34% with a technical yield of 89% was reported [20]. Galagan et al. studied the bilayer R2R slot die coated structure with PEDOT:PSS and P3HT:PCBM by focussing on using non-halogenated solvents for the active layer, obtaining a module efficiency of 0.7% [21]. Krebs et al. have implemented R2R processing of ITO-free modules in which the ITO has been replaced by a flexography printed Ag grid and rotary screen printed PEDOT:PSS [22]–[24]. With these structures, they have shown the real potential of OPV R2R processing by building solar parks [5], [25]. They obtained stabilized PCE of 1.6-1.8% with initial values >2% for an active area of 14.7 m^2. The module consisted of ~21000 series connected cells on a 100 m roll [5]. In addition, Kaduwal et al. have demonstrated ITO-free R2R slot die coated cells. These bilayer cells with a plastic substrate/Cr/Al/Cr/P3HT:PCBM/PEDOT:PSS/Ag structure reached an efficiency of up to 2.9% [26].

Although slot die coating is a powerful technique for fabricating OPV modules, its major drawback is that the patterning produced by the coating process is restricted to continuous stripes. In contrast, mechanical printing technologies such as gravure printing, flexography printing, screen printing and offset printing bring the advantage of large-area arbitrary shape and size using only additive process steps in sequence. This increases the freedom of product design and its integration into a range of applications. This will be an extremely valuable feature in the future. The gravure printing technique was chosen for thin-film deposition of the OPV structures presented in this thesis over the other mechanical printing technologies due to the following aspects: i) R2R processability, ii) ink and printing master requirements for <200 nm layer thickness, iii) solvent variability and iv) robustness and high repeatability of the printing method. The state of the art of gravure-printed OPVs is summarized in **Figure 1**. The articles included in this thesis are referred to as I–IV.

Tuomikoski et al. (2006) introduced a new approach, gravure printing, for fabricating OPV devices with an efficiency of 0.5% [27]. Ding et al. (2009) prepared small-area (0.03 cm^2) gravure-printed OPVs consisting of two printed layers, PEDOT:PSS and P3HT:PCBM. They investigated the dependence between the active solid weight on cylinder surface ($g\ m^{-2}$) and solar cell performance. A maximum PCE of 1.7% was attained. Additionally, they studied the spreading of the active material using total concentrations in the range of 24-53 $mg\ ml^{-1}$ [28]. Kopola et al. (*Article I*, 2010) focussed on the layer uniformity of PEDOT:PSS and P3HT:PCBM with standard configuration by testing different ink compositions and engraving parameters. They obtained a maximum efficiency of 2.8% with an active area of 0.19 cm^2 [29].

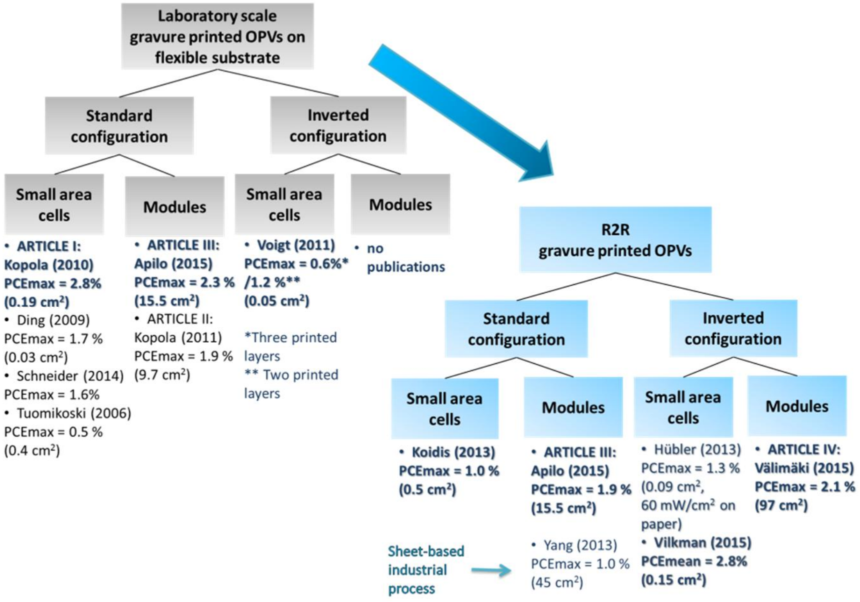

Figure 1. State of the art of gravure-printed OPVs.

In 2011 (*Article II*) the same research group also implemented side connected modules with an efficiency of 1.9% (area 9.7 cm^2) [30] and in 2014 (*Article III)* monolithically connected modules with an efficiency of 2.3% (area 15.5 cm^2) [31]. Schneider et al. (2014) used a poly[[4,8-bis[(2-ethylhexyl)oxy]benzo[1,2-b:4,5-b′]dithiophene-2,6-diyl][3-fluoro-2-[(2-ethylhexyl)carbonyl]thieno[3,4–b]thiophenediyl]] (PTB7) and PCBM blend as the active layer in their studies. They obtained 1.6% efficiency with small-area cells on flexible substrate [32]. Voigt et al. (2011, 2012) [33], [34] investigated inverted solar cells with a structure of plastic substrate/ITO/titanium oxide (TiO$_x$)/P3HT:PCBM/PEDOT:PSS. The benefit of inverted configuration in comparison to standard configuration is that the whole layer stack can be printed without any vacuum evaporation steps. Additionally, the stability of the structure is better than with standard configuration. The challenge was how to wet the high-surface-tension PEDOT:PSS ink on low-surface-energy P3HT:PCBM. Their solution was to use short, low-power plasma as a surface treatment and to modify the PEDOT:PSS with additives and solvents. A PCE of 0.6% was achieved with three printed layers [33], [34]. The first group to report on R2R-printed OPVs was Hübler et al. (2011) [35]. Interestingly, they fabricated inverted configuration small-area OPVs in R2R on paper substrate using a layered stack of paper/Zn/ZnO/P3HT:PCBM/PEDOT:PSS. The P3HT:PCBM was deposited by gravure printing followed by flexography printed PEDOT:PSS [35]. Koidis et al. (2013) studied PEDOT:PSS protection from air, and the effect of drying parameters on the morphology of P3HT:PCBM in the R2R environment [36], [37]. By careful drying optimization they achieved a maximum efficiency of 1.0% with 0.5 cm^2 small-area OPVs using a standard configuration [36]. Yang et al. (2013) were the first to process modules at industrial scale with an efficiency of 1.0% (active area 45 cm^2). However, they used a non-continuous sheet-based process in which the ink was applied to the doctor blade, which thus cannot be classed as R2R [38]. Apilo et al. (*Article III*, 2015) demonstrated R2R processing of large-area modules consisting of gravure-printed PEDOT:PSS and P3HT:PCBM. They noticed that when using a Ca/Ag electron contact the modules were all shorted due to detrimental pinholes with a diameter ranging from 20 µm to 50 µm. They investigated the insulation of holes and using a lithium fluoride (LiF)/Al electron contact obtained an efficiency of 1.9% for 15.5 cm^2 modules [31]. In 2015, the same research group announced fully printed polymer-fullerene OPV cells [39] and modules [40] combining gravure printing and rotary screen printing (*Article IV*). A maximum PCE of 2.1% was reached with module sizes up to 96 cm^2 [40]. This performance is comparable to the results obtained by slot die coating [19], [20]. The main differences between the competitive OPV manufacturing technologies, gravure printing and slot die coating, are summarized in **Table 1**. The most remarkable difference arises from the patterning capability of gravure printing, which gives design freedom for arbitrary shapes. However, the ink property requirements for gravure printing are more strict.

Table 1. Comparison of R2R gravure printing and slot die coating with respect to thin-film processing of OPV structures.

	Gravure printing	Slot die coating
Patterning	2D (arbitrary shapes)	1D (stripes)
Printing speed	OPV: 3–12 m min^{-1} [31], [35], [37], [40] Graphic industry: max 900 m min^{-1} [41]	OPV: 1–10 m min^{-1} [22]
Ink viscosity	OPV: 13–25 mPa·s [29], [40] Graphic industry: 50–200 mPa·s [41]	OPV: 1–270 mPa•s [19],[21]
Film preparation	OPV: challenging for low viscous ink	OPV: moderate
Dry film thickness	OPV: 50-240 nm [31], [37], [40] Graphic industry: 800–8000 nm [41]	OPV: 20–20000 nm [19]

In addition to OPVs, gravure printing has been introduced as an applicable technique for processing active layers in various other thin-film components such as organic light-emitting diodes (OLEDs) [42]–[48], organic thin-film transistors (OTFTs) [49]–[55], light-emitting cells [56] and diodes [57].

1.2 Motivation and structure of the thesis

This thesis examines gravure printing as a deposition method for manufacturing polymer-fullerene solar cells and modules. The thesis comprises six separate articles. Four of the articles cover research ranging from optimization of gravure printability and small-area device functionality at the laboratory scale to fully R2R-printed OPV modules processed in a pilot-scale environment. In addition, one of the articles focuses on testing complementary imaging techniques for understanding performance variations in monolithically connected modules. The last article deals with an alternative OPV structure with a fine line-printed grid.

The following research questions are addressed:

- Is gravure printing a feasible technique for preparing thin films for OPV structures with high uniformity and building functional small-area cells?
- Is the performance obtained with small-area cells (<cm^2) maintained when extending the active area (cm^2) and connecting separate cells electrically to modules?
- Can alternative structures be used to extend the active area of the cell without losing performance?
- Is the laboratory-scale process of OPV module preparation directly transferrable to R2R?
- How can functional OPV modules be R2R-processed despite detrimental nonidealities in the device layers?
- Can fully printed modules with high performance and high yield be R2R-processed?
- How can the defects and non-uniformities in OPV modules be characterized?

The relationship between articles and overview of the thesis content are summarized in **Figure 2**.

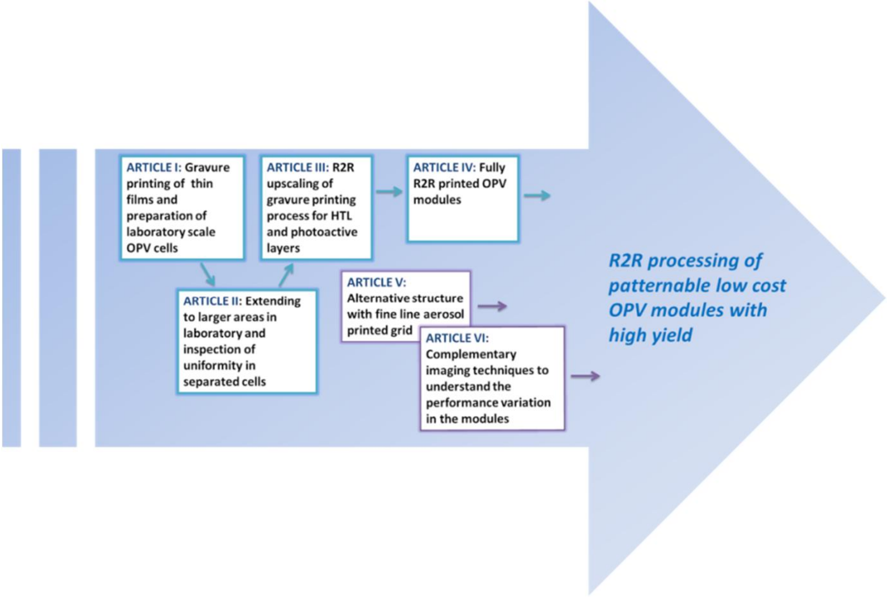

Figure 2. Overview of the content of the thesis. HTL refers to hole transport layer.

The thesis is organized as follows:

- Chapter 2 begins with an introduction to organic photovoltaics. The chapter covers the main physical processes occurring in organic photovoltaics as light energy is converted to electrical energy. The device structures and electrical characterization methods are also introduced.
- Chapter 3 focuses on the main processing approach used in this thesis, gravure printing. Additionally, other important processing methods are briefly described.
- Chapter 4 presents the imaging methods for characterization of OPV modules in terms of electrical inhomogeneities.

Chapters 5, 6, 7 and 8 include the scientific results and the materials and methods used in the research, followed by interpretation and discussion of the findings of the articles:

- Chapter 5 describes the materials used in the research. Additionally, the printing machinery used for deposition of OPV structures is introduced.
- In Chapter 6 the main results of the thesis are presented highlighting the results of the R2R processing of OPV modules.
- In Chapter 7 the results of the thesis are discussed as a whole and the significance of the results for the scientific community is critically evaluated. In addition, future research topics are highlighted.
- In Chapter 8 the results of the thesis are summarized.

2. Organic photovoltaics

In this chapter organic photovoltaics is introduced and the physical processes taking place in the organic solar cell structure during the conversion of sunlight to electrical energy are discussed. Furthermore, the device and module configurations and respective equivalent circuits are presented. The basics of the electrical characterization of solar cells are also presented.

2.1 Organic semiconductors

In 1977, Heeger, MacDiarmid and Shikarawa demonstrated that the conductivity of polyacetylene can be enhanced by many orders of magnitude by the addition of iodine [58]. This revolutionary discovery established the field of organic electronics and earned them the Nobel prize for Chemistry in 2000.

Organic semiconductors are based on conjugated polymers having alternating double bonds between carbon atoms. Sp^2 hybridization of the double bonded carbon atom forms three sp^2 hybridized orbitals and one unhybridized p_Z orbital. The three sp^2 hybridized orbitals form σ bonds with the neighbours and unhybridized p_Z orbital is available for π bonding. The p_Z orbital is located perpendicular to the sp^2 plane, as shown in **Figure 3**. The electrons in the π bond can be delocalized via conjugation with neighboring π bonds resulting in semiconducting properties of conjugated polymers. The ground state for conjugated polymers is formed by the upper π band edge named as highest occupied molecular orbital (HOMO). The lower π* band edge is known as the lowest unoccupied molecular orbital (LUMO). The optical bandgap of the conjugated polymers is determined by the HOMO and LUMO. The charge transport between molecules generally occurs by thermally activated hopping mechanism. [59]

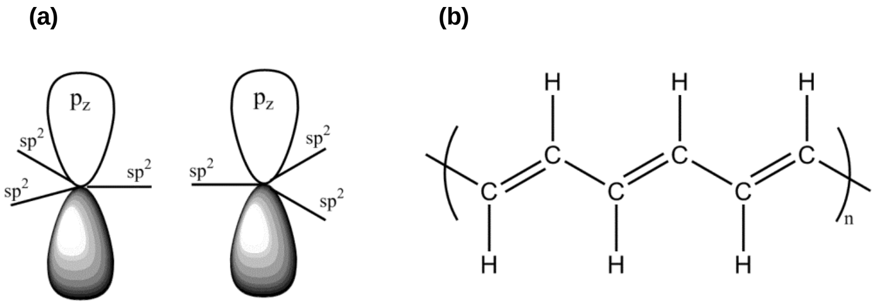

Figure 3. (a) Sp^2 hybridized and unhybridised p$_z$ orbitals. (b) Alternating double bonds between carbon atoms.

The most extensively investigated conjugated polymer for organic solar cells is P3HT, shown in **Figure 4**. P3HT is mainly responsible for absorption of light, transport of excitons, and transport of holes after charge separation. The operation principle of organic solar cells is described in the next section. Another well-known polymer material in organic electronics is PEDOT:PSS, which is used, e.g., in antistatic coatings, electronic components and displays. In organic solar cells it performs as a hole transport layer (HTL) [60].

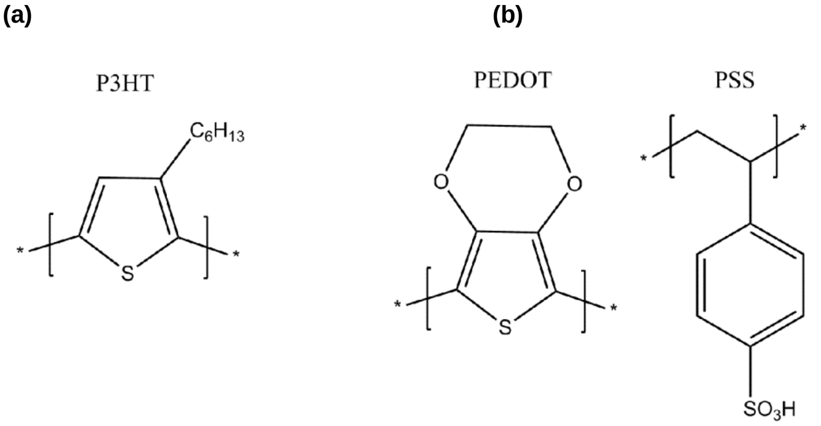

Figure 4. Chemical structures of (a) poly (3-hexylthiophene), P3HT and (b) poly (3,4-ethylenedioxythiophene) mixed with poly(styrenesulfonic acid), PEDOT:PSS.

2.2 Operation principle of organic solar cells

The first organic solar cells were based on a single photoactive layer placed between two electrodes. The efficiencies obtained were less than 1% [61]. A bilayer structure was invented in 1986 in which two organic materials were laid on top of each other. One acted as an electron donating material, the donor, and the other as an electron accepting material, the acceptor. With this configuration ~1% efficiency could be reached [12]. In 1995, bulk heterojunction configuration (**Figure 5**) was introduced for the first time. In bulk heterojunction, the donor and acceptor materials are mixed together in a single photoactive layer forming an interpenetrating network of donor and acceptor phases. [62]

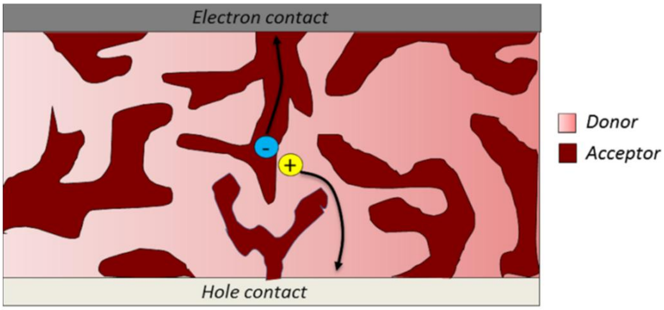

Figure 5. Bulk heterojunction configuration.

The operation principle of bulk heterojunction organic solar cells is schematically shown in **Figure 6**.

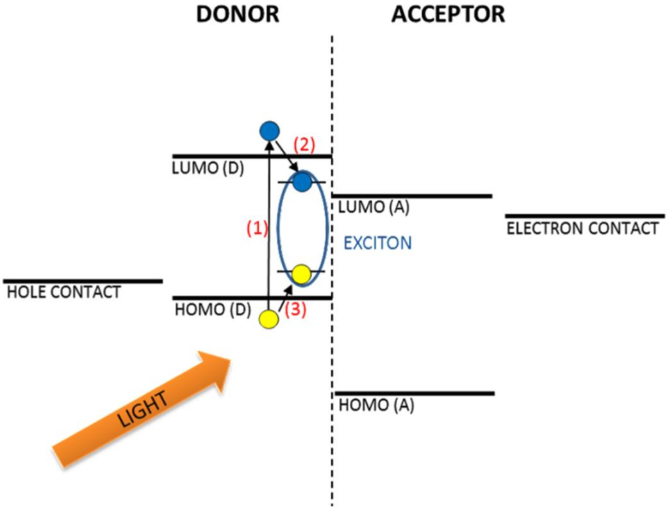

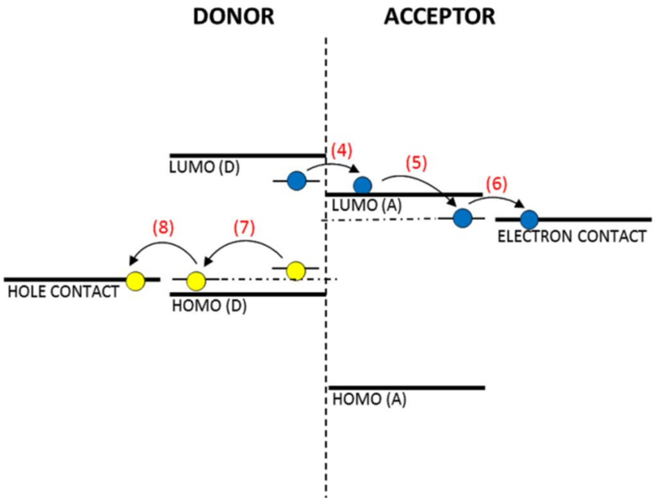

Figure 6. Basic physical processes in an organic solar cell, from light absorption to the extraction of charge carriers.

The light is absorbed (1) mainly in the donor material, i.e. conjugated polymer, forming photogenerated strongly bound electron-hole pairs, i.e. excitons (2, 3). The excitons are mobile and electrically neutral. The excitons diffuse along the polymer chains to the interfaces of the donor and acceptor. In the interface, electron charge transfer from the donor to the acceptor takes place (4). However, the charges are still bound due to the Coulomb interaction, although not as strongly as excitons. The binding energy is typically ~0.5 eV. The coulombically bound charge pair is called a polaron pair or charge-transfer state. The polaron pair needs to be dissociated to free charge carriers (5,7). The free charge carriers are transported to the respective electrodes (the electrons through the acceptor phases and holes through the donor phases) via percolated pathways (6,8) [8], [63].

The extracted photocurrent is highly dependent on the morphology of the photoactive material, i.e. how the donor and acceptor phases are arranged. The optimization of drying procedures to achieve better morphology for more efficient charge extraction has been extensively reported. It should be noted that for exciton dissociation the fine-structured donor phases are favourably limited by the exciton diffusion length [8], [63].

However, not all absorbed photons result directly in free charge carriers. Various recombination paths exist in organic solar cells. Exciton recombination may occur if the exciton does not reach the donor-acceptor interface during its lifetime. When an electron is transferred from donor to acceptor, the charge carriers are still bound by Coulombic attraction; if the bound pair does not separate by the impact of drift or diffusion, geminate recombination will occur. Another path is bimolecular recombination, in which the free charge carriers recombine during their way to the respective electrodes [64].

2.3 Solar cell characteristics

The performance and quality of a solar cell can be described based on various electrical parameters derived from the current-voltage (I–V) characteristics. The IV measurement is performed by applying an external voltage and measuring the electrical current as a function of the applied voltage. The measured cell is illuminated with a light source, a solar simulator, adjusted to a light intensity of 1000 Wm^{-2} with a spectrum approximating the air mass (AM) 1.5 global spectrum. AM refers to the length of path through the earth's atmosphere traversed by the direct solar beam, expressed as a multiple path traversed to a point at sea level with the sun directly overhead. For accurate characterization of solar cells the measurement conditions need be set according to the International Electrotechnical Commission (IEC) Standard 60904-3 edition 2 and American Society for Testing and Materials (ASTM) Standards G173 and E927 [65]–[70]. Irradiance is adjusted using a calibrated Si reference cell, taking into consideration the spectral error (mismatch factor) arising from the following: i) the spectral irradiance of the light source does not match the AM1.5 global reference spectrum and ii) the spectral responses of the cell under measurement and the reference cell are different. The mismatch factor is defined as follows:

$$M = \frac{\int_{\lambda_1}^{\lambda_2} E_{Ref}(\lambda)\, S_R(\lambda)\, d\lambda}{\int_{\lambda_1}^{\lambda_2} E_{Ref}(\lambda)\, S_T(\lambda)\, d\lambda}\;\frac{\int_{\lambda_1}^{\lambda_2} E_S\,(\lambda) S_T(\lambda)\, d\lambda}{\int_{\lambda_1}^{\lambda_2} E_S\,(\lambda) S_R(\lambda)\, d\lambda}$$

where E_{Ref} (λ) is the reference spectral irradiance, E_S (λ) is the source spectral irradiance, S_R (λ) is the spectral response of the reference cell and S_T (λ) is the spectral response of the cell under measurement [71].

A typical IV response curve of a solar cell under illumination is depicted in **Figure 7**. The illumination deflects the IV curve downwards.

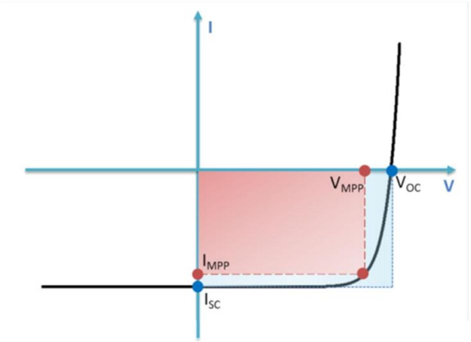

Figure 7. Typical IV response curve of a solar cell under illumination.

In the fourth quadrant the solar cell is producing power. The parameters derived from the IV curve include maximum power point (P_{MPP}), open-circuit voltage (V_{OC}), short-circuit current (I_{SC}) and fill factor (FF). The maximum power point is the point on the IV curve (V_{MPP}, I_{MPP}) where the output power is at its maximum. I_{SC} is the point where there is no externally applied voltage (V = 0V). Conversely, V_{OC} refers to the point where no external current is flowing through the solar cell (I = 0A). The FF is defined as the ratio of the two rectangles shown in **Figure 7**. It can be written as follows:

$$FF = \frac{V_{MPP} I_{MPP}}{V_{OC} I_{SC}}$$

The PCE is defined as the extracted power divided by the input power (P_{IN})

$$PCE = \frac{P_{MPP}}{P_{IN}} = \frac{V_{MPP} I_{MPP}}{P_{IN}} = \frac{FF V_{OC} I_{SC}}{P_{IN}}$$

The PCE shows how much of the input power can be converted to electrical power by means of a solar cell [72].

One diode equivalent circuit model for a solar cell is represented in **Figure 8**. The equivalent circuit consists of four parts: photocurrent source I_{PH}, diode D1, series resistance R_S and shunt resistance R_{SH}.

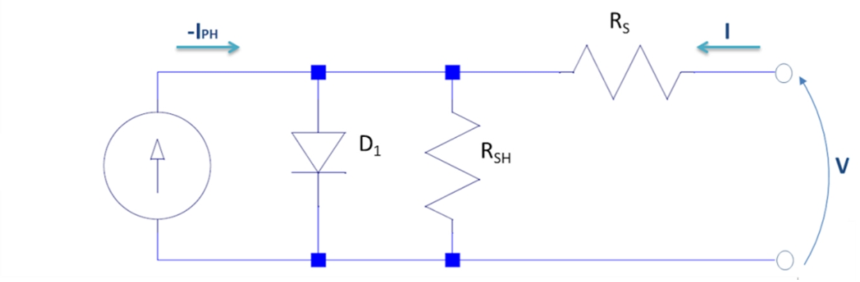

Figure 8. Equivalent circuit for a solar cell (one-diode model).

Mathematically, the relation is expressed as follows:

$$I = I_0 \left[\exp\left(\frac{e(V - IR_S)}{nk_B T} \right) - 1 \right] + \frac{V - IR_S}{R_{SH}} + I_{PH},$$

where I_0 is the reverse bias saturation current, e is the elementary charge (1.60217657 × 10^{-19} C), n is the diode ideality factor, k_B is Boltzmann's constant (1.3806488 x 10^{-23} J K^{-1}) and T is absolute temperature [72].

2.4 Organic photovoltaic device structures

There are three basic structural configurations for OPV solar cells: standard, inverted and tandem, as shown in **Figure 9**.

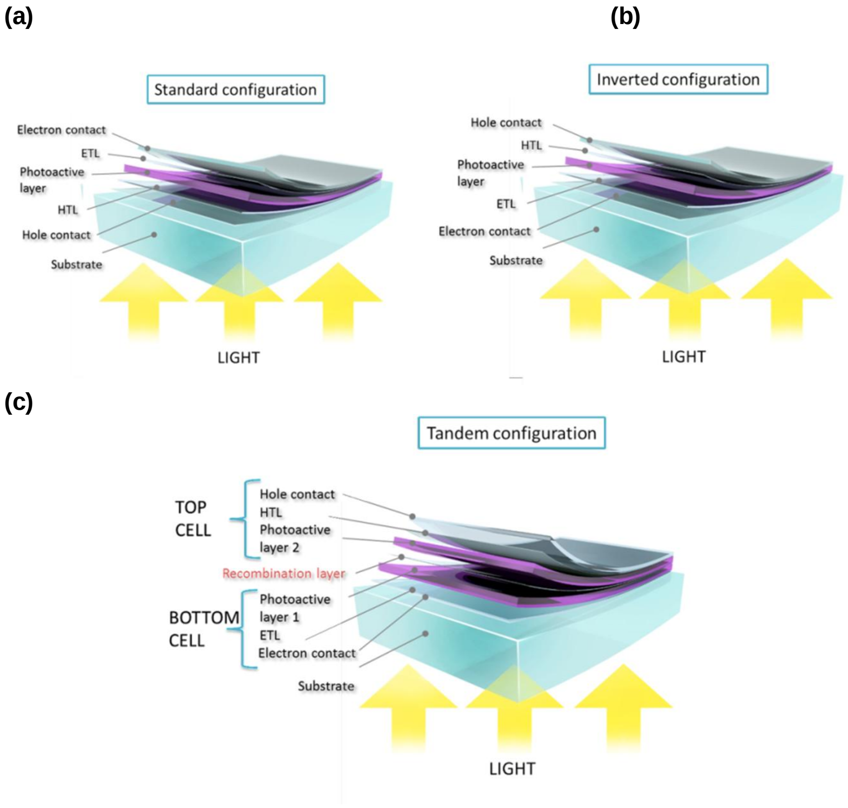

Figure 9. Basic OPV solar cell configurations: (a) standard, (b) inverted and (c) tandem. HTL refers to hole transport layer and ETL to the electron transport layer.

All basic OPV configurations are built on a transparent substrate, either rigid glass or a flexible substrate such as polyethylene terephthalate film (PET) suitable for R2R processing. ITO is the most used transparent electrode layer. In the standard configuration (**Figure 9**a) the high work function ITO is covered with a PEDOT:PSS interlayer followed by deposition of the photoactive layer. The main function of the PEDOT:PSS is to planarize the ITO surface. It also improves the transport of holes (HTL) to the ITO hole contact. Additionally, it partly covers local spikes originating from the ITO and thus diminishes the probability of electrical short circuits [60]. Ca and LiF, the most commonly used interfacial materials on the electron contact side (electron transport layer, ETL), are covered by an aluminium or silver electrode layer. The interfacial layers are mainly used to minimize the energy barrier between the photoactive layer and the electrodes and to enhance the selection of one type of charge carrier (either holes or electrons) to improve the PCE. In recent years, research has increasingly focussed on the inverted configuration (**Figure 9**b) in which the electron and hole contacts are inversed by changing the positions of the interfacial layers [73]–[75]. The main motivation for using the inverted configuration is to avoid low work function ETL materials, which are sensitive to oxygen and moisture and effectively limit the lifetime. In addition, the inverted configuration enables fully R2R-processed structures [5]. Metal oxides such as ZnO and TiO_x are employed as ETL alternatives [74], [76]–[82] and molybdenum trioxide has been introduced as an HTL substitute for PEDOT:PSS [77], [83]–[84] due to solution processability, lifetime extension and/or performance improvement.

In the tandem configuration (**Figure 9**c) two photoactive materials are stacked, one with high bandgap and other with low bandgap. With this concept, the light absorption band can be broadened by covering more of the solar spectrum [85].

ITO is expensive and the price of indium is expected to rise further due to limited indium resources [86]. In addition, the fragile nature of ITO is a drawback in some applications. Therefore, the search for alternative solutions to replace ITO is underway. PEDOT:PSS with a combination of metal grid [5], [26], [75], [87-95], silver nanowires [96], [97], carbon-based alternatives [98]–[103] and various gallium-indium-zinc-aluminium oxide compounds such as aluminium doped zinc oxide [104] are the main routes of investigation.

2.5 Modules

Organic solar cells can be monolithically connected to photovoltaic modules. This is necessary to obtain the desired output voltage and output current for a specified application. The output voltage of a single-junction organic solar cell is generally between 0.6–0.8 V depending on the materials used. The output voltage can be increased by connecting cells in series, as shown in **Figure 10**. The top electrode of the first cell is monolithically connected to the bottom electrode of the next cell. This connection sequence is repeated over the whole module structure. The patterning of the cells and direct monolithic connection can be made in the printing process without any additive processing steps. Also, with slot die coating a striped structure can be attained. If the deposition method used leads to a fully covered surface additional post-processing, such as laser patterning, is required [105].

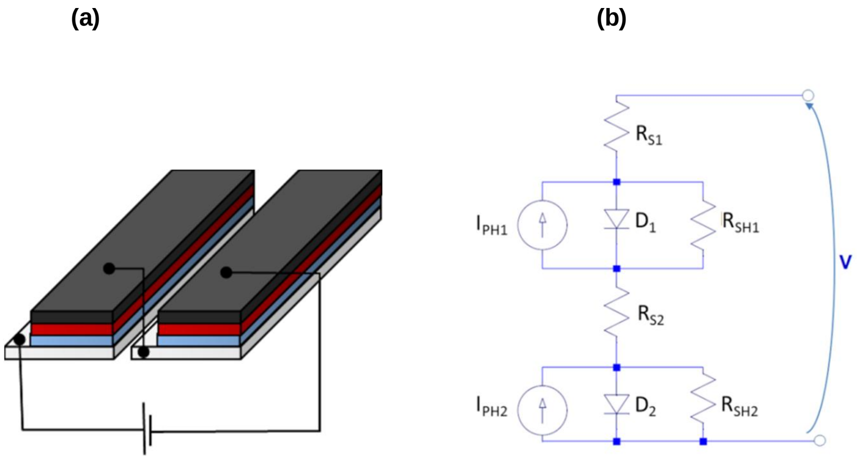

Figure 10. (a) Series connection of single cells to a photovoltaic module. (b) Equivalent circuit of two series connected cells.

The output voltage of the module is directly proportional to the number of cells connected in series. The output current is dependent on the photoactive area. The cell size is limited by the resistivity of the electrodes. To ensure low resistive losses, large cell sizes should be avoided. Additionally, by increasing the cell size the risk of detrimental processing defects becomes higher. The output current is also highly dependent on the illumination conditions, i.e. light intensity. In a series connection it is critical that all cells produce the same output current. The worst performing cell limits the output current of the whole module. Current variations can be due to internal or external sources. Internal variations can originate from large thickness deviations in the photoactive layer or defects. Conversely, external variations can be due to shadowing of the cells, i.e. differences in light intensity absorbed by the photoactive layer. To increase the output current, the solar cells can be connected in parallel [106].

3. Printing technologies

This chapter provides a general introduction to printing technologies, with a focus on gravure printing, its working principle and the structure of the image carrying medium – the printing cylinder. Additionally, the parameters affecting the print quality are defined. Furthermore, the differences in the requirements for printed electronics compared to traditional printing are briefly discussed. Metal aerosol jet printing is also introduced at the end of the chapter.

3.1 Printing technologies in general

The history of printing goes back to 3000 B.C. and the Near East, where relief printing onto clay via stone cylinders was invented. However, the most revolutionary step in the history of printing as a mass manufacturing method occurred in 1439 when Johannes Gutenberg introduced the first printing press [107]. Printing is a reproduction process in which printing ink is applied to a substrate in order to transfer information in a repeatable form using an image-carrying medium [41]. Printing techniques are additive processes in which ink is deposited on a substrate in a localized manner in order to obtain a desired pattern. Different physical processes are used to identify the areas where the material is to be deposited and the areas to be left uncovered. Printing technologies can be divided into two main categories, as shown in **Figure 11**. A common feature of all conventional mechanical printing techniques is that they require a printing master for the image transfer. Gravure, flexography, offset and screen printing are techniques where the information to be transferred is denoted by image elements (ink containing) and non-image elements. In gravure printing the printing elements are recessed, whereas in flexography printing the raised elements receive the ink and transfer it to the substrate. Ink can also be localized on a plate having areas of different surface energy, leading to wetted or dewetted areas, such as in offset printing. In screen printing the ink is pressed through the openings in the printing master. Non-contact printing techniques such as ink-jet printing and electrophotography do not use a printing master for image information transfer, instead the information for the printing head comes electronically direct from a computer. In ink-jet printing, for example, the ink is transferred through nozzles directly onto the substrate [41].

The choice of printing method in the graphic arts industry is inherently based on run length (cost structure) and required print quality as well as the end-use requirements for the substrate (paper, plastic, fabric, etc.) and whether personalized information is needed for each copy (mechanical vs. non-impact methods). In printed electronics the choice is more complex and highly dependent on the materials printed and the required printing layer thickness [108].

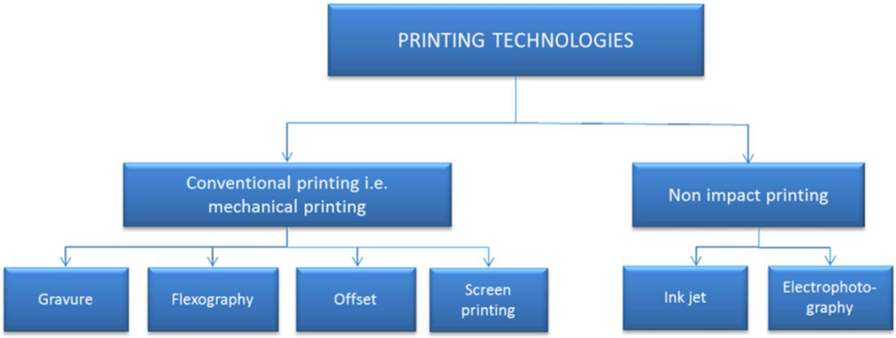

Figure 11. Printing technologies.

3.2 Gravure printing

Gravure printing is used to print high-quality and high-volume printed matter and packaging. The advantages of the gravure printing technique are its inherently simple working principle, simple printing equipment, high production speed, stability of the process, high through-put, and high resolution. Additionally, various solvents can be used in gravure printing as the printing cylinders are made of chrome plated copper. Disadvantages of gravure printing are the high cost of cylinders, high requirements for suitable process parameters and high quality demands of substrates (e.g. very smooth surface). The gravure printing unit consists of five parts: gravure cylinder, impression cylinder, doctor blade system, ink fountain, and dryers [41], [107], [109]. The working principle of gravure printing is illustrated schematically in **Figure 12**. The dryer unit is not shown in the schematics.

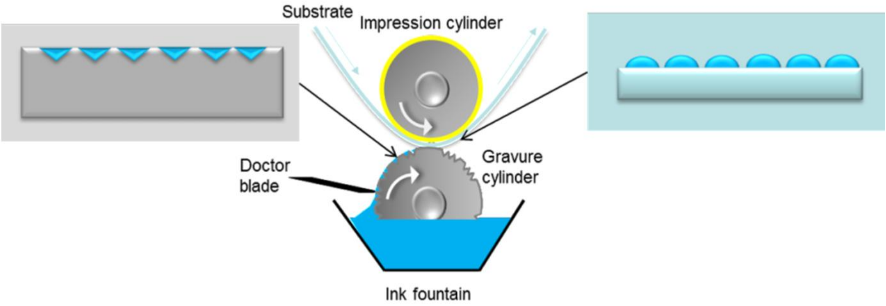

Figure 12. Schematic diagram of the gravure printing process.

The image elements, i.e. cells, are engraved onto the surface of the printing cylinder, whereas the non-image areas remain at the original level. In the gravure printing process, the engraved printing cylinder rotates in an ink fountain, resulting in a fully inked cylinder. At this point, the ink is also in the non-image areas. A doctor blade system wipes off the excess ink, leaving the ink only in the cells. In this way, the amount of ink assigned to the substrate is accurately controlled. The ink is transferred onto the substrate under high pressure in a nip formed between the printing cylinder and impression cylinder. The ink viscosity and adhesion between the ink and the printing cylinder greatly affect the emptying of the cells on the printing cylinder. Adhesive forces between the substrate and the ink also aid the ink transfer efficiency. Usually, the wet ink layer is dried by evaporation facilitated by hot air directly after each printing unit [41].

The printing cylinder is typically engraved either electromechanically or by laser [110]. In electromechanical engraving, the stylus of the engraving head penetrates the copper coating of the printing cylinder to form image elements with desired engraving parameters. The geometry of the cell is dependent on the stylus of the engraving head, the penetration depth and the rotating speed of the printing cylinder during the engraving process [41]. Electromechanically engraved cylinders with a line density (lines per centimetre) of 120 l cm^{-1} and 210 l cm^{-1} are shown in **Figure 13**. In laser engraving, the cylinder surface material is melted and vaporized by the laser beam to form recessed cells. By controlling the diameter of the beam, spherical cells with varying width and depth can be engraved [110], [111]. After engraving, the cylinder is plated with chrome to increase its durability and improve the filling and emptying of the cells. The cells are separated by the cell walls, resulting in printed dots on the substrate. The cell walls also support the doctor blade system in the wiping process [112].

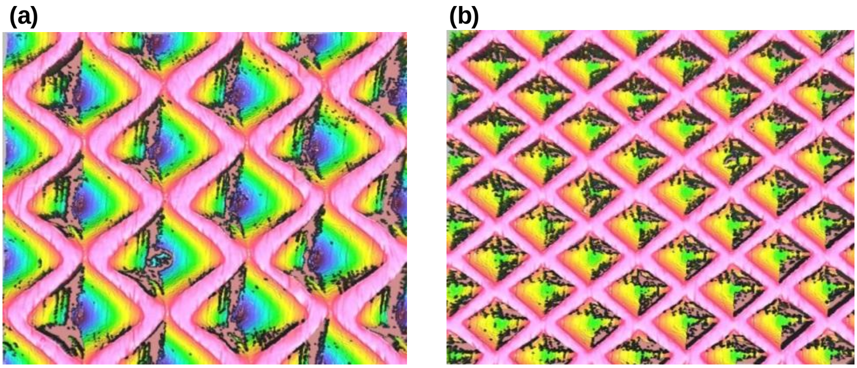

Figure 13. 3D images of an electromechanically engraved gravure printing cylinder with a line density of (a) 120 l cm^{-1} and (b) 210 l cm^{-1}.

In the graphic industry a discrete dot structure is desirable [113], [114]. The print quality and ink transfer are mainly affected by the viscosity of the ink and other ink properties, cell geometry, screen ruling i.e. line density, printing speed, nip pressure, doctor blade geometry and wetting properties of the printing substrate. Although the working principle and the printing unit for gravure printing are rather simple, a number of variables [41], [115], [116] affect the process, as shown in **Figure 14**.

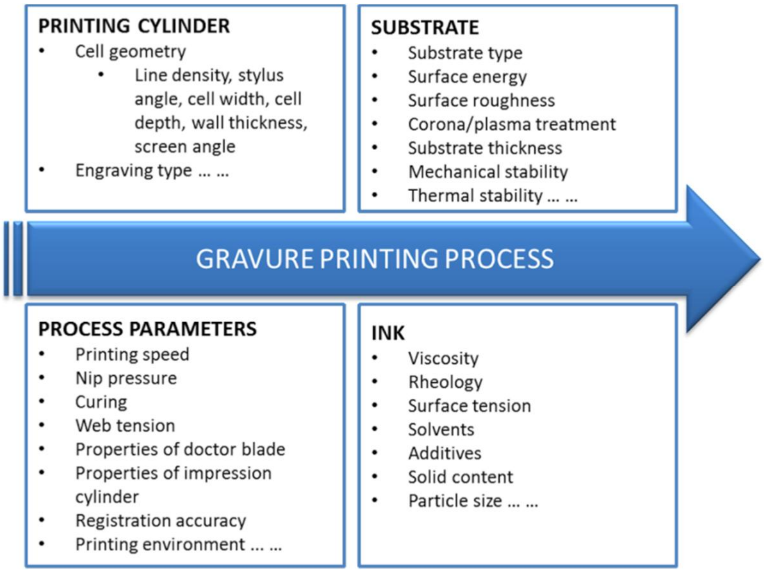

Figure 14. Process variables in gravure printing.

The viscosity is the resistance of the fluid to deformation in the presence of an external force [109]. Gravure printing requires low-viscosity inks, typically in the order of 50–200 mPa•s, since the ink has to flow in and out of the engraved cells at high printing speeds. Low-viscosity inks result in thin layers in the range of 0.8–2 µm [41]. The wetting properties of the ink on the substrate can be roughly estimated by measuring the relative contact angles and estimating the surface energy of the solid and by determining the surface tension of the liquid. The contact angle is defined by Young’s equation as follows:

$$\gamma_{SV} - \gamma_{SL} = \gamma_{LV} \cos\theta$$

where γ_{SV} is the surface energy of the solid (substrate), γ_{SL} is the interfacial tension between the solid (substrate) and liquid (ink), γ_{LV} is the surface tension of the liquid (ink) and Θ is the contact angle. Young expressed the equation in his publication only in written form [117]. A graphical representation of Young's equation is shown in **Figure 15**.

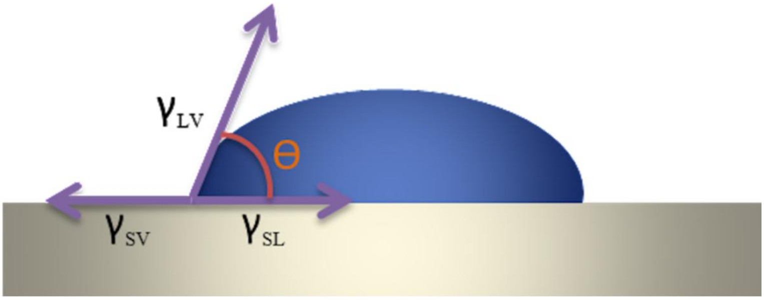

Figure 15. Graphical representation of Young's equation.

The requirements for thin films in printed electronics differ significantly from the graphical industry. The printing processes for the graphical industry have been designed according to the requirements set by the detection limit of the human eye. In printed electronics, the dot structure of gravure printing must be lost by merging the dots together to produce uniform films [109]. In addition, specific layer thickness and roughness are needed for each layer in order to obtain the desired electrical functionality in devices. Electronic devices have a multilayered structure. The properties of the interfaces between these layers are of importance for the charge carriers travelling through or along them. Furthermore, chemical interaction between the layers should be avoided, i.e. the layer on top should not dissolve the layer beneath [108], [109].

3.3 Metal aerosol jet printing

Metal aerosol jet printing is a non-contact printing method. The schematics of the operating principle are shown in **Figure 16**. First, an aerosol of the metal ink is created, e.g., ultrasonically. The aerosol is transferred to the deposition head via a heatable tube in which viscosity adjustment can be carried out. A sheath gas system is used to focus the aerosol stream. The gas stream is transported through the tip onto the substrate. The sheath gas ensures that the aerosol is not in contact with the tip, thus avoiding tip clogging. Aerosol jet printing enables the use of inks with a high viscosity and particle size range, so the ink properties are not tightly limited [118].

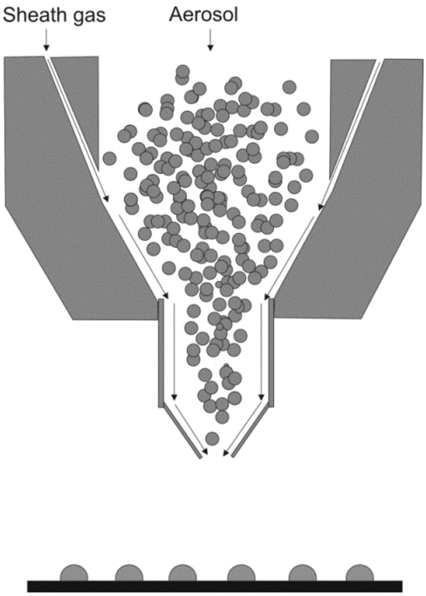

Figure 16. Working principle of the metal aerosol jet printing deposition head.

4. Electrical imaging of organic photovoltaics

Electrical characterization based on IV measurement only provides information on the overall functionality of the organic photovoltaic cells and modules. Electrical imaging methods, such as electroluminescence (EL) imaging, dark lock-in thermography (DLIT) and laser beam induced current (LBIC) introduced in this chapter, provide complementary information on, for example, defects, shunts and processing variations affecting electrical functionality [119], [120].

4.1 Electroluminescence imaging

EL imaging can be used for identifying multiple defect types, such as dark spots, electrode defects or areas with increased current density [121]. EL imaging relies on the following principle: the charge carriers are injected into the photoactive layer (electrons from electron contact and holes from hole contact), thus forcing the charges to recombine. Radiative recombination takes place via the charge transfer state at the donor-acceptor interface [64]. The operation in a solar cell is the time-reversed process to light-emission (OLED). The same states are responsible for both the photo-generation of charge-pairs as well as light-emission of injected charges. Nevertheless, EL efficiency of OPVs is not comparable to OLEDs, being a few orders of magnitude less. As previously explained, a forward current is passed through the solar cell. Since the injection current is forced through the active layer and the interfaces, the electrical functionality of both can be detected simultaneously [120]. A schematic of the EL imaging system is shown in **Figure 17**.

The EL spectra of P3HT:PCBM with a ratio of 1:1 ranges from 900–1600 nm and the emission peak lies in the vicinity of ~1200 nm [64], [121]. This sets requirements for detection of the EL signal, especially when using silicon charge-coupled device (Si-CCD) camera, as only a small part of the EL signal is in the camera detection region (350–1100 nm) [121].

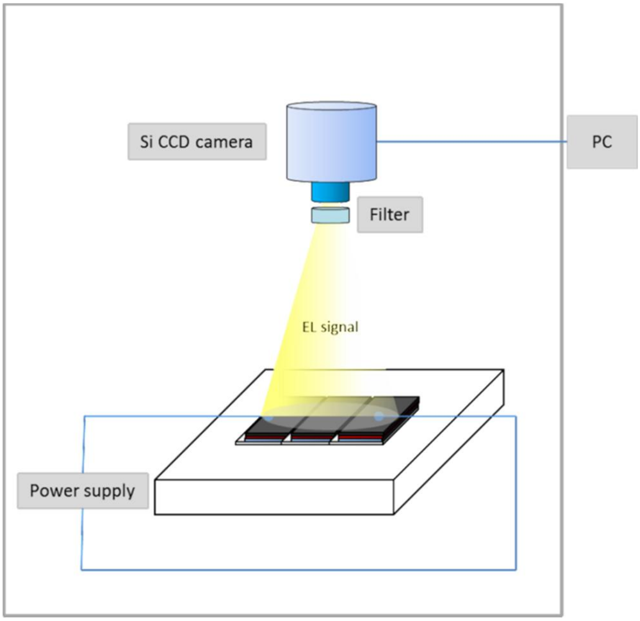

Figure 17. Schematics of the EL imaging system.

4.2 Dark lock-in thermography

DLIT is used mainly for the detection of shunts in the solar cell structures. Nominal thermal sensitivity of the most recent infrared (IR) cameras is in the order of 10–20 mK. In order to measure even weaker heat sources, an application of lock-in procedure is required to extract the signal from statistical noise. In DLIT a periodic voltage signal with lock-in frequency ($f_{lock\text{-}in}$) is applied to the sample without illumination and thus causing the dark current to flow in the solar cell. At possible shunt positions (low resistivity point or short cut) the current flow creates local power dissipation and increased temperature point. The working principle of the DLIT is described in **Figure 18**. In the first half of each lock-in period, periodic voltage signal is applied to the solar cell. An IR camera operating with selected frame rate converts the 2-dimensional solar cell surface temperature distribution into an image. The generated IR images are digitally processed in two channels multiplying the images by a set of weighting factors and summing up the results in two frame storages. In the first channel the frames are weighted with the weighting factors following the sine function, and in the second channel with the cosine function. The weighting factors are synchronised to the periodic voltage signal applied to the sample. Two images are resulted from a lock-in thermography experiment, an in-phase image (S^{0°) and a quadrature image (S^{-90°). The in-phase image has the best spatial resolution and is used to display point-like heating sources. Correspondingly, quadrature image shows homogeneous heating and point sources with low spatial resolution [122], [123].

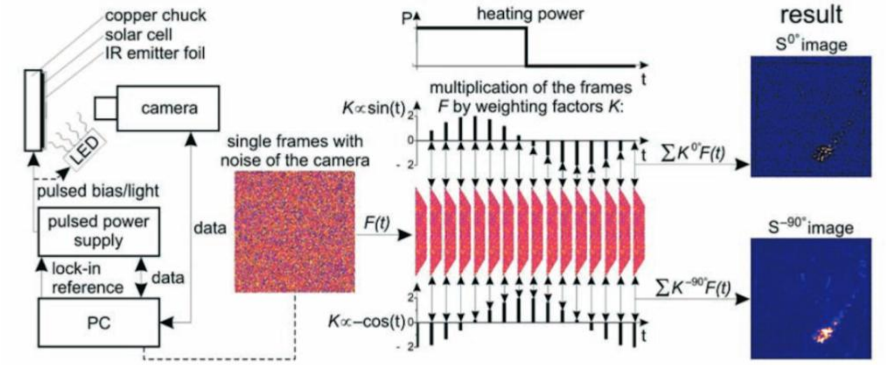

Figure 18. Measurement setup of a camera based dark lock-in process. Here, 15 frames per period are taken resulting in the summed $S^{0°}$ and $S^{-90°}$ images. In DLIT a periodic voltage signal is used. For illuminated LIT the light is pulsed with LED (light-emitting diode). *Reprinted with the permission of ASM International* [123].

4.3 Laser beam induced current

LBIC imaging can be used for detecting localized areas of deposition defects, shunting, and interconnection problems [124]. In LBIC imaging, the solar cell is scanned with a focused laser beam point-by-point deflecting the beam stepwise in x-and y-direction (see **Figure 19**). The extracted local photocurrent at each point is measured and combined with the information of the laser beam's x-y position. As a result, a two-dimensional LBIC map is collected and constructed by a computer. The resolution of LBIC is limited by the diameter of the laser spot, which is usually around 100 µm. The light applied by the laser is absorbed into the photoactive layer and the current passes through the interfaces to the electrodes, enabling the total functionality of the solar cells to be investigated [120]. The measurement system essentially consists of various lasers with different wavelengths, current measurement, and a computer for preparing the data analysis and compiling the photocurrent maps.

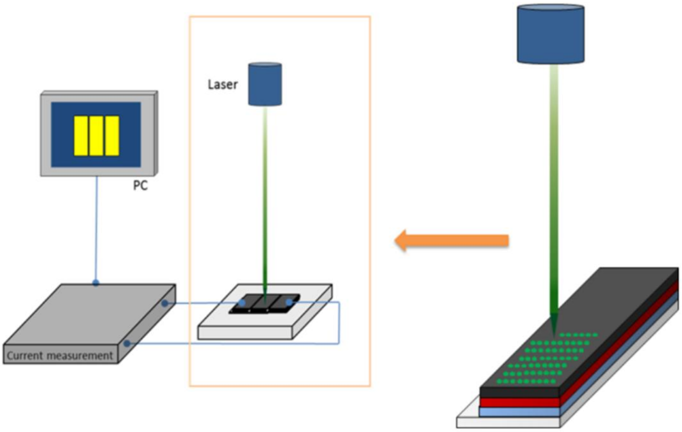

Figure 19. Schematic of a LBIC measurement system.

By data handling, the extracted current is scaled to high-resolution maps of external quantum efficiency (EQE), internal quantum efficiency (IQE) and reflectance (R). EQE is the number of electrons extracted from the solar cell per photon absorbed and is defined as: [60]

$$\eta_{EQE} = \eta_{abs}\eta_{exharvest}\eta_{CT}\eta_{GS}\eta_{CC}$$

where η_{abs} is absorption, $\eta_{exharvest}$ exciton harvesting, η_{CT} charge transfer, η_{GS} geminate separation and η_{CC} charge collection efficiency. IQE takes into consideration only the photons that are absorbed by the photoactive layer. The relation between IQE, EQE and R is: [72]

$$\eta_{IQE} = \frac{\eta_{EQE}}{1 - R}$$

5. Materials and methods

In this chapter the printing machinery used for deposition of OPV cells and modules in laboratory and R2R pilot environments are introduced. Additionally, the materials, processing and characterization details are summarized.

5.1 Gravure printing machines

The gravure printing experiments at the laboratory scale were conducted with a table top sheet-based printer, Schläfli Labratester I (Articles I, II and III) shown in **Figure 20**. In the printing machine, the printing speed can be varied between 10 levels. For instance, level 3 corresponds to ~7 metres per minute (m min^{-1}) and level 8 to ~18 m min^{-1}. Other parameters that can be adjusted include nip pressure, doctor blade angle, the distance between the doctor blade and the printing plate and doctor blade pressure. The following settings are used (if not otherwise mentioned in Section 5.2 in which the deposition details for each layer are described): printing speed 18 m min^{-1}, doctor blade angle 72°, adjusting screw for the nip pressure 42 mm, adjusting screw for the distance between the doctor blade and printing plate 17 mm, adjusting spring for the doctor blade pressure 17 mm and applied amount of ink 500 µl.

Figure 20. Laboratory-scale sheet-based gravure printing machine (Schläfli Labratester I).

The pilot printing experiments and fabrication of OPV modules were performed with a ROKO printing machine, as shown in **Figure 21**, which has four replaceable units including gravure, flexography and rotary screen printing. However, in this study (Article III and IV) only the first unit for direct gravure printing or rotary screen printing was used in order to maximize the total drying capacity to four meters. In **Figure 21**, the different parts of the pilot printing machine are indicated by numbers and described briefly in the figure caption. The used printing parameters for gravure printing and rotary screen printing are described in Section 5.2 in which also the material, processing and characterization details are summarized.

(a)

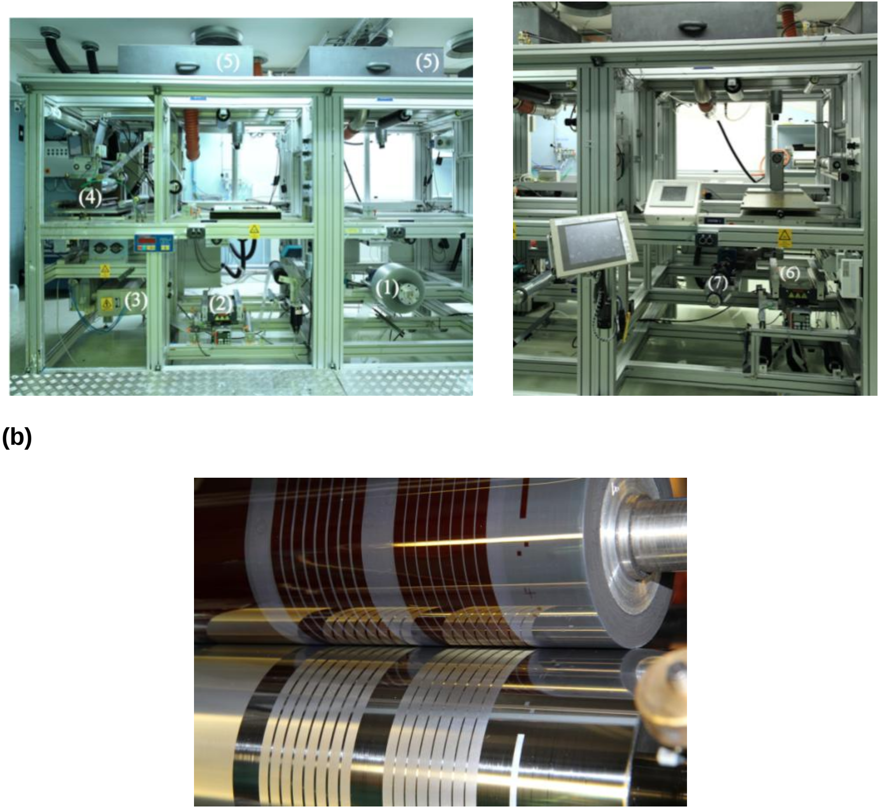

Figure 21. (a) ROKO pilot printing machine used for R2R processing of OPV modules. The following units are indicated, starting from the beginning of the web path: (1) unwinder, (2) web guide 1, (3) plasma treatment unit, (4) printing unit, (5) hot air drying units, (6) web guide 2 and (7) rewinder. (b) Direct gravure printing of the photoactive layer of OPV modules.

5.2 Device preparation of gravure-printed, standard configuration OPV cells (Article I) and modules (Article II and III)

***Structure*:** The structure of the standard configuration OPV cells and modules investigated in this study is presented in **Figure 22**. The selected materials and the layer thicknesses are also summarized.

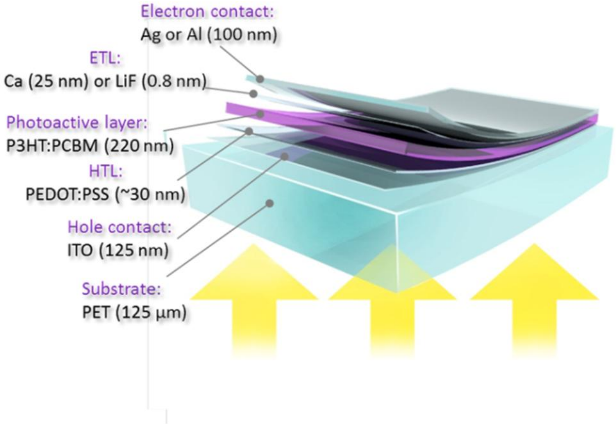

Figure 22. Structure of standard configuration OPV cells and modules. The layer thicknesses depicted refer to the R2R-printed modules in Article IV.

Substrate and hole contact – ITO-PET: PET covered with ITO (sheet resistance of 40–60 Ω sq^{-1}) supplied by Eastman (trademark OC50) was used as a basis. In Article I the ITO patterning was carried out by acid etching. The substrates were ultrasonically washed with ethanol for one hour and with 2-propanol (IPA) for one hour. After cleaning, the substrates were rinsed with de-ionized water, dried by blowing nitrogen and then put in an oven for several hours. In Articles II and III, definition of the ITO patterns was performed as an indirect image of the desired pattern using Isishape HiperEtch 09S etching paste (Merck). In Article II the paste was screen printed with a semi-automatic flatbed screen printer (Baccini S.R.L Treviso). The paste was dried in an oven and cleaned in a multistep process including ultrasonic baths in deionized water, ethanol, IPA and finally rinsing with deionized water. After the cleaning, the substrates were placed in an oven for drying. In Article III, patterning was carried out with a rotary screen printing unit for both the laboratory-processed and R2R-processed modules using a printing speed of 1.1 m min^{-1}. After printing, the paste was thermally treated and cleaned to remove excess paste. In Article II, Au busbars with a thickness of 80 nm were evaporated at the edge of the ITO in order to ensure contact with the ITO after gravure printing the subsequent layers (individual cells) and to diminish the impact of the high resistivity of ITO in large-area cells. In Articles I and II, the ITO-based substrates were O_2 plasma treated at an etching power of 300 W for 5 minutes (Technics Plasma GmbH, TePla 440-G)

HTL – PEDOT:PSS: The HTL of PEDOT:PSS (Heraeus, Clevios P VP AI4083, solid content 1.3–1.7%) was gravure printed in air. In Article I, different ink formulations in terms of solvent mixtures, additives and engraving parameters were tested prior to the final preparation of small-area solar cells. In Articles I and II, the PEDOT:PSS formulation was Clevios P VP AI4083:IPA:dimethylsulfoxide 75:22:3 wt%. A line density of 100 l cm^{-1} (cell volume 7.6–8.0 ml m^{-2}) was used. The printed films were oven dried overnight at 80°C. In Article III, the gravure printing ink formulation was based on a Clevios P VP AI4083 and IPA ink composition with a weight ratio of 75:25 wt% in both laboratory and R2R processing. A line density of 100 l cm^{-1} (7.9 ml m^{-2}) was used in the engraving. The R2R-processed modules were printed with a printing speed of 8 m min^{-1} and with an applied nip pressure of 1 bar. The printed layer was subsequently dried in a continuous process by hot air ovens at 120°C for 30 s. Correspondingly, the laboratory-scale modules were oven dried at 120°C for 15 min after gravure printing the PEDOT:PSS layer.

Photoactive layer – P3HT:PCBM: The photoactive layer, consisting of P3HT (#4002-E, Rieke Metals):PCBM[C60] (Nano-C, 99.5% purity), was prepared by gravure printing in air. The optimization procedure for the ink formulation and engraving parameters is described in Article I. The prepared photoactive layer for small-area solar cells was dried in a covered petri dish for slow film growth [125]. In Article II, the ink formulation for the photoactive layer was as follows: P3HT:PCBM[C60] (Nano-C, 99.5% purity) 131 mg in ml of 80:20 V% 1.2-dichlorobenzene (o-DCB):chloroform (CF). A line density of 120 l cm^{-1} (3.2 ml m^{-2}) was used for engraving. The photoactive layer was dried in a covered petri dish for slow film growth. In Article III, the ink formulation for the photoactive layer both in the laboratory and in R2R was P3HT:PCBM[C60] (131 mg) in o-DCB (1 ml). The printing plate and R2R printing cylinder were engraved with a line density of 120 l cm^{-1} (3.6–5.0 ml m^{-2}). In R2R, the printing speed was 8 m min^{-1} and the applied nip pressure was 1 bar. The printed layer was dried in a continuous drying process at 120°C for 30 s directly after printing in the R2R process. The laboratory-scale modules were slow dried.

ETL and electron contact – Ca/Ag or LiF/Al: In Article II the modules were post-treated on a hotplate under nitrogen at 110°C for 5 minutes prior to the evaporation of ETL and electron contact. In Articles I and II the electron contact was composed of Ca (25 nm) and Ag (80 nm). In Article III the modules were placed on a hotplate at 120°C for 5 minutes before evaporation. The layer sequence composed of either LiF (0.8 nm)/Al (100 nm) or Ca (25 nm)/Ag (100 nm).

Encapsulation: In Article I the organic solar cells were encapsulated with ultraviolet curable epoxy (Delo-Katiobond LP651) and a glass lid prior to IV measurement. The curing was performed in an ultraviolet unit (Loctite UVALOC Type 97035) with a power of 1000W for 2x40s.

5.3 Device preparation of gravure-printed, inverted configuration OPV modules (Article IV)

Structure: The structure of the fully printed inverted configuration OPV module is presented in **Figure 23**. The materials and the respective layer thicknesses for each layer are also presented.

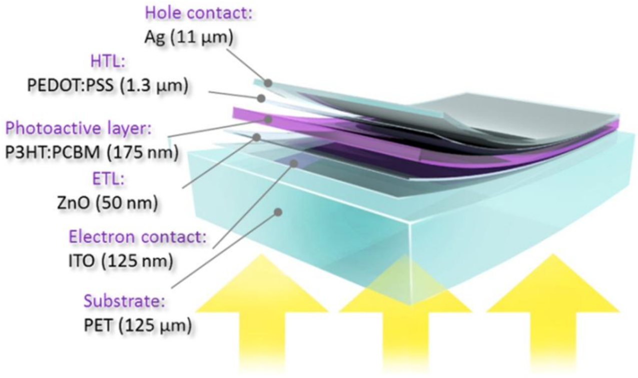

Figure 23. Structure of inverted configuration OPV modules.

Substrate and electron contact – ITO-PET: The substrate details and the patterning of ITO in Article IV follows the same procedure as described in the previous chapter for Article III.

ETL – ZnO: The ZnO nanoparticle suspension dissolved in ethanol was supplied by Nanograde, Switzerland. The ZnO layer was R2R gravure printed and dried at 140°C for 30s (hot air drying). [39]

Photoactive layer – P3HT:PCBM: Regioregular P3HT (#4002-E, Rieke Metals) was used as the donor and PCBM [C60] (purity 99.5%, Nano-C) as the acceptor in the photoactive blend. Both were received as solid materials and dissolved in o-DCB with a total concentration of 130 mg ml^{-1}. The photoactive layer was deposited by R2R gravure printing. The printing speed was 8 m min^{-1} and the applied nip pressure was 1 bar. The printing cylinder contained engravings with a line density of 120 lines cm^{-1} (4.8 ml m^{-2}).

HTL – PEDOT:PSS: High viscous PEDOT:PSS (EL-P 5015, Agfa) was R2R rotary screen printed. The printing was conducted with a Stork RotaPlate 215V screen. The printing speed was 2 m min^{-1}. The hot air drying units were adjusted to 130°C with a total drying time of 120s.

Hole contact – Ag: Heat curable silver paste (XPVS-670, Spraylat) was chosen as the hole contact. R2R rotary screen printing was prepared with a 275 L inch^{-1} steel mesh screen (RVS) from Gallus. The printing speed was 2 m min^{-1}.

The drying temperature was 130°C with a total drying time of 120s. No light soaking or thermal treatments were carried out for the modules prior to electrical characterization.

5.4 Device preparation of ITO-free spin coated cells (Article V) and slot die coated modules (Article VI)

Structure: The structures of the ITO-free spin coated cells and slot die coated modules under research in Articles V and VI are presented in **Figure 24**. The device configuration was based on a previously introduced concept [75], [89], [126], [127].

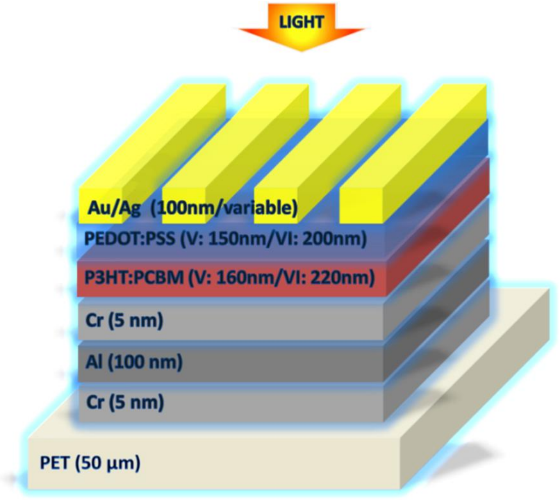

Figure 24. Structure of ITO-free inverted configuration OPV cells and modules

Substrate – PET: The organic solar cells were processed on top of PET (50 µm) supplied by Mitsubishi Polyester Film GmbH Europe. The substrates were washed with IPA, rinsed with deionized water, dried, attached to a glass carrier and placed in vacuum overnight prior to evaporation of the electron contact and ETL.

Electron contact and ETL – Cr/Al/Cr: The electron contact was composed of Cr (5 nm)/Al (100 nm)/Cr (5 nm). The Cr layers were electron-beam evaporated and the Al layer thermally evaporated. Additionally, for the modules, Cr (5 nm) and Au (30 nm) were evaporated for series connection supports.

Photoactive layer – P3HT:PCBM: The photoactive blend solution consisted of P3HT (4002-E, Rieke Metals) and PCBM[C60] (purity 99%, Solenne BV) dissolved in o-xylene with a mixing ratio of 1:0.7 by weight (total concentration 25.5 mg ml^{-1}). For the cells, the substrates containing Cr/Al/Cr electron contact were solvent pretreated with ethanol and, for the modules, with toluene, before deposition of the photoactive layer. In Article V the P3HT:PCBM solution was spin coated at 500 rpm for 360 s resulting in an active layer thickness of 160 nm. In Article VI the slot die coating was prepared with a Basecoater (Coatema) in a sheet-based process as full layer deposition. A speed of 1 m min^{-1} was used.

HTL – PEDOT:PSS: Prior to the deposition of PEDOT:PSS, solvent pre-treatment with 1-butanol was carried out. In Article V the PEDOT:PSS ink (Clevios^{TM} F CPP 105DM) supplied by Heraeus was spin coated at 2000 rpm for 60 s. In Article VI the PEDOT:PSS layer was prepared by slot die coating. A coating speed of 1 m min^{-1} was used. In Article V the PEDOT:PSS and photoactive layers were wiped outside the active area in order to define an active area of 1.1 cm^2. In Article VI wiping was employed to series connect the cells. The cells were annealed at 80°C on a hotplate under nitrogen atmosphere for 15 min, and the modules for 10 min in order to remove the water from the PEDOT:PSS layer.

Hole contact – Au or Ag: In Article V the grid was either aerosol jet printed using fine particle silver ink CSD66 (Cabot) or, for reference cells, the gold grid was thermally evaporated. The grid design was composed of 22 lines with a line separation (centre to centre) of 1 mm. For aerosol jet printing, a Maskless Mesoscale Material Deposition (M3D system from Optomec INC.) was used. After grid preparation, the samples were thermally annealed on a hotplate under nitrogen atmosphere at 120°C for 10 min. In Article VI an Au grid of 100 nm was evaporated and the annealing was performed at 120°C for 10 minutes prior to IV measurement.

***Encapsulation*:** In Article VI the modules were laminated with flexible barrier film.

5.5 Characterization

Various measurement systems were used throughout the thesis for characterization:

Electrical characterization: IV measurements under illumination were carried out using the following AM1.5G solar simulators: Oriel Sol3A Class AAA (Article II and III), Atlas SolarTest1200 (larger set of samples in Article III and IV), Steuernagel SolarCellTest 575 (Article V and VI) and Cermax 300W lamp-based solar simulator (Article I). In Articles II–VI the measurements were prepared in an inert gas atmosphere of N_2 and the intensity was calibrated using a certified National Renewable Energy Laboratory reference silicon solar cell with a KG5 filter. In Articles III, V and VI the light intensity was corrected with the spectral mismatch factor.

Lifetime measurement (Article III): In shelf lifetime measurement, the modules were stored in ambient conditions in dark. In operational stability testing, the modules were stressed in an Atlas XXL+ weathering chamber under the following conditions: sunlight simulated by xenon lamps using daylight filters (irradiance level 42 W m^{-2} at 300–400 nm), relative humidity 50 RH% and black standard temperature 65°C.

Electrical imaging (Article VI): For DLIT an IR camera with 320 x 256 pixels was used for thermal radiation detection. The heat was introduced periodically using a lock-in frequency of 10 Hz. A square-wave pulsed voltage signal was applied to the modules in the forward direction with a maximum amplitude of below 1V per cell. A camera frequency of 40 Hz was used, i.e. four images per lock-in period. The recorded lock-in signal was averaged over 3000 periods for every pixel. EL imaging was conducted with a back-illuminated silicon CCD camera (1024 x 1024 pixel). Optical long-pass filters were used to filter light below 975 nm. An integration time of 20 minutes was used in the EL imaging. For LBIC mapping, six lasers with different wavelengths were selected. The lasers emitted in the following wavelengths: 405 nm, 532 nm, 670 nm, 780 nm, 925 nm and 1064 nm. The scanning laser spot had an approximate diameter of 50 µm. One cell was measured in time, and the remaining cells were illuminated using OLED panels. The light intensities in the filtering approach were reduced by four neutral density filter foils (13%, 29%, 49% and 64%). The transparency of these foils was calibrated for their spectral mismatch with the used sun simulator.

Surface, layer and printing ink properties: The layer thicknesses were determined with a Dektak 150 Surface Profilometer. In Article I the surface roughnesses were also measured with the Dektak Profilometer on a line of 0.5 mm. Images of the layer properties were taken with a Smartscope OGP250. The surface measurements were obtained using a contact angle meter (KSV Instruments Cam 200) and surface energy calculations were performed based on Wu’s method [128]. In Article IV, the surface roughnesses were measured using a Veeco Dimension 3100 in tapping mode. A high quality silicon tip with a radius less than 10 nm was used to probe the sample surfaces. The aerosol jet printed silver lines in Article V were characterized in terms of line width, height and profile with a LEXT OLS4000 Measuring Laser Confocal Microscope.

6. Results

This chapter summarizes the results of this research. The chapter is divided into three main sections. The first section, spanning subsections 6.1–6.4, covers the investigation of gravure printing as a manufacturing method for organic photovoltaics. The investigated procedure for ink modification applicable to gravure printing, as well as the optimization of printing plate engraving parameters and printing parameters at the laboratory scale are presented. The results from testing optimized layers in functional standard configuration cells and modules processed in the laboratory are also presented (Section 6.2). These results were further exploited in the R2R upscaling of the standard configuration modules presented in Section 6.3 and in successful processing of fully R2R-printed inverted modules (Section 6.4), demonstrating the outstanding potential of gravure printing. Section 6.5 investigates aerosol printing for fabrication of a fine-line current collecting grid in order to extend the size of cells without losing performance. In the last section, a novel approach for investigating series-connected modules, i.e. filtering, is introduced. Complementary imaging technologies (DLIT, EL and LBIC) were used to verify the results obtained with filtering.

6.1 Gravure printing for thin-film deposition

6.1.1 Gravure printability of HTL of PEDOT:PSS

PEDOT:PSS acts as the HTL in the standard OPV configuration. Since the resistivity of the PEDOT:PSS dispersion (Clevios P VP AI 4083) is 500–5000 Ω·cm, the layer should be thin, namely ~40 nm. The printing experiments are started with Clevios P VP AI 4083 used as-received. The patterns are printed with eight different engraved areas the line density ranging from 70 l cm^{-1} to 210 l cm^{-1} (ink volume 3.6–12.2 ml m^{-2}).

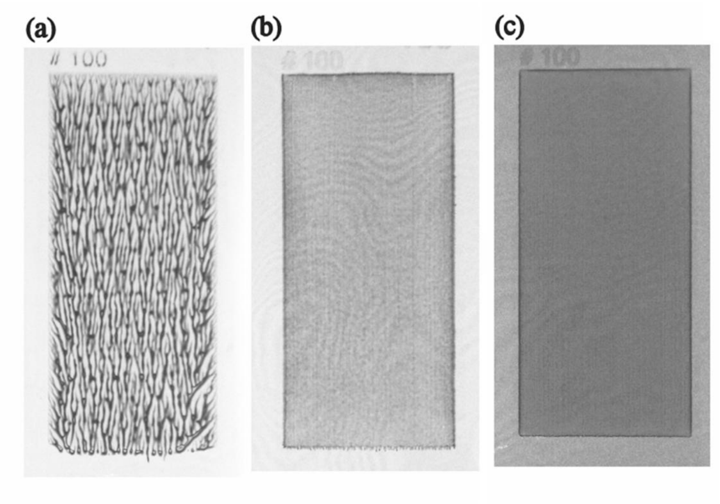

Figure 25. Photographs of gravure-printed (a) PEDOT:PSS (Clevios P VP AI4083) used as received, and (b) PEDOT:PSS:IPA 75:25 wt%, (c) PEDOT:PSS:IPA 50:50 wt% with line density of 100 l cm^{-1}.

The poor coverage of PEDOT:PSS, i.e. inadequate wetting, shown in **Figure 25**a is attributed to the high surface tension of the aqueous PEDOT:PSS solution. The surface tension of the as-received PEDOT:PSS is 71 mN m^{-1}, whereas the surface energy of the O_2 plasma-treated ITO surface is also high at 74 mN m^{-1}. To ensure proper wetting of the ink on the substrate, the surface energy of the substrate must be higher than the surface tension of the ink. Various approaches were used to find suitable solvent(s) and/or additives to enhance printability while maintaining electrical performance. Initially the effect of solvent(s) and/or additives on the surface tension, printability, layer thickness among other parameters are investigated. Then formulations are tested as hole transport layer in organic solar cells. The first approach was to decrease the surface tension and to improve the printability by addition of solvent such as IPA from 25 wt% up to 50 wt%. Addition of 25 wt% IPA to PEDOT:PSS dispersion decreases the surface tension to 27 mN m^{-1}. The printability is highly enhanced by addition of 25 wt% of IPA resulting in uniform printed films (**Figure 25**b). With line densities of 90 l cm^{-1} and 100 l cm^{-1} the targeted layer thickness can be reached. The mean layer thicknesses were 38±4 nm and 33±3 nm with 90 l cm^{-1} and 100 l cm^{-1}, respectively. When the amount of IPA is further increased up to 50 wt%, the surface tension decreases down to 22 mN m^{-1}. However, the layer thickness is out of the targeted thickness range. It is worth noting that the addition of a single solvent is already sufficient for making PEDOT:PSS gravure printable. Other solvents and additives were tested to further improve the printability of PEDOT:PSS (see Article I).

6.1.2 Gravure printability of photoactive layer of P3HT:PCBM blend

In this section, a procedure for P3HT:PCBM ink modification and optimization of engraving parameters and printing parameters is covered. Ink composition was optimized in terms of total concentration. Only halogenated solvents which dissolve both P3HT and PCBM over a wide solid content range were used. The effect of engraving parameters on layer properties was also studied by varying the ink volume, i.e. line density. The printing parameters have already been examined in the pre-study, so only printing speed is considered as a variable in the present study. It should be noted that optimization of the ink, engraving and printing properties was carried out simultaneously. For spin coated structures, low total concentrations of P3HT:PCBM were used. Gravure printing usually requires an increase in solid content in comparison to spin coating in order to control the ink flow and to be able to produce patterned structures with sharp edges. The I_{SC} fluctuates as a function of photoactive layer thickness due to interference. To maximize the photocurrent, the thickness of the photoactive layer should lie in the vicinity of the maximum points, which are located at ~80 nm and ~210 nm for a P3HT:PCBM conventional configuration [80]. Photographs of gravure-printed active layers demonstrating the effect of ink formulation, engraving parameters and printing parameters on layer uniformity are shown in **Figure 26**.

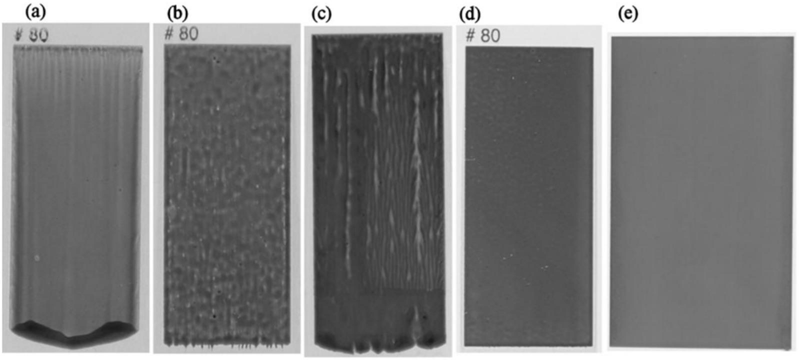

Figure 26. Photographs showing the print quality of gravure-printed P3HT:PCBM layers with varied ink composition, engraving parameters and printing parameters. (a) P3HT:PCBM 50 mg ml^{-1} in o-DCB, line density 80 l cm^{-1}, speed 7 m min^{-1}, layer thickness 109±22 nm (b) 50 mg ml^{-1}, 80 l cm^{-1}, 18 m min^{-1}, 151±22 nm (c) 50 mg ml^{-1}, 45 l cm^{-1}, 18 m min^{-1}, 261±48 nm, (d) 100 mg ml^{-1}, 80 l cm^{-1}, 18 m min^{-1}, 334±15 nm (e) 150 mg ml^{-1}, 120 l cm^{-1}, 18 m min^{-1}, 210±11 nm. *(Article I © Solar Energy Materials and Solar Cells, Reprinted with the permission of Elsevier)*

Optimization of the gravure printability of P3HT:PCBM started with a photoactive ink of P3HT:PCBM 50 mg ml^{-1} (1:1) dissolved in o-DCB (boiling point 179°C). One of the dominant printing parameters affecting layer quality is printing speed, as can be seen in **Figure 26a** and **b**. With a printing speed of 7 m min^{-1}, the ink spreads out uncontrollably from the cells in the nip, more closely resembling a coating process than a printing process. In addition, accumulation of ink outside the engraved area can be observed at the lower edge of the printed pattern. This most likely occurred because the time taken for the ink to be transferred from the cells to the substrate in the nip is too long for this type of low-viscous ink. By increasing the printing speed to 18 m min^{-1} (see **Figure 26**b), the ink flow dynamics are improved and the photoactive ink remains within the patterned area. It should be emphasized that the printing speed is machine dependent. Here, the ink is applied directly on the surface of the printing plate and the process is non-continuous, thus the printing speed has point-to-point variation. This sheet-based laboratory-scale process differs significantly from continuous roll-to-roll printing, especially in the application of ink. Therefore, the printing parameters need to be adjusted machine-specifically. Secondly, the engraving parameters in terms of line density (ink volume) were screened. The tested line densities varied from 45 l cm^{-1} to 210 l cm^{-1}. In **Figure 26**b the thin film was printed with a line density of 80 l cm^{-1} (ink volume 12.2 ml m^{-2}). When the line density was decreased to 45 l cm^{-1} while increasing the ink volume to 17.2 ml m^{-2}, the uniformity significantly deteriorated. As can be seen in **Figure 26**c, an ink formulation with low solid content (3.8% of total weight) combined with high ink volume does not produce a uniform film.

The last approach used to optimize the printability of P3HT:PCBM was to increase the total concentration from the initial 50 mg ml^{-1} to 150 mg ml^{-1}. Due to the limited solubility of PCBM in o-DCB, the PCBM concentration was kept unchanged at 50 mg ml^{-1}. Increasing the PCBM concentration further would have presented a high risk, especially considering R2R pilot processing, as open ink fountains were used. Higher concentration leads to better uniformity and also finer resolution, which is an essential property in arbitrary shaped and sized OPV structures. However, the line density should be increased to 120 l cm^{-1} while increasing the total concentration to 150 mg ml^{-1} in order to keep the layer thickness at an adequate level. Furthermore, a two-solvent system combining a low boiling point solvent CF (boiling point 62°C) with the used main solvent o-DCB was examined. Based on the literature, CF can increase the interfacial areas and thus lead to improved electrical performance [129]. Therefore, CF was selected as a co-solvent in the P3HT:PCBM blend. Additionally, its excellent solubility and beneficial solvent properties in terms of low boiling point and high vapour pressure can be utilized in further controlling the spread of photoactive material in the printing process. Surface roughness was measured with respect to varying ink composition (volume ratio of o-DCB and CF, total concentration) and line density. The results are summarized in **Table 2**. Spin coated film was used as a reference.

Table 2. Average surface roughness of gravure-printed photoactive layers with varying ink composition and engraving parameters.

Deposition method	**Line density ($l\ cm^{-1}$)**	**Solvent ratio of o-DCB/CF in volume percent**	**Total concentration ($mg\ ml^{-1}$)**	**Ra (nm) (profilometer 0.5 mm)**
Spin coating		Reference		1.8
Gravure printing	120	100/0	150	21.7
	120	80/20	150	4.6
	120	66/33	150	9.2
	120	80/20	131	2.7
	100	80/20	131	8.0
	80	80/20	131	7.8
	120	80/20	112.5	20.7

Macroscopic surface roughness, measured with a profilometer, decreased significantly to 4.6 nm when 20 V% CF was added with a total concentration of 150 mg ml^{-1}. Additionally, the same measurements were conducted for the printed films with total concentrations ranging from 112.5 mg ml^{-1} to 150 mg ml^{-1}. The lowest surface roughness of 2.7 nm was exhibited with a total concentration of 131 mg ml^{-1}, which was comparable to the spin coated reference sample. Additionally, the effect of the engraving parameters (120 l cm^{-1}, 100 l cm^{-1} and 80 l cm^{-1}) on surface roughness was examined. The results revealed that surface roughness increases with decreasing line density.

6.2 Laboratory-scale printed cells and modules

6.2.1 Gravure-printed polymer-based solar cells

Based on the printability examination and characterization of layer properties presented in Section 6.1, the most effective ink formulations and printing and engraving parameters were selected for gravure printing the PEDOT:PSS and P3HT:PCBM blend. The functionality of these layers was tested in standard configuration OPVs consisting of PET/ITO/PEDOT:PSS/P3HT:PCBM/Ca/Ag. The properties of the PEDOT:PSS layer were kept unchanged. Instead, the subject of investigation was the effect of the photoactive layer properties in terms of ink formulation and engraving parameters on the photovoltaic response. Two approaches were used. Firstly, the total concentration of the photoactive blend was varied from 113 mg ml^{-1} to 150 mg ml^{-1} keeping the line density unaltered. Secondly, the engraving parameters in terms of line density were varied from 80 l cm^{-1} (7.0 ml m^{-2}) to 120 l cm^{-1} (4.0 ml m^{-2}) using a constant total concentration. The solid materials were dissolved in 80:20 V% o-DCB:CF. The electrical parameters including V_{OC}, short-circuit current density (J_{SC}), FF and PCE of the examined solar cells with a cell area of 0.19 cm^2 are summarized in **Table 3**.

Table 3. Photovoltaic response (V_{OC}, J_{SC}, FF, PCE) of the encapsulated cells with varying parameters for gravure-printed active layer (total concentration, ratio of P3HT:PCBM, line density of the engraved cells in the printing plate). The average thickness of the active layer (d) is also presented. *(Article I © Solar Energy Materials and Solar Cells, reprinted with the permission of Elsevier.)*

	Active layer (Total concentration, ratio, line density)	**d* (nm)**	**Voc (mV)**	**Jsc (mA cm^{-2})**	**FF**	**PCE$_{max}$ (%)**
S1	113 mg ml^{-1}, 1:0.8, 120 l cm^{-1}	152	580	7.57	0.60	2.5
S2	131 mg ml^{-1}, 1:0.6, 120 l cm^{-1}	192	600	7.91	0.57	2.8
S3	150 mg ml^{-1}, 1:0.5, 120 l cm^{-1}	191	580	7.28	0.49	2.0
S4	131 mg ml^{-1}, 1:0.6, 100 l cm^{-1}	271	550	6.42	0.55	1.8
S5	131 mg ml^{-1}, 1:0.6, 80 l cm^{-1}	305	570	6.46	0.52	1.8

*measured directly from the solar cell samples

The best performance of 2.8% was exhibited with a total concentration of 131 mg ml^{-1} (1:0.62). The highest tested total concentration of 150 mg ml^{-1} resulted in decreased maximum power point. This could be attributed to unbalanced hole and electron transport, caused by the ratio of P3HT:PCBM (1:0.5) [130]. Additionally, the dependence of the engraving parameters in terms of line density on electrical performance was examined. The solar cells prepared with line densities of 100 l cm^{-1} and 80 l cm^{-1} had a lower Jsc compared to the active layer printed with 120 l cm^{-1}. Usually, a thicker active layer should have a higher Jsc due to improved absorption. However, it should be emphasized that the layer properties do not remain unaltered (120 l cm^{-1}) as the line density changes. The engraving parameters significantly affect the layer properties, so thicker layer do not automatically lead to improved absorption. Based on the surface roughness measurements, the most homogeneous layer was prepared with a line density of 120 l cm^{-1}, which also gave the best performance. However, it should be noted that a uniform photoactive layer with low surface roughness does not ensure better electrical performance. How the engraving parameters of the gravure cylinder, ink formulation and the printing parameters affect the nanomorphology of the active layer in the R2R process and thus electrical performance is a key area for future investigation.

6.2.2 Gravure-printed side-connected modules

Individual organic solar cells can be combined to form photovoltaic modules for increased output current and/or output voltage. The power output required to drive a specific application must be defined. The open-circuit voltage is typically in the order of 0.6 V for P3HT:PCBM based solar cells in outdoor conditions. Here, the OPV modules were used as a part of an integrated flexible energy harvesting system comprising a printed lithium-ion battery, Si transistor circuitry and the OPV modules. The nominal voltage of the battery to be charged was 3.6–3.7 V. Therefore, series connection of eight cells in the OPV modules was needed. Nevertheless, it should be noted that the output voltage is dependent on the illumination conditions. **Figure 27**a shows the side-connected OPV module structure. The module structure is built up of eight separate cells which can be first measured independently, enabling individual electrical testing to inspect the uniformity of gravure printing for large-area cells (> cm^2). Contact pads on the sides can be used for series connection of the cells with a conductive ink. However, the current flow through the side connection increases the series resistance loss which directly decreases the FF of the modules. The width of single cell was determined on the basis of electrical calculations (see Article II) by assuming that the sheet resistance of the ITO anode is a limiting factor in collecting the current generated in the photoactive layer. Thus, the length and width of a single cell in the multi-strip pattern was designed as 4.6 cm and 0.42 cm, respectively. **Figure 27**b shows the gravure-printed OPV module structure.

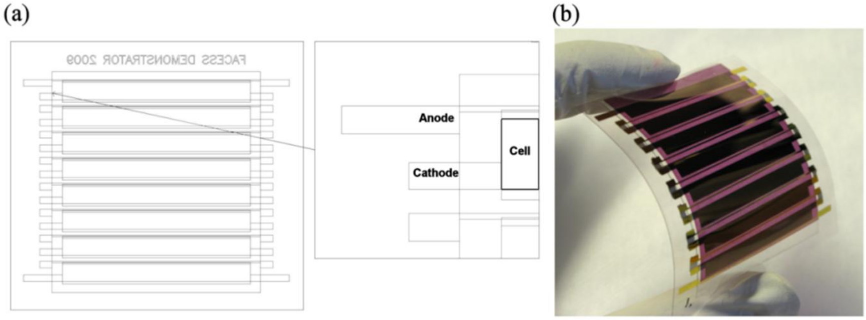

Figure 27. (a) Layout of the side-connected module. The cells can be measured separately and connected in series with a conductive ink from the sides. (b) Flexible gravure-printed side-connected module composed of eight series-connected cells. *(Article II © Solar Energy Materials and Solar Cells, reprinted with the permission of Elsevier.)*

The IV characteristics of the individual cells with an active area of 1.93 cm^2 are shown in **Figure 28**a. Based on the IV characteristics, good reproducibility is exhibited. Current matching of the series-connected cells is essential, as the weakest performing cell limits the total current. With the best individual solar cell an I_{SC} of 14.01 mA, V_{OC} voltage of 0.61 V, a FF of 35% and PCE of 1.55% can be attained. Secondly, the cells are connected in series from the sides. IV measurements (see **Figure 28**b) were performed on the modules consisting of 5-8 series-connected cells.

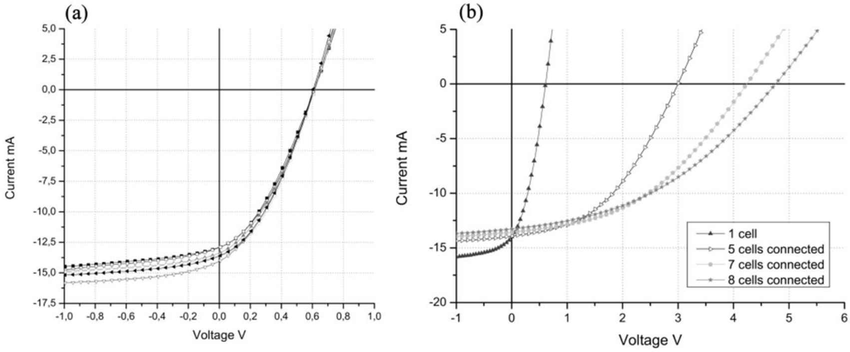

Figure 28. IV characteristics of (a) identically processed individual cells with an active area of 1.93 cm^2 and of (b) modules consisting of 1,5,7 and 8 cells in series connection. *(Article II © Solar Energy Materials and Solar Cells, reprinted with the permission of Elsevier.)*

As **Figure 28** shows, the V_{OC} changes linearly as the number of cells connected in series increases. This indicates that the series connection works in the module structures, as the V_{OC} of the module should be the sum of the V_{OC} of the connected individual cells. With the eight series-connected cells, the V_{OC} increased up to 4.76 V. The I_{SC} of the modules ranges from 13.29 mA (8 cells) to 13.91 mA (5 cells). In the I_{SC} conditions a slight variation of ~4% was detected. Internal differences in the performance of the cells can cause variation in I_{SC}. The modules consisting of 5, 7 and 8 cells exhibited an active area PCE of 1.92%, 1.79% and 1.68%, respectively.

6.3 R2R gravure printing of standard configuration OPV modules

The feasibility of gravure printing for thin-film deposition for building OPV cells (Article I) and modules (Article II) at laboratory scale was shown in Section 6.2. The next step was to transfer the gravure printing processes of PEDOT:PSS and P3HT:PCBM from the laboratory to a R2R pilot production environment. The main focus was the comparison of thin-film formation in the laboratory and R2R gravure printing processes and its influence on OPV module performance. As the ETL and electron contact were evaporated in a sheet-based process, the modules were cut into sheets after deposition of the photoactive layer. The R2R process steps for fabricating the standard configuration modules are depicted in **Figure 29**.

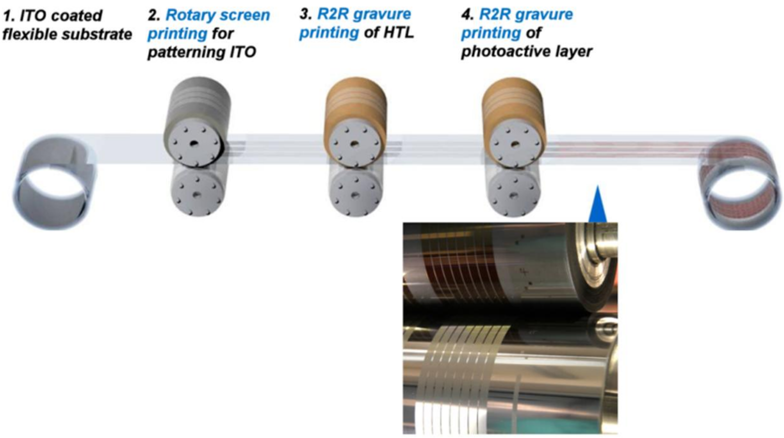

Figure 29. Schematic image of the R2R process for fabrication of standard configuration OPV modules consisting of eight monolithically series-connected cells. *(Article III © Progress in Photovoltaics: Research and Applications, reprinted with the permission of John Wiley and Sons.)*

First, the printing quality of the R2R and laboratory gravure-printed photoactive layers based on P3HT:PCBM blend was inspected by optical microscopy. The same ink formulation and engraving parameters in the printing cylinder were used in both cases in order to compare the laboratory and R2R gravure printing processes. More processing details can be found in Article III. The optical microscopy images are presented in **Figure 30.** The figures reveal that the R2R-printed P3HT:PCBM layer contains pinholes extending to the surface of the underlying PEDOT:PSS. Conversely, no similar defects were detected in the laboratory-scale printed P3HT:PCBM. It should be noted that the pinholes were concentrated in the thinnest parts of the R2R gravure-printed active layer. The diameter of the pinholes varied from 20 µm to 50 µm. The cause of the hole formation is still ambiguous. Based on the surface energy and tension measurements it is unlikely that the holes could be due to incomplete ink transfer or dewetting. Another explanation could be missing dots due to incomplete printing of clogged cells. However, it should be seen as a regular pattern repetitive in a sequence of every repeat length of the printing cylinder. This type of regularity nevertheless could not be detected. Alternatively, electrostatic discharge can easily form holes through the thinnest parts of the active layer. The presence of round-shaped holes supports more the electrostatic discharge presumption (see **Figure 30**d).

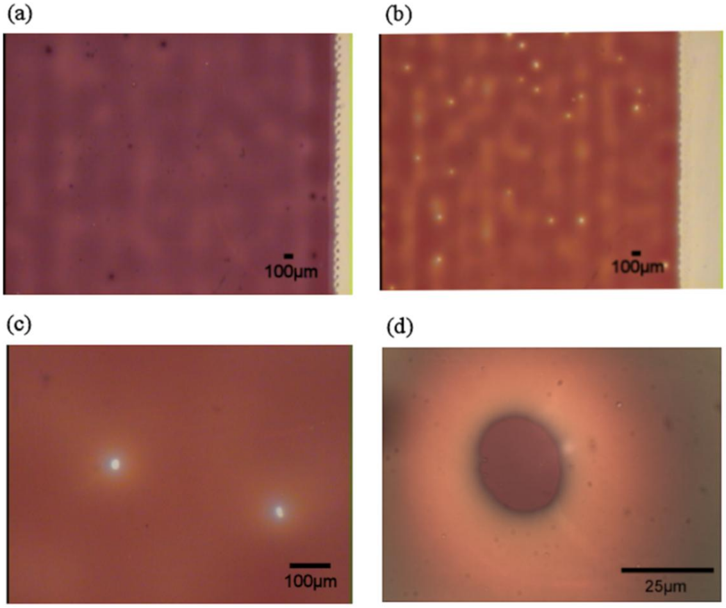

Figure 30. Gravure-printed photoactive layer of P3HT:PCBM on top of an HTL of PEDOT:PSS prepared in (a) laboratory and (b) R2R. In the close-up images (c, d) the pinholes in the R2R-printed photoactive layer with a diameter ranging from 20µm to 50µm could be clearly observed. *(Article III © Progress in Photovoltaics: Research and Applications, reprinted with the permission of John Wiley and Sons.)*

Pinhole insulation was investigated in detail by producing R2R-printed OPV modules with different interfacial layer materials and performing electrical measurements under dark and AM1.5 illumination conditions. Two ETL and electron contact configurations were investigated: Ca/Ag and LiF/Al. The Ca/Ag combination was used in Articles I and II for the laboratory-scale cells and modules. LiF is a well-known interfacial material in OPV structures for facilitating electron extraction [131]-[133]. Here, LiF was tested as an insulative ETL because it was presumed that pinholes with an evaporated electron contact might cause shorted modules. Firstly, a larger batch of R2R-printed modules with LiF/Al electron contact were measured, resulting in a mean efficiency of 1.77% ± 0.15% for 50 modules. Secondly, a smaller batch of R2R-printed modules with both electron contact combinations and laboratory-scale modules were tested more accurately with the Class AAA solar simulator. Each category contains four parallel modules. In these measurements, the actual active area is also determined precisely microscopically. **Figure 31** shows the mean current-voltage characteristics of laboratory and R2R gravure-printed modules including standard deviation bars. The module structures comprised eight cells monolithically connected in series with a total active area of ~15 cm^2.

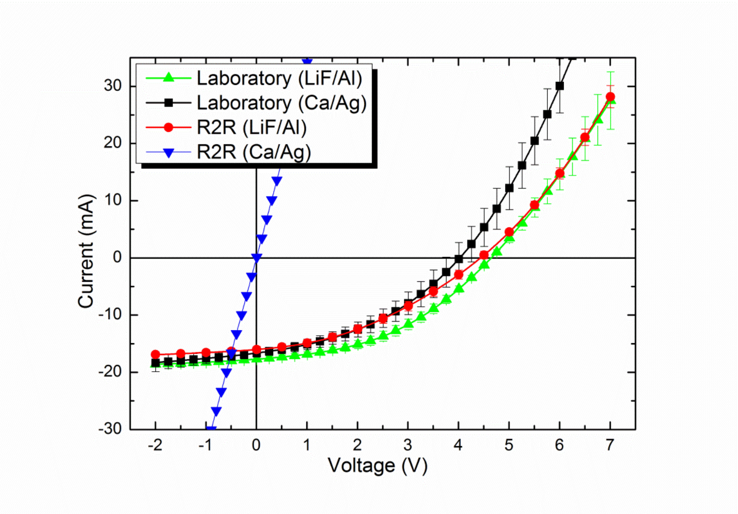

Figure 31. Mean current-voltage characteristics and standard deviation bars of R2R gravure-printed OPV modules with LiF/Al (red circles) and Ca/Ag (blue triangles) as the ETL and electron contact, respectively. Correspondingly, mean current-voltage characteristics of laboratory gravure-printed modules with LiF/Al (green triangles) and with Ca/Ag (black squares) are shown. *(Article III © Progress in Photovoltaics: Research and Applications, reprinted with the permission of John Wiley and Sons.)*

Figure 31 reveals that the R2R-fabricated modules with a Ca/Ag electron contact layer were all electrically shorted. Presumably, the pinholes in the active layer are at least partially filled with calcium and silver providing a conductive path to short the device. Notably, the evaporated top electrode sets high requirements with respect to uniformity and defects for the underlying photoactive layer. By replacing the interfacial layer of calcium with LiF, remarkable enhancement of module performance can be observed. Thus, the detrimental effect of the pinholes can be prevented leading to well-performing monolithic R2R modules with a mean PCE of 1.7% (max 1.9%) being in good accordance with the results obtained by characterizing a larger batch of modules. In comparison, reference modules with an efficiency of 2.2% (max 2.3%) were fabricated using a laboratory-scale sheet-level process.

The insulating behaviour of LiF was investigated by building up equivalent circuit models (see **Figure 32**). For simplicity, the module structures are presented as one diode model in which the R_S and R_{SH} cover the respective resistances of the whole module. The approximation of the respective R_S and R_{SH} from the IV curves is explained in Article III. The equivalent circuit for laboratory-scale modules with Ca/Ag used as a reference is presented in **Figure 32**a. The mean R_S value for these reference structures is 58 Ω. Correspondingly, the R_{SH} was approximately 36 kΩ. The total R_S in the reference structure can be split into two parts, R_S and $R_{S\_CONTACT}$. $R_{S\_CONTACT}$ is a sum of the R_S of ITO, PEDOT:PSS, and Ca/Ag. Due to the high conductivity of Ca/Ag, it is a good approximation to use $R_{S\_CONTACT}$ in the LiF-based modules to cover the R_S of ITO and PEDOT:PSS. The insertion of LiF to R2R-printed modules leads to two additional resistances in the equivalent circuit, R_{S_LIF} and R_{SH_LIF} (see **Figure 32**b). The increase in total R_S originates from the high resistivity of LiF. The mean total R_{SH} of the R2R-printed modules with LiF/Al is ~14 kΩ. It can be approximated that R_{SH_LIF} and R_{SH} are connected in parallel due to the low R_S values of R_{S_LIF} and R_S. The assumption of parallel connection leads to R_{SH_LIF} of ~23 kΩ.

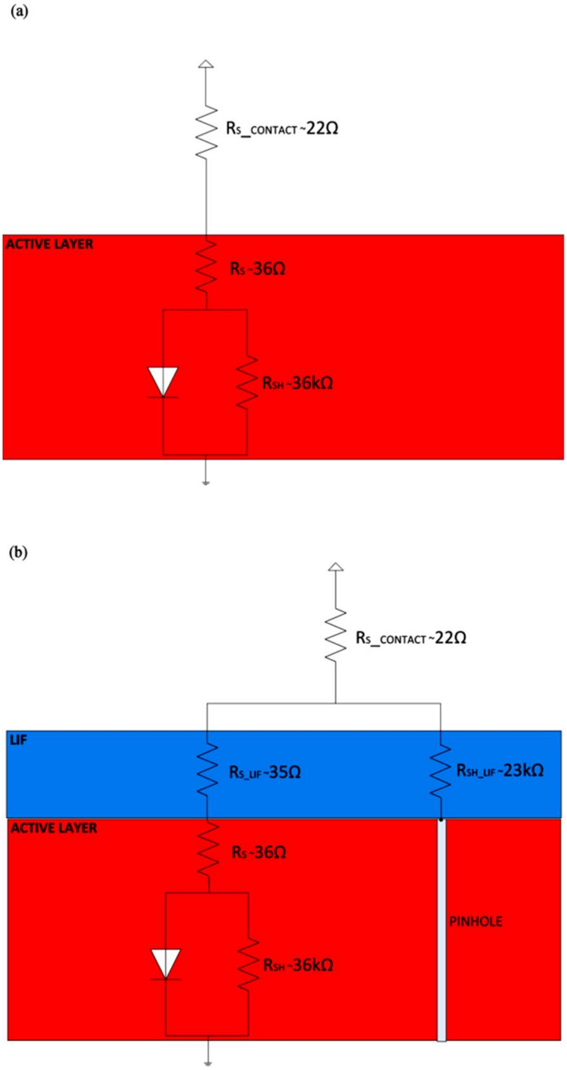

Figure 32. Simplified equivalent circuits for (a) laboratory-scale printed modules (with Ca/Ag ETL and electron contact) and (b) R2R-printed modules with detrimental pinholes insulated by a thin layer of LiF. *(Article III © Progress in Photovoltaics: Research and Applications, reprinted with the permission of John Wiley and Sons.)*

The equivalent circuit models indicate that the thin LiF layer effectively insulates pinholes, resulting in remarkably increased R_{SH} while only modestly increasing the R_S. These results support the performance difference observed in the IV measurements performed for laboratory and R2R-printed modules with different ETL and electron contact. The relation between resistance and resistivity explains the difference arising from the R_{SH} and R_S values. The area coverage of defects in comparison to total area of the module is small, thus leading to a two orders of magnitude difference between R_{SH_LIF} and R_{S_LIF} ($R_{SH\_LIF} >> R_{S\_LIF}$). Namely, R_{SH_LIF} is dependent on the area of the pinholes, whereas R_{S_LIF} is dependent on the effective operating area of the module.

Furthermore, an artificial layer of pinholes was prepared lithographically on top of patterned ITO-gravure-printed PEDOT:PSS samples to validate the assumption that an LiF layer effectively prevents electrical shorting through the pinholes. Holes of two diameters, 33 µm and 57 µm, were selected for the experiment. A defect density of ~2.3% of overall area was used. Thereby, the defect density was 26.9 defects mm^{-2} with 33 µm holes and, correspondingly, 9.3 defects mm^{-2} with 57-µm holes. Either LiF/Al or Al was evaporated on top of the artificial layer of pinholes. Notably, the devices with an Al-containing top electrode were all shorted. Addition of an interfacial layer of LiF between the PEDOT:PSS and electron contact insulated the pinholes by preventing shorting of the device (see Figure in Article III).

The shelf and operational lifetime of the R2R-printed modules were measured according to International Summit on OPV Stability (ISOS) testing protocols for organic solar cells [134]. The R2R-printed modules were encapsulated with a flexible barrier. It was found that the modules in shelf lifetime measurement decayed 50% of the initial PCE after 4500 hours. In the operational lifetime tests, the PCE of the modules decreased to 50% of the initial value after 250 hours. The instability of conventional configuration devices with glass and stainless steel encapsulation in accelerated full sun simulation has also been reported [135].

6.4 Fully R2R-printed inverted modules

In this paper, the first demonstration of fully R2R-printed inverted OPV modules using gravure printing and rotary screen printing processes is described. The structure investigated comprised five layers, which were either gravure printed (ZnO, P3HT:PCBM), rotary screen printed (PEDOT:PSS, Ag) or patterned in a R2R process (ITO). The process flow for inverted OPV modules in a R2R pilot environment is depicted in **Figure 33**.

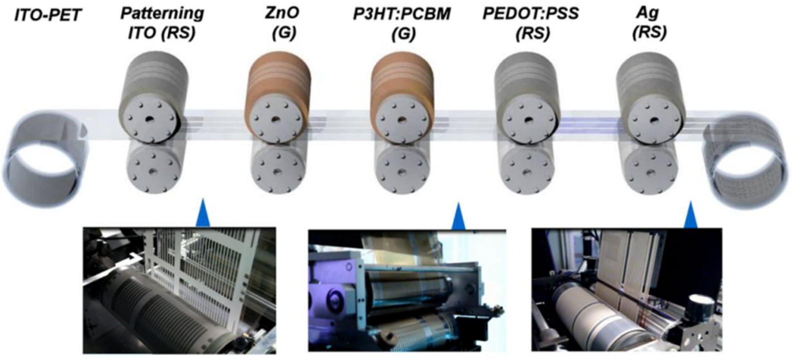

Figure 33. R2R process for fully printed inverted OPV modules. Used printing methods for separated OPV layers are abbreviated as RS=rotary screen printing, G=gravure printing. *(Article IV © Nanoscale, reproduced by permission of the Royal Society of Chemistry.)*

The selection of the printing method for each layer was made on the basis of the material properties and the target layer thickness. The etching paste for ITO, the selected PEDOT:PSS grade and the silver paste chosen on the basis of the laboratory compatibility tests (see Article IV) have all been developed for flat-bed screen printing, so rotary screen printing can be considered an obvious choice as the processing method. The lower viscosity of ZnO and P3HT:PCBM and the target layer thickness range from tens of nanometres to a few hundred nanometres supports the selection of gravure printing.

The ZnO and P3HT:PCBM layers processed with gravure printing are printed with a continuous stripe design. Therefore, the layer alignment needs to be adjusted only in the direction perpendicular to the printing direction, i.e. cross directional alignment (CD). In contrast, PEDOT:PSS and Ag are rotary screen printed in a rectangular pattern, so these layers also require alignment in the printing direction with respect to the patterned ITO. The layout of the modules with a cell length of 15 cm is depicted in **Figure 34**. The ZnO and P3HT:PCBM layers are aligned with respect to the ITO, whereas PEDOT:PSS is aligned with P3HT:PCBM, and Ag correspondingly with PEDOT:PSS.

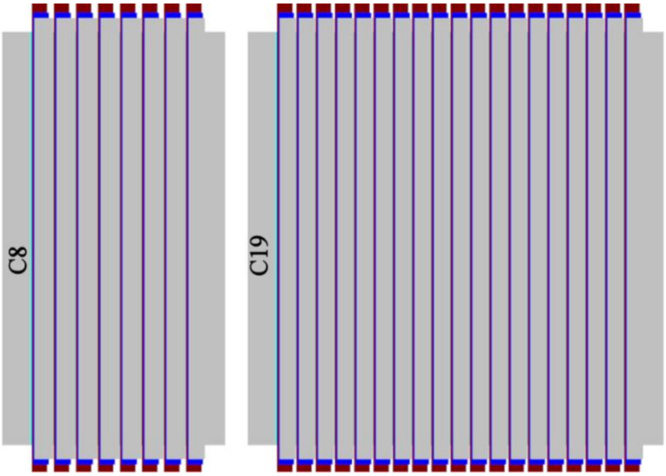

Figure 34. Layouts of the printed modules in the R2R process. C refers to the longest module (15 cm). The number 8 refers to 8 monolithically series-connected cells, and the number 19 refers to 19 monolithically series connected cells. *(Article IV © Nanoscale, reproduced by permission of the Royal Society of Chemistry.)*

The rheological properties of the printing ink significantly affect the ability to obtain good uniformity and well-defined edges in the R2R-printed layers. The same ink formulation for P3HT:PCBM was used as in the standard configuration modules described in Section 6.3. The viscosity of P3HT:PCBM was measured at different shear rates. The ink is shear-thinning (43.3 mPa·s @ 1s^{-1} → 24.8 mPa·s @ 6000 s^{-1}), so the viscosity decreases as a function of the shear rate. During the printing process P3HT:PCBM viscosity can be estimated at approximately 25 mPa·s. With R2R gravure printing of P3HT:PCBM ink, a uniform layer with a thickness of 175 (±12) nm was obtained. The surface roughness measurements showed a root mean square roughness value of 1.45 nm and a maximum height variation (peak-to-valley) of 13 nm. Also, the dimensional accuracy of the P3HT:PCBM ink was excellent, exhibiting an average dimension of 5.6 mm ±0.5% (5.6 mm engraved pattern). The dimensional accuracy is defined as the difference between the module layout and the actual printed pattern in the CD direction.

The fully printed inverted modules were produced in six module sizes. Three cell sizes (A–C) were applied by varying the cell length from 5 to 15 cm (A=0.34x5.0 cm^2, B=0.34x10.0 cm^2 and C=0.34x15 cm^2). One side of the roll is composed of eight monolithically series-connected cells and the other side of 19 series-connected cells. Thus, the total active area of the modules ranges from 13.6 cm^2 to 96.5 cm^2. Electrical characterization was carried out on a total of 220 printed modules. The IV measurement of the modules was prepared without any thermal post treatment or light soaking. The mean efficiencies varied from 1.7–1.8%, whereas the maximum values surpassed 2.0–2.2% depending on the module size. Excellent repeatability was detected in the characterized modules. Furthermore, repeatability analysis was carried out by characterizing two 12-module series for each of the three module sizes with 19 cells. The modules for both series were consecutive modules from the R2R-produced roll (different part of the roll). The electrical parameters in terms of I_{SC}, V_{OC}, FF and PCE as a function of sample number are depicted in **Figure 35**. The parameters for the Series 1 are shown with filled circles and for the Series 2 with open circles. The abbreviation A19 refers to a total active area of 32.2 cm^2 (cell length 5 cm), B19 to 64.4 cm^2 (cell length 10 cm) and C19 to 96.5 cm^2 (cell length 15 cm).

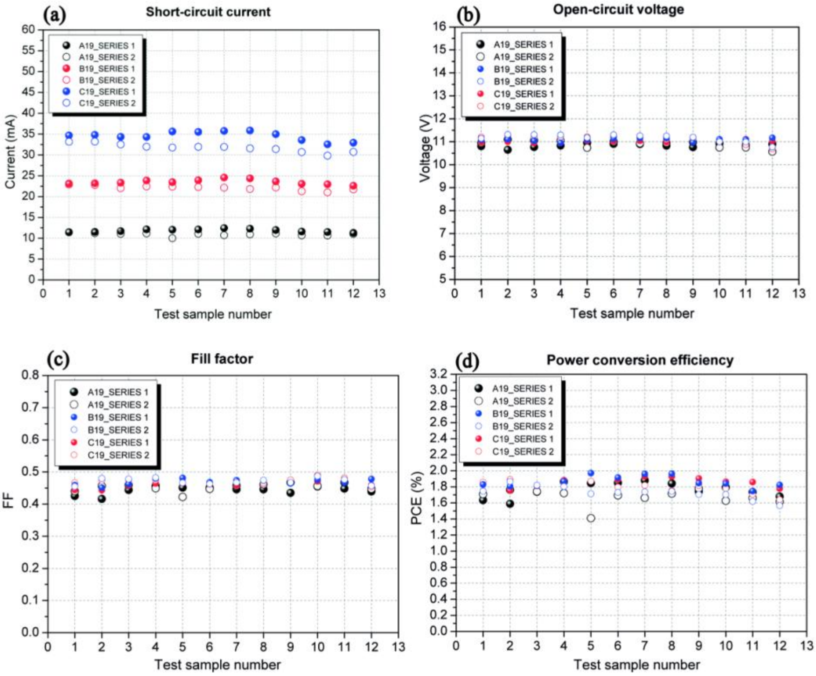

Figure 35. (a) I_{SC}, (b) V_{OC}, (c) FF and (d) PCE of fully R2R-printed modules. Two test series of three different module sizes (A19= 32.2 cm^2, B19=64.4 cm^2 and C19=96.5 cm^2) are depicted as a function of test sample number. In total, 72 modules were characterized in the repeatability test series. *(Article IV © Nanoscale, reproduced by permission of the Royal Society of Chemistry.)*

Small fluctuations were observed for the short-circuit current values. It should be noted that the pilot printing machine used in these experiments is equipped with control cameras, but the registration is manually controlled. The manual registration control and the limited detection of highly transparent layers of ZnO and ITO challenge the layer alignment. The design tolerance for the influences of misalignment between printed layers and the spread or shrinkage of the wet film was 600 µm per layer. The ZnO layer showed the highest average misalignment of up to 300 µm. Conversely, P3HT:PCBM, PEDOT:PSS and Ag were aligned according to the specifications with few exceptions. P3HT:PCBM dislocates only 100 µm from the average. The variation observed in the I_{SC} correlated with the manually operated registration, which affects the size of each cell in all sizes of modules printed at the same time and, consequently, the short-circuit current values as well. A CD variation of 100 µm changes the cell area with the largest module (C19) by 3%. This means that a variation of 100 to 200 µm will affect the short-circuit current value by ±1-2 mA. The mean electrical parameters of the test series are summarized in **Table 4**.

Table 4. Mean electrical parameters for three different module sizes (A19= 32.2 cm^2, B19=64.4 cm^2 and C19=96.5 cm^2) in repeatability testing (two 12-module batches per category). The mean value is calculated as an average of both test series shown in **Figure 35**. The J_{SC} per cell is calculated by dividing the I_{SC} by the area of one cell in the module structure. *(Article IV © Nanoscale, reproduced by permission of the Royal Society of Chemistry.)*

Module area	Yield	Mean Isc [mA]	Mean Jsc per cell [$mAcm^{-2}$]	Mean Voc [V]	Mean Voc per cell [V]	Mean Pmpp [mW]	Mean FF	Mean PCE [%]	Max PCE [%]
32.2 cm^2 (A19)	100% (24/24)	11.39 (±0.59)	6.72	10.87 (±0.13)	0.57	55.40 (±3.40)	0.45 (±0.01)	1.72 (±0.11)	1.88
64.4 cm^2 (B19)	100% (24/24)	22.80 (±0.92)	6.73	11.06 (±0.13)	0.58	117.59 (±4.61)	0.47 (±0.01)	1.83 (±0.07)	1.93
96.5 cm^2 (C19)	100% (24/24)	33.16 (±1.78)	6.53	11.13 (±0.13)	0.59	173.44 (±9.88)	0.47 (±0.01)	1.80 (±0.10)	1.97

The cell width in all 19 cell designs was set at 3.4 mm, supposing accurate registration. As **Table 4** shows, the mean PCE remains constant at 1.7–1.8%. This implies that the printing quality of the different layers is uniform in both the printing (machine) direction and the perpendicular (cross) direction. Notably, all of the modules function properly with a yield of 100%. This implies that no detrimental processing defects resulting in electrically shorted cells can be detected. The I_{SC} is directly proportional to the active area. As the B19 module has twice the length of A19 its mean Isc value is twice as high. With the largest module size, C19, the mean Isc is 1 mA less than it should be (three times higher than with A19). The number of cells in series connection is the same in all module sizes, so the Voc should be constant. Thus, the Voc of the modules is in the range 10.9–11.1 V.

6.5 Aerosol printing of fine line grid structures

The applicability of aerosol printing technology in the fabrication of fine line printed current collecting grids was investigated. Aerosol printing can be considered an alternative to other competitive methods such as screen printing and ink-jet printing when fine line deposition is required. The inverted device configuration investigated here consists of a non-transparent electron contact (Cr/Al/Cr) and a partly transparent hole contact consisting of highly conductive PEDOT:PSS and a silver grid. Evaporated Au grid is used as a reference. Due to the non-transparency of the bottom contact, the cells are illuminated from the grid side. Optimization of the grid design is a compromise between the area coverage and the conductivity of the grid lines. The more area the grid lines cover, the less illumination can reach the active layer. However, by minimizing the line width and generally also the line height, resistive losses are increased. In aerosol printing, these parameters are influenced, for instance, by the chuck temperature, printing speed and the number of printing passes. The influence of the above-mentioned parameters on the grid properties and, subsequently, on the performance of small-area solar cells was studied. Firstly, single pass printing was investigated by varying the printing speed and chuck temperature. Secondly, with a constant printing speed and chuck temperature, multiple pass printing was examined using two to four printing passes in order to increase the conductivity of the grid lines. The printing parameter combination dependence on the integrated area, line width, height, effective sheet resistance, resistivity and aspect ratio of the grid lines are summarized in **Table 5**.

Table 5. Mean cross-sectional area, line width, height, effective sheet resistance, resistivity and aspect ratio of aerosol jet printed lines with different printing parameter combinations (number of printing passes, chuck temperature and printing speed). The standard deviation values are shown after the mean value in brackets. *(Article V © Solar Energy Materials and Solar Cells, reproduced with the permission of Elsevier.)*

Number (layers/T(°C)/ v (mm s^{-1}))	Area (μm^2)	Width (µm)	Height (µm)	Eff. sheet resistance (Ω)	Resistivity (Ω·cm)	Aspect ratio
#1 (1/70/5)	228.0 (91.3)	119.3 (34.5)	1.6 (0.3)	1.5 (0.2)	3.4×10^{-5}	0.013
#2 (1/70/10)	75.9 (9.2)	76.6 (5.5)	1.0 (0.0)	3.2 (0.6)	2.4×10^{-5}	0.012
#3 (1/70/20)	43.8 (11.2)	58.1 (9.4)	0.8 (0.0)	8.9 (2.2)	3.9×10^{-5}	0.013
#4 (1/120/10)	70.3 (7.3)	70.0 (5.3)	1.2 (0.0)	3.0 (0.5)	2.1×10^{-5}	0.017
#5 (2/70/10)	142.2 (15.9)	93.8 (7.8)	1.7 (0.3)	1.7 (0.3)	2.5×10^{-5}	0.018
#6 (4/70/10)	307.1 (81.6)	111.8 (18.0)	3.7 (0.3)	0.7 (0.1)	2.0×10^{-5}	0.032

As the printing speed is increased in single pass printing (#1-#3) less material is transferred to the substrate. With this approach narrower and thinner grid lines can be deposited. However, this leads to an increase in effective sheet resistance. With the lowest tested printing speed of 5 mm s^{-1} the standard deviation of the width is the highest. This is due to ink accumulation in random intervals forming over 100 µm wider and thicker areas. When the printing speed is increased further to 10 mm s^{-1}, the expanded areas are no longer detected. With the used silver ink a minimum line width of 58 µm was achieved on a PEDOT:PSS layer. By multiple pass printing (#5-#6) the line height could be increased while only modestly affecting the line width. This approach significantly improved the aspect ratio. Correspondingly, the effective sheet resistance was decreased as a function of the number of printing passes without increasing the area coverage. A microscope image of the grid structure with parameter combination #2 with a line separation of 1 mm is shown in **Figure 36**.

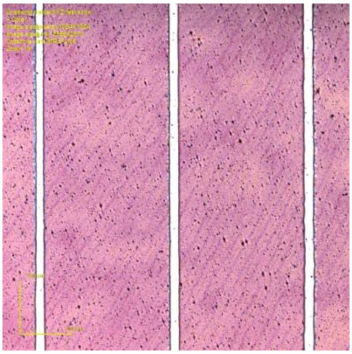

Figure 36. Aerosol printed grid structure used in the inverted solar cells. In each cell, the grid is composed of 22 lines with a line separation of 1 mm. The lines were printed with a chuck temperature of 70 °C and a printing speed of 10 mm s^{-1}. *(Article V © Solar Energy Materials and Solar Cells, Reproduced with the permission of Elsevier)*.

It was verified that with a single cell structure (cell length 6 mm, total active area 1.1 cm^2) the highest current density and the best efficiency of 2.6% was reached with the narrowest and thinnest grid lines. The solar cells with a single pass printed grid showed a similar efficiency as the reference cells prepared with an evaporated Au grid. The electrical measurements showed that increased conductivity through multiple pass printing does not result in improved performance of small-area cells. However, the higher conductivity is favoured in the module efficiency as larger cell strips can be used. The optimization of the aerosol printed grids presented here has also been used later for preparation of R2R slot die coated bilayer cells [26].

6.6 Characterization of slot die coated OPV modules with complementary imaging techniques

Modules with series-connected cells are prone to lower I_{SC} than individual cells. This is because the cell with the lowest I_{SC} limits the overall current produced by the module. In order to optimize module performance, spatial photocurrent characterization is essential. For single cells this is commonly performed with LBIC. Applying LBIC to modules is, however, more complicated as the current of the cell under light scanning is blocked by the other cells of the module. One means of overcoming this blocking is to use bias lighting for the other cells.

The slot die coated ITO-free modules consisting of 11 monolithically series-connected cells were characterized using the LBIC method and bias illumination. Strong cell-to-cell photocurrent variation could be observed in the typical slot die coated module shown in the LBIC map (**Figure 37**a). The electrical parameters of the module were as follows: V_{OC}=5.1V, J_{SC}=7.7mA cm^{-2}, FF=42%, and PCE=1.5% (active area). The V_{OC} of this particular module lacked the voltage of approximately 2–3 cells. The module J_{SC} was approximately 1–2 mA cm^{-2} lower compared to the J_{SC} of a single cell. However, the J_{SC} for this module type is typically in the range 5–6 mAcm^{-2}. Similar features inside the cell areas could also be detected in the EL measurements performed on the same module (**Figure 37**b). Conversely, the strong cell-to-cell variation observed in LBIC could not be detected. Therefore, it could be assumed that LBIC does not provide a real photogenerated current of the module. For instance, cell 4 shows a relatively high EQE and average EL intensity. Cells 9 and 10 differ strongly in LBIC signal, but the EL responses are comparable.

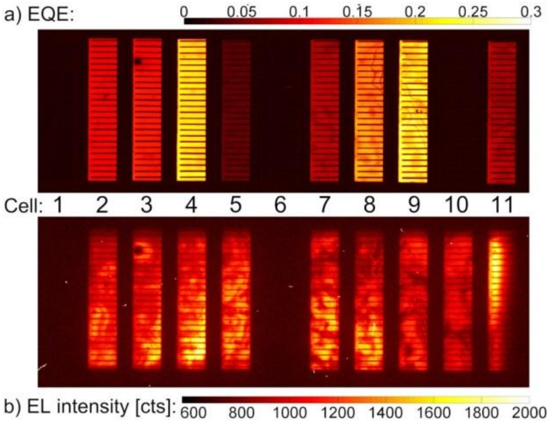

Figure 37. (a) LBIC EQE map of an organic solar cell module for an excitation wavelength of 532nm. The image was assembled from 11 LBIC mappings with OLED bias-illumination. (b) EL measurement of the same module at low forward current densities. *(Article VI © Solar Energy Materials & Solar Cells, reproduced with the permission of Elsevier.)*

A novel filtering approach was used to investigate the observed behaviour. In the filtering, all cells are illuminated with one sun illumination (100 mW cm^{-2}). The cell under measurement is covered with neutral density filter to decrease the photocurrent below the limiting cell current. The module is maintained at external I_{SC} conditions and "the filtered module current" is measured. The filtered current depends on the photocurrent of the respective solar cell if the photocurrent of the latter is lower than the photocurrents of all the fully illuminated cells and as long as the shunt resistance is infinitely large. If these conditions are fulfilled all fully illuminated cells are under forward bias conditions ($0 \leq V \leq V_{OC}$) and the filtered cell is under negative bias ($V_i = -\sum_{j \neq i} V_j$ with i being the measured cell and j≠i all other cells of the module) as the whole module is kept at 0 V. Conversely, if a certain cell has a finite shunt resistance, negative voltage causes leakage current resulting in overestimation of the photocurrent of the filtered cell. Therefore, the filtering approach can deliver reliable results only if the investigated cell has a reasonably high shunt resistance.

The investigation was continued by varying the transmission of the filter, i.e. using multiple negative bias voltages (four different transmission levels) in order to evaluate the reverse blocking behaviour of the cells. The filtered I_{SC} as a function of cell number is depicted in **Figure 38**a. It is important to emphasize that for cells with infinitely large shunt resistance, the photocurrent is expected to be proportional to the light intensity. Any deviation detected from the expected behaviour could be attributed to a finite shunt resistance. Interestingly, the filtering approach correlates well with the LBIC EQE measurement. Cells that are insensitive to filtering are completely dark in LBIC measurement (cells 1, 6 and 10 in **Figure 38**a). Additionally, it was found that in the cells showing low EQE values in LBIC the current was not proportional to different transmission levels. On the other hand, the cells with the strongest response to filtering (cells 4, 8, and 9) also showed the highest EQE values in the LBIC. It is therefore evident that module LBIC measurements with bias illumination are strongly dependent on the shunt resistance of the cells and thus on the blocking behaviour under reverse bias voltages.

A thermographic map obtained with DLIT was measured to derive understanding of the cause of bad blocking behaviour (see **Figure 38**b). It is apparent from the DLIT image that several cells suffer from shunts. Furthermore, the shunt distribution correlates well with the results of both LBIC and the filtering approach. For instance, the cells (1, 6 and 10) that were completely insensitive to filtering show detrimental hot-spots, while the low-performing cells 5 and 7 show the highest number of small hot-spots. Three cells without any visible hotspots (cells 4, 8, and 9) show the highest degree of proportionality in the filtering approach and also the highest EQE values in the LBIC measurement. Cell 10, which shows no blocking behaviour at all, broke down completely after the DLIT measurement and possibly during the filtering measurement. All other characterization methods mentioned so far were applied before this event. In a second DLIT measurement after filtering, cell 10 showed no response from the cell area. The only remaining heat source was the already visible hot-spot in the first thermography measurement. It is likely that the large negative bias voltages during the filtering are responsible for damaging the cell. It has been reported by Steim et al. that applying negative bias voltages for extended periods of time can negatively affect blocking behaviour [136]. However, the measured cell in the filtering approach is stressed only for a few seconds with each filter. Therefore, it cannot be expected that applying the filtering approach would damage the cells, except in extreme cases where the cells are already severely shunted.

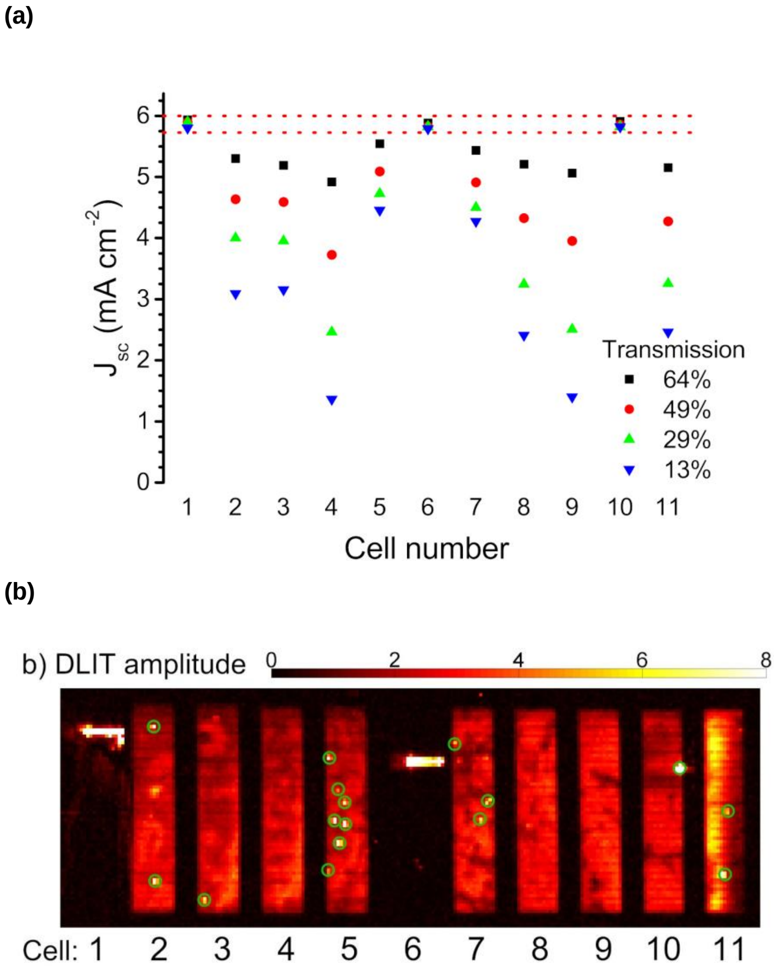

Figure 38. (a) Filtering results using four transmission levels. The effect on the J_{SC} of the module is shown. The two dashed lines specify the error margins of the unfiltered J_{SC} of the module. b) DLIT amplitude image of the measured module. The green circles mark the position of the less visible hot-spots. *(Article VI © Solar Energy Materials & Solar Cells, reproduced with the permission of Elsevier.)*

7. Discussion

In this chapter the results of the study are discussed and recommendations for future research are presented.

7.1 Theoretical and practical implications

The main objective of this work was to examine gravure printing as a deposition method for R2R manufacturing of flexible P3HT:PCBM-based solar modules. Earlier research reported on R2R-processed modules has used slot die coating as a deposition method [5]. The motivation for the present research arose from the possibility to directly pattern OPV modules in the printing process as arbitrary shapes and sizes and to accurately control the layer properties and edge formation in the printing process.

The capability of gravure printing for deposition of thin films was first proven on small-area cells (<cm^2) based on a standard configuration with an efficiency of 2.8%. Significant effort was focussed on modifying materials to gravure printable ink form and determining optimal cylinder and printing parameters. The wetting properties of PEDOT:PSS were modified in order to obtain a uniform layer. For the P3HT:PCBM photoactive ink, the solid content and viscosity were increased for gravure printing compared to spin coating. Also the engraving parameters were screened in order to obtain adequate layer thickness and high uniformity. The uniformity of the gravure-printed cells was investigated by increasing the active area to several cm^2 and processing eight cells in parallel to form series-connected modules. The I_{SC} showed a ~5% difference when the best cell was compared with the whole module. It was also found that the laboratory-scale process cannot be directly transferred to the R2R pilot production environment. However, laboratory-scale testing was essential for material selection and for screening the ink formulations and engraving parameters. It was also found that pinholes of diameter range 20 to 50 µm were formed in the photoactive layer in R2R processing of standard configuration modules, leading to electrical shorts with evaporated Ca/Ag electron contact. However, these processing non-idealities can be overcome by applying an insulative ultra-thin layer of LiF. This finding led us to obtain comparable results with laboratory and R2R-processed modules with standard configuration. Furthermore, fully R2R-printed modules with an inverted device structure (ITO/ZnO/P3HT:PCBM/PEDOT:PSS/Ag) were developed and successfully

demonstrated. Two batches containing 12 modules per module category (32.2, 64.4 and 96.5 cm^2) were selected for repeatability analysis. With a total active area of 96.5 cm^2 a mean efficiency of 1.8% was achieved (maximum efficiency 2.0%). The same performance was measured despite the increase in active area. Manual registration of the printing machine caused small active area deviations reflected in slight fluctuation of the I_{SC} of the modules. The efficiency values obtained with fully R2R-printed modules were nearly identical to the reported slot die coated modules using the same device and layer structure.

In this work, different characterization methods (LBIC, EL, DLIT, filtering approach) were investigated for imaging cell-to-cell variations in OPV modules. LBIC with bias illumination showed strong cell-to-cell variation, which was not detected in EL. Combined information from LBIC, DLIT and the novel filtering approach verified that spatial photocurrent characterization by LBIC using bias illumination was strongly dependent on cell shunt resistance.

The most remarkable results of this research are i) novel gravure printing based R2R thin-film deposition technology for OPV, ii) printed standard and inverted device structures, iii) R2R manufactured large-area flexible solar modules, iv) OPV process upscaling to R2R pilot level and v) investigation of characterization methods for OPV modules. These results confirm that gravure printing combined with other mechanical printing methods are applicable to OPV fabrication. The use of direct patterning as a means for structuring OPVs in the printing process has aroused interest among companies and research groups working in the OPV field. Due to structural, material and processing similarities, the findings of this study can also be extensively employed in the deposition of other thin-film components such as OLEDs and OTFTs.

7.2 Limitations

The extensive optimization of ink properties, engravings and printing parameters was carried out using a sheet-based laboratory-scale printing machine due to the high research material costs.

In this work, the solvents in the photoactive ink were limited to halogenated solvents to ensure high variability of solid content and viscosity range and to ensure that the ink remains soluble also in the R2R process in which open ink fountains are used.

The fabrication of fully R2R-printed OPV modules was demonstrated. However, the total number of modules characterized is limited to a few hundred, as the measurements were prepared manually. In order to examine the developed OPV process at the “production” level, the number of modules produced and measured must be increased significantly. In addition, the printing machine used in this study is equipped with control cameras but the registration is manually controlled, so slight variation in module performance was observed, especially due to correction of registration accuracy during processing.

7.3 Future research

The main motivation to use printing techniques for OPV fabrication is the possibility to directly pattern thin-film layers in the printing process as well as scalability to larger web widths and higher printing speeds. Therefore, future work will focus on the process development of arbitrary shaped and sized OPV modules. This will require transferring the developed OPV process to a printing machine equipped with an automatic registration system. **Figure 39** shows an example of printed leaf-shaped OPV modules [137]. OPV modules offer huge potential for integration into a broad spectrum of end-use applications, such as energy harvesting autonomous sensors.

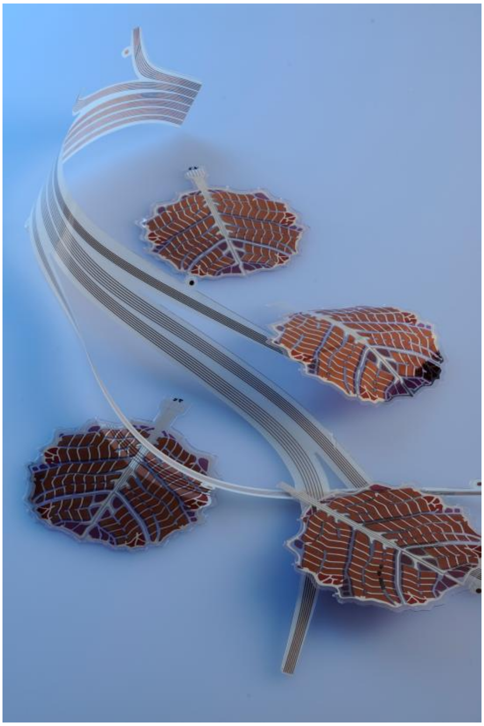

Figure 39. Leaf-shaped OPV modules produced with additive printing methods [137].

Another key future area of focus will be the development of cost-efficient encapsulation solutions for extending module lifetime. This, too, will involve the incorporation of novel interfacial layer and electrode materials. The present work was conducted using the most extensively studied polymer-fullerene combination, P3HT:PCBM. Future research will also investigate advanced, high-performance photoactive materials and their printability optimization. Non-halogenated solvents should also be examined for their important role in production-oriented printability optimization. In addition, extensive morphology analysis and electrical imaging of fully R2R-printed solar modules will further assist the process development. Finally, future production-oriented research should include long test runs for specifying yield and reliability.

8. Summary

The main objective of this research was to investigate gravure printing as a R2R thin-film deposition technique for fabrication of OPV layers and device structures. The work started with laboratory experiments to outline ink formulation, engraving and printing parameter alternatives for a printed two-layer structure (PEDOT:PSS and P3HT:PCBM) in a standard OPV cell configuration (ITO/PEDOT:PSS/P3HT:PCBM/Ca/Ag). Printability engineering was used to control the layer uniformity and thickness in thin-film deposition. The typical average surface roughness of the deposited photoactive layer after printability optimization was 2.7 nm (profilometer result). Additionally, optimal engraving parameters and ink formulation were specified to obtain a 190 nm average layer thickness. The electrical functionality of gravure-printed thin films was examined in small-area cells (<cm^2). A maximum efficiency of 2.8% was achieved. Furthermore, the active area of one cell was upscaled to the cm^2 level. The first module design consisted of eight cells connected in series to increase the output voltage to 3–4 V. The total active area of this module type was 15 cm^2. A maximum module efficiency of 1.7% was obtained with a side-connected configuration and 2.3% with a monolithically-connected configuration.

Processing conditions with the highest potential for standard configuration OPV module fabrication were examined in high-throughput R2R pilot fabrication. In microscopic analysis, detrimental pinholes in the R2R gravure-printed photoactive layer were discovered. By replacing the interfacial layer of Ca with LiF the pinholes were insulated and remarkable enhancement in module performance was observed. Electrical measurements showed that comparable performance was achieved in both the R2R (mean 1.7%, max 1.9%) and laboratory (mean 2.2%, max 2.3%) OPV manufacturing processes. Also, a larger batch of R2R-printed modules with LiF interlayer was measured resulting in a mean efficiency of 1.77% ± 0.15% for 50 modules. In these standard configuration modules, the process included two sheet-based evaporation steps (LiF and Al).

With the aim of achieving fully R2R-printed structures, the research focused on inverted configuration (ITO/ZnO/P3HT:PCBM/PEDOT:PSS/Ag). The ITO layer was R2R patterned and the other layers R2R printed. The R2R gravure-printed P3HT:PCBM layer had a thickness of 175 (±12) nm. Surface roughness measurements showed an Rq value of 1.45 nm and maximum height variation (peak-to-valley) of 13 nm (AFM measurement). In addition, the dimensional accuracy of the P3HT:PCBM ink in the CD direction was excellent, exhibiting an average dimension of 5.6 mm ±0.5% (5.6 mm engraved pattern). A total of 220 modules of six different sizes (from 13.6 cm^2 to 96.5 cm^2) were electrically measured. The mean efficiency ranged from 1.7–1.8% with maximum values of up to 2.0–2.2%. With the largest module size (efficiency of 1.80±0.10%) nearly identical performance to state-of-art R2R slot die coated counterparts (efficiency of 1.79±0.09%, [19]) using the same device and layer structure was attained.

Finally, different characterization methods (LBIC, EL, DLIT, filtering approach) were used to examine cell-to-cell variation in series-connected modules. LBIC showed strong cell-to-cell variation, which was not detected in EL. Combined results from LBIC, DLIT and the novel filtering approach revealed spatial photocurrent characterization by LBIC using bias illumination to be strongly dependent on cell shunt resistance.

The results of this work verify that gravure printing based R2R thin-film deposition is high-potential method for OPV manufacture. The OPV process for both standard and inverted module configurations was successfully upscaled to the R2R pilot level. The most significant achievement regarding the coating technologies arises from the patterning capability, enabling arbitrary shaped and sized OPV structures to be used for energy harvesting in a broad spectrum of end-use applications.

References

[1] International Energy Agency, Statistics (2011) http://www.iea.org/statistics/

[2] International Renewable Energy Agency (2013). Solar Photovoltaics. Technology Brief.

[3] O'Regan B, Grätzel M (1991) A low-cost, high-efficiency solar cell based on dye-sensitized colloidal TiO_2 films. Nature 353:737-739.

[4] Krebs FC (2009) Fabrication and processing of polymer solar cells: A review of printing and coating techniques. Solar Energy Materials & Solar Cells 93:394-412.

[5] Krebs FC, Espinosa N, Hösel M, Søndergaard RR, Jørgensen M (2014) 25th Anniversary Article: Rise to Power – OPV-Based Solar Parks. Advanced Materials 26:29-39.

[6] Søndergaard RR, Hösel M, Krebs FC (2013) Roll-to-Roll Fabrication of Large Area Functional Organic Materials. Journal of Polymer Science 51:16-34.

[7] Søndergaard RR, Hösel M, Angmo D, Larsen-Olsen TT, Krebs FC (2012) Roll-to-roll fabrication of polymer solar cells. Materials Today 15:36-49.

[8] Deibel C, Dyakonov V (2010) Polymer-fullerene bulk heterojunction solar cells. Reports on Progress in Physics 73:096401-1-096401-37.

[9] Chen C-C, Dou L, Zhu R, Chung C-H, Song T-B, Zheng YB, Hawks S, Li Gang, Weiss PS, Yang Y (2012) Visibly Transparent Polymer Solar Cells Produced by Solution Processing. ACS Nano 6:7185-7190.

[10] Lunt RR, Bulovic V (2011) Transparent, near-infrared organic photovoltaic solar cells for window and energy-scavenging applications. Applied Physics Letters 98:113305-1-113305-3.

[11] IDTechEx, Organic Photovoltaics (OPV) 2012-2022: Technologies, Markets, Players

[12] Tang CW (1986) Twolayer organic photovoltaic cell. Applied Physics Letters 48:183-185.

[13] Scharber MC, Mühlbacher D, Koppe M, Denk P, Waldauf C, Heeger AJ, Brabec CJ (2006) Design Rules for Donors in Bulk-Heterojunction Solar Cells – Towards 10% Energy-Conversion Efficiency. Advanced Materials 18:789-794.

[14] You J, Dou L, Yoshimura K, Kato T, Ohya K, Moriarty T, Emery K, Chen C-C, Gao J, Li G, Yang Y (2013) A polymer tandem solar cell with 10.6% power conversion efficiency. Nature Communications 4:1-10.

[15] Service R (2011) Outlook Brightens for Plastic Solar Cells. Science 332:293.

[16] Hosoya M, Oooka H, Nakao H, Mori S, Gotanda T, Shida N, Hayase R, Nakano Y, Saito M (2013) Module development for organic thin-film photovoltaics. 28th European Photovoltaic Solar Energy Conference and Exhibition 2013. Pp. 2236-2238.

[17] Blankenburg L, Schultheis K., Schache H, Sensfuss S, Schrödner M (2009) Reel-to-reel wet coating as an efficient up-scaling technique for the production of bulk-heterojunction polymer solar cells. Solar Energy Materials & Solar Cells 93:476-483.

[18] Krebs FC, Gevorgyan SA, Alstrup J (2009) A roll-to-roll process to flexible polymer solar cells: model studies, manufacture and operational stability studies. Journal of Materials Chemistry 19:5442-5451.

[19] Krebs FC, Tromholt T, Jørgensen M (2010) Upscaling of polymer solar cell fabrication using full roll-to-roll processing. Nanoscale 2:873-886.

[20] Krebs FC, Fyenbo J, Jørgensen M (2010) Product integration of compact roll-to-roll processed polymer solar cell modules: methods and manufacture using flexographic printing, slot-die coating and rotary screen printing. Journal of Materials Chemistry 20:8994-9001.

[21] Galagan Y, de Vries IG, Langen AP, Andriessen R, Verhees WJH, Veenstra SC, Kroon JM (2011) Technology development for roll-to-roll production of organic photovoltaics. Chemical Engineering and Processing: Process Intensification 50:454-461.

[22] Angmo D, Gevorgyan S, Larsen-Olsen TT, Søndergaard RR, Hösel M, Jørgensen M, Gupta R, Kulkarni GU, Krebs FC (2013) Scalability and stability of very thin roll-to-roll processed, large area, indium-tin-oxide free polymer solar cell modules. Organic Electronics 14:984-994.

[23] Hösel M, Søndergaard RR, Jørgensen M, Krebs FC (2013) Fast Inline Roll-to-Roll Printing for Indium-Tin-Oxide-Free Polymer Solar Cells Using Automatic Registration. Energy Technology 1:102-107.

[24] Krebs FC, Hösel M, Corazza M, Roth B, Madsen MV, Gevorgyan SA, Søndergaard RR, Karg D, Jørgensen M (2013) Freely available OPV – The fast way to progress, Energy Technology 1:378-381.

[25] Sommer-Larsen P, Jørgensen M, Søndergaard RR, Hösel M, Krebs FC (2013) It is all in the Pattern – High Efficiency Power Extraction from Polymer Solar Cells through High-Voltage Serial Connection. Energy Technology 1:15-19.

[26] Kaduwal D, Schleiermacher H-F, Schulz-Gericke J, Kroyer T, Zimmermann B, Würfel U (2014) ITO-free organic solar cells with roll-to-roll coated organic functional layers from non-halogenated solvents. Solar Energy Materials & Solar Cells 124:92-97.

[27] Tuomikoski M, Suhonen R (2006) Manufacturing of polymer solar cells using gravure printing. Proceedings of TPE06, 2nd International Symposium Technologies for Polymer Electronics 83.

[28] Ding JM, de la Fuente Vornbrock A, Ting C, Subramanian V (2009) Patternable polymer bulk heterojunction photovoltaic cells on plastic by rotogravure printing. Solar Energy Materials & Solar Cells 93:459-464.

[29] Kopola P, Aernouts T, Guillerez S, Jin H, Tuomikoski M, Maaninen A, Hast J (2010) High-efficient plastic solar cells fabricated with a high throughput gravure printing method. Solar Energy Materials & Solar Cells 94:1673-1680.

[30] Kopola P, Aernouts T, Sliz R, Guillerez S, Ylikunnari M, Cheys D, Välimäki M, Tuomikoski M, Hast J, Jabbour G, Myllylä R, Maaninen A (2011) Gravure printed flexible organic photovoltaic modules. Solar Energy Materials & Solar Cells 95:1344-1347.

[31] Apilo P, Hiltunen J, Välimäki M, Heinilehto S, Sliz R, Hast J (2015) Roll-to-Roll Gravure Printing of Organic Photovoltaic Modules – Insulation of Processing Defects by an Interfacial Layer. Progress in Photovoltaics: Research and Applications 23:918-928.

[32] Schneider A, Traut N, Hamburger M (2014) Analysis and optimization of relevant parameters of blade coating and gravure printing processes for the fabrication of highly efficient organic solar cells. Solar Energy Materials & Solar Cells 126:149-154.

[33] Voigt MM, Mackenzie RCI, King SP, Yau CP, Atienzar P, Dane J, Keivanidis PE, Zadrazil I, Bradley DDC, Bradley DDC, Nelson J (2012) Gravure Printing inverted solar cells: The influence of ink properties on film quality and device performance. Solar Energy Materials & Solar Cells 105:77-85.

[34] Voigt MM, Mackenzie RCI, Yau CP, Atienzar P, Dane J, Keivanidis P, Bradley DDC, Nelson J. (2011) Gravure printing of three subsequent solar cell layers of inverted structures on flexible substrates. Solar Energy Materials & Solar Cells 95:731-734.

[35] Hübler A, Trnovec B, Zillger T, Ali M, Wetzold N, Mingebach M, Wagenpfahl A, Deibel C, Dyakonov V (2011) Printed Paper Photovoltaic Cells. Advanced Energy Materials 1:1018-1022.

[36] Koidis C, Logothetidis S, Ioakeimidis A, Laskarakis A, Kapnopoulos C (2013) Key factors to improve the efficiency of roll-to-roll printed organic photovoltaics. Organic Electronics 14:1744-1748.

[37] Koidis C, Logothetidis S, Kassavetis S, Kapnopoulos C, Karagiannidis PG, Georgiou D, Laskarakis A (2013) Effect of process parameters on the morphology and nanostructure of roll-to-roll printed P3HT:PCBM thin films for organic photovoltaics. Solar Energy Materials & Solar Cells 112:36-46.

[38] Yang J, Vak D, Clark N, Subbiah J, Wong WWH, Jones DJ, Watkings SE, Wilson G (2013) Organic photovoltaic modules fabricated by an industrial gravure printing proofer. Solar Energy Materials & Solar Cells 109:47-55.

[39] Vilkman M, Apilo P, Välimäki M, Ylikunnari M, Bernardi A, Po R, Corso G, Hast J (2015) Energy Technology 3:407-413.

[40] Välimäki M, Apilo P, Po R, Jansson E, Bernardi A, Ylikunnari M, Vilkman M, Corso G, Puustinen J, Tuominen J, Hast J (2015) R2R-printed inverted OPV modules – towards arbitrary patterned designs. Nanoscale 7:9570-9580.

[41] Kipphan H (Ed.) (2001) Handbook of Print Media. Berlin Heidelberg Germany, Springer-Verlag. Ch 1.3, 1.5, 2.2.

[42] Tuomikoski M, Suhonen R, Välimäki M, Maaninen T, Maaninen A, Sauer M, Rogin P, Mennig S, Heusing J, Puetz J, Aegerter MA (2006) Manufacturing of polymer light-emitting device structures Proceedings of SPIE 6192 Organic Optoelectronics and Photonics II 619204.

[43] Kopola P, Tuomikoski M, Suhonen R, Maaninen A (2009) Gravure printed organic light emitting diodes for lighting applications. Thin Solid Films 517:5757-5762.

[44] Hernandez-Sosa G, Bornemann N, Ringle I, Agari M, Dörsam E, Mechau N, Lemmer U (2013) Rheological and Drying Considerations for Uniformly Gravure-Printed Layers: Towards Large-Area Flexible Organic Light-Emitting Diodes. Advanced Functional Materials 23:3164-3171.

[45] Tekoglu S, Hernandez-Sosa G, Kluge E, Lemmer U, Mechau N (2013) Gravure printed flexible small-molecule organic light emitting diodes. Organic Electronics 14:3493-3499

[46] Chung D-Y, Huang J, Bradley DDC, Campbell AJ (2010) High performance, flexible polymer light-emitting diodes (PLEDs) with gravure contact printed hole injection and light emitting layers. Organic Electronics 11:1088-1095.

[47] Bornemann N, Sauer HM, Dörsam E (2011) Gravure Printed Ultrathin Layers of Small-Molecule Semiconductors on Glass. Journal of Imaging Science and Technology 55:040201-1-040201-8.

[48] Michels JJ, de Winter SHPM, Symonds LHG (2009) Process optimization of gravure printed light-emitting polymer layers by a neural network approach. Organic Electronics 10:1495-1504.

[49] Huebler AC, Doetz F, Kempa H, Katz HE, Bartzsch M, Brandt N, Hennig I, Fuegmann U, Vaidyanathan S, Granstrom J, Liu S, Sydorenko A, Zillger T, Schmidt G, Preissler K, Reichmanis E, Eckerle P, Richter F, Fischer T, Hahn U (2007) Ring oscillator fabricated completely by means of mass-printing technologies. Organic Electronics 8:480-486.

[50] Hambsch M, Reuter K, Stanel M, Schmidt G, Kempa H, Fügmann U, Hahn U, Hübler AC (2010) Materials Science and Engineering B170:93-98.

[51] Voigt MM, Guite A, Chung D-Y, Khan RUA, Campbell AJ, Bradley DDC, Meng F, Steinke JHG, Tierney S, McCulloch I, Penxten H, Lutsen L, Douheret O, Manca J, Brokmann U, Sönnichsen K, Hülsenberg D, Bock W, Barron C, Blanckaert N, Springer S, Grupp J, Mosley A (2010) Polymer Field-Effect Transistors Fabricated by the Sequential Gravure Printing of Polythiophene, Two Insulator Layers and a Metal Ink Gate. Advanced Functional Materials 20:239-246.

[52] Schmidt GC, Bellmann M, Meier B, Hambsch M, Reuter K, Kempa H, Hübler AC (2010) Modified mass printing technique for the realization of source/drain electrodes with high resolution. Organic Electronics 11:1683-1687.

[53] Verilhac J-M, Benwadih M, Seiler A-L, Jacob S, Bory C, Bablet J, Heitzman M, Tallal J, Barbut L, Frère P, Sicard G, Gwoziecki R, Chartier I, Coppard R, Serbutoviez C (2010) Step toward robust and reliable amorphous polymer field-effect transistors and logic functions made by the use of roll to roll compatible printing processes. Organic Electronics 11:456-462.

[54] de la Fuente Vornbrock A, Sung D, Kang H, Kitsomboonloha R, Subramanian V (2010) Fully gravure and ink-jet printed high speed pBTTT organic thin film transistors. Organic Electronics 11:2037-2044.

[55] Hassinen T, Sandberg HGO (2013) Gravure printed low voltage polymer transistors and inverters 548:585-589.

[56] Hernandez-Sosa G, Tekoglu S, Stolz S, Eckstein R, Teusch C, Trapp J, Lemmer U, Hamburger M, Mechau N (2014) The Compromises of Printing Organic Electronics: A Case Study of Gravure-Printed Light-Emitting Electrochemical Cells. Advanced Materials 26:3235-3240.

[57] Lilja KE, Bäcklund TG, Lupo D, Hassinen T, Joutsenoja T (2009) Gravure printed organic rectifying diodes operating at high frequencies. Organic Electronics 10:1011-1014.

[58] Chiang CK, Fincher CR, Park YW, Heeger AJ, Shirakawa H, Louis EJ, Gau SC, MacDiarmid AG (1977) Electrical conductivity in Doped Polyacetylene. Physical Review Letters 39:1098-1101.

[59] Klauk H (2012) Organic Electronics II More Materials and Applications. Weinheim Germany, Wiley-VCH Ch 1.

[60] Brabec C, Dyakonov V, Scherf U (Eds.) (2010) Organic Photovoltaics Materials, Device Physics and Manufacturing Technologies. Weinheim Germany, Wiley-VCH. Ch 7, 12.

[61] Chamberlain GA (1982) Organic Solar Cells: A Review. Solar Cells 8:47-83.

[62] Yu G, Gao J, Hummelen JC, Wudl F, Heeger AJ (1995) Polymer Photovoltaic Cells: Enhanced Efficiencies via a Network of Internal Donor-Acceptor Heterojunctions. Science 270:1789-1791.

[63] Deibel C, Dyakonov V, Brabec CJ (2010) Organic Bulk-Heterojunction Solar Cells. IEEE Journal of Selected Topics in Quantum Electronics 16:1517-1527.

[64] Tvingstedt K, Vandewal K, Gadisa A, Zhang F, Manca J, Ingänas O (2009) Electroluminescence from Charge Transfer States in Polymer Solar Cells. Journal of American Chemical Society 131:11819-11824.

[65] IEC Standard 60904, Photovoltaic Devices, International Electrotechnical Commission, Geneva, Switzerland.

[66] ASTM Standard G173, Standard Tables for Reference Solar Spectral Irradiances: Direct Normal and Hemispherical on 37° Tilted Surface, ASTM International, West Conshohocken, PA.

[67] NREL's AM1.5 Standard Dataset, http://rredc.nrel.gov/solar/spectra/am1.5/

[68] ASTM Standard E 927, Standard Specification for Solar Simulation for Photovoltaic Testing, ASTM International, West Conshohocken, PA, USA.

[69] Editorial (2008) Reporting solar cell efficiencies in Solar Energy Materials and Solar Cells. Solar Energy Materials & Solar Cells 92:371-373.

[70] Shrotriya V, Li G, Yao Y, Moriarty T, Emery K, Yang Y (2006) Accurate Measurement and Characterization of Organic Solar Cells. Advanced Functional Materials 16:2016-2023.

[71] Emery KA, Osterwald CR, Cannon TW, Myers DR (1985) Methods for Measuring Solar Cell Efficiency Independent of Reference Cell or Light Source. 18th IEEE Photovoltaic Specialist Conference Proceedings 623-628.

[72] Brabec C, Dyakonov V, Parisi J, Sariciftci NS (Eds.) (2003) Organic Photovoltaics Concepts and Realization. Heidelberg Germany, Springer-Verlag. Ch 4, 6.

[73] Li G, Chu CW, Shrotriya V, Huang J, Yang Y (2006) Efficient inverted polymer solar cells. Applied Physics Letters 88:253503-1-253503-3.

[74] Waldauf C, Morana M, Denk P, Schilinsky P, Coakley K, Choulis SA, Brabec CJ (2006) Highly efficient inverted organic photovoltaics using solution based titanium oxide as electron selective contact. Applied Physics Letters 89:233517-1-233517-3.

[75] Glatthaar M, Niggemann M, Zimmermann B, Lewer P, Riede M, Hinsch A, Luther J (2005) Organic solar cells using inverted layer sequence. Thin Solid Films 491:298-300.

[76] Lee K, Kim JY, Park SH, Kim SH, Cho S, Heeger AJ (2007) Air-Stable Polymer Electronic Devices. Advanced Materials 19:2445-2449.

[77] Kyaw AKK, Sun XW, Jiang CY, Lo GQ, Zhao DW, Kwong DL (2008) An inverted organic solar cell employing a sol-gel derived ZnO electron selective layer and thermal evaporated MoO_3 hole selective layer. Applied Physics Letters 93:221107-1-221107-3.

[78] Hayakawa A, Yoshikawa O, Fujieda T, Uehara K, Yoshikawa S (2007) High performance polythiophene/fullerene bulk-heterojunction solar cell with a TiOx hole blocking layer. Applied Physics Letters 90:163517-1-163517-3.

[79] White MS, Olson DC, Shaheen SE, Kopidakis N, Ginley DS (2006) Inverted bulk-heterojunction organic photovoltaic device using a solution-derived ZnO underlayer. Applied Physics Letters 89:143517-1-143517-3.

[80] Gilot J, Barbu I, Wienk MM, Janssen RAJ (2007) The use of ZnO as optical spacer in polymer solar cells: Theoretical and experimental study. Applied Physics Letters 91:113520-1-113520-3.

[81] Kim JY, Kim SH, Lee H-H, Lee K, Ma W, Gong X, Heeger AJ (2006) New Architecture for High-Efficiency Polymer Photovoltaic Cells Using Solution-Based Titanium Oxide as an Optical Spacer. Advanced Materials 18:572-576.

[82] Hau SK, Yip H-L, Baek NS, Zou J, O'Malley K, Jen AK-Y (2006) Air-stable inverted flexible polymer solar cells using zinc oxide nanoparticles as an electron selective layer. Applied Physics Letters 92:253301-1-253301-3.

[83] Shrotriya V, Li G, Yao Y, Chu C-W, Yang Y (2006) Transition metal oxides as the buffer layer for polymer photovoltaic cells. Applied Physics Letters 88:073508-1-073508-3.

[84] Girotto C, Voroshazi E, Cheyns D, Heremans P, Rand BP (2011) Solution-Processed MoO_3 Thin Films As a Hole-Injection Layer for Organic Solar Cells. ACS Applied Materials & Interfaces 3:3244-3247.

[85] Kim JY, Lee K, Coates NE, Moses D, Nguyen T-Q, Dante M, Heeger AJ (2007) Efficient Tandem Polymer Solar Cells Fabricated by All-Solution Processing. Science 317:222-225.

[86] Cohen D (2007) Earth's natural wealth: an audit. New Scientist Magazine 23 May 2007.

[87] Aernouts T, Vanlaeke P, Geens W, Poortmans J, Heremans P, Borghs S, Mertens R, Andriessen R, Leenders L (2004) Printable anodes for flexible organic solar cell modules. Thin Solid Films 451-452:22-25.

[88] Galagan Y, Rubingh J-EJM, Andriessen R, Fan C-C, Blom PWM, Veenstra SC, Kroon JM (2011) ITO-free flexible organic solar cells with printed current collecting grids. Solar Energy Materials & Solar Cells 95:1339-1343.

[89] Zimmermann B, Schleiermacher H-F, Niggemann M, Würfel U (2011) ITO-free flexible inverted organic solar cell modules with high fill factor prepared by slot die coating. Solar Energy Materials & Solar Cells 95:1587-1589.

[90] Galagan Y, Coenen EWC, Sabik S, Gorter HH, Barink M, Veenstra SC, Kroon JM, Andriessen R, Blom PWM (2012) Evaluation of ink-jet printed current collecting grids and busbars for ITO-free organic solar cells. Solar Energy Materials & Solar Cells 104:32-38.

[91] Yu J-S, Kim I, Kim J-S, Jo J, Larsen-Olsen TT, Søndergaard RR, Hösel M, Angmo D, Jørgensen M, Krebs FC (2012) Silver front electrode grids for ITO-free all printed polymer solar cells with embedded and raised topographies, prepared by thermal imprint, flexographic and inkjet roll-to-roll processes. Nanoscale 4:6032-6040.

[92] Galagan Y, Zimmermann B, Coenen EWC, Jørgensen M, Tanenbaum DM, Krebs FC, Gorter H, Sabik S, Sloof LH, Veenstra SC, Kroon JM, Andriessen R (2012) Current Collecting Grids for ITO-Free Solar Cells. Advanced Energy Materials 2:103-110.

[93] Kopola P, Zimmermann B, Filipovic A, Schleiermacher H-F, Greulich J, Rousu S, Hast H, Myllylä R, Würfel U (2012) Aerosol jet printed grid for ITO-free inverted organic solar cells. Solar Energy Materials & Solar Cells 107:252-258.

[94] van de Wiel HJ, Galagan Y, van Lammeren TJ, de Riet JFJ, Gilot J, Nagelkerke MGM, Lelieveld RHCAT, Shanmugam S, Pagudala A, Hui D, Groen WA (2013) Roll-to-roll embedded conductive structures integrated into organic photovoltaic devices. Nanotechnology 24:484014-1-4840414-8.

[95] Galagan Y, Coenen EWC, Zimmermann B, Slooff LH, Verhees WJH, Veenstra SC, Kroon JM, Jørgensen M, Krebs FC, Andriessen R (2013) Scaling Up ITO-Free Solar Cells. Advanced Energy Materials 4: 1300498-1-1300498-7.

[96] Lee J-Y, Connor ST, Cui Y, Peumans P (2008) Solution-Processed Metal Nanowire Mesh Transparent Electrodes. Nanoletters 8:689-692.

[97] Ajuria J, Ugarte I, Cambarau W, Etxebarria I, Tena-Zaera R, Pacios R (2012) Insights on the working principles of flexible and efficient ITO-free organic solar cells based on solution processed Ag nanowire electrodes. Solar Energy Materials & Solar Cells 102:148-152.

[98] Wang Y, Chen X, Zhong Y, Zhu F, Loh KP (2009) Large area, continuous, few-layered graphene as anodes in organic photovoltaic devices. Applied Physics Letters 95:063302-1-063302-3.

[99] Wang Y, Tong SW, Xu XF, Özyilmaz B, Loh KP (2011) Interface Engineering of Layer-by-Layer Stacked Graphene Anodes for High-Performance Organic Solar Cells. Advanced Materials 23:1514-1518.

[100] Choe M, Lee BH, Jo G, Park J, Park W, Lee S, Hong W-K, Seong M-J, Kahng YH, Lee K, Lee T (2010) Efficient bulk-heterojunction photovoltaic cells with transparent multi-layer graphene electrodes. Organic Electronics 11:1864-1869.

[101] Barnes TM, Bergeson JD, Tenent RC, Larsen BA, Teeter G, Jones KM, Blackburn JL, van de Lagemaat J (2010) Carbon nanotube network electrodes enabling efficient organic solar cells without a hole transport layer. Applied Physics Letters 96:243309-1-243309-3.

[102] Rowell MW, Topinka MA, McGehee MD, Prall H-J, Dennler G, Sariciftci NS, Hu L, Gruner G (2006) Organic solar cells with carbon nanotube network electrodes. Applied Physics Letters 88:233506-1-233506-6.

[103] Kim S, Wang X, Yim JH, Tsoi WC, Kim J-S, Lee S, deMello JC (2012) Efficient organic solar cells based on spray-patterned single wall carbon nanotube electrodes. Journal of Photonics for Energy 2:021010-1-021010-9.

[104] Kohlstädt M, Grein M, Reinecke P, Kroyer T, Zimmermann B, Würfel U (2013) Inverted ITO- and PEDOT:PSS-free polymer solar cells with high power conversion efficiency. Solar Energy Materials & Solar Cells 117:98:102.

[105] Brabec C, Hauch J (2009) Roll to Roll Manufacturing of Organic Solar Modules. Unites States Patent US 7,476,278 B2.

[106] Aernouts T (2006) Organic Bulk Heterojunction Solar Cells, From Single Cell Towards Fully Flexible Photovoltaic Module. PhD Thesis, Katholieke Universiteit Leuven, Leuven, Belgium.

[107] The Gravure Education Foundation and Gravure Association of America (1991) Gravure: Process and Technology. Rochester NY, USA. Gravure Association of America. Ch 1, 2.

[108] Hübler A, Hahn U, Beier W, Lasch N, Fischer T (2002) High Volume Printing Technologies for the Production of Polymer Electronic Structures. IEEE Polytronic Conference Proceedings 172-176.

[109] Gamota DR, Brazis P, Kalyanasundaram K, Zhang J (Eds.) (2004) Printed organic and molecular electronics. Kluwer Academic Publishers USA. Ch 3.1, 3.4.

[110] Rong X, Pekarovic J, Pekarovicova A (2002) Gravure printability from laser and electromechanically engraved cylinder. 11th International Printing and Graphics Arts Conference, Toronto, Canada 151-154.

[111] Hennig G, Frauchiger J (2001) Direct laser system for rotogravure printing. Gravure 15:58-61.

[112] Blasche DW (1993) Methods of cylinder engraving for gravure printing. Tappi Journal 76:169-174.

[113] Davies GR, Hamblyn SM, Claypole TC, Gethin DT (2007) Effect of Viscosity on Halftone Reproduction in Rotogravure Printing. TAGA Proceedings (Doc ID: 70506).

[114] Sprycha R, Krishnan R (1997) Impact of ink/paper interactions on printability of aqueous publication gravure inks, Part IV Ink Transfer and Spreading on Paper. TAGA Proceedings 829-843 (Doc ID:970829).

[115] Kunz W (1975) Ink transfer in gravure process. TAGA Proceedings 151-176 (Doc ID: 750151).

[116] Bohan MFJ, Claypole TC (2004) The influence of viscosity in rotogravure halftone production, 12th IPGAC International Printing and Graphics Arts Conference 155-160.

[117] Young T (1805) An Essay on the Cohesion of Fluids. Philosophical Transactions of the Royal Society of London 95:65-87.

[118] Mette A, Richter PL, Hörteis M, Glunz SW (2007) Metal Aerosol Jet Printing for Solar Cell Metallization. Progress in Photovoltaics: Research and Applications 15:621-627.

[119] Rösch R, Krebs FC, Tanenbaum DM, Hoppe H (2012) Quality control of roll-to-roll processed polymer solar modules by complementary imaging methods. Solar Energy Materials & Solar Cells 97:176-180.

[120] Rösch R, Tanenbaum DM, Jørgensen M, Seeland M, Bärenklau M, Hermenau M, Voroshazi E, Lloyd MT, Galagan Y, Zimmermann B, Würfel U, Hösel M, Dam HF, Gevorgyan SA, Kudret S, Maes W, Lutsen L, Vanderzande D, Andriessen R, Teran-Escobar G, Lira-Cantu M, Rivaton A, Uzunoğlu GY, Germack D, Andreasen B, Madsen MV, Norrman K, Hoppe H, Krebs FC (2012) Investigation of the degradation mechanisms of a variety of organic photovoltaic devices by combination of imaging techniques – the ISOS-3 inter-laboratory collaboration. Energy & Environmental Science 5:6521-6540.

[121] Hoyer U, Wagner M, Swonke TH, Bachmann J, Auer R, Osvet A, Brabec CJ (2010) Electroluminescence imaging of organic photovoltaic modules. Applied Physics Letters 97:233303-1-233303-3.

[122] Breitenstein O, Warta W, Langenkamp M (2010) Lock-in Thermography Basics and Use for Evaluating Electronic Devices and Materials. Berlin Heidelberg, Springer-Verlag. Ch 2.2.

[123] Bauer J, Breitenstein O, Wagner J-M (2009) Lock-in Thermography: A Versatile Tool for Failure Analysis of Solar Cells. ASM International Electronic Device Failure 11:6-12.

[124] Vorasayan P, Betts TR, Tiwari AN, Gottschalg R (2009) Multi-laser LBIC system for thin film PV module characterisation. Solar Energy Materials & Solar Cells 93:917-921.

[125] Li G, Shrotriya V, Huang J, Yao Y, Moriarty T, Emery K, Yang Y (2005) High-efficiency solution processable polymer photovoltaic cells by self-organization of polymer blends. Nature Materials 4:864-868.

[126] Zimmermann B, Würfel U, Niggemann M (2009) Longterm stability of efficient inverted P3HT:PCBM solar cells. Solar Energy Materials & Solar Cells 93:491-496.

[127] Manceau M, Angmo D, Jørgensen M, Krebs FC. (2011) ITO-free flexible polymer solar cells: From small model devices to roll-to-roll processed large modules 12:566-574.

[128] Liu F, Shen W, Parker I (2006) Surface analysis, a way better understand lithographic printing problems. Appita Journal 59:108-113.

[129] Kawano K, Sakai J, Yahiro M, Adachi C (2009) Effect of solvent on fabrication of active layers in organic solar cells based on poly(3-hexylthiophene) and fullerene derivatives. Solar Energy Materials & Solar Cells 93:514-518.

[130] Li G, Yao Y, Yang H, Shrotriya V, Yang G, Yang Y (2007) “Solvent Annealing” Effect in Polymer Solar Cells Based on Poly(3-hexylthiophene) and Methanofullerenes. Advanced Functional Materials 17:1636-1644.

[131] Brabec CJ, Shaheen SE, Winder C, Sariciftci S, Denk P (2002) Effect of LiF/metal electrodes on the performance of plastic solar cells. Applied Physics Letters 80:1288-1290.

[132] Jönsson SKM, Carlegrim E, Zhang F, Salaneck WR, Fahlman M (2005) Photoelectron Spectroscopy of the Contact between the Cathode and the Active Layers in Plastic Solar Cells: The Role of LiF. Japanese Journal of Applied Physics 44:3695-3701.

[133] Ahlswede E, Hanisch J, Powalla M (2007) Comparative study of the influence of LiF, NaF, and KF on the performance of polymer bulk heterojunction solar cells. Applied Physics Letters 90: 163504-1-163504-3.

[134] Reese MO, Gevorgyan SA, Jørgensen M, Bundgaard E, Kurtz SR, Ginley DS, Olson DC, Lloyd MT, Morvillo P, Katz EA, Elschner A, Haillant O, Currier TR, Shrotriya V, Hermenau M, Riede M, Kirov KR, Trimmel G, Rath T, Inganäs O, Zhang F, Andersson M, Tvingstedt K, Lira-Cantu M, Laird D, McGuiness C, Gowrisanker S, Pannone M, Xiao M, Hauch J, Steim R, DeLongchamp DM, Rösch R, Hoppe H, Espinosa N, Urbina A, Yaman-Uzunoglu G, Bonekamp JB, vanBreemen AJJM, Girotto C, Voroshazi E, Krebs FC (2011) Consensus stability testing protocols for organic photovoltaic materials and devices. Solar Energy Materials & Solar Cells 95: 1253-1267.

[135] Tanenbaum DM, Hermenau M, Voroshazi E, Lloyd MT, Galagan Y, Zimmermann B, Hösel M, Dam HF, Jørgensen M, Gevorgyan SA, Kudret S, Maes W, Lutsen L, Vanderzande D, Würfel U, Andriessen R, Rösch R, Hoppe H, Teran-Escobar G, Lira-Cantu M, Rivaton A, Uzunoğlu GY, Germack D, Andreasen B, Madsen MV, Norrman K, Krebs FC (2012) The ISOS-3 inter-laboratory collaboration focused on the stability of a variety of organic photovoltaic devices. RSC Advances 2: 882-883.

[136] Steim R, Choulis SA, Schilinsky P, Lemmer U, Brabec CJ (2009) Formation and impact of hot spots on the performance of organic photovoltaic cells. Applied Physics Letters 94:43304-1-43304-3.

[137] Yrjänä S (2014) Decorative energy autonomous sensor platform concept with printed OPV cells. The IMAPS Nordic Annual Conference Proceedings, Oulu, Finland 8:1-9.

ARTICLE I

High efficient plastic solar cells fabricated with a high-throughput gravure printing method

Solar Energy Materials & Solar Cells 94:1673–1680.

Solar Energy Materials & Solar Cells 94 (2010) 1673–1680

Contents lists available at ScienceDirect

Solar Energy Materials & Solar Cells

journal homepage: www.elsevier.com/locate/solmat

High efficient plastic solar cells fabricated with a high-throughput gravure printing method

P. Kopola [a,*], T. Aernouts [b], S. Guillerez [c], H. Jin [a], M. Tuomikoski [a], A. Maaninen [a], J. Hast [a]

[a] VTT, Kaitoväylä 1, FIN-90571 Oulu, Finland
[b] IMEC, Organic PhotoVoltaics, Polymer & Molecular Electronics, Kapeldreef 75, B-3001 Leuven, Belgium
[c] CEA-INES RDI, 50 Avenue Du Lac Léman, 73370 Le Bourget Du Lac, France

ARTICLE INFO

Article history:
Received 18 January 2010
Received in revised form
6 May 2010
Accepted 9 May 2010
Available online 1 June 2010

Keywords:
Organic photovoltaics
Polymer solar cell
Gravure printing
Solution processing

ABSTRACT

We report on polymer-based solar cells prepared by the high-throughput roll-to-roll gravure printing method. The engravings of the printing plate, along with process parameters like printing speed and ink properties, are studied to optimise the printability of the photoactive as well as the hole transport layer. For the hole transport layer, the focus is on testing different formulations to produce thorough wetting of the indium-tin-oxide (ITO) substrate. The challenge for the photoactive layer is to form a uniform layer with optimal nanomorphology in the poly-3-hexylthiophene (P3HT) and [6,6]-phenyl-C61-butyric acid methyl ester (PCBM) blend. This results in a power conversion efficiency of 2.8% under simulated AM1.5G solar illumination for a solar cell device with gravure-printed hole transport and a photoactive layer.

1. Introduction

Polymer-based solar cells are under extensive research due to their attractive features, which include flexibility and the possibility to prepare large-area solar cells with high throughput methods. Such cells open up new application areas and allow for cost-efficient production in comparison to silicon-based inorganic solar cells [1].

Polymer solar cells produced by printing techniques [2] have attracted considerable attention due to their potential of high commercial value at a low cost and the feasibility for mass production. To date, several printing techniques have been utilised to fabricate the hole transport layer and the photoactive layer in polymer solar cells. Ink jet printing has been investigated for use in the deposition of polymer solar cells [3–5]. With an ink jet printed active layer, a power conversion efficiency (PCE) of 3.5% had been obtained on glass substrate [4].

Doctor blading [6], screen printing [7–10], pad printing [11], spray coating [12,13] and slot-die coating techniques [14,15] were also introduced to fabricate active layers. In addition, the hole transport layer and even electrodes [16–19] have been prepared by printing/coating techniques. Very recently, a polymer solar cell based on gravure-printed poly(3,4-ethylenedioxythiophene):poly(styrenesulfonate) (PEDOT:PSS) and poly-3-hexylthiophene (P3HT) and [6,6]-phenyl-C61-butyric acid methyl ester (PCBM) layers was reported by Ding et al. [20] and a PCE of 1.68% under 100 mW/cm^2 illumination was achieved. Due to its high-throughput and print quality, gravure printing has become a promising candidate for printing large-area and smooth functional layers in optoelectronic devices [21].

In the present work, we discuss and analyse polymer-based solar cells prepared with a high-throughput printing method. The focus is on optimising the printability of the photoactive and hole transport layer considering the ink properties, printing parameters and engraving parameters of the printing cylinder. The resulting printed solar cells showed a PCE of 2.8% on flexible substrate under AM 1.5 illumination (~100 mW/cm^2).

2. Experiment details

The printing experiments for solution-processed polymer solar cells were performed with a Schläfli Labratester, which is presented in Fig. 1a. The principle of gravure printing machines (Fig. 1b) is briefly described as follows. The printing plate/printing cylinder has engraved cells patterned on the surface. Engraving parameters such as cell density, depth, width, screen angle and stylus angle can be adjusted in order to optimise the plate/cylinder design for the printing ink and vice versa. The printing plate/cylinder moves against the doctor blade, which removes excess ink from the surface of the printing plate/cylinder. The ink is transferred to the surface of the substrate in the nip between printing plate/cylinder and impression cylinder. The printing

---

* Corresponding author. Tel.: +358 20 722 2046; fax: +358 20 722 2320.
E-mail address: palvi.kopola@vtt.fi (P. Kopola).

0927-0248/$ - see front matter © 2010 Elsevier B.V. All rights reserved.
doi:10.1016/j.solmat.2010.05.027

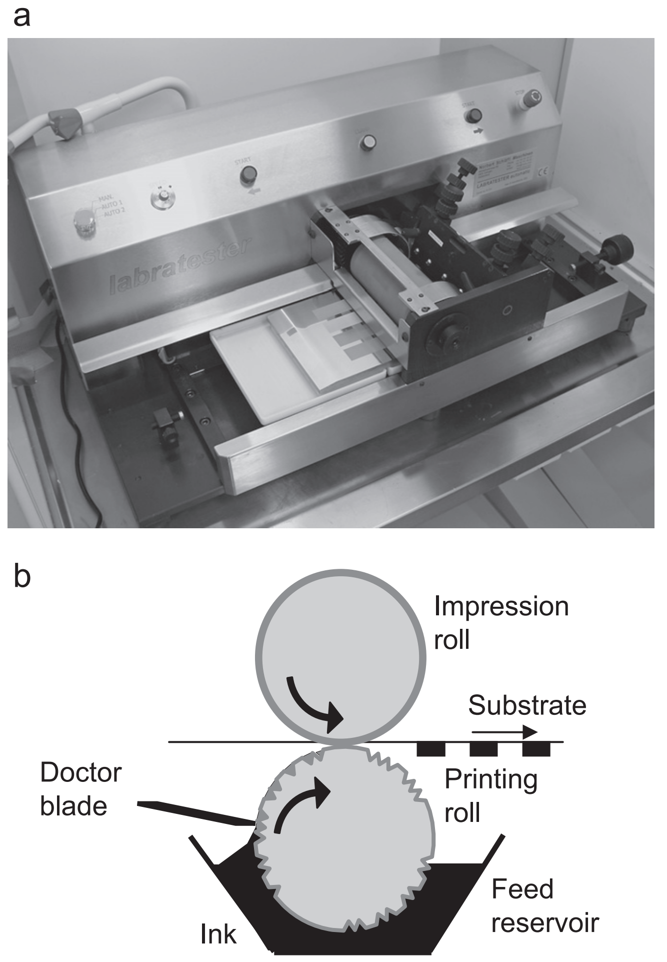

Fig. 1. (a) Schläfli Labratester table-top gravure printing machine, (b) Schematic illustration of gravure printing process.

parameters that can be adjusted with the Schläfli Labratester are the printing speed, the pressure between the printing plate and the impression cylinder i.e. nip pressure, doctor blade angle, distance between the doctor blade and the printing plate, and doctor blade pressure.

Polyethyleneterephthalate film (PET) covered with indium tin oxide (ITO, sheet resistivity of 50 ohms/sq) and purchased from CP films was used as a substrate. The patterned ITO substrates were cleaned sequentially with ethanol and isopropanol (IPA) by ultrasonication. After cleaning, the substrates were rinsed with de-ionised water, dried by blowing nitrogen and then put in an oven for several hours. To wet PEDOT:PSS dispersion, O_2 plasma treatment was used on the fully dried ITO–PET substrates at 300 W for 5 min. Formulated PEDOT:PSS ink based on Clevios P VP AI4083 (H.C. Starck, average solid content 1.5%) was processed on top of the ITO–PET substrate with gravure printing. The resulting PEDOT:PSS films were dried in an oven overnight at 80 °C. The photoactive layer composed of P3HT (Rieke metals):PCBM (Nano-C) was also prepared with gravure printing on top of the printed PEDOT:PSS layer. The films were dried in a covered petri dish for slow film growth [22]. Finally, to complete the devices, a cathode of calcium (25 nm) and silver (80 nm) was thermally evaporated. The size of the active area was defined with a shadow mask and measured 19 mm^2. The organic solar cells were encapsulated with ultraviolet curable epoxy and a glass lid.

The characterisation of the encapsulated organic solar cells was performed in ambient air at room temperature. Current–voltage characteristics were measured with a Keithley 2400 source unit. Illumination tests were carried out under AM1.5G irradiation using a 300 W Cermax lamp-based solar simulator. Atomic force microscopy (AFM) images were recorded on a PicoSPM LE from molecular imaging in ambient conditions. The layer thicknesses were determined with a Dektak 150 surface profilometer. The viscosities were measured with an AR-G2 rheometer from TA Instruments.

3. Results and discussion

3.1. Printability of the hole transport layer

For successful processing of the hole transport layer on top of the ITO anode, it is important for this surface to be thoroughly wet with PEDOT:PPS dispersion. The surface tension of the as-received water-based PEDOT:PSS is 71 mN/m, whereas the surface energy of the O_2 plasma-treated ITO surface is also high, with a value of 74 mN/m. The approach taken here is aimed at finding suitable chemicals which, when combined with PEDOT:PPS dispersion, lower the surface tension while maintaining good printability and electro-optical performance. Initially, the effect of several chemicals on the surface tension, viscosity and printability was investigated. Then different formulations were tested for the hole transport layer by checking their performance in organic solar cells.

Types of chemicals vary from pure solvents, which can result in a lower surface tension of the PEDOT:PSS dispersion, to additives that are known to have properties to enhance film formation or the electrical conductivity of the final layer. Generally, our studies were aimed at gravure printing a thin layer of PEDOT:PSS with a layer thickness of ~40 nm on top of the ITO anode.

The surface tension could be lowered with solvents like IPA. In the case of IPA, an addition of 25 wt% to PEDOT:PSS decreased the surface tension to 27 mN/m and the printability improved significantly. The amount of IPA was further varied by up to 50 wt%, leading the surface tension to drop to 22 mN/m. At the same time, however, excess ink started to spread. In addition, high boiling point solvents such as N-methylpyrrolidone (NMP) can be used to decelerate the drying process so that the printed PEDOT:PSS film has more time to level. Moreover, NMP serves as a lubricant between the doctor blade and cylinder, diminishing the wear of the printing elements and facilitating the cleaning of the equipment. Furthermore, different additives are known to have an impact on film formation; these additives include emulsifiers or adhesion promoters such as Tween$^{®}$80, polyvinyl alcohol (4 wt% in H_2O) and polyurethane diol solutions. These were tested in small quantities, less than 1 wt% of total ink weight, in order to improve the gravure printability. A polyurethane diol solution (18–72 wt% of the solid content of PEDOT:PSS) deteriorated printability. With higher quantities, the polyurethane diol solution caused holes to form in the PEDOT:PSS film. Another tested additive was polyvinyl alcohol (10–80 wt% of the solid content of PEDOT:PSS). As hypothesised, the addition of polyvinyl alcohol increased the surface tension since it dissolves in water. However, the uniformity of the printed PEDOT:PSS film was improved when 10–40 wt% polyvinyl alcohol was used in the formulation. One disadvantage to this process was that ink accumulated along the edges of the engraved areas. Tween$^{®}$80 as 10–80 wt% of the solid content of PEDOT:PSS improved the resolution by making the printed features more easily observable.

Based on this initial information, five different PEDOT:PSS formulations (F1–F5) have been prepared to investigate the effects of solvent and additive combinations. Viscosity measurements with applied shear rates between 10 and 1200 s^{-1} were prepared for three different PEDOT:PSS formulations (F1, F2 and F5). The viscosity values with a shear rate of 1200 s^{-1} are presented in Table 1. Formulation F3 was successfully used in organic light emitting diodes and therefore, they were also tested on organic solar cells [21]. Formulation F5 contained 3 wt% of dimethylsulfoxide (DMSO) as a conductivity enhancer and 22 wt% of IPA as a solvent. According to the viscosity measurements, adding organic solvents and conductivity enhancers (NMP, DMSO) to the PEDOT:PSS ink formulation increased the viscosity, but the flow behaviour was not altered. The addition of Tween®80 seemed to have an influence on the rate of shear thinning. Based on the results in terms of viscosity values and flow behaviour, both of the formulations with added organics (solvents, surfactants, conductivity enhancers) could be suitable for gravure printing at room temperature.

The relationship between the additives and solar cell performance was investigated by preparing samples with spin coating. In addition, reference samples were produced by using PEDOT:PSS as received. Four ink formulations were examined. These are listed in Table 2. Formulations F2 and F4 were chosen based on the printability optimisation presented in this article. Table 2 summarises the electrical parameters of the spin-coated organic solar cells with different PEDOT:PSS formulations.

Fig. 2 depicts the *IV*-measurements for spin-coated samples containing different PEDOT:PSS formulations.

From the shape of the *IV* curve in the 4th quadrant of formulation F4, a strong counter diode effect can be observed. This is a clear sign of the presence of a barrier for charge injection caused by the addition of polyvinyl alcohol. As a result, the fill factor decreased to 18% in comparison to the fill factor of 60% obtained when PEDOT:PSS was used as-received. Open-circuit voltage and short-circuit current were decreased as Tween®80 and IPA (F2) were added to the PEDOT:PSS ink formulation. Ink formulations F2 and F4 led to higher series resistances and lower shunt resistances than with PEDOT:PSS used as-received. Formulation F3 is comparable to PEDOT:PSS used as-received in terms of series and shunt resistances but open-circuit voltage fell significantly. These PEDOT:PSS results indicate that even in small quantities, tested additives like polyvinyl alcohol and Tween®80 negatively affect the OSC performance. Therefore, additives should be avoided if possible in the preparation of organic solar cells. Instead, the addition of solvents or conductivity enhancers is recommended in order to prepare a uniform gravure-printed PEDOT:PSS layer. In the final preparation of organic solar cells, PEDOT:PSS ink formulation F5 will be used (75 wt% PEDOT:PSS, 22 wt% IPA and 3 wt% DMSO).

Table 1
Viscosity values for different PEDOT:PSS formulations at a shear rate of 1200 s^{-1} at a temperature of 20 °C.

Formulation	Viscosity (mPa s)
F1. Clevios P VP AI4083	6.7
F3. Clevios P VP AI4083 72 wt%, Tween®80 1 wt%, 2-propanol 25 wt%, N-methylpyrrolidone 2 wt%	14.7
F5. Clevios P VP AI4083 75 wt%, Dimethylsulfoxide 3 wt% 2-propanol 22 wt%	13.3

3.2. *Gravure-printed active layer of P3HT:PCBM*

In the optimisation process of printability of the photoactive layer, the ink composition was varied in terms of solvent mixtures, total concentration and the P3HT:PCBM ratio. In addition, the printing plate design (cell structure, line density, etc.) was optimised for the photoactive ink. As a starting point for the gravure printing ink optimisation, a total concentration higher than, for instance, that utilised in the spin coating of P3HT:PCBM was used in order to produce uniform photoactive films with a thickness of few hundred nanometres and variations of under 10 nm. In addition, the printability of the ink should be controllable i.e. the ink should not spread across the engraved pattern, as this feature is needed when processing solar cell modules, which require patterning of the printed layers. The optimisation process of the active layer was initiated with the photoactive ink of P3HT:PCBM 50 mg/ml (1:1) in 1,2-dichlorobenzene by testing two different printing speeds 7 m/min (Fig. 3a) and 18 m/min (Fig. 3b) and two different engraving parameters in terms of line density of 80 l/cm (Fig. 3a and b) and 45 l/cm (Fig. 3c). As can be pointed out in Fig. 3a, with a printing speed of 7 m/min, the ink spread directly from the cells, leading ink to accumulate outside the engraved area; this can be observed in the downside of the image. By increasing the printing speed to 18 m/min (Fig. 3b), the ink flow dynamics was improved and the photoactive ink remained within the patterned area defined in the printing plate. However, as can be visually observed and concluded from the layer thickness measurements presented in Table 3, the printed layer did not fulfil the uniformity requirements defined for the active layer. The next approach was to test lower line density (Fig. 3c) i.e. larger cell volume in order to transfer ink dots with higher mass to the substrate and

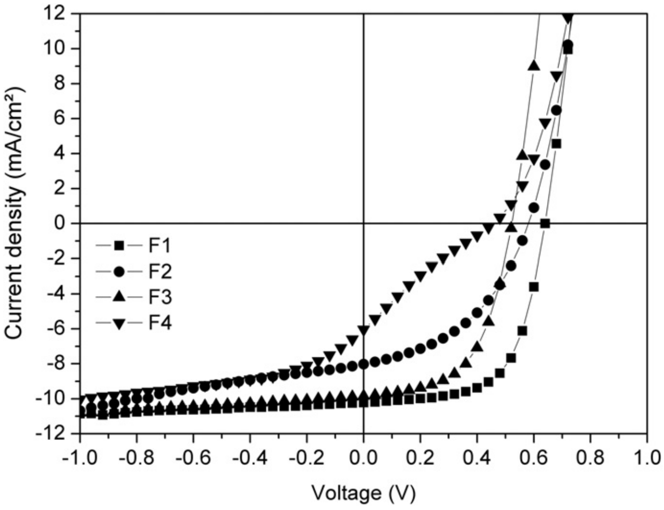

Fig. 2. Current–voltage characteristics of different PEDOT:PSS ink formulations.

Table 2
Summary of organic solar cell performance for various PEDOT:PSS formulations.

Formulation	V_{oc} (mV)	I_{sc} (mA/cm^2)	FF	PCE (%)
F1. Clevios P VP AI4083	634	9.96	0.60	3.83
F2. Clevios P VP AI4083 75 wt%, Tween®80 0.45 wt%, 2-propanol 24.6 wt%	567	8.30	0.32	1.50
F3. Clevios P VP AI4083 72 wt%, Tween®80 1 wt%, 2-propanol 25 wt%, N-methylpyrrolidone 2 wt%	453	9.76	0.49	2.17
F4. Clevios P VP AI4083 74.9 wt%, Polyvinyl alcohol 4 wt% in H_20 solution 11.25 wt%, 2-propanol 13.82 wt%	422	5.19	0.18	0.41

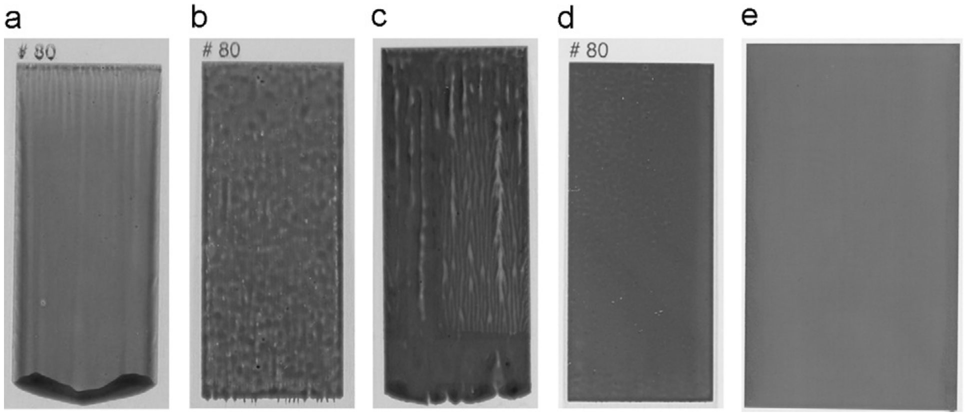

Fig. 3. (a) P3HT:PCBM 50 mg/ml in o-DCB (80 l/cm), speed 7 m/min, (b) 50 mg/ml, 80 l/cm, speed 18 m/min, (c) 50 mg/ml, 45 l/cm, speed 18 m/min, (d) 100 mg/ml, 80 l/cm, speed 18 m/min, (e) 150 mg/ml, 120 l/cm, speed 18 m/min.

Table 3
Layer thickness measurement results of the printed layers presented in Fig. 3.

Total concentration (mg/ml)	Printing speed (m/min)	Line density (l/cm)	Average layer thickness (nm)	Standard deviation of layer thickness (nm)
50	7	80	109	22
50	18	80	151	22
50	18	65	261	48
100	18	80	334	15
150	18	120	210	11

force them to merge. However, the low viscosity of the photoactive ink (<10 mPas) and the low line density in the cells of the printing plate were not a successful combination. Instead, the uniformity of the photoactive layer was deteriorated with the line density of 45 l/cm. This was also seen as an increase of the standard deviation of the layer thickness. Another approach which was examined was to increase the total concentration of the photoactive ink (Fig. 3d and e). Furthermore, higher line densities were examined in order to keep the layer thickness at an adequate level. Due to the limited solubility of PCBM in 1,2-dichlorobenzene, the concentration of PCBM was kept constant, at 50 mg/ml, with the total concentration ranging from 100 to 150 mg/ml. As can be concluded from Fig. 3d and e, the higher total concentration led to a better resolution and higher uniformity of the printed film.

In addition, layer thicknesses were measured from the printed photoactive layers as presented in Table 3. It is clear from this table that the standard deviation of the layer thickness can be decreased to 11 nm by increasing the total concentration and line density.

AFM and profilometer measurements were used to investigate the differences in the film formation of gravure-printed active layers by using a two-solvent system comprised of 1,2-dichlorobenzene (bp. 179 °C, vapour pressure 1.2 mmHg) and chloroform (bp. 62 °C, vapour pressure 159 mmHg) with the total concentration of 150 mg/ml. Chloroform was chosen as the co-solvent due to the fact that it increased the interfacial areas of solar cell materials and led to improved solar cell performance [23]. In addition, chloroform as a low boiling point solvent can be used for controlling the spreading of the photoactive ink. In addition, the effect of ranging the total concentration from 112.5 to 150 mg/ml and the impact of the engraving parameters on the line density on the film formation was under research.

AFM images [24] representing the surface topographies of the gravure-printed films with different 1,2-dichlorobenzene:chloroform ratios are shown in Fig. 4. Additionally, the roughness plots of gravure-printed films at a macroscopic (0.5 mm) and microscopic scale ($5\times5\ \mu m^2$) are presented in Fig. 4. A spin-coated sample was used as a reference. At this high level of concentration, 150 mg/ml (Fig. 4a—c), the addition of chloroform facilitated the solubility. The 1,2-dichlorobenzene based film exhibited a rms roughness ($5\times5\ \mu m^2$) of 8.7 nm and an average roughness at the macroscopic scale (0.5 mm) of 21.7 nm. As depicted in Fig. 4b, the surface roughness at the macroscopic scale decreased to 4.6 nm when 20 v% of chloroform was added. However, at the same time, the rms roughness nearly doubled, rising to 16.3 nm. As a compromise, the optimisation will be continued with solvent mixture of 80:20 v% 1,2-dichlorobenzene:chloroform.

Another focus of the investigation was to examine the relationship between the total concentration and the nanomorphology of the P3HT:PCBM photoactive layer. The roughness plots and AFM images are shown in Fig. 5. With the lowest total concentration of 112.5 mg/ml (Fig. 5a), the printed layer was less homogenous, which led to high surface roughness values. The roughness values were diminished as the total concentration of P3HT:PCBM increased. The lowest roughness values for the macroscopic and microscopic scale were obtained at a total concentration of 131 mg/ml (Fig. 5b). The macroscopic surface roughness was 2.7 nm and correspondingly, the microscopic surface roughness was 12.0 nm for a measurement area of $5\times5\ \mu m^2$. These values for gravure-printed film approached the values obtained with a spin-coated active layer.

Furthermore, the dependence among the engraving parameters was examined in terms of line density and the nanomorphology of the P3HT:PCBM photoactive layer. The ink formulation of P3HT:PCBM 131 mg/ml in 80:20 v% 1,2-dichlorobenzene:chloroform was examined. The AFM images and roughness plots of the printed active layers with three different line densities are depicted in Fig. 6. With a line density of 120 l/cm, a layer thickness with an average of 192 nm is obtained with a surface roughness of 2.7 nm at a macroscopic scale and 12.0 nm at a

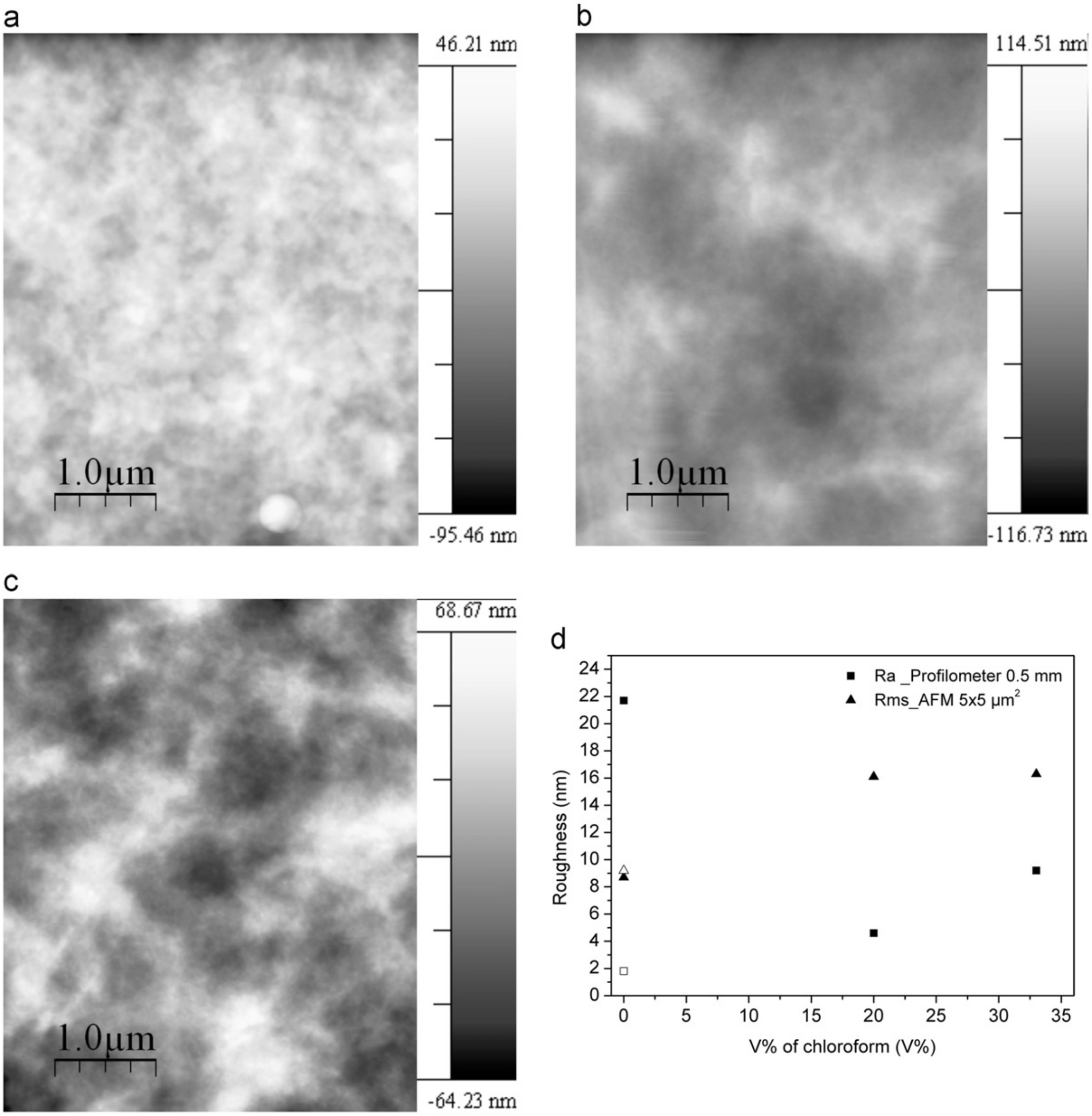

Fig. 4. AFM images (a–c) and roughness plot (d) of gravure-printed films with different 1,2-dichlorobenzene:chloroform ratios at a macroscopic scale (0.5 mm) and a microscopic scale ($5\times5\ \mu m^2$). Open symbols depict the roughness values for the spin-coated reference sample. Total concentration of 150 mg/ml dissolved in (a) 1,2-dichlorobenzene, (b) 80:20 v% 1,2-dichlorobenzene:chloroform, (c) 66:33 v% 1,2-dichlorobenzene:chloroform.

microscopic scale. As the line density is decreased to 100 l/cm, the layer thickness increased to 271 nm with a roughness value of 8.0 nm at a macroscopic scale and 15.8 nm at a microscopic scale. Correspondingly, with a line density of 80 l/cm, the layer thickness was 305 nm with a surface roughness of 7.8 nm at a macroscopic scale and 19.7 nm at a microscopic scale. In conclusion, with a line density of 120 l/cm, the lowest surface roughness values were obtained with gravure-printed films. The next step will involve testing different ink formulations in the organic solar cell structure.

3.3. *Gravure-printed polymer-based solar cells*

Solar cells were prepared as previously introduced in the experimental section. The PEDOT:PSS formulation of 75 wt% of PEDOT:PSS, 22 wt% of IPA and 3 wt% of DMSO was used to prepare organic solar cells. In the following section, we analyse the electrical performance and efficiency of gravure-printed solar cells with an active layer prepared with several different total concentrations and ratios of P3HT:PCBM, and various engraving parameters. Three ink formulations were examined by printing the active layer with three different engravings; line densities ranged from 80 to 120 l/cm. A summary of the important solar cell performance parameters (open-circuit voltage V_{oc}, short-circuit current I_{sc}, fill factor FF, series resistance R_s, shunt resistance R_{sh} and power conversion efficiency PCE) including the active layer thickness d, are shown in Table 4. In addition, the current–voltage characteristics are presented in Fig. 7. R_s and R_{sh} are estimated from the slope close to 1 and 0 V in terms of the J–V characteristics in the dark [25].

For the first three samples (S1–S3), the total concentration and the ratio of P3HT:PCBM were varied at a constant line density. It is important to note that the highest power conversion efficiency (2.8%) was reached with ink formulation P3HT:PCBM 1:0.62 131 mg/ml dissolved in 80:20 V% 1,2-dichlorobenzene:chloroform

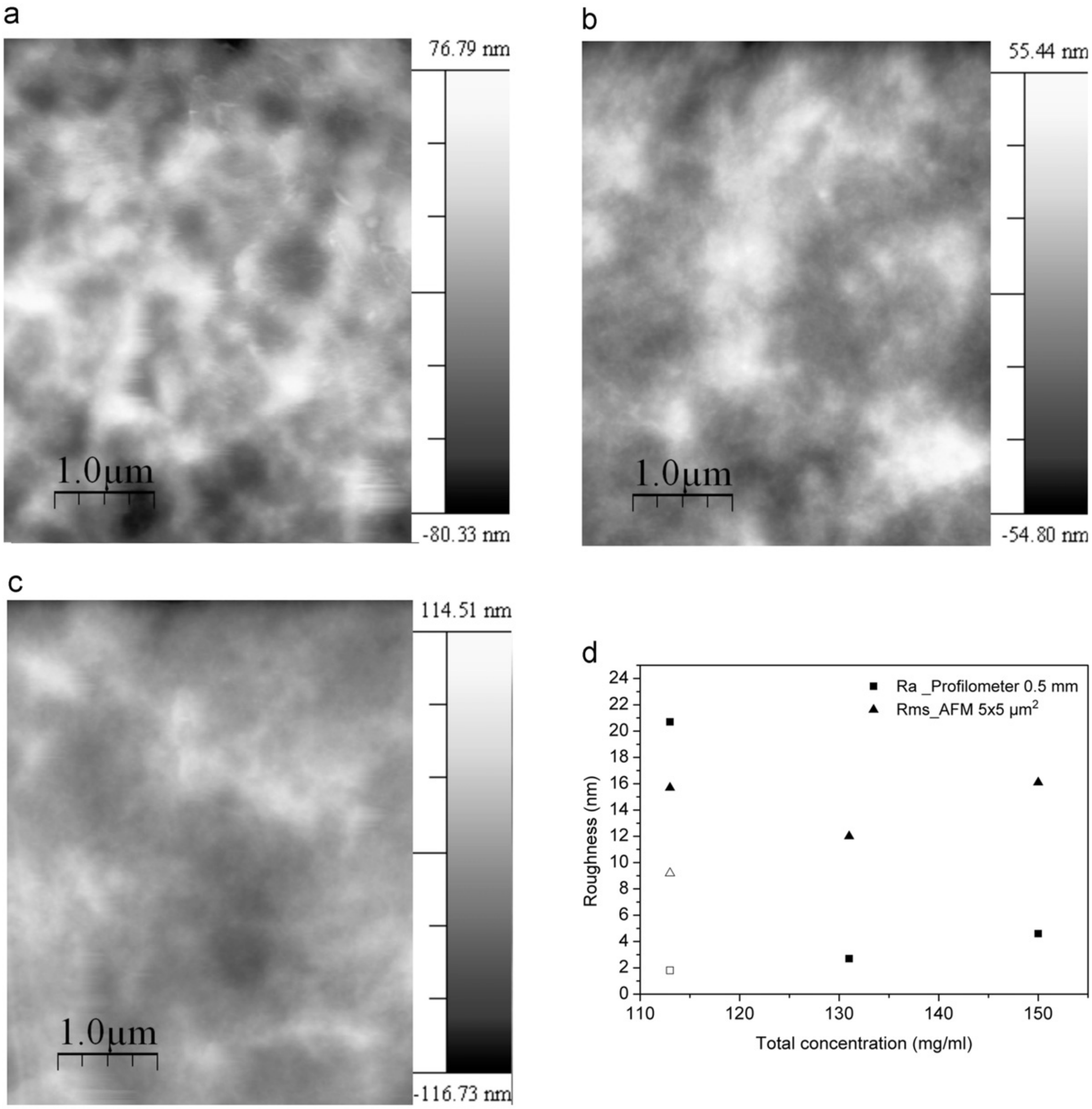

Fig. 5. AFM images (a–c) and roughness plot (d) of gravure-printed film with different total concentration for a solvent mixture of 80:20 v% 1,2-dichlorobenzene:chloroform at a macroscopic scale (0.5 mm) and a microscopic scale (5 × 5 μm2). Open symbols depict the roughness values for the spin-coated reference sample. Total concentration (a) 113 mg/ml, (b) 131 mg/ml and (c) 150 mg/ml.

by using a line density of 120 l/cm to achieve an active layer thickness of 192 nm. This ink formulation and engraving parameters also produced the lowest surface roughness as the AFM images already indicated. Based on the performance data presented in Table 4, with the concentrations of 150 mg/ml and 113 mg/ml the OSC performance in terms of I_{sc} and PCE was declined. Furthermore, FF is significantly reduced with a total concentration of 150 mg/ml mainly due to the decrease in R_{sh}. The engraving parameters affect the film formation of the active layer and thus influence the performance of the organic solar cell. As the line density decreases i.e. the cell volume increases, a non-uniform layer with high surface roughness is obtained, as already seen in the AFM characterisation of printed active layers. The high surface roughness obtained using line densities of 100 and 80 l/cm is observed and the device performance deteriorated in comparison to the printing with a line density of 120 l/cm. With a line density of 80 l/cm, an active layer thickness of over 300 nm is reached, inducing higher series resistance (R_s), a lower short circuit current and a lower fill factor, thus reducing efficiency. A thicker active layer led to higher bulk series resistance, which is seen as an increase of the total series resistance. Normally, with uniform active layers, an increase of J_{sc} due to higher absorption would be expected as the active layer thickness increases. However, within this contribution, the engraving parameters affect the film morphology significantly, so a similar effect is not observed. According to the experiments prepared with gravure-printed solar cells, the engraving of the printing plate and the total concentration significantly affect the homogeneity of the printed active area and the layer thickness, thus influencing the performance of the solar cell.

Future work will be focused on investigating the relationship between the printing/engraving parameters and the internal structure of the active layer. In addition, the gravure-printed organic solar cell modules will be researched along with the possibility of expanding the gravure printing process obtained in the laboratory to a pilot scale.

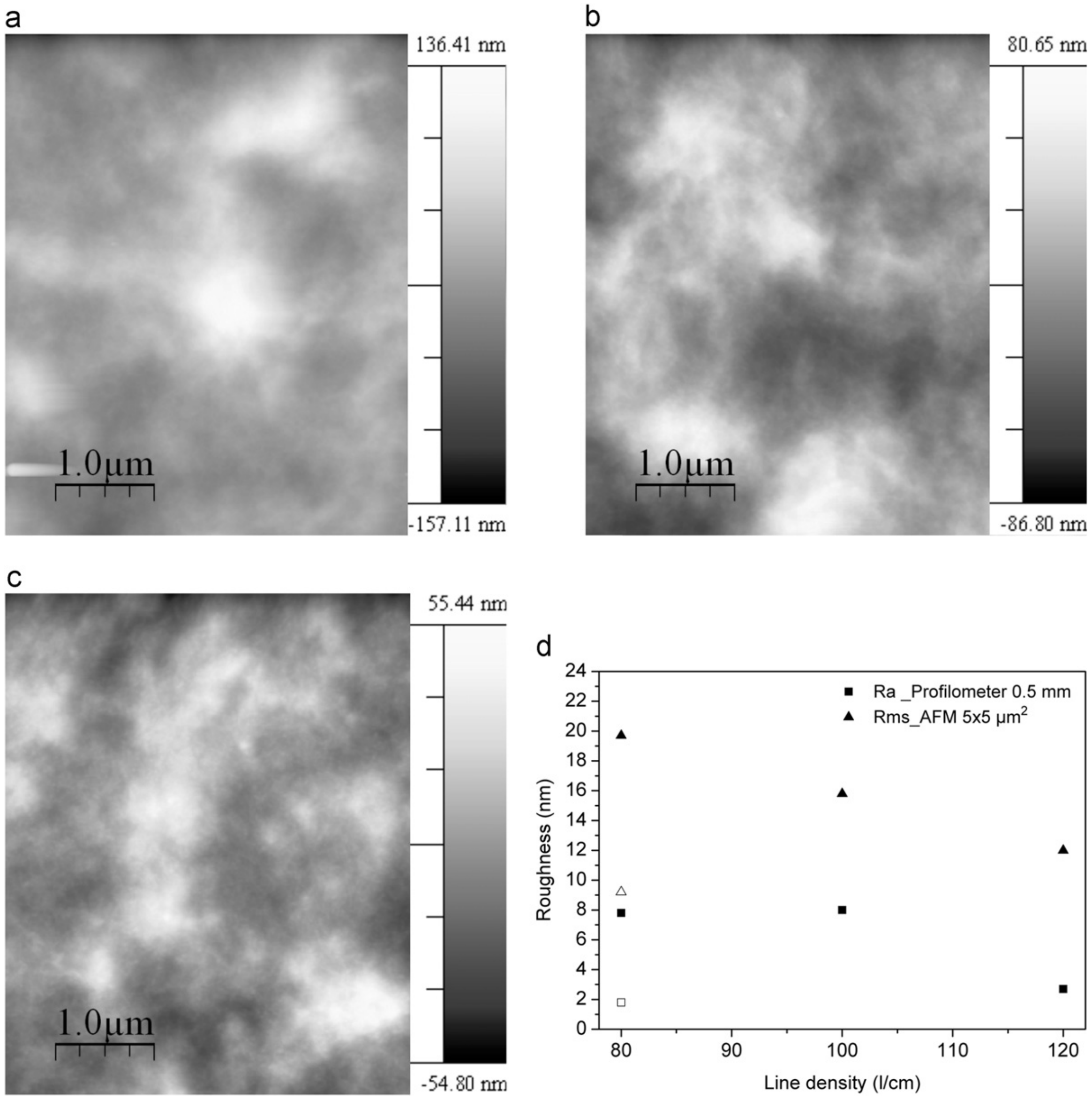

Fig. 6. AFM images (a–c) and roughness plots (d) at a macroscopic scale (0.5 mm) and a microscopic scale represent the surface topographies of the gravure-printed films with different engraving parameters in terms of line density. Ink formulation P3HT:PCBM 131 mg/ml in 80:20 v% 1,2-dichlorobenzene:chloroform. Line densities (a) 80 l/cm, (b) 100 l/cm and (c) 120 l/cm. Open symbols depict the roughness values for the spin-coated reference sample.

Table 4
Photovoltaic response including the active layer thickness of gravure-printed organic solar cells prepared with different ink formulations and engraving parameters.

	Description (total concentration, P3HT:PCBM ratio, line density)	d (nm)	V_{oc} (mV)	I_{sc} (mA/cm^2)	FF	R_s_dark (Ω cm^2)	R_{sh}_dark (Ω cm^2)	PCE_{max}%
S1	113 mg/ml, 1:0.8, 120 l/cm	152	580	7.57	0.60	6.28	1586	2.5
S2	131 mg/ml, 1:0.6, 120 l/cm	192	600	7.91	0.57	8.71	8661	2.8
S3	150 mg/ml, 1:0.5, 120 l/cm	191	580	7.28	0.49	6.85	702	2.0
S4	131 mg/ml, 1:0.6, 100 l/cm	271	550	6.42	0.55	7.30	1721	1.8
S5	131 mg/ml, 1:0.6, 80 l/cm	305	570	6.46	0.52	9.54	1239	1.8

4. Conclusions

In conclusion, in this work we have reported on gravure-printed organic solar cells with a printed hole injection layer and an active layer. A power conversion efficiency of 2.8% under AM1.5G solar illumination was obtained. In addition, the effect of engraving parameters, printing parameters and ink composition on the printability and performance of the organic solar cell was investigated. We showed that by using the above-mentioned methods to optimise printability, the surface roughness values approached those obtained with the spin-coated sample. The high power conversion efficiency of 2.8% obtained with fully gravure-printed organic solar cells confirms gravure printing's potential as a manufacturing method for organic electronics.

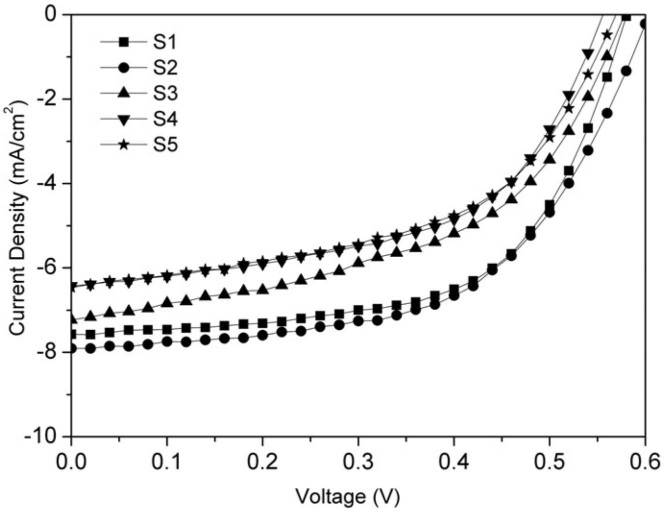

Fig. 7. Current–voltage characteristics of gravure-printed organic solar cells prepared with different ink formulations and engraving parameters.

Acknowledgement

The work was done in the FACESS project, which was funded by the European Commission within the 7th framework ICT-2007.3.2 organic and large area-electronics, visualisation and display systems research area under contract number FP7-2007-ICT-1-215271. The authors express their gratitude to Elina Hakola, Marja Välimäki, Terho Kololuoma and Solenn Berson for their useful insight and Antti Veijola for technical assistance.

References

[1] C.J. Brabec, Organic photovoltaics: technology and market, Sol. Energy Mater. Sol. Cells 83 (2004) 273–292.
[2] F.C. Krebs, Fabrication and processing of polymer solar cells: a review of printing and coating techniques, Sol. Energy Mater. Sol. Cells 93 (2009) 394–412.
[3] C.N. Hoth, S.A. Choulis, P. Schilinsky, C.J. Brabec, High photovoltaic performance of inkjet printed polymer:fullerene blends, Adv. Mater. 19 (2007) 3973–3978.
[4] C.N. Hoth, S.A. Choulis, P. Schilinsky, C.J. Brabec, On the effect of poly(3-hexylthiophene) regioregularity on inkjet printed organic solar cells, J. Mater. Chem. 19 (2009) 5398–5404.
[5] T. Aernouts, T. Aleksandrov, C. Girotto, J. Genoe, J. Poortmans, Polymer based organic solar cells using ink-jet printed active layers, Appl. Phys. Lett. 92 (2008) 033306-1–033306-3.
[6] P. Schilinsky, C. Waldauf, C.J. Brabec, Performance analysis of printed bulk heterojunction solar cells, Adv. Funct. Mater. 16 (2006) 1669–1672.
[7] S.E. Shaheen, R. Radspinner, N. Peyghambarian, G.E. Jabbour, Fabrication of bulk heterojunction plastic solar cells by screen printing, Appl. Phys. Lett. 79 (2001) 2996–2998.
[8] T. Aernouts, P. Vanlaeke, J. Poortmans, P.L. Heremans, Polymer solar cells: screen-printing as a novel deposition technique, Proc. SPIE 5464 (2004) 252–260.
[9] F.C. Krebs, J. Alstrup, H. Spanggaard, K. Larsen, E. Kold, Production of large-area polymer solar cells by industrial silk screen printing, lifetime considerations and lamination with polyethyleneterephthalate, Sol. Energy Mater. Sol. Cells 83 (2004) 293–300.
[10] F.C. Krebs, H. Spanggard, T. Kjær, M. Biancardo, J. Alstrup, Large area plastic solar cell modules, Mater. Sci. Eng. B. 138 (2007) 106–111.
[11] F.C. Krebs, Pad printing as a film forming technique for polymer solar cells, Sol. Energy Mater. Sol. Cells 93 (2009) 484–490.
[12] C. Girotto, B.P. Rand, J. Genoe, P. Heremans, Exploring spray coating as a deposition technique for the fabrication of solution-processed solar cells, Sol. Energy Mater. Sol. Cells 93 (2009) 454–458.
[13] C.N. Hoth, R. Steim, P. Schilinsky, S.A. Choulis, S.F. Tedde, O. Hayden, et al., Topographical and morphological aspects of spray coated organic photovoltaics, Org. Electron. 10 (2009) 587–593.
[14] F.C. Krebs, S.A. Gevorgyan, J. Alstrup, A roll-to-roll process to flexible polymer solar cells: model studies, manufacture and operational stability studies, J. Mater. Chem. 19 (2009) 5442–5451.
[15] F.C. Krebs, All solution roll-to-roll processed polymer solar cells free from indium-tin-oxide and vacuum coating steps, Org. Electron. 10 (2009) 761–768.
[16] T. Aernouts, P. Vanlaeke, W. Geens, J. Poortmans, P. Heremans, S. Borghs, et al., Printable anodes for flexible organic solar cell modules, Thin Solid Films 451-452 (2004) 22–25.
[17] T. Maaninen, M. Tuomikoski, A. Maaninen, All-printed flexible OLEDs, IMID'07 Technical Digest (2007) 721–723.
[18] J.Y. Lee, S.T. Connor, Y. Cui, P. Peumans, Solution-processed metal nanowire mesh transparent electrodes, Nano Lett. 8 (2008) 689–692.
[19] C. Girotto, B.P. Rand, S. Steudel, J. Genoe, P. Heremans, Nanoparticle-based, spray-coated silver top contacts for efficient polymer solar cells, Org. Electron. 10 (2009) 735–740.
[20] J.M. Ding, A. de la Fuente Vornbrock, C. Ting, V. Subramanian, Patternable polymer bulk heterojunction photovoltaic cells on plastic by rotogravure printing, Sol. Energy Mater. Sol. Cells 93 (2009) 459–464.
[21] P. Kopola, M. Tuomikoski, R. Suhonen, A. Maaninen, Gravure printed organic light emitting diodes for lighting applications, Thin Solid Films 517 (2009) 5757–5762.
[22] G. Li, V. Shrotriya, J. Huang, Y. Yao, T. Moriarty, K. Emery, et al., High-efficiency solution processable polymer photovoltaic cells by self-organization of polymer blends, Nat. Mater. 4 (2005) 864–868.
[23] K. Kawano, J. Sakai, M. Yahiro, C. Adachi, Effect of solvent on fabrication of active layers in organic solar cells based on poly(3-hexylthiophene) and fullerene derivatives, Sol. Energy Mater. Sol. Cells 93 (2009) 514–518.
[24] I. Horcas, R. Fernandez, J.M. Gomez-Rodriguez, J. Colchero, J. Gomez-Herrero, A.M. Baro, WSxM: a software for scanning probe microscopy and a tool for nanotechnology, Rev. Sci. Instrum. 78 (2007) 013705-1–013705-8.
[25] F.A. Shirland, The history, design, fabrication and performance of CdS thin film solar cells, Adv. Energy Conversion 6 (1966) 201–222.

ARTICLE II

Gravure printed flexible organic photovoltaic modules

Solar Energy Materials & Solar Cells 95:1344–1347.

Solar Energy Materials & Solar Cells 95 (2011) 1344–1347

Contents lists available at ScienceDirect

Solar Energy Materials & Solar Cells

journal homepage: www.elsevier.com/locate/solmat

Gravure printed flexible organic photovoltaic modules

Pälvi Kopola [a,*], Tom Aernouts [b], Rafal Sliz [c], Stéphane Guillerez [d], Mari Ylikunnari [a], David Cheyns [b], Marja Välimäki [a], Markus Tuomikoski [a], Jukka Hast [a], Ghassan Jabbour [c], Risto Myllylä [c], Arto Maaninen [a]

[a] *VTT Technical Research Centre of Finland, Printed Functional Solutions, Kaitoväylä 1, FIN-90571 Oulu, Finland*
[b] *IMEC, Organic PhotoVoltaics, Polymer and Molecular Electronics, Kapeldreef 75, B-3001 Leuven, Belgium*
[c] *University of Oulu, Optoelectronics and Measurement Techniques Laboratory, P.O. BOX 4500, 90014 University of Oulu, Finland*
[d] *CEA-INES RDI, 50 Avenue Du Lac Léman, 73370 Le Bourget Du Lac, France*

ARTICLE INFO

Available online 13 January 2011

Keywords:
Organic photovoltaics
Polymer solar cell
Gravure printing
Solution processing
Module fabrication

ABSTRACT

In this letter, organic solar cell modules based on poly-3-hexylthiophene (P3HT) and [6.6]-phenyl-C61-butyric acid methyl ester (PCBM) blend films with a module active area of 15.45 cm^2 prepared by roll-to-roll (R2R) compatible gravure printing method are demonstrated. The gravure printed organic photovoltaic modules consist of eight serially connected solar cells in same substrate. Indium-tin-oxide (ITO) is patterned by screen printable etching paste. Hole injection layer and active layer are prepared by gravure printing method. All processing steps excluding cathode evaporation are performed in air. Electrical measurements are done to modules consisting of 5–8 serially connected solar cells. The photovoltaic modules comprising 5, 7 and 8 serially connected cells exhibit an active area power conversion efficiency of 1.92%, 1.79% and 1.68%, respectively (Oriel Sol3A Class AAA, AM1.5G, 100 mW cm^{-2}).

1. Introduction

Photovoltaic cells based on conjugated polymers [1] have high potential for a low-cost photovoltaic technology. In recent years, active research of polymer-based solar cells has improved the energy conversion efficiency [2] and stability [3,4] to an attractive level for commercialisation. One of the main advantages in polymer-based solar cells is the possibility to process solar cells in high volumes on flexible, light-weight substrates by exploiting roll-to-roll (R2R) compatible processing methods including printing and coating methods. Several research groups have addressed on different printing or coating techniques in laboratory scale especially focusing on small area solar cells on glass substrate with an active area $\ll 1$ cm^2 [5]. For a photovoltaic converter made by a single solar cell of a given size, enough energy might be delivered to empower low power applications, but the voltage level remains limited by its open-circuit voltage. Therefore, it is essential to use series connected solar cells in order to increase the voltage to an adequate level or parallel connected solar cells if higher current is needed [6,7]. There are few publications of flexible large area coated or printed organic solar cell modules [8–10]. However, to best of our knowledge, gravure printed organic photovoltaic modules have not been reported. In this letter, we demonstrate organic solar cell modules consisting of several series connected cells (active area ranging from 9.65 to 15.45 cm^2) prepared with R2R compatible gravure printing method.

2. Experimental

The indium-tin-oxide (ITO) coated polyethyleneterephthalate (PET) substrates used in this work were purchased from CP Films (sheet resistance $40-60\,\Omega$ square^{-1}). The definition of ITO patterns were performed with etching paste for screen printing, Isishape HiperEtch 09S, supplied by Merck. The paste was screen printed with a flat bed screen printing machine Bacchini on top of ITO-PET substrate as an indirect image, i.e. etching paste was not applied on top of the ITO stripes. The substrates were placed on an oven and afterwards the etching paste was cleaned with water-based solution in ultrasonic bath. Subsequently, the substrates were washed with deionised water and dried by blowing nitrogen. The patterned ITO substrates were cleaned sequentially with ethanol and isopropanol (IPA) by ultrasonication. After cleaning, the substrates were rinsed with deionised water, dried by blowing nitrogen and then put in an oven for drying. The busbars of gold (80 nm) were evaporated on the edge of ITO in order to get anode contacts on the ITO as gravure printed layers were processed on whole area in the development phase. Additionally, the busbars diminish the impact of high resistivity of ITO in large area cells. After the busbar evaporation, the substrates

---

[*] Corresponding author. Tel.: +358 207222046; fax: +358 207222320.
E-mail address: palvi.kopola@vtt.fi (P. Kopola).

0927-0248/$ - see front matter © 2010 Elsevier B.V. All rights reserved.
doi:10.1016/j.solmat.2010.12.020

were O_2 plasma treated at the etching power of 300 W for 5 min. The hole transport layer, poly(3,4-ethylenedioxythiophene):poly(styrenesulfonate) (PEDOT:PSS), and photoactive layer for solution-processed solar cells were applied by gravure printing method using Schläfli Labratester in air. The PEDOT:PSS ink was based on Clevios P VP AI 4083 (H.C. Starck), IPA and dimethylsulfoxide (DMSO). The PEDOT:PSS films were dried in an oven overnight at 80 °C. The ink formulation for the photoactive layer was as follows: poly-3-hexylthiophene (P3HT, Rieke Metals): [6.6]-phenyl-C61-butyric acid methyl ester (PCBM, Nano-C) 131 mg/ml in 80:20 V% 1.2-dichlorobenzene:chloroform. More detailed description of the optimisation of the ink compositions (PEDOT:PSS, P3HT:PCBM) for gravure printing has already been published [11]. The films were dried in a covered petri dish for a slow film growth. The modules were transferred to a glove box for post-treatment on a hotplate under nitrogen at 110 °C for 5 min. The thermal evaporation of cathode was carried out under high vacuum level. A shadow mask was used to pattern the cathode composing of calcium (25 nm) and silver (80 nm). The photovoltaic modules were transferred to another glove box in order to perform the electrical measurements of processed photovoltaic structures. The AM1.5G solar simulator (Oriel Sol3A Class AAA) was used to simulate solar spectrum with an intensity of 100 mW cm^{-2}. The intensity of the solar simulator was calibrated by using the certified National Renewable Energy Laboratory (NREL) reference silicon solar cell with a KG5 filter. The current–voltage (IV) characteristics were measured at room temperature under inert gas atmosphere N_2. The simulations were based on existing equations used for top-contact grid design of silicon solar cells [12].

3. Results and discussion

Organic solar cells can be monolithically combined into photovoltaic modules. The layout of such monolithic module has to encompass the power output needs for driving specified applications and be able to be integrated in an inline production process. In this module design, the purpose is to empower the charging of a screen printed lithium-ion thin film battery and the production process is envisaged to be based on R2R printing technology. The output power of a photovoltaic device is on one hand area specific and on the other hand dependent on the incoming light spectrum and intensity. For P3HT:PCBM based organic solar cells, the open-circuit voltage is typically in the order of 0.6 V or lower. To be able to empower the charging of lithium-ion printed thin film battery, it will be essential to use series interconnected solar cells. The sheet resistivity of the ITO anode can be a limiting factor in collecting the electric current generated in the photoactive layer. It is assumed that the top electrode has a conductivity that is considerable higher than the anode layer, and therefore its effect on current collection can be neglected in respect to the anode resistance. Also contact resistances in between active layer and electrodes or at external contacting points are assumed to be negligible. Using this as a starting point, electrical calculations were done based on the configuration as depicted in Fig. 1(a). The light grey, horizontal area indicates the metallic cathode, whereas the dark grey, vertical area represents the anode. The top black marker is the general contacting point for the electric current carried by the anode layer. As such, there are two distinct pathways for the current collection along the anode. The first pathway is in the cross-section area of both anode and cathode, whereby the total electric current under operation of the attributed solar cell is increasing along the direction of the anode structure towards the contacting point (depicted with number 1 in Fig. 1(a)). In the second pathway, the current has to flow from the cross-section area towards the collecting point; this current stays constant during this flow (depicted with number 2 in Fig. 1(a)). Fig. 1(b) shows the effect of an increasing length of pathway 1 on the power production of a standard solar cell, resulting in a reduction of efficiency by 30% for a length of 1 cm, going to 70% reduction for 2 cm and even to 99% reduction for 10 cm. An ITO anode with a sheet resistance of 60 Ω $square^{-1}$ on PET substrate was used as a reference in these calculations.

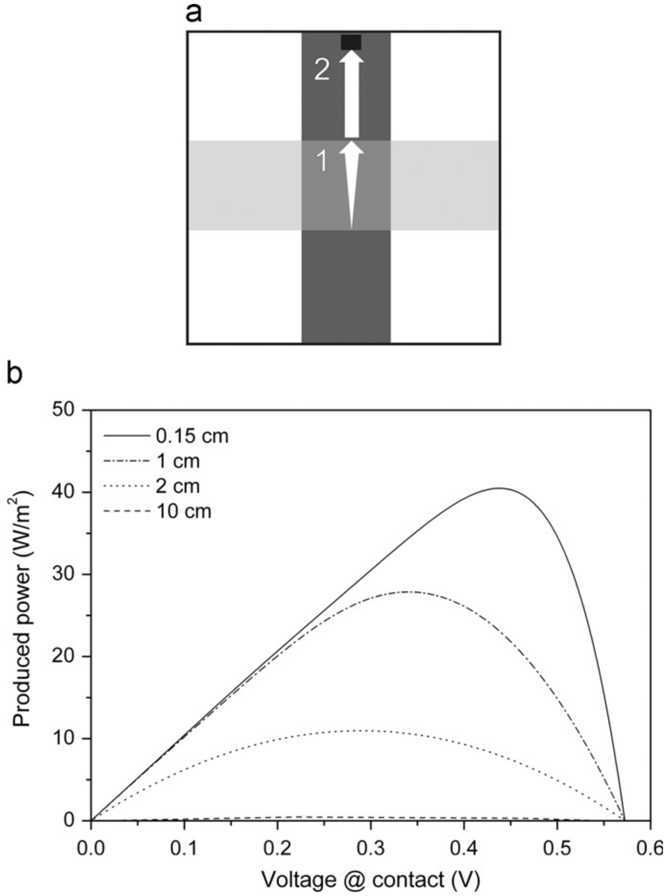

Fig. 1. (a) Schematic representation of the anode (depicted dark grey) and cathode (depicted light grey) structure for the electrical calculations, indicating two main current collecting pathways (pathways 1 and 2). The top black marker is the general contacting point for the electric current carried by the anode layer. The pathway 1 is in the cross-section area of both anode and cathode and in pathway 2, the current has to flow from the cross-section area towards the general contacting point. (b) indicates the loss of produced power for varying the length of pathway 1.

Based on the electrical calculations and considering the registration requirements of a laboratory scale printing machine, a pattern based on a multistrip structure was designed (Fig. 2). In order to achieve 4 V required for charging a lithium-ion printed thin film battery, eight strips were mounted in series. The length and the width of one cell in the multistrip pattern were 4.6 and 0.42 cm. In the development phase, the cells were independent allowing individual testing. With individual testing, it is possible to estimate the reliability of gravure printing for large area cells. Series connection of cells was realized in this phase by connecting contact pads with conductive ink. The nominal voltage of the battery to be charged by organic solar cells will be 3.6–3.7 V, working on the potential range comprised between 3.0 and 4.0 V. Charging requires, therefore, the interconnection of up to eight organic solar cells in series. In outdoor operation conditions, this series interconnection should deliver an output voltage clearly

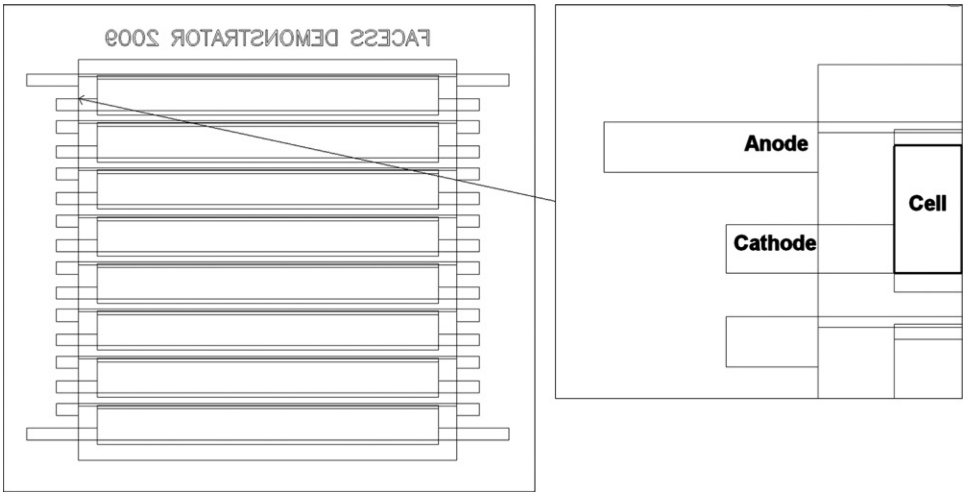

Fig. 2. Layout of gravure printed photovoltaic module.

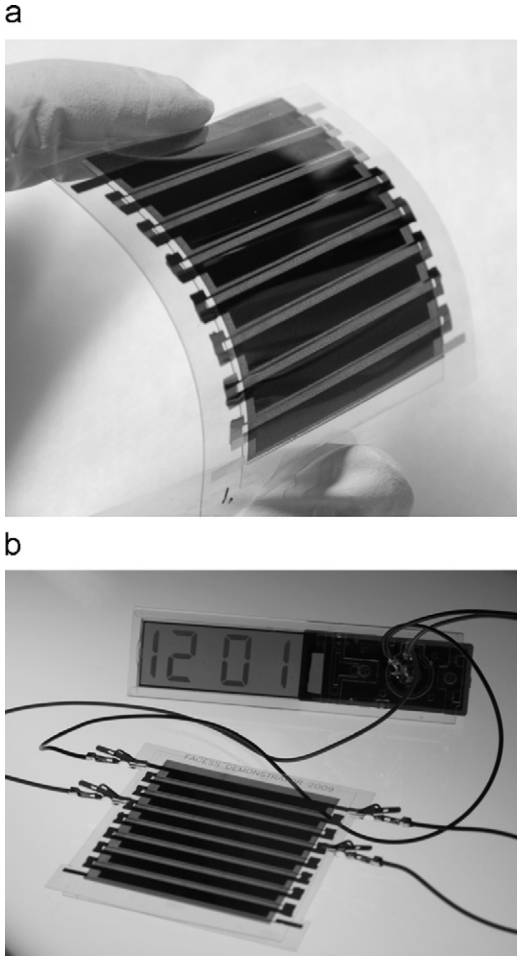

Fig. 3. (a) Flexible gravure printed organic solar cell module. (b) Three cells connected in series used as a power source for a clock.

above 4 V. However, it should be noted that the output voltage varies strongly with illumination conditions. In varying illumination conditions the Si transistor circuitry, which was designed in the system, will convert the output voltage from the organic solar cells into the voltage needed to charge the battery. The output current of a solar cell is proportional to the active device area and almost linearly dependent on the incoming light intensity.

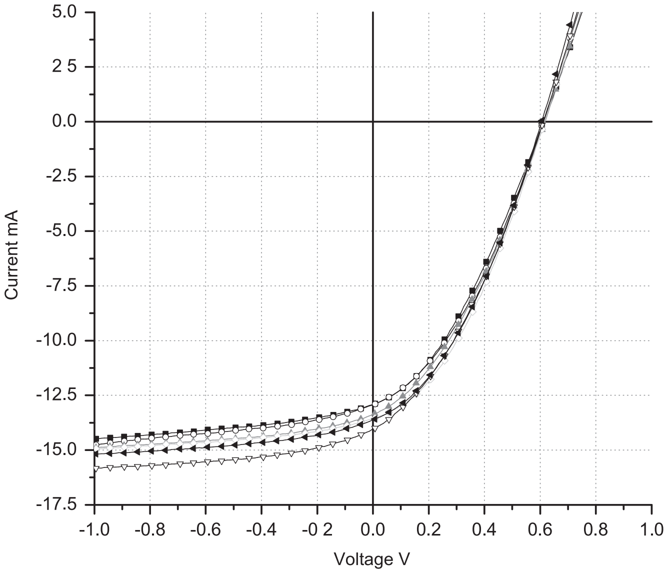

Fig. 4. IV-characteristics of identically processed single cells with an active area of 1.93 cm^2 measured under 100 mW cm^{-2} AM1.5G solar simulator Oriel Sol3A Class AAA.

Different short-circuit currents can be caused by internal differences in the performance of the device or by external influences like shadowing of one of the cells. Thus, series interconnected solar cells require good current matching of the neighbouring devices, since the weakest cell limits strongly the total performance [6].

The gravure printed organic solar cell module consisting of eight series connected cells shown in Fig. 3(a). In Fig. 3(b), the part of the module is used as a power source for a clock.

Two different approaches were used for the electrical measurements of gravure printed organic solar cell modules. At first, the electrical measurements were performed to each cell in organic solar cell module structures in order to compare the variation between the cells. Each cell was measured by connecting two anode contacts and two cathode contacts which were located at the end of the cell as showed in Fig. 2. The IV-characteristics of individual solar cells (active area of 1.93 cm^2) are shown in Fig. 4. As it can be noticed from the graphs, a good reproducibility with gravure printed cells can be attained. The best single solar cell exhibited a short-circuit current of 14.01 mA, an open-circuit voltage of 0.61 V, and a fill factor of 35% thus leading to a power conversion efficiency of

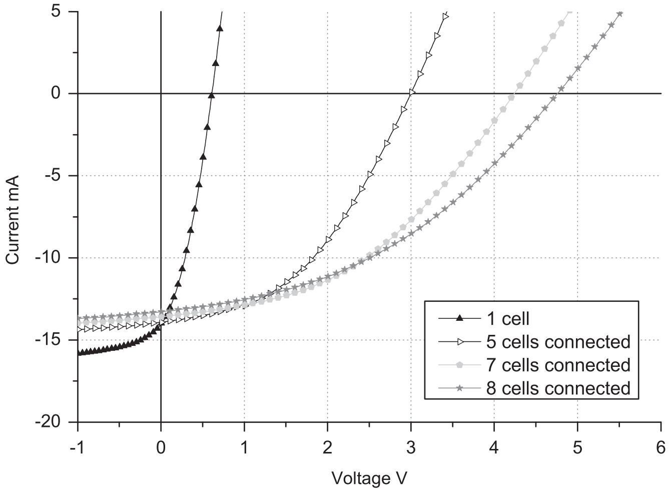

Fig. 5. IV-characteristics of 1,5,7,8 cells connected in series measured under 100 mW cm^{-2} AM1.5G solar simulator Oriel Sol3A Class AAA.

Table 1
Summary of the performance of individual solar cell and organic solar cell modules consisting of 5, 7 and 8 cells connected in series.

Cells connected in series	Cells area (cm^2)	I_{SC} (mA)	U_{OC} (V)	FF (%)	Maximum power (mW)	PCE (%)
1	1.93	14.01	0.61	35	2.97	1.55
5	9.65	13.91	3.02	44	18.62	1.92
7	13.51	13.59	4.24	42	24.66	1.79
8	15.45	13.29	4.76	41	25.71	1.68

1.55%. Second, the modules were connected in series by using conductive ink to combine the cathode and anode contact pads of the adjacent cells. Different amount of cells were serially connected in order to investigate if the voltage level increases linearly as the amount of cells connected in series increases. The IV characteristics of the modules consisting of 5–8 cells connected in series under illumination is presented in Fig. 5.

The electrical parameters including the open-circuit voltage (V_{oc}), the short-circuit current (I_{sc}), the fill factor (FF), the maximum power and power conversion efficiency (PCE) of individual cell and the modules consisting of 5-8 cells connected in series are summarised in Table 1.

When the individual cells are connected in series, the voltage output should increase. The open-circuit voltage of the module should be the sum of the open-circuit voltages of the connected individual solar cells. With one cell, an open-circuit voltage of 0.61 V was obtained. As eight cells were serially connected, the open-circuit voltage increased up to 4.76 V as expected. The short-circuit current of the modules was in the range of 13.29–14.01 mA. The short-circuit current conditions remained rather stable which refers that to a good reprocibility of individual cell output characteristics. The maximum power point of eight cell module was at 25.71 mW and at that point the output voltage was 2.88 V. The attained power conversion efficiencies were 1.92% with five cells, 1.79% with seven cells and 1.68% with eight cells. These initial module results prove that gravure printing is a promising method for processing large area PEDOT:PSS and active layers for organic solar cell module structure.

4. Conclusions

In conclusion, we have demonstrated that a high-throughput gravure printing method is feasible for preparing large area organic solar cell modules ($A = 15.45$ cm^2) consisting of eight cells connected in series. PEDOT:PSS and active layer of P3HT:PCBM were prepared by gravure printing method. Additionally, screen printing was used for patterning the ITO layer. The power conversion efficiencies of 1.92%, 1.79% and 1.68% were obtained with 5 cells, 7 cells and 8 cells, respectively, by connecting the contact pads of individual cells in series. With the gravure printed modules demonstrated in this work, low power electronic devices can be powered. However, there is a need for improvement in terms of module performance especially by diminishing the resistive losses due to the series connection done from the ends of the cells. In a second generation module structure, the PEDOT:PSS and active layers will be patterned as rectangles and the cells will be monolithically connected, i.e. so there is no need for busbars in this design. As a next step, the gravure printed solar cell modules will be tested with respect to stability. Additionally, the manufacturing process of gravure printed organic solar modules will be transferred to a large scale R2R machine.

Acknowledgements

This work was funded by the European Commission within the 7th framework ICT-2007.3.2 Organic and large area-electronics, visualisation and display systems research area under Contract number FP7-2007-ICT-1-215271 (FACESS project). The electrical measurements of the gravure printed organic solar cell modules were performed at University of Oulu. Additionally, the authors express their gratitude to Antti Veijola for technical assistance and high quality photographs.

References

[1] B. Thompson, J. Fréchet, Polymer-fullerene composite solar cells, Angewandte Chemie International Edition 47 (2008) 58–77.

[2] M. Osborne, New polymers push solarmer's OPV efficiency to record 8.13%, 〈http://www.pv-tech.org/news/_a/new_polymers_push_solarmers_opv_efficiency_to_record_8.13/〉, 2010.

[3] J.A. Hauch, P. Schilinsky, S.A. Choulis, R. Childers, M. Biele, C.J. Brabec, Flexible organic P3HT:PCBM bulk-heterojunction modules with more than 1 year outdoor lifetime, Solar Energy Materials and Solar Cells 92 (2008) 727–731.

[4] J.A. Hauch, P. Schilinsky, S.A. Choulis, S. Rajoelson, C.J. Brabec, The impact of water vapor transmission rate on the lifetime of flexible polymer solar cells, Applied Physics Letters 93 (2008) 103306-1–103306-3.

[5] F.C. Krebs, Fabrication and processing of polymer solar cells: a review of printing and coating techniques, Solar Energy Materials and Solar Cells 93 (2009) 394–412.

[6] T. Aernouts, Organic bulk heterojunction solar cells from single cell towards fully flexible photovoltaic module, Dissertation, Katholieke Universiteit Leuven, 2006.

[7] M. Niggemann, B. Zimmermann, J. Haschke, M. Glatthaar, A. Gombert, Organic solar cell modules for specific applications-from energy autonomous systems to large area photovoltaics, Thin Solid Films 516 (2008) 7181–7187.

[8] F.C. Krebs, S.A. Gevorgyan, J. Alstrup, A roll-to-roll process to flexible polymer solar cells: model studies, manufacture and operational stability studies, Journal of Materials Chemistry 19 (2009) 5442–5451.

[9] F.C. Krebs, H. Spanggard, T. Kjær, M. Biancardo, J. Alstrup, Large area plastic solar cell modules, Materials Science and Engineering: B 138 (2007) 106–111.

[10] L. Blankenburg, K. Schultheis, H. Schache, S. Sensfuss, M. Schrödner, Reel-to-reel wet coating as an efficient up-scaling technique for the production of bulk-heterojunction polymer solar cells, Solar Energy Materials and Solar Cells 93 (2009) 476–483.

[11] P. Kopola, T. Aernouts, S. Guillerez, H. Jin, M. Tuomikoski, A. Maaninen, J. Hast, High efficient plastic solar cells fabricated with a high-throughput gravure printing method, Solar Energy Materials and Solar Cells 94 (2010) 1673–1680.

[12] M.A. Green, Solar Cells: Operating Principles, Technology and System Applications, Prentice-Hall, Inc., Englewood Cliffs, NJ, 1982.

ARTICLE III

Roll-to-roll gravure printing of organic photovoltaic modules – insulation of processing defects by an interfacial layer

Progress in Photovoltaics:
Research and Applications 23:918–928.

Progress in
PHOTOVOLTAICS

PROGRESS IN PHOTOVOLTAICS: RESEARCH AND APPLICATIONS
Prog. Photovolt: Res. Appl. 2015; **23**:918–928
DOI: 10.1002/pip.2508

RESEARCH ARTICLE

Roll-to-roll gravure printing of organic photovoltaic modules—insulation of processing defects by an interfacial layer

Pälvi Apilo[1]*, Jussi Hiltunen[1], Marja Välimäki[1], Santtu Heinilehto[2], Rafal Sliz[3] and Jukka Hast[1]

[1] Printed Functional Solutions, VTT Technical Research Centre of Finland, Kaitoväylä 1, 90571 Oulu, Finland
[2] Center of Microscopy and Nanotechnology, University of Oulu, PO Box 7150, 90014 Oulu, Finland
[3] Optoelectronics and Measurement Techniques Laboratory, University of Oulu, PO Box 4500, 90014 Oulu, Finland

ABSTRACT

Gravure printing as direct patterning roll-to-roll (R2R) production technology can revolutionize the design of thin-film organic photovoltaic (OPV) devices by allowing feasible manufacturing of arbitrary-shaped modules. This makes a distinction to coating methods, such as slot die coating, in which the pattern is limited to continuous stripes. Here, we analyze the thin-film formation and its influence on OPV module performance as the gravure printing of hole transport and photoactive layers are transferred from laboratory to R2R pilot production environment. Insertion of a 0.8-nm layer of lithium fluoride (LiF) as an interfacial layer between the active layer and the electron contact provided insulation against the detrimental pinholes formed in the R2R printing process. Using this device configuration, we produced well-performing R2R-printed monolithic modules with a mean efficiency of 1.7%. In comparison, reference modules with an efficiency of 2.2% were fabricated using laboratory-scale bench top sheet-level process. Surface energy and tension measurements together with optical microscopy were used to analyze the printability of the materials. The pinhole insulation was investigated in detail by processing R2R-printed OPV modules with different interfacial layer materials and performing electrical measurements under dark and AM1.5 illumination conditions. Furthermore, we analyzed the LiF distribution using X-ray photoelectron spectroscopy. The insulating nature of the LiF layer to improve module performance was confirmed by manufacturing lithographically artificial pinholes in device structures. The results show the possibility to loosen the production environment constraints and the feasibility of fabricating well-performing thin-film devices by R2R gravure printing.

KEYWORDS
organic photovoltaics; roll-to-roll; gravure printing; flexible electronics; thin films; low cost

***Correspondence**
P. Apilo (formerly Kopola), Printed Functional Solutions, VTT Technical Research Centre of Finland, Kaitoväylä 1, 90571 Oulu, Finland.
E-mail: Palvi.Apilo@vtt.fi

Received 10 September 2013; Revised 18 March 2014; Accepted 31 March 2014

1. INTRODUCTION

Organic photovoltaic (OPV) is an emerging technology for producing clean and sustainable energy from solar radiation [1]. OPV has attracted great research interest in the last decade due to the potential for large-scale and low-cost production on flexible substrates [2]. The main research aims are to improve the efficiency of organic solar cells, extend the stability of the OPV structures, and exploit non-vacuum roll-to-roll (R2R) processing methods for low-cost manufacturing. Today, the state-of-the-art efficiency is 11.1% for OPV small-area devices [3] and 2.8% for R2R-coated modules [4]. Although OPV technology does not have a competitive edge compared to its inorganic photovoltaic counterparts in terms of efficiency and long-term stability, its advantages are cost and ease of manufacturing on different flexible substrates using R2R printing and coating technologies. R2R printing and coating methods are high-volume production technologies that enable more cost-efficient industrial production compared to vacuum processes. The key advantage of printing in comparison to coating is the possibility of direct patterning in the printing process, which increases the flexibility for module design, allowing for the fabrication of OPV modules with large areas and of arbitrary shapes and sizes for use in various applications. Contrary to printing, coating methods, such as slot die coating, are used for full-layer deposition, and patterning is limited to stripes [2]. The R2R upscaling of slot die-coated modules has already been demonstrated in [5–8]. In these structures, the active material and electron transport layer (ETL) were R2R slot die-coated, while the hole transport layer (HTL) and the top electrode were rotary screen-printed. Indium tin oxide (ITO) has been replaced by flexography printed silver grid and rotary screen-printed poly(3,4-ethylenedioxythiophene) : poly(styrenesulfonate) (PEDOT : PSS). In [5], 10 randomly selected modules (66 cm^2 active area) exhibited an average efficiency of 1.5% (max 1.6%) with a hexagonal grid structure. Krebs *et al.* have shown the real potential of OPV R2R processing by building up solar parks [6,7]. They obtained stabilized power conversion efficiency (PCE) of 1.6–1.8% with initial PCE $>$ 2% for an active area of 14.7 m^2 with a slanted grid structure. A slight decrease in performance was observed (PCE = 1.5%) for a large active area of 88.2 m^2 [7].

Gravure printing is an attractive technique for printing thin films due to its capability for high-resolution patterning, high throughput and speed, excellent solvent resistance, and precise ink application [9]. Importantly, gravure printing has been already used to produce laboratory-scale-processed OPV cells [10,11] and modules (no monolithic connection) [12]. In our previous research, we reported the production of ITO-based modules in which bench top sheet-level gravure printer was used to produce the HTL and photoactive layer, and evaporated calcium was used for the ETL [12]. Moreover, sheet-based processing of monolithically connected modules with a relatively high speed industrial gravure printing proofer was demonstrated with a maximum PCE of 1.0% [13]. Despite the relatively high speed, the gravure printing process was not a continuous R2R process, however, and the ink was applied directly to the surface of the printing cylinder. In contrast, in an R2R process, a rotating gravure printing cylinder is immersed into an ink pan filled with gravure printing ink [9]. Voigt *et al.* investigated the correlation between gravure printing process parameters and device performance of laboratory-processed inverted solar cells, which attained an efficiency of 0.6% for a device with three printed layers [14,15]. Interestingly, Hübler *et al.* used a paper substrate instead of plastic as a basis for R2R-printed inverted solar cells and obtained an efficiency of 1.3% (at 600 W/m^2) for a layer sequence of Zn/ZnO/photoactive layer/PEDOT : PSS. The combination of flexography and gravure printing was used to fabricate the devices [16].

The gravure printing process, widely used in the packaging industry, is based on a system comprising two cylinders, a printing cylinder and an impression cylinder. The image patterns engraved into the surface of a metallic printing cylinder consist of separated cells, whereas the non-image elements remain at the surface. The cell dimensions of the gravure printing cylinder define the maximum amount of ink that can be transferred onto the printing surface. As the printing cylinder rotates in the ink pan, the engraved cells are filled with ink. The doctor blade wipes off the excess ink so that only the engraved cells contain ink. The ink from the cells is then transferred as separated dots directly onto the substrate in a printing nip under high printing pressure. Cell emptying is incomplete due to ink splitting [13,17]. Ink wetting and spreading place great demands on the control of ink-substrate interactions, ink transfer, ink properties, and printing conditions. Efficient ink transfer, proper ink wetting, and controlled spreading are essential for forming uniform and precise printed layers to make up the OPV stack and modules by gravure printing. Pinholes can be easily formed due to missing dots in the gravure printing or ink repelling due to impurities. Additionally, controlling the charging and discharging of plastic foil is essential in R2R processing to avoid electric breakdown through thin solution-processed layers.

Here, we report that detrimental pinholes in the R2R gravure-printed photoactive layer can be prevented by incorporating a thin lithium fluoride (LiF) layer as an ETL. LiF is widely used in organic light-emitting diodes to enhance electron injection [18–20] and in OPV structures to facilitate electron extraction [21–25]. In addition, LiF acts herein as an insulating layer to prevent shorts through the pinholes in the R2R gravure-printed photoactive layer.

First, we describe the module preparation and characterization in Section 2. Second, we compare the printability of poly(3-hexylthiophene-2,5-diyl) (P3HT) : methanofullerene [6,6]-phenyl C61-butyric acid methyl ester (PCBM) in R2R and laboratory-scale processing. Third, we analyze the results of R2R and laboratory-scale-processed OPV modules with two different ETL and electron contact configurations (Ca/Ag and LiF/Al). This includes the determination of LiF uniformity on top of R2R-printed photoactive layer by X-ray photoelectron spectroscopy (XPS). Fourth, we perform electrical measurements of pinholes simulated by lithographically producing defects on top of ITO-PEDOT : PSS. Finally, we summarize the results with concluding remarks.

2. EXPERIMENTAL

2.1. R2R processing of modules

OPV modules for these experiments were constructed on top of ITO-coated polyethylene terephthalate (PET) roll purchased from Eastman (40-60 ohms sq^{-1}, Eastman Corporate, Kingsport, Tennessee). The ITO structures were patterned using etching paste, Isishape HiperEtch (Merck KGaA, Darmstadt, Germany). The paste was R2R rotary screen-printed on top of the ITO as an indirect image, thermally treated, and cleaned to remove the excess paste. R2R-patterned ITO was used as a substrate for R2R-processed and laboratory-processed modules. The HTL of PEDOT : PSS (Clevios P VP AI4083, Heraeus, Hanau, Germany) was R2R gravure-printed in a pilot printing machine on top of an ITO surface. A line density of 100 lines cm^{-1} was used for the engraving of the HTL. The gravure printing ink formulation was based on Clevios P VP AI4083 and 2-propanol ink composition with a weight ratio of 75:25 wt.%.

A speed of $8\,\mathrm{m\,min^{-1}}$ and an applied nip pressure of 1 bar were used for printing. The R2R printing machine contains totally 4 m of ovens, so the total drying time is limited to 30 s with a printing speed of $8\,\mathrm{m\,min^{-1}}$. The printed layer was subsequently dried after gravure printing in a continuous process by hot air ovens at 120 °C for 30 s. The PEDOT : PSS was aligned in the printing process to keep the ITO edge open for monolithic connection. The ink formulation for the photoactive layer was as follows: P3HT (#4002-E, Rieke Metals Inc., Lincoln, Nebraska) : PCBM [C60] (99.5% purity; 0.131g, Nano-C, Westwood, Massachusetts) in 1.2-dichlorobenzene (1 ml). In addition, the photoactive layer was deposited by R2R gravure printing. The printing speed was $8\,\mathrm{m\,min^{-1}}$, and the applied nip pressure was 1 bar. The printing cylinder contained engravings with a line density of $120\,\mathrm{lines\,cm^{-1}}$. The printed layer was dried in a continuous drying process at 120 °C for 30 s directly after printing in the R2R process. The monolithic connection was taken into consideration when aligning the photoactive layer. The modules were transferred to a glove box for thermal evaporation of the ETL and electron contact. The modules were placed on top of a hotplate at 120 °C for 10 min before the evaporation in order to verify that no outgassing occurs during evaporation. On top of the photoactive layer, LiF/Al or Ca/Ag was thermally evaporated through a shadow mask.

2.2. Laboratory processing of modules

The same ink formulations were used for the HTL and photoactive layer as in the R2R process. The printing was performed with a sheet-based gravure printing machine, Schläfli Labratester (Norbert Schläfli Maschinen, Zofingen, Switzerland). The optimization of the engraving parameters was initially carried out in laboratory scale, and the same engraving parameters were also used in R2R printing. The HTL of PEDOT : PSS was printed at a speed of $18\,\mathrm{m\,min^{-1}}$ and directly dried in an oven at 120 °C for 15 min. Correspondingly, the photoactive layer was printed with a printing speed of $18\,\mathrm{m\,min^{-1}}$ and subsequently slowly dried. The modules were transferred to a glove box for thermal evaporation. The modules were placed on top of a hotplate at 120 °C for 10 min before the evaporation. On top of the photoactive layer, LiF/Al or Ca/Ag was thermally evaporated through a shadow mask.

2.3. Characterization

The current–voltage (*IV*) characteristics of the larger batch of R2R-printed modules were measured with a solar simulator SolarTest 1200 (Atlas, Linsengericht, Germany) calibrated to $100\,\mathrm{mW\,cm^{-2}}$ using a calibrated Si-reference cell with a KG5 filter (mismatch factor corrected, VLSI Standards Inc., Milpitas, California) . For more accurate analysis, smaller batch of photovoltaic modules was transferred to another glove box to perform the electrical measurements of processed photovoltaic structures. An AM1.5G solar simulator Oriel Sol 3A Class AAA (Newport Corporation, Irvine, California) was used to simulate the solar spectrum with an intensity of $100\,\mathrm{mW\,cm^{-2}}$. The intensity of the solar simulator was calibrated using a reference silicon solar cell with a KG5 filter. The *IV* characteristics were measured at room temperature under an inert gas atmosphere of N_2. The PCE values were corrected by taking the mismatch factor into consideration and determining the actual active area of the printed modules using a Smartscope OGP250 (Optical Gaging Products, Rochester, New York) microscope. The distribution of LiF on the surface of R2R-printed P3HT : PCBM was studied using the ESCALAB 250Xi XPS (Thermo Fischer Scientific Inc, Waltman, Massachusetts) system. Monochromatic Al Kα (1486.6 eV) X-ray radiation was used in all measurements. The survey spectrum was measured by setting the detector pass energy to 150 eV and 1-eV step size. For narrow scans, we used 20-eV pass energy and 0.1-eV step size. All the spectra were acquired using the 650 μm X-ray spot. The sample was not tilted during the XPS measurement. The spectral resolution of the system used in this experiment was 0.36 eV, but the peak position can be determined with the accuracy of 0.1 eV. The elemental surface mapping was conducted over an area of 1.4 mm × 1.4 mm, and the analysis area at each measurement point was set to 100 μm. In the mapping experiment, we used a 200-μm X-ray spot, 50-eV detector pass energy, and 0.2-eV step size. Surface measurements were obtained using a contact angle meter (CAM200, Biolin Scientific, Stockholm, Sweden), and surface energy calculations were performed based on Wu's method [26]. Calculation according to Wu is based on harmonic mean and considered to give better accuracy for high-energy systems [26]. The layer thickness of LiF was measured by evaporating 30 nm of LiF on top of the silicon substrate. The measurement was prepared using a Wyko NT3300 (Veeco, Plainview, New York) white light interferometer. The diameter of the holes was determined using a Smartscope OGP250. Both sides of the modules were laminated with a flexible barrier and pressure sensitized adhesive FTB3-125a (3M, Saint Paul, Minnesota) in a sheet-based process. In the shelf lifetime measurement, the modules were stored at ambient laboratory conditions (about 20 °C, 30–40 RH%). The operational lifetime measurement was performed with XXL+ weathering chamber (Atlas, Linsengericht, Germany) by using the following parameters: sunlight simulated by xenon lamps using daylight filters (irradiance level of $42\,\mathrm{W\,m^{-2}}$ at 300–400 nm), relative humidity of 50 RH%, and black standard temperature of 65 °C. The modules were tested in open-circuit conditions.

2.4. Lithographically processed pinholes

The artificial pinholes were fabricated using an Ultra-I 123 positive tone photoresist (Rohm and Haas, Philadelphia, Pennsylvania) that was spin-coated and patterned with contact aligner (Karl Süss MA6, Süss MicroTec AG, Garching, Germany). The resist layer was processed on top of patterned ITO-gravure-printed PEDOT : PSS. Either LiF/Al or Al was evaporated on top of the artificial layer of pinholes.

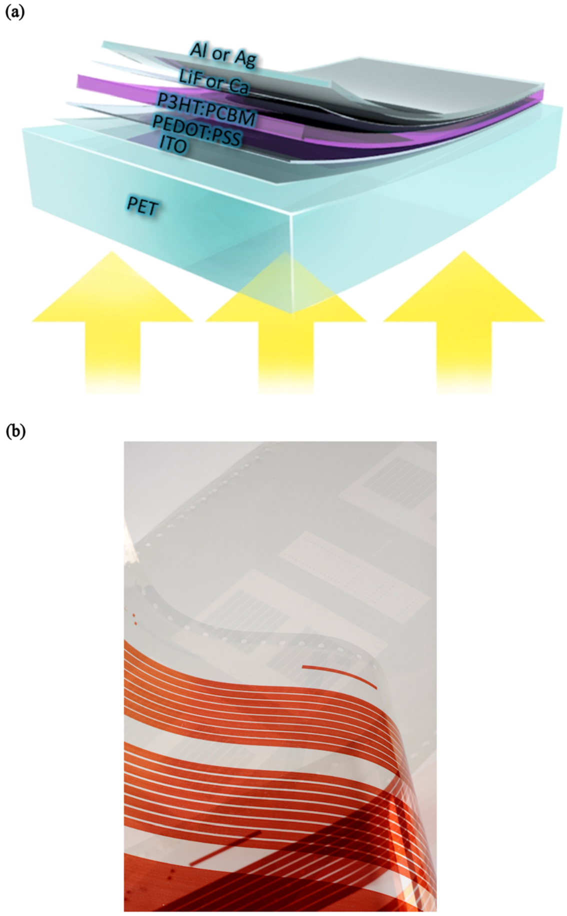

Figure 1. (a) OPV device architecture used for processing; (b) R2R gravure-printed OPV module foils comprising eight monolithic series connected cells. ITO is structured with R2R rotary screen printing.

3. RESULTS AND DISCUSSION

The device architectures of R2R and laboratory-printed OPV modules and the module design investigated in this work are shown in Figure 1. OPV structures (Figure 1a) were fabricated on top of an ITO-coated PET substrate. The ITO layer was patterned by R2R rotary screen printing [9] of etching paste as a negative image followed by drying and a cleaning sequence, all in an R2R process. The HTL of PEDOT : PSS and the photoactive blend layer of P3HT and PCBM were processed by R2R gravure printing and, for comparison, a sheet-based gravure printing process in the laboratory. Two different ETL and electron contact alternatives, Ca/Ag and LiF/Al, were investigated. The module structures comprised eight cells monolithically connected in series with a total active area of ~15 cm^2. The R2R gravure-printed roll of the photoactive layer on top of PEDOT : PSS/ITO and R2R patterned ITO are shown in Figure 1(b).

The R2R pilot machine used for printing the OPV modules is shown in Figure 2(a), and the R2R process description is depicted in Figure 2(b). In the Supporting information, an example video of gravure printing of photoactive layer is presented. The R2R gravure printing unit used for printing PEDOT : PSS and P3HT : PCBM is shown in Figure 2(b).

The R2R and laboratory gravure-printed photoactive layers comprising of P3HT : PCBM were characterized by optical microscopy to analyze the printing quality of laboratory- and R2R-printed P3HT : PCBM layers. Figure 3 represents microscopy images of a laboratory-scale gravure-printed P3HT : PCBM layer and R2R gravure-printed P3HT : PCBM layer. The figures show that the R2R-printed P3HT : PCBM layer contained pinholes extending to the surface of PEDOT : PSS. Similar types of defects were not detected in the laboratory-scale-printed P3HT : PCBM layer. The diameter of the pinholes varied from 20 to 50 µm. As the microscopy images reveal, the pinholes were located in the thinnest parts of the R2R gravure-printed active layer. The wetting of P3HT : PCBM ink on top of the PEDOT : PSS–ITO–PET substrate was evaluated by comparing the surface tension of the liquid and the surface energy of the solid. In printing, the ideal solid surface is flat, smooth, and chemically homogeneous and has a high surface energy value. The ink is expected to spread completely because the surface tension of the liquid is much lower than the surface energy of the solid surface [27]. Typically, the surface energy calculations are based on the contact angle values for diiodomethane, ethylene glycol, and water droplets on top of the inspected surface. Water could not be used as a test solvent because it dissolves the PEDOT : PSS layer. The effect of diiodomethane and ethylene glycol on the PEDOT : PSS layer was evaluated by microscopy because PEDOT : PSS is slightly soluble in ethylene glycol and insoluble in diiodomethane. The microscopy observations indicated that the layer was not damaged by these solvents. To further confirm the compatibility of ethylene glycol for surface energy determination, the contact angles of ethylene glycol on PEDOT : PSS and on underlying ITO were measured. The contact angle of ethylene glycol on top of PEDOT : PSS was 25° and that on top of ITO was 62°. This clear difference indicates that dry PEDOT : PSS film is not dissolved by ethylene glycol, and therefore, ethylene glycol can be used as a test solvent for determining the surface energy. The surface energy value of the PEDOT : PSS layer was 50 mN m^{-1}, which comprised the dispersive part of 41.5 mN m^{-1} and the polar part of 8.5 mN m^{-1}. Correspondingly, the surface tension of P3HT : PCBM ink was 34 mN m^{-1}, determined from droplets. The surface characteristics indicate good wetting between the P3HT : PCBM ink and the PEDOT : PSS layer, and therefore, it is unlikely that the origin of the holes was due to incomplete ink transfer or dewetting of P3HT : PCBM on top of PEDOT : PSS. Alternatively, the hole formation could be attributed to the following phenomena. The pinholes could be due to the engraved cells that do not print completely (missing dots). The cell width in the engraved patterns was 100 µm, and the wall width between the cells was 14 µm,

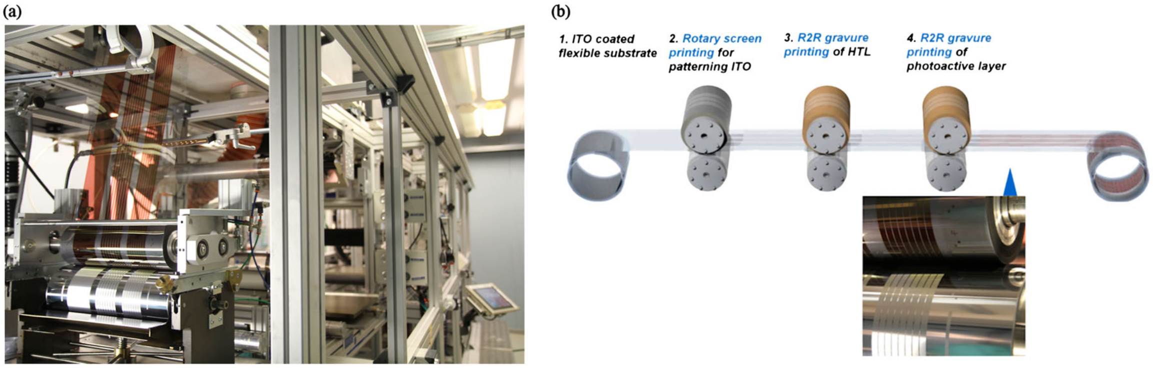

Figure 2. (a) R2R pilot machine used to prepare R2R-printed modules (machine not in operation) and (b) description of R2R process prepared with the pilot machine depicted in (a). See a video of the gravure printing process of photoactive layer in the Supporting information. The ITO patterning is prepared by R2R rotary screen printing followed by cleaning to remove the excess paste. The hole transport layer of PEDOT : PSS and photoactive layer of P3HT : PCBM (bottom right) are processed in R2R gravure printing. The modules are cut into sheets, and the electron transport layer and the electron contact are thermally evaporated with a separate unit in a sheet-based process.

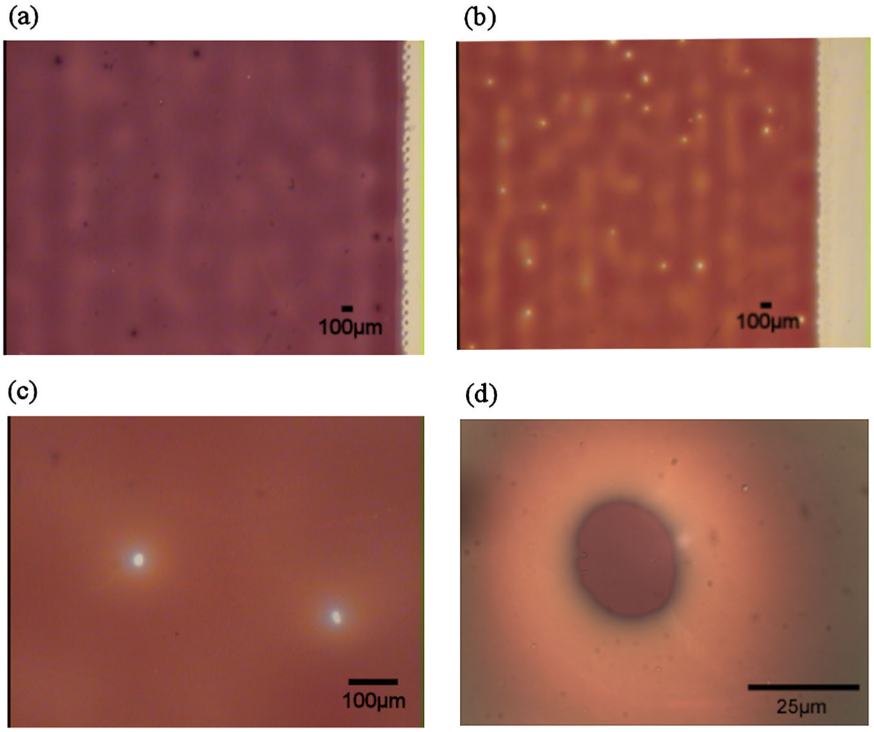

Figure 3. Microscopy images of (a) laboratory gravure-printed and (b) R2R gravure-printed P3HT : PCBM layer on top of PEDOT : PSS. Note the holes in the R2R-printed P3HT : PCBM layer in (c) and (d).

respectively. Due to the proper wetting of P3HT : PCBM, the missing dot could be partly filled by the ink from the adjacent cells. Generally, the missing dots in gravure printing are caused by clogging of the cells. In a continuous R2R process, the regular pattern of missing dots should be repetitive in a sequence of repeat length of the printing cylinder. This type of regularity, however, was not detected. Another possibility is that electrostatic discharge caused holes through the thinnest parts of the active layer. The presence of round-shaped holes supported more the electrostatic discharge hypothesis.

The electrical performance of R2R gravure-printed OPV modules was compared to that of laboratory gravure-printed modules. The measurements were carried out before exposing the modules to environmental stress. Two electron transport and electron contact combinations were tested, Ca/Ag and LiF/Al. First, a larger batch of R2R-printed modules with LiF/Al electron contact was measured resulting in a mean efficiency of 1.77 ± 0.15% for 50 modules. A smaller batch of R2R-printed modules with both electron contact combinations and the laboratory-scale-processed modules were tested more accurately with the class AAA solar simulator. In these measurements, the actual active area was also determined precisely microscopically. The mean *IV* characteristics of R2R gravure-printed OPV modules compared to those of laboratory gravure-printed modules are shown in Figure 4. The electrical characteristics and active layer thicknesses are summarized in Table I.

Notably, the graphs and data from Table I confirm that the R2R gravure-printed OPV modules with Ca/Ag are detrimentally shorted. Interestingly, the R2R-printed modules with LiF/Al performed well, with a mean PCE of 1.7% being in good accordance with the results obtained by characterizing larger batch of modules. As already observed in the microscopic characterization, the R2R gravure-printed photoactive layer contained pinholes. Presumably, these pinholes in the active layer are at least partially filled with calcium and silver forming electrical shorts in the devices. By replacing the interfacial layer of the calcium with LiF, we insulated the holes in the active layer and fabricated well-performing modules. R2R gravure-printed modules with LiF/Al had a maximum PCE of 1.9%. The laboratory-scale-printed samples with LiF/Al had a maximum PCE value of 2.3% and for Ca/Ag, a maximum PCE value of 2.0%. In these module structures, an evaporated top electrode was used that sets high requirements with respect to uniformity and defects for the underlying photoactive layer. The key reason for the performance difference between the laboratory- and R2R-processed OPV modules with LiF/Al is the fill factor. The mean fill factor of the R2R-printed modules was 14% lower than that of the laboratory-scale-processed modules. It should be emphasized that the reduction in the fill factor was mainly due to decreased shunt resistance. The series resistance was only slightly different between the laboratory- and R2R-processed modules with LiF/Al. The effect of shunt and series resistances on the module performance is presented at the end of Section 3. We performed XPS analysis to further identify the distribution of LiF on top of the photoactive layer and to obtain deeper insight into the insulating role of LiF. Furthermore, structures with lithographically produced holes on top of patterned PEDOT : PSS-ITO were prepared to confirm that the LiF layer effectively eliminates electrical shorts. LiF and Al were evaporated on top of these structures. For comparison, only Al was evaporated on some of the samples.

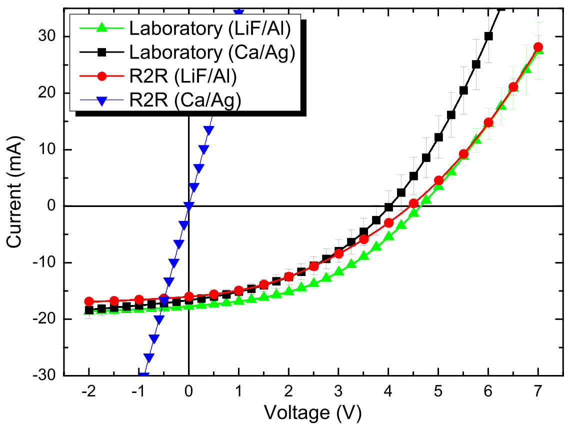

Figure 4. Mean current–voltage characteristics and standard deviation bars of R2R gravure-printed OPV modules with LiF/Al (red circles) and Ca/Ag (blue triangles) as the electron transport layer and electron contact, respectively. Correspondingly, mean current–voltage characteristics of laboratory gravure-printed modules with LiF/Al (green triangles) and with Ca/Ag (black squares) are shown.

In XPS, a flux of X-ray photons is focused on the sample surface to induce the emission of photoelectrons. XPS is a surface-sensitive method because the photoelectrons are emitted from only the first 10 nm of the surface [28]. The wide energy range XPS survey spectrum measured from the LiF-covered R2R-printed PEDOT : PSS/P3HT : PCBM sample showed peaks originating from lithium, sulfur, carbon, oxygen, and fluorine. A high-resolution scan of the F 1s peak (original measured XPS data) is presented in Figure 5(a). The F 1s peak energy was 685.3 eV, which matched well with Li-bonded F and thus confirmed the presence of the LiF layer on top of the sample [29,30]. The distribution of the LiF on the surface of the photoactive layer was investigated by conducting

Table I. Mean electrical parameters of R2R gravure-printed and laboratory-scale-printed modules using Ca/Ag and LiF/Al as electron contacts.

Process for HTL and PA	ETL/electron contact	Mean PA thickness (nm)	V_{OC} (V)	V_{OC} per cell (V)	I_{SC} (mA)	J_{SC} (mA cm^{-2})	FF	PCE (%)	PCE$_{MAX}$ (%)
R2R gravure	LiF/Al	221	4.52 (0.04)	0.57	16.35 (0.33)	8.26 (0.06)	0.37 (0.02)	1.72	1.86
R2R gravure	Ca/Ag	221				Shorted			
LAB gravure	LiF/Al	244	4.65 (0.04)	0.58	17.70 (0.37)	8.82 (0.53)	0.43 (0.03)	2.20	2.32
LAB gravure	Ca/Ag	244	4.17 (0.10)	0.52	16.72 (0.83)	8.78 (0.23)	0.41 (0.01)	1.87	1.96

Standard deviation values are shown in brackets after the mean value. The module structure consists of eight monolithically connected cells. Each category comprises four parallel modules. PA is the photoactive layer, V_{OC} is the open-circuit voltage, I_{SC} the short-circuit current, J_{SC} is the short-circuit current density in reference to a single cell area, and FF is the fill factor.

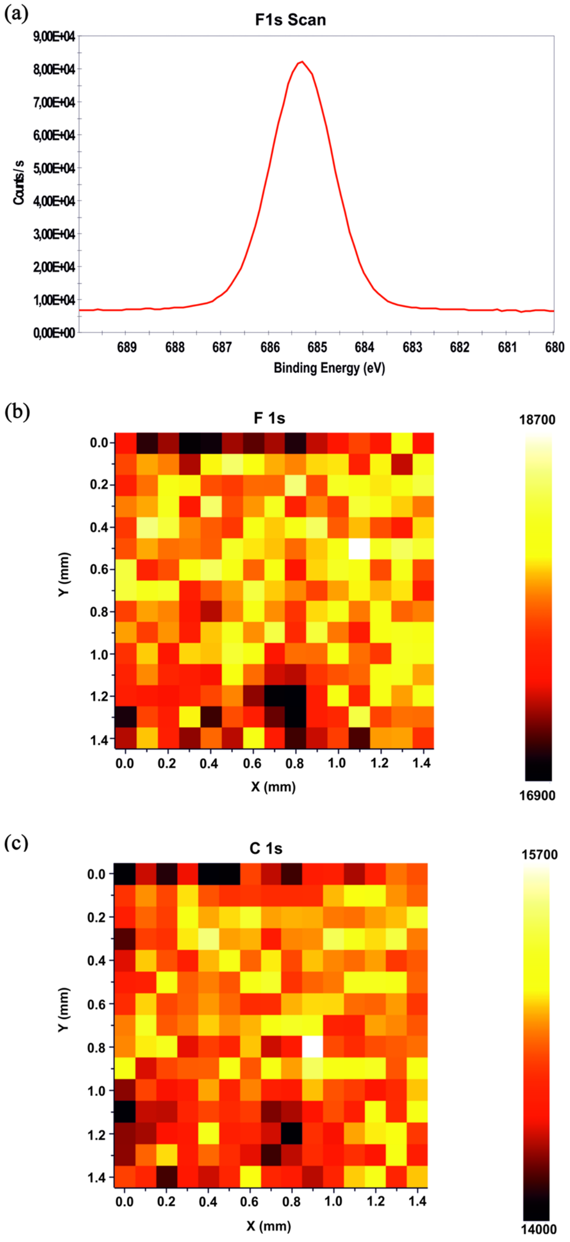

Figure 5. (a) High-resolution XPS scan of the F 1s peak of ITO/R2R-printed PEDOT : PSS/R2R-printed P3HT : PCBM/LiF sample and XPS area profiles of (b) fluorine and (c) carbon from the same sample.

XPS elemental surface mapping. The spectra of two elements, fluorine and carbon, were measured in the experiment. Fluorine refers to the amount of LiF and carbon to the underlying layers and possible adventitious carbon. The elemental surface maps of fluorine and carbon are presented in Figure 5(b and c) as counts that refer to the integrated peak area of each element's XPS spectrum in the respective pixel. The pixel size in the images was 100 µm, and the mapping was performed over a total area of 1.4 mm × 1.4 mm. The elemental maps revealed that LiF was uniformly distributed over the surface of the photoactive layer. This finding indicates that also pinholes are covered with LiF. The remarkable enhancement in module performance by the addition of LiF was due to the increased shunt resistance. According to the crystal oscillator, calibrated with optical profilometer, LiF had a mean thickness of 0.8 nm in this work. The insulating behavior of LiF in the R2R-printed module structures can be explained by investigating the equivalent circuit model. For simplicity, the module structures are presented as a single-diode model in which the series resistances and shunt resistances cover the respective resistances of the whole module. Mathematically, a single-diode model under illumination is represented by Equation (1).

$$J = J_0\left[\exp\left(\frac{e(V - JR_S)}{nk_BT}\right) - 1\right] + \frac{V - JR_S}{R_{SH}} - J_{PH} \quad (1)$$

in which J_0 is the reverse bias saturation current density, R_S is the series resistance, n is the diode ideality factor, and R_{SH} is the shunt resistance. Because the evaluation will be performed in the dark for shunt inspection, the current source J_{PH} is extracted from the equivalent circuits shown in Figure 6. The respective series and shunt resistances are approximated from the *IV* curves of the modules. For the high forward voltage regime, series resistance is the dominating parameter, and for the low voltage regime, shunt resistance dominates. Therefore, series resistance is extracted from high forward voltages in the *IV* curves (+6.0 V → +7.0 V), and shunt resistance is extracted from the slope at 0 V. The equivalent circuit for laboratory-scale-processed modules with Ca/Ag as the ETL and electron contact used as a reference is presented in Figure 6(a). The mean series resistance value for these reference structures was 58 ± 11 Ω. Correspondingly, the shunt resistance was approximately 36 kΩ. The total series resistance in the reference structure was divided into two parts, R_S and $R_{S\_CONTACT}$. $R_{S\_CONTACT}$ was estimated from the shorted R2R modules (with Ca/Ag contact) as the slope of the *IV* curve, which was 22 ± 5 Ω. This covers the series resistance of ITO, PEDOT : PSS, and Ca/Ag. It can be approximated that the series resistance of Ca/Ag was negligible, so $R_{S\_CONTACT}$ could be also used in the LiF-based modules to cover the series resistance of ITO and PEDOT : PSS. Because insulating LiF was used as an ETL, the equivalent circuit for R2R-printed modules is shown in Figure 6(b). Due to the insertion of LiF, two additional resistances were added, R_{S_LIF} and R_{SH_LIF}. According to the curves in Figure 4, the total series resistance with R2R-printed modules having LiF/Al electron contact was 93 ± 10 Ω. The increase in series resistance was due to the high resistivity of LiF. The mean total R_{SH} of the R2R-printed modules with LiF/Al was ~14 kΩ. Due to the low series resistance values of R_{S_LIF} and R_S, it can be estimated that R_{SH_LIF} and R_{SH} are connected in parallel. Therefore, the calculated R_{SH_LIF} was ~23 kΩ. It should be

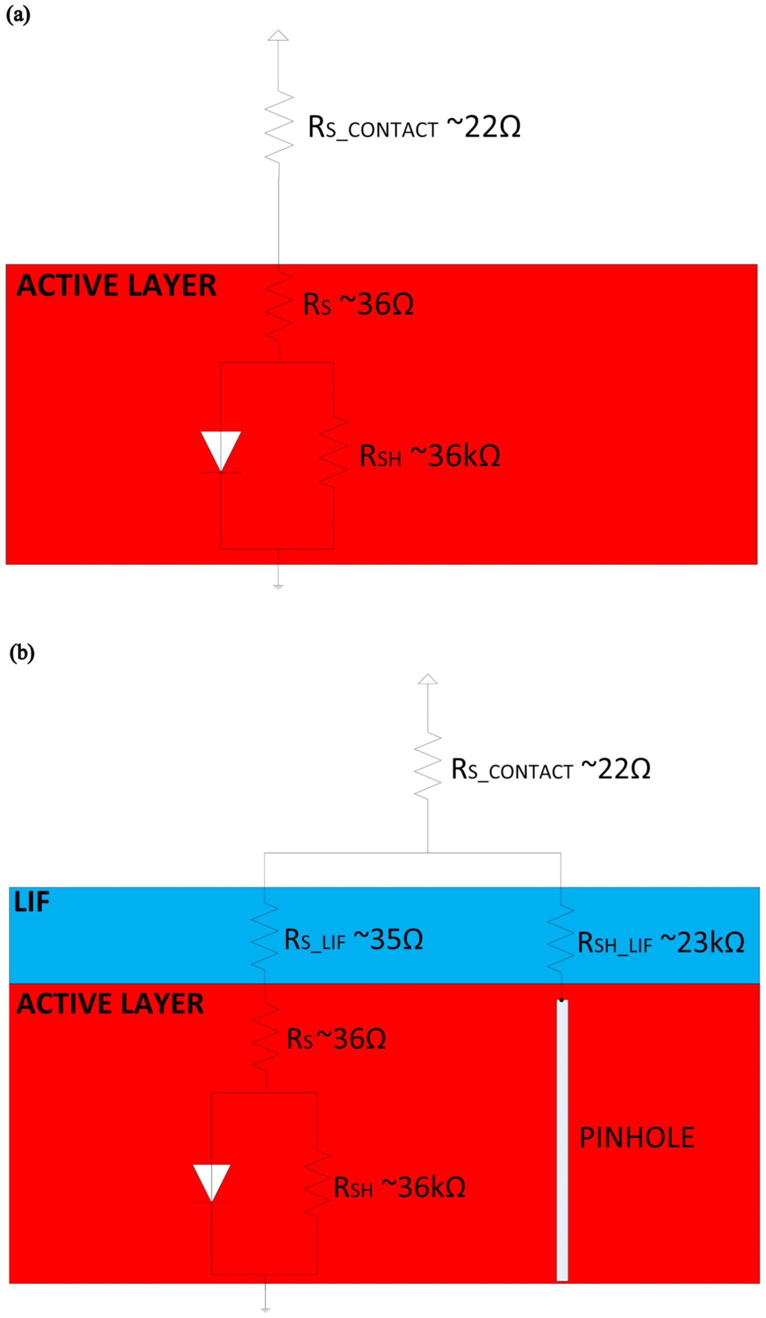

Figure 6. Simplified equivalent circuits for (a) laboratory-scale-printed modules (with Ca/Ag electron transport layer and electron contact) and (b) R2R-printed modules with detrimental pinholes insulated by a thin layer of LiF.

pointed out that the $R_{SH\_LIF} < R_{SH}$ as R_{SH} is the shunt resistance of the laboratory-scale-processed modules (no pinholes). To summarize, the additional shunt resistance caused by LiF is the reason for the insulation of detrimental pinholes in the R2R-printed module structures. Major influence on shunt resistance can be explained by the relation between resistance and resistivity $R = \rho d/A$. The resistance is inversely proportional to the area and directly proportional to the resistivity and thickness of the layer [31]. The two orders of magnitude difference between R_{SH_LIF} and R_{S_LIF} is due to the differences in area. When the area of the defects is very small compared to the overall area of the module, then $R_{SH\_LIF} >> R_{S\_LIF}$. Namely, R_{SH_LIF} is dependent on the area of the pinholes, whereas R_{S_LIF} is dependent on the effective operating area of the module. As LiF acts as an insulation layer in the module structure, it is important to determine the breakdown field over the LiF layer. Sun *et al.* [32] defined the intrinsic breakdown strength of LiF. The calculated breakdown field is 12.9 MV cm^{-1}, and the experimentally determined breakdown field is 12.2 MV cm^{-1} [32]. This corresponds to a maximum applied voltage of ~1 V over one cell in the module structure with an LiF layer thickness of 0.8 nm.

The equivalent circuit analysis of the effect of LiF in R2R-printed module structures was confirmed by lithographically producing holes on top of patterned ITO-gravure-printed PEDOT : PSS samples. We created holes with two diameters, 33 and 57 µm. The defect density with the 33-µm holes was 26.9 defects mm^{-2} and that with the 57-µm holes was 9.3 defects mm^{-2}. In both cases, the defect density was ~2.3% of the total area. To understand the shorting associated with the metallic top electrode/ETL, either LiF/Al or Al was evaporated through a shadow mask on top of the resist layer. Figure 7(a) illustrates the lithographically produced 33-µm-diameter hole structures. According to Figure 7(b) in which the mean *IV* characteristics of the hole samples are presented, the samples with an Al-containing top electrode were all shorted. Single graphs used to calculate the mean *IV* characteristics are depicted beneath the mean graphs. By adding an interfacial layer of LiF between the PEDOT : PSS layer and electron contact, the shorts were prevented (Figure 7b).

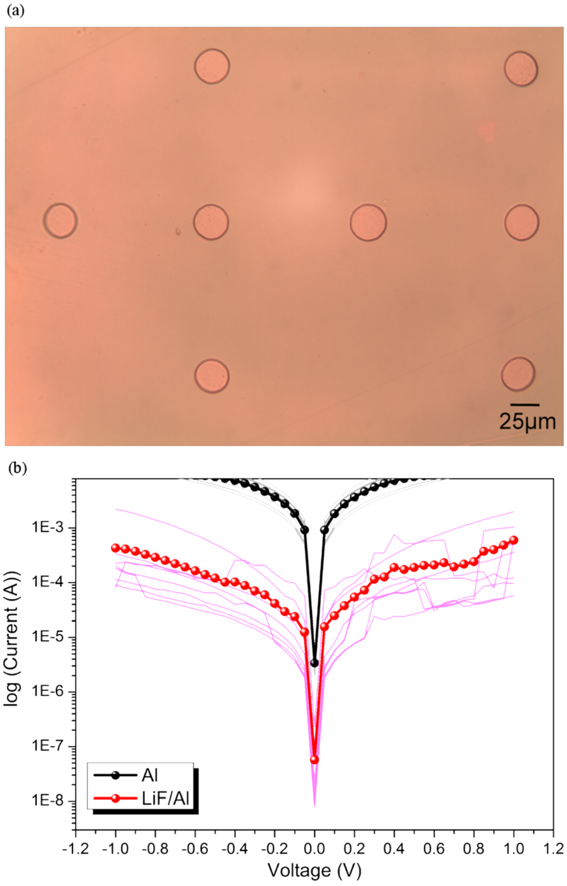

Figure 7. (a) Lithographically produced holes (diameter 33 µm) on top of patterned ITO. The image was obtained with a magnification of 20×. (b) *IV* characteristics of a patterned ITO-gravure-printed PEDOT : PSS-resist layer containing holes—LiF/Al (red circles) or Al (black circles).

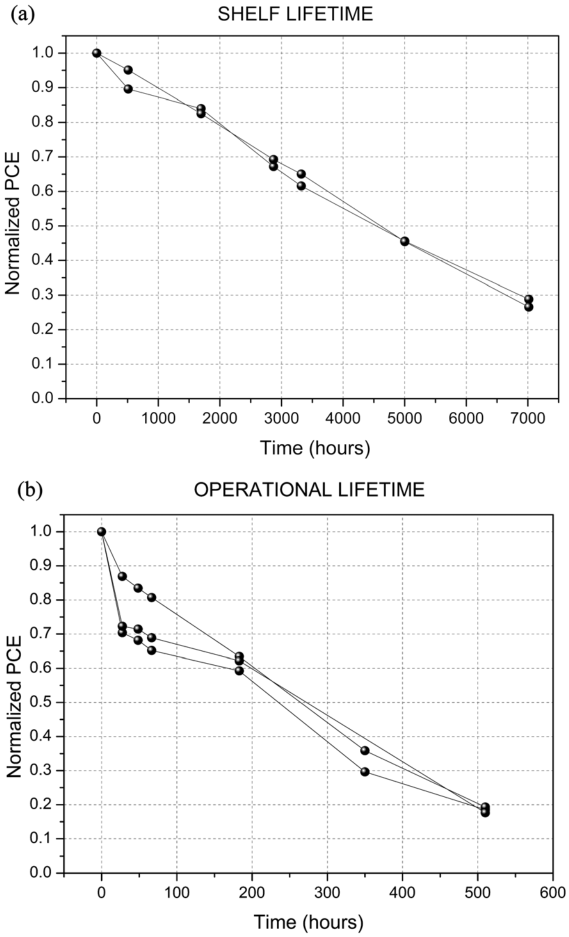

Figure 8. (a) Shelf lifetime and (b) operational lifetime of R2R-printed OPV modules.

For shelf lifetime (two modules) and operational lifetime (three modules) measurements of R2R-printed modules, International Summit on OPV Stability (ISOS) testing protocols were utilized [33]. The R2R-printed modules were encapsulated with a flexible barrier. In shelf lifetime measurement, the modules were stored at ambient conditions in the dark. It was found that the modules decayed 50% of the initial PCE after 4500 h. In the operational stability testing, the modules were stressed in Atlas XXL+ weathering chamber with the following conditions: sunlight simulated by xenon lamps using daylight filters (irradiance level of 42 W m^{-2} at 300–400 nm), relative humidity of 50 RH%, and black standard temperature of 65 °C. In these tests, the PCE of the modules decreased to 50% of the initial value after 250 h of stressing as shown in Figure 8. The instability of conventional structure devices also with glass and stainless steel encapsulation in accelerated full sun simulation has been reported [34].

4. CONCLUSION

We studied the upscaling of the gravure printing process of monolithic OPV modules to high throughput R2R fabrication. Detrimental pinholes in the R2R gravure-printed photoactive layer were observed in microscopic analysis. The pinhole formation was attributed to either missing dots or to electrostatic discharge in the printing process. The R2R-fabricated modules with a Ca/Ag electron contact layer were all electrically shorted. By inserting 0.8 nm of homogenous LiF as an interfacial layer, we fabricated well-performing monolithic modules with a mean PCE of 1.7%. The equivalent circuit model suggests that the thin LiF layer effectively insulates pinholes, resulting in remarkably increased shunt resistance while only modestly increasing the series resistance. The results demonstrate that well-performing thin-film devices can be fabricated despite the detrimental nonidealities in device layers. This loosens the constraints on the printing conditions and environment. This on the other hand can ultimately facilitate the realization of inverted OPV module designs of arbitrary shapes and sizes fabricated entirely with high throughput, additive R2R printing methods (such as gravure, rotary screen, and/or flexography) as well as their integration into smart systems.

ACKNOWLEDGEMENTS

The authors thank Mari Ylikunnari and Johanna Hiitola-Keinänen for development of the R2R patterning process for ITO, Antti Veijola for the photographs, and Dr Sanna Rousu and Elina Jansson for valuable discussions related to printing process development. This work was funded by TEKES, the Finnish Funding Agency for Technology and Innovation (under funding decision 482/31/2011).

REFERENCES

1. Brabec CJ, Gowrisanker S, Halls JJM, Laird D, Jia S, Williams SP. Polymer–fullerene bulk-heterojunction solar cells. *Advanced Materials* 2010; **22**: 3839–3856.
2. Søndergaard RR, Hösel M, Krebs FC. Roll-to-roll fabrication of large area functional organic materials. *Journal of Polymer Science Part B: Polymer Physics* 2013; **51**: 16–34.
3. Green MA, Emery K, Hishikawa Y, Warta W, Dunlop ED. Solar cell efficiency tables (version 41). *Progress in Photovoltaics: Research and Applications* 2013; **21**: 1–11.
4. Krebs FC, Fyenbo J, Jørgensen M. Product integration of compact roll-to-roll processed polymer solar cell modules: methods and manufacture using flexographic printing, slot-die coating and rotary screen printing. *Journal of Materials Chemistry* 2010; **20**: 8994–9001.
5. Hösel M, Søndergaard RR, Jørgensen M, Krebs FC. Fast inline roll-to-roll printing for indium-tin-oxide free polymer solar cells using automatic registration. *Energy Technology* 2013; **1**: 102–107.
6. Sommer-Larsen P, Jørgensen M, Søndergaard RR, Hösel M, Krebs FC. It is all in the pattern—high efficiency power extraction from polymer solar cells through high-voltage serial connection. *Energy Technology* 2013; **1**: 15–19.
7. Krebs FC, Espinosa N, Hösel M, Søndergaard RR, Jørgensen M. 25th anniversary article: rise to power—OPV-based solar parks. *Advanced Materials* 2014; **26**: 29–39.
8. Krebs FC, Hösel M, Corazza M, Roth B, Madsen MV, Gevorgyan SA, Søndergaard RR, Karg D, Jørgensen M. Freely available OPV—the fast way to progress. *Energy Technology* 2013; **1**: 378–381.
9. Kipphan H, Fuchs B, Ipsen H. *Handbook of Print Media*, Kipphan H (eds). Springer-Verlag: Berlin, 2001, Ch. 1.3, 2.2, and 2.4.
10. Kopola P, Aernouts T, Guillerez S, Jin H, Tuomikoski M, Maaninen A, Hast J. High efficient plastic solar cells fabricated with a high-throughput gravure printing method. *Solar Energy Materials and Solar Cells* 2010; **94**: 1673–1680.
11. Ding JM, De la Fuente Vornbrock A, Ting C, Subramanian V. Patternable polymer bulk heterojunction photovoltaic cells on plastic by rotogravure printing. *Solar Energy Materials and Solar Cells* 2009; **93**: 459–464.
12. Kopola P, Aernouts T, Sliz R, Guillerez S, Ylikunnari M, Cheyns D, Välimäki M, Tuomikoski M, Hast J, Jabbour G, Myllylä R, Maaninen A. Gravure printed flexible organic photovoltaic modules. *Solar Energy Materials and Solar Cells* 2011; **95**: 1344–1347.
13. Yang J, Vak D, Clark N, Subbiah J, Wong WWH, Jones DJ, Watkins SE, Wilson G. Organic photovoltaic modules fabricated by an industrial gravure printing proofer. *Solar Energy Materials and Solar Cells* 2013; **109**: 47–55.
14. Voigt MM, Mackenzie RCI, Yau CP, Atienzar P, Dane J, Keivanidis PE, Bradley DDC, Nelson J. Gravure printing for three subsequent solar cell layers of inverted structures on flexible substrates. *Solar Energy Materials and Solar Cells* 2011; **95**: 731–734.
15. Voigt MM, Mackenzie RCI, King SP, Yau CP, Atienzar P, Dane J, Keivanidis PE, Zadrazil I, Bradley DDC, Nelson J. Gravure printing inverted organic solar cells: the influence of ink properties on film quality and device performance. *Solar Energy Materials and Solar Cells* 2012; **105**: 77–85.
16. Hübler A, Trnovec B, Zillger T, Ali M, Wetzold N, Mingebach M, Wagenpfahl A, Deibel C, Dyakonov

V. Printed paper photovoltaic cells. *Advanced Energy Materials* 2011; **1**: 1018–1022.

17. Yin X, Kumar S. Flow visualization of the liquid emptying process in scaled-up gravure grooves and cells. *Chemical Engineering Science* 2006; **61**: 1146–1156.
18. Shaheen SE, Jabbour GE, Morrell MM, Kawabe Y, Kippelen B, Peyghambarian N, Nabor M-F, Schlaf R, Mash EA, Armstrong NR. Bright blue organic light-emitting diode with improved color purity using a LiF/Al cathode. *Journal of Applied Physics* 1998; **84**: 2324–2327.
19. Brown TM, Friend RH, Millard IS, Lacey DJ, Burroughes JH, Cacialli F. LiF/Al cathodes and the effect of LiF thickness on the device characteristics and built-in potential of polymer light-emitting diodes. *Applied Physics Letters* 2000; **77**: 3096–3098.
20. Hung LS, Tang CW, Mason MG. Enhanced electron injection in organic electroluminescence devices using an Al/LiF electrode. *Applied Physics Letters* 1997; **70**: 152–154.
21. Brabec CJ, Shaheen SE, Winder C, Sariciftci NS, Denk P. Effect of LiF/metal electrodes on the performance of plastic solar cells. *Applied Physics Letters* 2002; **80**: 1288–1290.
22. Jönsson SKM, Carlegrim E, Zhang F, Salaneck WR, Fahlman M. Photoelectron spectroscopy of the contact between the cathode and the active layers in plastic solar cells: the role of LiF. *Japanese Journal of Applied Physics* 2005; **44**: 3695–3701.
23. Ahlswede E, Hanisch J, Powalla M. Comparative study of the influence of LiF, NaF, and KF on the performance of polymer bulk heterojunction solar cells. *Applied Physics Letters* 2007; **90**: 163504 1–163504 3.
24. Chen L-M, Xu Z, Hong Z, Yang Y. Interface investigation and engineering—achieving high performance polymer photovoltaic devices. *Journal of Materials Chemistry* 2010; **20**: 2575–2598.
25. Steim R, Kogler FR, Brabec CJ. Interface materials for organic solar cells. *Journal of Materials Chemistry* 2010; **20**: 2499–2512.
26. Liu F, Shen W, Parker I. Surface analysis, a way to better understand lithographic printing problems. *Appita Journal* 2006; **59**: 108–113.
27. Israelachvili JN. *Intermolecular and Surface Forces*. Academic Press: San Diego, 1992; Ch. 9 and 15.
28. Van der Heide P. *X-ray Photoelectron Spectroscopy: An Introduction to Principles and Practices*. John Wiley & Sons Inc: Princeton, 2012.
29. Xiao T, Cui W, Cai M, Liu R, Anderegg JW, Shinar J, Shinar R. Thin air-plasma-treated alkali fluoride layers for improved hole extraction in copper phthalocyanine/C70-based solar cells. *Journal of Photonics for Energy* 2012; **2**: 021006 1–021006 11.
30. Zhou L, Lucht BL. Performance of lithium tetrafluorooxalatophosphate (LiFOP) electrolyte with propylene carbonate (PC). *Journal of Power Sources* 2012; **205**: 439–448.
31. Young HD, Freedman RA. *University Physics Tenth Edition*. Addison-Wesley Longman: USA, 2000.
32. Sun Y, Boggs SA, Ramprasad R. The intrinsic electrical breakdown strength of insulators from first principles. *Applied Physics Letters* 2012; **101**: 132906 1–132906 5.
33. Reese MO, Gevorgyan SA, Jørgensen M, Bundgaard E, Kurtz SR, Ginley DS, Olson DC, Lloyd MT, Morvillo P, Katz EA, Elschner A, Haillant O, Currier TR, Shrotriya V, Hermenau M, Riede M, Kirov KR, Trimmel G, Rath T, Inganäs O, Zhang F, Andersson M, Tvingstedt K, Lira-Cantu M, Laird D, McGuiness C, Gowrisanker S, Pannone M, Xiao M, Hauch J, Steim R, DeLongchamp DM, Rösch R, Hoppe H, Espinosa N, Urbina A, Yaman-Uzunoglu G, Bonekamp J-B, van Breemen AJJM, Girotto C, Voroshazi E, Krebs FC. Consensus stability testing protocols for organic photovoltaic materials and devices. *Solar Energy Materials & Solar Cells* 2011; **95**: 1253–1267.
34. Tanenbaum DM, Hermenau M, Voroshazi E, Lloyd MT, Galagan Y, Zimmermann B, Hösel M, Dam HF, Jørgensen M, Gevorgyan SA, Kudret S, Maes W, Lutsen L, Vanderzande D, Würfel U, Andriessen R, Rösch R, Hoppe H, Teran-Escobar G, Lira-Cantu M, Rivaton A, Uzunoğlu GY, Germack D, Andreasen B, Madsen MV, Norrman K, Krebs FC. The ISOS-3 inter-laboratory collaboration focused on the stability of a variety of organic photovoltaic devices. *RSC Advances* 2012; **2**: 882–893.

SUPPORTING INFORMATION

Additional supporting information may be found in the online version of this article at the publisher's web site.

ARTICLE IV

R2R-printed inverted OPV modules – towards arbitrary patterned designs

Nanoscale 7:9570–9580.

Nanoscale

PAPER

View Article Online
View Journal | View Issue

Cite this: *Nanoscale*, 2015, **7**, 9570

R2R-printed inverted OPV modules – towards arbitrary patterned designs

M. Välimäki,*[a] P. Apilo,[a] R. Po,[b] E. Jansson,[a] A. Bernardi,[b] M. Ylikunnari,[a] M. Vilkman,[a] G. Corso,[b] J. Puustinen,[c] J. Tuominen[a] and J. Hast[a]

We describe the fabrication of roll-to-roll (R2R) printed organic photovoltaic (OPV) modules using gravure printing and rotary screen-printing processes. These two-dimensional printing techniques are differentiating factors from coated OPVs enabling the direct patterning of arbitrarily shaped and sized features into visual shapes and, increasing the freedom to connect the cells in modules. The inverted OPV structures comprise five layers that are either printed or patterned in an R2R printing process. We examined the rheological properties of the inks used and their relationship with the printability, the compatibility between the processed inks, and the morphology of the R2R-printed layers. We also evaluate the dimensional accuracy of the printed pattern, which is an important consideration in designing arbitrarily-shaped OPV structures. The photoactive layer and top electrode exhibited excellent cross-dimensional accuracy corresponding to the designed width. The transparent electron transport layer extended 300 μm beyond the designed values, whereas the hole transport layer shrank 100 μm. We also examined the repeatability of the R2R fabrication process when the active area of the module varied from 32.2 cm^2 to 96.5 cm^2. A thorough layer-by-layer optimization of the R2R printing processes resulted in realization of R2R-printed 96.5 cm^2 sized modules with a maximum power conversion efficiency of 2.1% (mean 1.8%) processed with high functionality.

Received 10th January 2015,
Accepted 15th April 2015

DOI: 10.1039/c5nr00204d

www.rsc.org/nanoscale

1. Introduction

Organic solar cells, constructed from solution-processed polymers and fullerenes, are a promising disruptive technology for affordable, sustainable, and decentralized energy production. Since the discovery of organic photovoltaics (OPV) in the 1980s, extensive research efforts have focused on improving the power conversion efficiency (PCE) beyond 10%.[1–3] To date, the use of high performance photoactive materials has provided PCEs approaching 11%.[4] These small area record cells are usually processed with energy-intensive or non-scalable techniques, however, such as vacuum evaporation and spin coating, often on glass substrates under inert conditions.[5–8] On the other hand, with large-area roll-to-roll (R2R) modules processed in air using conventional materials such as poly(3-hexylthiophene):[6,6]-phenyl C61 butyric acid methyl ester (P3HT:PCBM), PCEs are produced in the range of only 2% to 3%.[9] There are several reasons for this performance gap:[10–13] (i) fundamental issues related to the dimensions of the elementary cell; (ii) final synthetic accessibility and cost of the materials; and (iii) the current lack of ink formulations that are applicable for R2R processing techniques, which limits the range of materials transferable from the laboratory to the pilot and further to the industrial scale.[10–15] Indeed, the device behavior is greatly affected by the active layer morphology, which in turn depends on both the selected deposition technique, and the deposition and post-treatment conditions.[16–20] Ink formulations for all layers must be re-optimized to achieve suitable rheological properties as well as ideal nano- and micromorphologies by considering the chemical compatibility and wetting issues of the overlapping layers. Importantly, the laboratory scale fabrication of solar cells does not actually indicate the technical feasibility or the economic sustainability of the flexible OPV technology, as often claimed in the literature, that is real PV modules for commercial applications on flexible substrates must be fabricated using an R2R process.[21]

Slot-die coating is the most often used and well-established technique for R2R manufacturing of OPV modules.[22–32] The key advantage of slot die coating is that there are no strict limitations on the properties of the coating inks. Inks with a wide viscosity and solid content range can be successfully coated.[22] Krebs *et al.* demonstrated the possibility of manufacturing ITO-free modules, with all-R2R-processed layers, and

---

[a] *VTT Technical Research Centre of Finland Kaitoväylä 1, FIN-90571 Oulu, Finland. E-mail: Marja.Valimaki@vtt.fi*
[b] *ENI S.p.A Research Center for non-Conventional Energies Istituto ENI Donegani, Novara, Italy*
[c] *University of Oulu, Microelectronics and Materials Physics Laboratories, PO BOX 4500, 90014 Finland*

the outstanding potential of OPV by building solar parks.[30,31] The major limitation of the slot-die process, however, is its patterning capability, which limits the pattern shape to stripes. Among the digital printing processes, inkjet printing is a technique that enables customized OPV cells and modules.[26,27,33–35] In contrast, mechanical printing technologies, such as gravure printing, flexography printing, screen printing, and offset printing, have the advantage of large-area arbitrary shape and size processing using additive R2R process steps in a sequence. This increases the freedom of product design and its integration into various applications. The potential of gravure printing as an OPV manufacturing technique has been demonstrated in small area cells and modules on the laboratory scale, and in a sheet-to-sheet industrial scale process.[36–41] Some groups have also reported R2R gravure-printed conventional cells and modules.[18,19,42] These fabrication processes, however, still involve an evaporation step. Hübler *et al.* reported the deposition of R2R-printed small-area OPV cells on a paper substrate by a combination of flexography and gravure printing for preparation of the devices.[43]

In the present study, we describe R2R-printed inverted OPV modules created using gravure printing and rotary screen printing techniques. Here we focused on R2R processing of an indium tin oxide (ITO)–zinc oxide (ZnO)–P3HT:PCBM–poly(3,4-ethylenedioxythiophene):poly(styrenesulfonate) (PEDOT:PSS)-silver structure in terms of printability and patterning. We have used only printing methods to manufacture OPV modules except that sputtered ITO-PET is employed as a basis. ITO can be replaced for instance with transparent/semi-transparent conducting materials,[44,45] *i.e.* printed metal grids and PEDOT:PSS,[46–52] coated silver nanowires[53] for further cost reduction. First, we discuss the rheological properties of the inks used and their relationship with the printability. Furthermore, we investigate the morphology of the R2R-printed layers. Second, we perform compatibility tests prepared with four different silver pastes on the laboratory scale. Third, we examine the spreading of the inks, *i.e.* the accuracy of the printed pattern and registration in the R2R process in a cross-machine direction (CD). Fourth, we investigate the electrical performance and repeatability of the R2R-printed modules throughout the run with varying module sizes. Finally, we provide a summary of the results with concluding remarks, and a description of the module preparation and characterization in the Experimental section.

2. Results and discussion

2.1. R2R process

The inverted OPV structure investigated in this work comprised a total of five layers that are either printed or patterned in separate R2R process steps (Fig. 1). As a first process step, ITO is patterned as a negative image using rotary screen printing to define the desired pattern.[54] Next, ZnO, which acts as an electron transport layer, is R2R gravure-printed. The gravure printing of ZnO is described in a separate article.[55] The photoactive layer of P3HT:PCBM is also R2R gravure printed. We used PEDOT:PSS as the hole transport layer and silver ink as the hole contact, both printed using the R2R rotary screen printing process. The printing methods were selected based on the properties of the selected material and the targeted layer thickness. The etching paste for ITO, PEDOT:PSS grade and silver paste were developed for flat-bed screen printing, and therefore rotary screen printing was selected for R2R processing. Moreover, the lower viscosity of the ZnO and P3HT:PCBM inks favors the use of gravure printing in their deposition, allowing for construction of the desired layer thickness of tens or hundreds of nanometers in the OPV cell structure. Details of the materials, inks/pastes and processing are provided in the Experimental section.

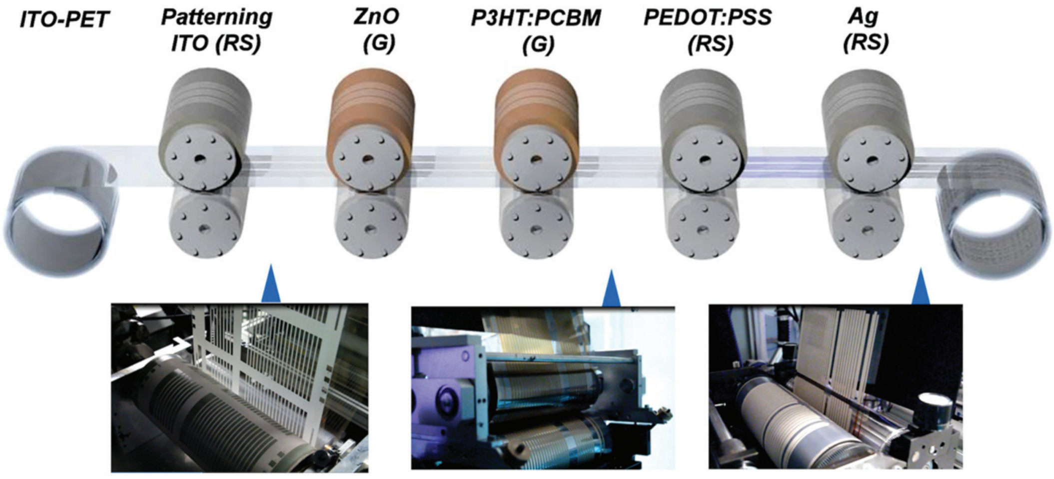

Fig. 1 R2R process of printed inverted OPV modules. The used printing methods for separated OPV layers are abbreviated as RS = rotary screen printing, G = gravure printing.

2.2. Rheological properties and printability of R2R-printed layers

The rheological properties are crucial for obtaining good uniformity and well-defined edges in the R2R-printed layers. The rheological properties of the PEDOT:PSS and P3HT:PCBM inks and their relationship with printability were investigated. The viscosity values of PEDOT:PSS and P3HT:PCBM at different shear rates are shown in Fig. 2. Both the inks are shear-thinning and the thinning behavior is very rapid, which is beneficial in the printing processes. As a screen printing paste, the viscosity of PEDOT:PSS ink is significantly higher than that of the P3HT:PCBM ink for gravure printing. During the printing process, the PEDOT:PSS and P3HT:PCBM ink viscosities are approximately 600 mPa s and 25 mPa s, respectively. Higher shear rates cannot be measured with the equipment used, but it should be noted that shear rate can exceed values up to 100 000 s^{-1} in gravure printing.[56] The thixotropy and amplitude sweep curves of PEDOT:PSS and P3HT:PCBM are also shown in Fig. 2. The high flow point (≫10%) and fast viscosity recovery after the high shear load of the PEDOT:PSS ink indicates that the ink might have some leveling issues on the substrate during printing. This ink also has significant gel-like behavior ($G' > G''$) at low strain values, which leads to an uneven ink distribution within the printed layers. P3HT:PCBM ink has a lower flow point, which facilitates the formation of uniform layers. The P3HT:PCBM ink viscosity recovers rather quickly after the high shear load, but not to the same level as before shearing, which indicates that the ink layer has a different structure (polymer matrix structure and orientation) from that before printing and that the ink distribution within the printed layer might be uneven.

As described earlier, the rheological measurement of P3HT:PCBM ink predicts good leveling of the ink layer, but the blend of two different materials in the ink might cause some unevenness in the material distribution within the printed layer. Gravure printing of the P3HT:PCBM layer, however, provided excellent control of the ink and a uniform layer with a thickness of 175 (±12) nm on top of the ZnO layer in the R2R process.

The rheology measurement indicates limited leveling and distribution of PEDOT:PSS in printing. Furthermore, the aqueous dispersion of PEDOT:PSS cannot provide good print quality directly on top of the hydrophobic surface of P3HT:PCBM. Various strategies can be used to improve the printability, which involve the addition of co-solvents and/or additives to the PEDOT:PSS or pre-treatment of the P3HT:PCBM surface with plasma/corona or solvents. Generally, the addition of a suitable co-solvent improves the leveling and distribution of the ink, but even minor additions of co-solvent remarkably change the rheological behavior of PEDOT:PSS paste.[57] Surfactants, such as Triton X-100, Zonyl FS-300, and Capstone FS-31 have been used to enhance the surface properties of PEDOT:PSS; thus, most studies have focused on improving the wettability of PEDOT:PSS.[39,40,58] Surfactants might lead to lower cell performance and/or shortened lifetime, and extensive studies are required to confirm their device compatibility. Lim *et al.* reported that the use of Capstone FS-31 with PEDOT:PSS improves the wettability while maintaining a device efficiency of 3.1%, and even increases the device lifetime.[58] The surface treatment of P3HT:PCBM with plasma or corona increases the surface energy of P3HT:PCBM, but has detrimental effects on the device performance. The wetting and leveling of PEDOT:PSS can be also improved with the surface treatment

Ink	1 s^{-1}	100 s^{-1}	1000 s^{-1}	6000 s^{-1}
PEDOT:PSS	104.0 Pa•s	5.6 Pa•s	1.7 Pa•s	0.6 Pa•s
P3HT:PCBM (130 mg/ml in o-DCB)	43.3 mPa•s	26.0 mPa•s	24.9 mPa•s	24.8 mPa•s

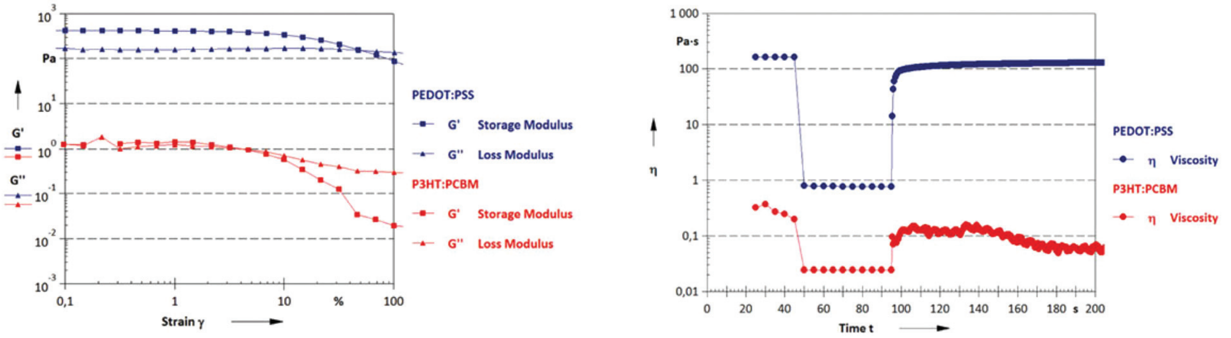

Fig. 2 Amplitude sweep (left) and thixotropic behaviour (right) of PEDOT:PSS (blue) and P3HT:PCBM (red) inks. Amplitude sweep was performed using strain levels from 0.1% to 100%. The flow point is the crossing point of G' and G'' curves. In the thixotropy test, the initial and final shear rates were 0.5–1 s^{-1} and the high shear rate was 4000–6000 s^{-1}. Higher shear rate values were used for lower viscosity active ink.

of P3HT:PCBM, which can also improve device performance.[39,40,59] The hydrophobic effect of the P3HT:PCBM surface can be reduced by wetting the P3HT:PCBM surface with a polar solvent that has limited solubility with P3HT:PCBM, such as isopropyl alcohol and 1-octanol.[24,25,60] In addition, the residence time should be short to achieve good print quality of PEDOT:PSS on top of P3HT:PCBM and also to avoid negative impact on device performance.

In the R2R rotary screen printing process described here, ink distribution is controlled by the choice of the printing screen, the pressure of the squeegee, the speed of printing, and the drying profile. The screen printable PEDOT:PSS inks are recommended for use with polyester screens instead of metallic screens. Because the rotary screen printing unit is limited to metallic screens, the test screens were either hexagonally patterned nickel plates or woven steel threads. The structures of the test screens were developed for solid area printing with line thicknesses of 200, 215, and 305 lines per inch (= L). The wet deposit varies from 15 to 18 µm, aiming at a final film thickness close to 1 µm. As the woven screen with 200 L steel threads copies the meshwork into the printed surface, a nickel plate with 215 L hexagonal patterning provides significantly better leveling of PEDOT:PSS. A 305 L nickel plate prints the sharpest image, but reduces the uniformity within the printed areas, thus the 215 L plate gives the best print quality. The pressure of the squeegee was set as low as possible to avoid PEDOT:PSS oozing out through the screen with a 1.5 bar value. A clear influence of the web speed on the quality of printed PEDOT:PSS was not detected as the web speed ranged from 2 to 6 m min^{-1}; thus, 2 m min^{-1} was chosen to increase the efficiency of drying and the time of leveling before hot air drying at +130 °C temperature. The P3HT:PCBM surface was pre-treated with a solvent before the printing of PEDOT:PSS to provide proper wetting and leveling of the ink. The PEDOT:PSS layer was printed at a thickness of 1.3 (±0.1) µm, which was considered thick enough to protect the P3HT:PCBM layer from the silver paste and thin enough to avoid delamination of PEDOT:PSS.[24] As presented here, the uniform layer of PEDOT:PSS could be printed on top of P3HT:PCBM in the R2R process, despite the challenging rheology of the PEDOT:PSS and the hydrophobic surface of the P3HT:PCBM. In addition, the R2R printing process described in this paper is repeatable, thus providing good print quality constantly throughout the R2R run.

2.3. Compatibility of silver pastes

Various silver pastes were investigated on the laboratory scale in terms of cell performance to determine a suitable paste for R2R processing of the conductive top electrode. Two main aspects were emphasized in the paste selection: (i) compatibility of the silver paste on the underlying layers, and (ii) R2R processability by means of thermal capacity limited by the size and maximum temperature of the drying units. Thermally curable silver pastes containing low amounts of acetate-based solvents were purchased from DuPont and Spraylat. The pastes PV 410 and PV 414 from DuPont and pastes XCMS-015 and XPVS-670 from Spraylat were flat-bed screen-printed on top of the laboratory scale-processed small-area cells, with a defined active area of 18 mm^2. The cells were fabricated using table top printers and the drying was set to respond to the drying efficiency of the moving web in R2R process. The effect of the silver pastes PV 410, PV 414, XCMS-015 and XPVS-670 on the electrical parameters involving the open circuit voltage (V_{oc}), short-circuit current density (J_{sc}), and PCE is shown in Fig. 3. According to current–voltage characteristics, a PCE between 2% and 3% was obtained with silver pastes PV 410, PV 414 and XPVS-670 whereas paste XCMS-015 had a PCE of only 1%. Notably, however, the performance was overestimated by the area of PEDOT:PSS, which was designed to be larger than the area of silver to avoid direct contact between the silver paste and the P3HT:PCBM layer. Because the highly conductive PEDOT:PSS also acts as a hole contact, a larger area of PEDOT:PSS can increase the cell performance by ~20%. Further, the effect of PEDOT:PSS as a hole contact will diminish as the active area of cells/modules increases. Even though PV 410 silver paste exhibited good cell performance as a hole contact, the processing of the paste was considered suitable only for flat-bed screen printers due to clogging of the screen. PV 414 silver paste was a promising candidate for R2R printing in terms of cell performance and processability. Silver paste XCMS-015 exhibited the lowest cell performance, and the current density was 30% lower compared to the other cells with a PCE just above 1%. The solvents of the silver pastes were similar. However, the lower performance with silver paste XCMS-015 could be attributed to the lower solid content of the silver paste, which resulted in a significant increase of the solvent.[24] Silver paste XPVS-670 provided the best cell performance among the tested silver pastes with excellent printing quality and easy processability.

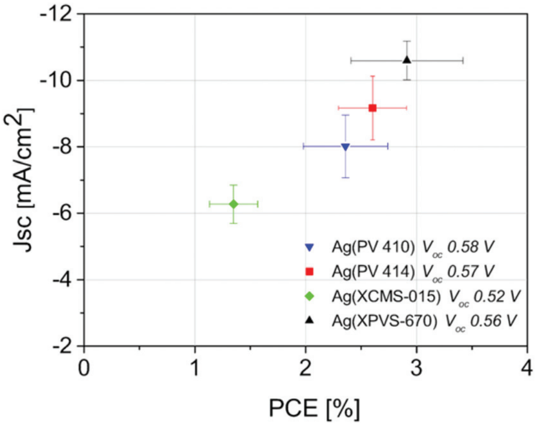

Fig. 3 Comparison of organic solar cells produced with four different silver paste products. The performance of the laboratory scale printed cells is presented in terms of the open circuit voltage and the current density with the power conversion efficiency.

Based on the laboratory scale experiments, silver paste XPVS-670 was selected for fabrication of the R2R modules since it exhibited high cell performance, sufficiently low requirements for curing, and excellent processing. Rotary screen printing of XPVS-670 in the R2R process was achieved using a 275 mesh metallic screen, and it was designed to provide a wet thickness of 14 μm. A printing speed of 2 m min^{-1} allowed for drying under a hot air unit at +130 °C for 2 min. The following processing conditions resulted in a final layer thickness of 11 (±0.4) μm and good quality printing, which were maintained throughout the run. The dimensions of the printed structures are presented in Sections 2.4 and 2.5.

2.4. Patterning accuracy and registration

The ZnO and P3HT:PCBM materials processed with gravure printing were printed as continuous lines with a striped design on top of the patterned ITO, so only cross machine alignment (CD, perpendicular to the printing direction) required adjustment during the run. PEDOT:PSS and silver, however, were rotary screen-printed to a rectangular pattern, so these layers also needed to be aligned in the printing direction (machine direction, MD). The layout is shown in Fig. 4. The layout was designed with a CD overlap between the printed layers in order to obtain the serial connection between the cells through the ITO and silver layers. Thus, each layer was aligned on the previous layer except for the P3HT:PCBM that was aligned on the ITO pattern. Respectively, in the MD the PEDOT:PSS was positioned with respect to the ITO pattern and silver with respect to the PEDOT:PSS layer.

It should be noted that the pilot printing machine used for these experiments was equipped with control cameras, but registration was performed manually. In addition, the R2R printing alignment accuracy was challenged by the detection of the highly transparent layers of ZnO and ITO. The alignment tolerance covering the influences caused by the misalignment between the printed layers and the spreading or shrinking of the wet film was designed to be at maximum 600 μm for each layer. The accuracy of the CD alignment between the printed layers was measured microscopically afterwards, and the sampling distance comprised 50 repeat lengths of R2R processed modules (Fig. 5). The repeat length was defined as the circumference of the printing cylinder/screen and the repeat length of the R2R machine was 409.6 mm; thus, 50 repeat lengths corresponded to a web length of 20 meters. As mentioned earlier, ZnO and P3HT:PCBM layers were aligned with ITO whereas PEDOT:PSS was aligned with P3HT:PCBM and silver with PEDOT:PSS. The limited detection of the transparent layers increased the CD distance to the previous layer; thus, the mean dislocation of the ZnO layer was 300 μm further and periodically fluctuated. The P3HT:PCBM, PEDOT:PSS, and silver were aligned according to the specifications with few exceptions. The CD alignment of the P3HT:PCBM layer shifted only 100 μm from the mean and, the silver layer followed the fluctuation of the PEDOT:PSS. In some cases, the layer alignment exceeded the specified tolerance, although it was compensated by the high accuracy of the alignment of the other layers (see Fig. 6a).

The dimensional accuracy of the printed image is influenced by the rheology of the ink, the surface properties of the ink and substrate, the precision provided by the printing cylinder or the screen, and the processing conditions. Here, the dimensional accuracy in the CD of the printed layers (Fig. 6b) was compared to the layout of the module by measuring the samples that had been introduced as the alignment of the R2R-printed modules was examined. The R2R gravure-printed ZnO layer was broadened from the designed 5.0 mm to a 5.3 mm layer due to the low viscosity of the ink and the good wetting properties on top of the ITO layer. As described earlier, the accuracy of the cell alignment of each layer was designed to be within 600 μm; nevertheless, the ZnO layer spreading over the other edge of the cell was accepted up to 1000 μm. Gravure printing, however, enables excellent control of ink, as shown by the R2R-printed P3HT:PCBM layer corresponding to a 5.6 mm width as designed in the layout of the module. Thus, the good precision achieved in the edge area of printed features is an absolute strength of gravure printing. The R2R rotary screen-printed layer of PEDOT:PSS was reduced 1% from

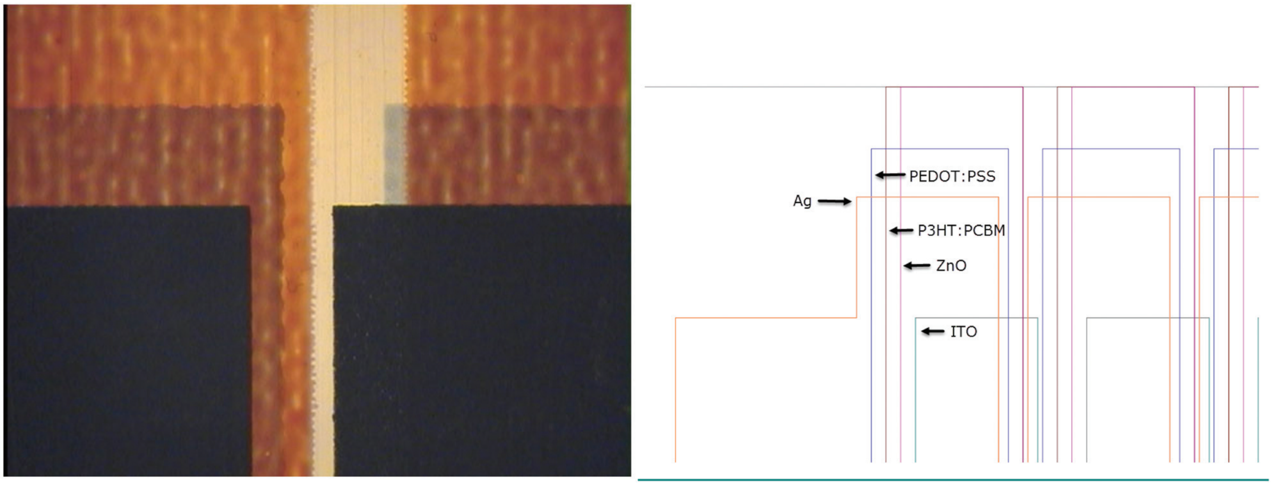

Fig. 4 The serially connected OPV module where the layers from the left are as follows: Silver, PEDOT:PSS, P3HT:PCBM, ZnO and ITO.

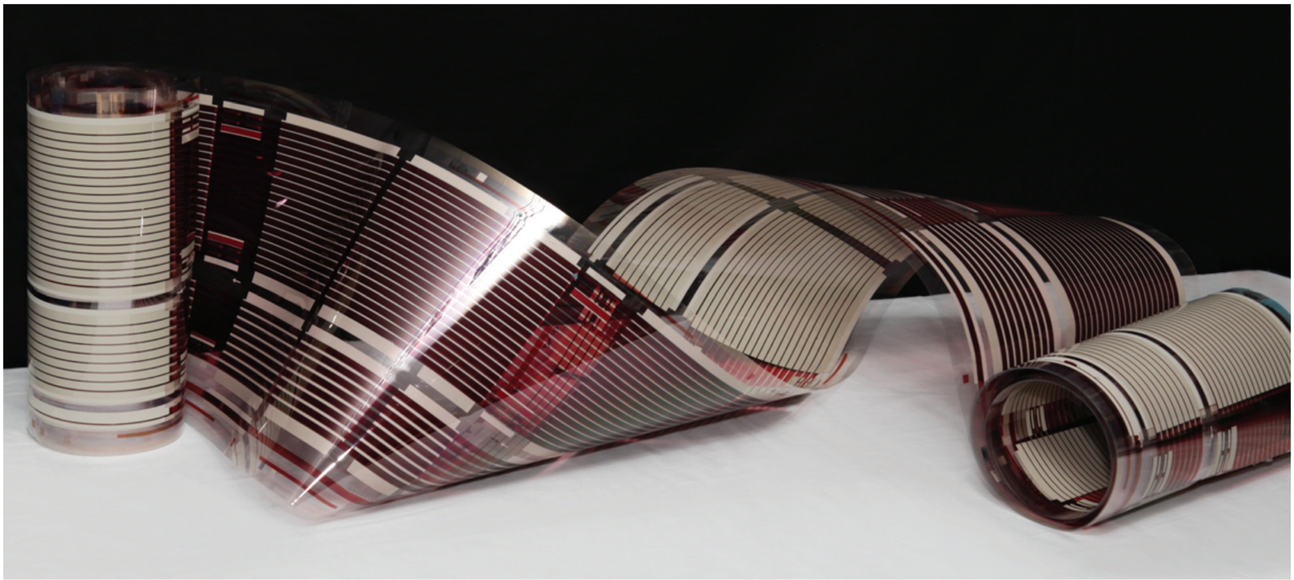

Fig. 5 R2R fabricated printed inverted OPV modules using gravure printing and rotary screen printing techniques.

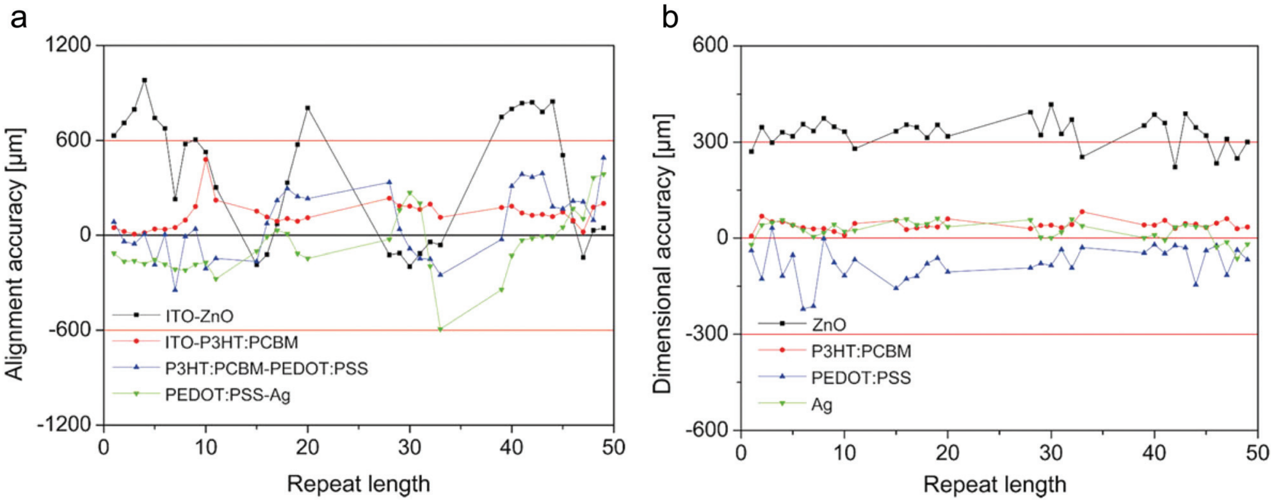

Fig. 6 Cross machine direction profile of the alignment (a) and dimensions (b) of R2R gravure-printed (ZnO, P3HT:PCBM) and rotary screen-printed (PEDOT:PSS, silver) layers of the OPV module showing the deviation from the nominal value (ZnO and P3HT:PCBM with respect to ITO, PEDOT:PSS with respect to P3HT:PCBM and silver with respect to PEDOT:PSS).

the specified width of 5.6 mm, resulting in a final dimension of 5.5 mm. Shrinkage likely occurred during the thermal drying of the layer rather than by printing. The dimensional control of the R2R rotary screen-printed silver paste showed excellent dimensional accuracy, corresponding to a 5.8 mm width of the layout. The dimensional accuracy of the printed layers over a sampling distance of 50 repeat lengths corresponded to a mean dimension of 5.3 mm ± 1.0% for ZnO (5.0 mm engraved pattern), 5.6 mm ± 0.5% for P3HT:PCBM (5.6 mm engraved pattern), 5.5 mm ± 1.0% for PEDOT:PSS (5.6 mm engraved pattern), and 5.8 mm ± 1.0% for silver (5.8 mm engraved pattern).

2.5. Electrical performance of the printed modules

Six sizes of printed modules by gravure printing and rotary screen printing were processed. The layout of the R2R module process is shown in Fig. 7. One side of the roll comprised 8 monolithically serially connected cells and, the other side comprised 19 serially connected cells, and 3 different cell sizes were prepared ($A = 0.34 \times 5.0$ cm^2, $B = 0.34 \times 10.0$ cm^2 and $C = 0.34 \times 15$ cm^2). Thus, the total active area of the modules varied from 13.6 cm^2 to 96.5 cm^2.

The surface morphologies of the P3HT:PCBM, PEDOT:PSS, and silver measured by using atomic force microscopy and

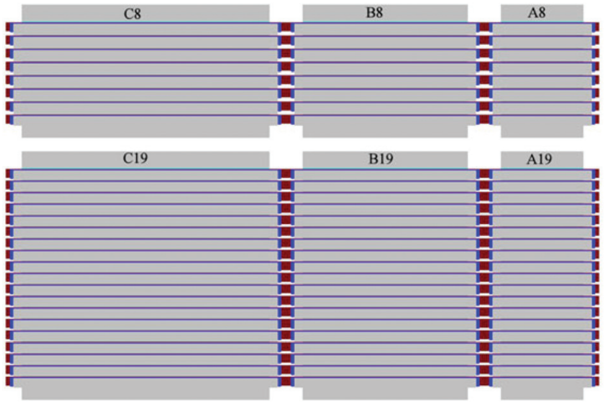

Fig. 7 Layouts of the printed modules in the R2R process. A refers to the shortest module (5 cm), B to the medium length module (10 cm), and C to the longest module (15 cm). The number 8 refers to 8 monolithically series connected cells, and the number 19 refers to 19 monolithically series connected cells.

topography images of the samples are shown together with optical microscopy images in Fig. 8. R2R gravure printing of P3HT:PCBM provided a smooth and uniform surface with a root mean square roughness (R_q) value of 1.45 nm and a maximum height variation (peak-to-valley) of 13 nm on a cross-section of the image. The rheological properties of P3HT:PCBM ink favored a balanced transfer and leveling of the ink, leading to good printed film formation. The optimal drying profile was not examined in this work, and therefore the morphology might be improved by optimizing the heat transfer conditions during film formation. The topography image of the R2R rotary screen-printed PEDOT:PSS layer has an R_q of 23.6 nm and a height variation of 0.2 μm on a cross-section of the image. These values are higher than P3HT:PCBM due to the rheological properties of the PEDOT:PSS ink and the type of printing screen. As explained earlier, the rheology of PEDOT:PSS indicates a potential risk with respect to uneven ink distribution and limited leveling. In addition, the ink and target layer thicknesses define the mesh and emulsion thickness of the screen, thus having a major impact on the quality of the printed layer together with the process parameters. Because the mean layer thickness of PEDOT:PSS was 1.3 μm and the height variation was 0.2 μm, the result was acceptable. The silver layer shows an agglomerated surface topography structure with a surface roughness of 655 nm and a height variation ~3.1 μm on a cross-section of the image. The agglomerates contained smaller entities with a diameter of ~400 nm referring to the particle size of the silver.

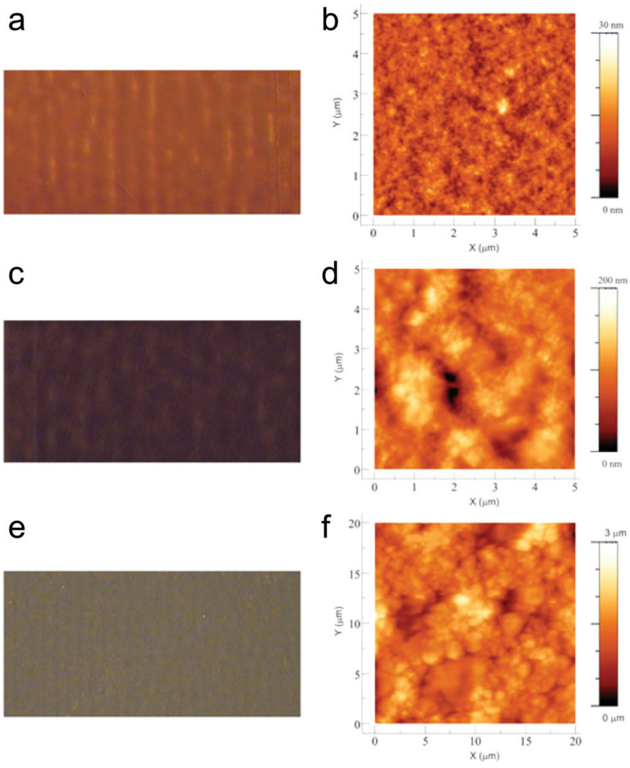

Fig. 8 Optical microscopic images with a magnification of 38× (a, c, and e, respectively) and AFM topographies of P3HT:PCBM, PEDOT:PSS, and silver layers (b, d, and f, respectively). The *x*-direction of the AFM image is parallel to the machine direction and the *y*-direction is parallel to the cross machine direction of printing.

A total of 220 printed modules were electrically characterized. No thermal post treatment or light soaking was used for the modules prior to the current–voltage measurements. Mean efficiencies ranged from 1.7% to 1.8%, while the maximum values exceeded from 2.0% to 2.2% depending on the module size. This shows the excellent repeatability of the R2R printing of the modules. In addition, we investigated repeatability by characterizing two series of modules with 19 serially connected cells. The first test series contained 36 modules of repeat lengths of 8–19, and the second series contained 36 modules of repeat lengths of 38–49. Both the series of modules were consecutive modules from the R2R-produced roll in three different module sizes. The short circuit current (I_{sc}), V_{oc}, fill factor (FF), and PCE of the modules are depicted in Fig. 9. The parameters for the repeat lengths of 8–19 (series 1) are indicated with filled circles and the repeat lengths of 38–49 (series 2) are indicated with open circles. The module size of A19 refers to the total active area of 32.2 cm^2, B19 to 64.4 cm^2, and C19 to 96.5 cm^2.

Small fluctuations were observed for the short circuit current values. The variation correlated with the manually operated registration, which affects the size of each cell in all sizes of modules printed at the same time, and consequently the short circuit current values as well. The CD variation of 100 μm will change the area of the cell with the largest module (C19) by 3%. This means that a variation of 100 to 200 μm will affect the short circuit current value by ±1–2 mA. The mean electrical parameters of the test series are summarized in Table 1. The mean value is calculated as an average of both test series shown in Fig. 9. J_{sc} per cell is calculated by dividing

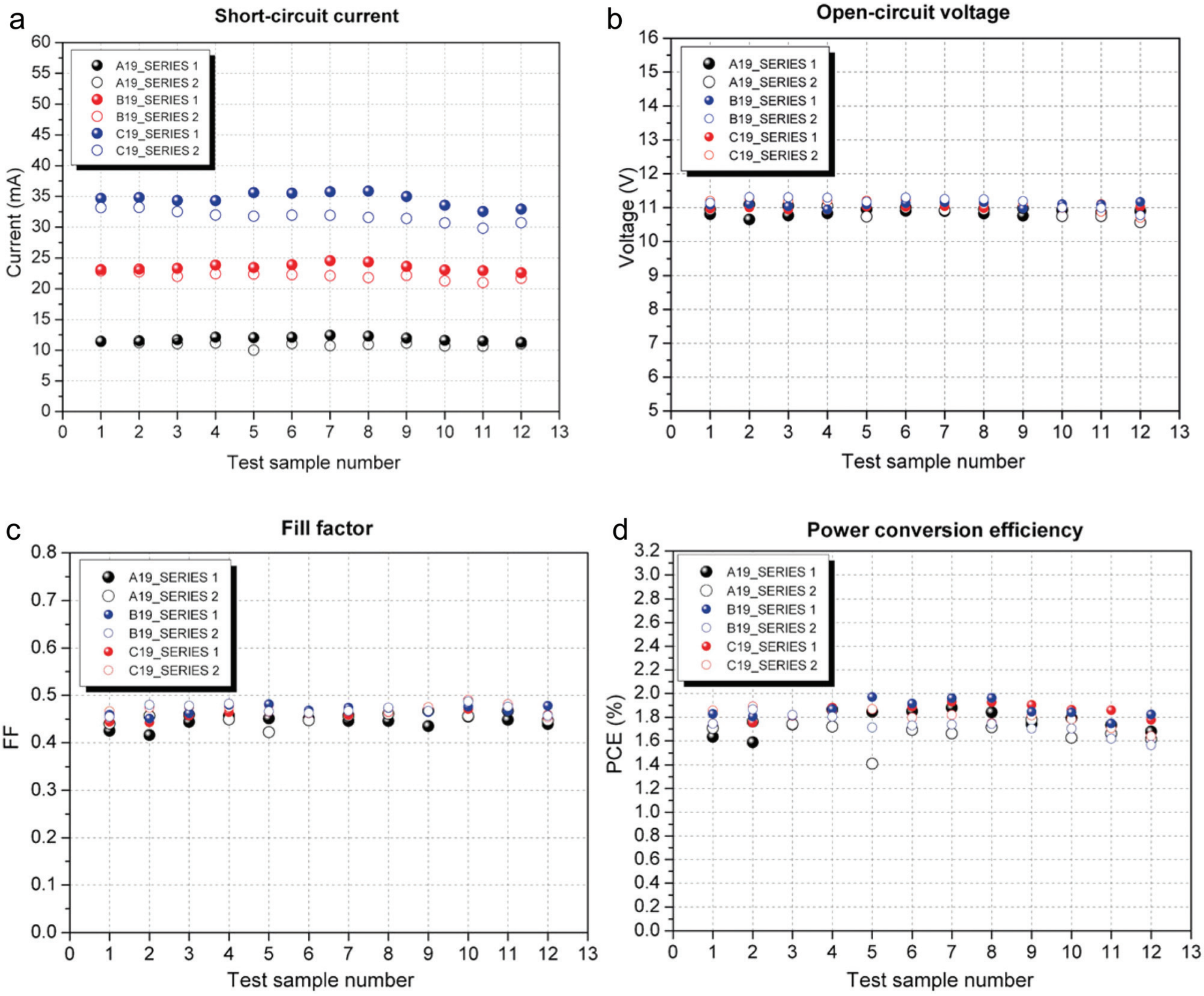

Fig. 9 (a) Short circuit current, (b) open-circuit voltage, (c) fill factor, and (d) power conversion efficiency of fully R2R-printed modules. Two test series of three different module sizes (A19 = 32.2 cm^2, B19 = 64.4 cm^2 and C19 = 96.5 cm^2) are depicted as a function of the test sample number. The parameters for the repeat lengths of 8–19 (series 1) are shown with filled circles and the repeat lengths of 38–49 (series 2) with open circles.

Table 1 Mean electrical parameters for three different module sizes (A19 = 32.2 cm^2, B19 = 64.4 cm^2, and C19 = 96.5 cm^2). The mean value is calculated as an average of both test series shown in Fig. 6. J_{sc} per cell is calculated by dividing the short circuit current by the area of one cell in the module structure

Module area	Yield	Mean I_{sc} [mA]	Mean J_{sc} per cell [mA cm^{-2}]	Mean V_{oc} [V]	Mean V_{oc} per cell [V]	Mean P_{mpp} [mW]	Mean FF	Mean PCE [%]	Max PCE [%]
32.2 cm^2 (A19)	100% (24/24)	11.39 (±0.59)	6.72	10.87 (±0.13)	0.57	55.40 (±3.40)	0.45 (±0.01)	1.72 (±0.11)	1.88
64.4 cm^2 (B19)	100% (24/24)	22.80 (±0.92)	6.73	11.06 (±0.13)	0.58	117.59 (±4.61)	0.47 (±0.01)	1.83 (±0.07)	1.93
96.5 cm^2 (C19)	100% (24/24)	33.16 (±1.78)	6.53	11.13 (±0.13)	0.59	173.44 (±9.88)	0.47 (±0.01)	1.80 (±0.10)	1.97

the short circuit current by the area of one cell in the module structure.

If the registration was aligned as in the design, the width of the cell in all 19 cell module sizes should be 3.4 mm. The gap between the ITO patterns was 2.0 mm. Based on the design, the length of the cells with A19 was 50 mm, B19 100 mm, and C19 150 mm. The mean PCE remained at a rather constant level during processing, from 1.7% to 1.8% (Table 1). This implies that a uniform print quality of the different layers is maintained through the run. Because all the modules taken to the test series functioned properly, there were no detrimental processing defects that could be detected such as shorted cells. The V_{oc} of the modules ranged from 10.9 V to 11.1 V. The number of cells in a series connection was the same in all module sizes investigated, so the V_{oc} should not vary. The short circuit current is directly proportional to the active area. The B19 module had double the length of A19 and a two-fold greater mean short circuit current value. With the largest module size, C19, the values were similar although the mean short circuit current was 3% lower (compared to A19 with a three-fold higher value).

3. Conclusions

R2R-printed inverted OPV modules were fabricated with gravure printing and rotary screen printing processes which allow 2D patterning. The rheological properties of the inks and their relationship with printability, the compatibility of the silver paste with the device, and the process limits were examined to define the parameters for each process step. R2R processing produced a large amount of information as the morphology of the R2R-printed layers, the cross machine accuracy of the printed pattern and registration, the repeatability of the R2R fabrication process, and the influence of registration on the module performance were studied. As an outcome, we fabricated R2R-printed OPV modules with an active area up to 96.5 cm^2 in size achieving good surface properties of the printed layers, good process control, and a mean power conversion efficiency of 1.8% with uniform quality. To the best of our knowledge, this is the first report of printed OPV modules using the R2R gravure and screen printing processes, and the data presented here increase our understanding in terms of processing and patterning of OPV structures as the module layout is changed into arbitrary shapes and sizes.

4. Experimental

The printed OPV modules were constructed on top of ITO-coated PET rolls purchased from Solutia/Eastman (40–60 Ω sq^{-1}). The PET and ITO thicknesses were 125 μm and 0.125 μm, respectively. As a first process step, the ITO was patterned with Isishape HiperEtch 09S Type 40 paste (Merck) as a negative image to the desired pattern. R2R rotary screen printing was performed with a printing speed of 1.1 m min^{-1}. After printing, the printed film continued directly into the R2R hot air drying units set to a temperature of 140 °C for 218 s. The paste was washed off in baths of water and 2-propanol. After patterning, the surface was ultrasonically washed and dried in the R2R process. ZnO nanoparticle suspension in ethanol (Nanograde, Switzerland) was used for the electron transport layer. The ZnO layer was R2R gravure-printed and dried at 140 °C for 30 s (hot air drying). The details of the R2R gravure printing of ZnO are presented in a separate article by Vilkman *et al.*[55] Regioregular P3HT (#4002-E, Rieke Metals) was used as the donor, and PCBM [C60] (purity 99.5%, Nano-C) as the acceptor in the photoactive blend. Both were received as solid materials and dissolved in 1,2-dichlorobenzene to obtain a total concentration of 0.13 g ml^{-1}. In addition, the photoactive layer was deposited by R2R gravure printing. The printing speed was 8 m min^{-1} and the applied nip pressure was 1 bar. The printing cylinder contained engravings with a line density of 120 lines cm^{-1}. Highly viscous PEDOT:PSS (Agfa, EL-P 5015) was R2R rotary screen-printed. Preliminary tests were performed using GV screen with 200 L mesh from Gallus and rotaplate screens 215 V and 305 V from Stork. Fabrication of the modules was achieved with a Stork rotaplate 215 V screen. The printing speed was 2 m min^{-1}. The hot air drying units were set to 130 °C with a total drying time of 120 s. Compatibility of the silver paste was tested using four thermally curable pastes: PV 410 and PV 414 from DuPont and, XCMS-015 and XPVS-670 from Spraylat with a flat-bed screen printer on the laboratory scale. XPVS-670 heat curable silver paste was chosen as the hole contact in the inverted module configuration. R2R rotary screen printing was performed with a 275 L steel mesh screen (RVS) from Gallus. The printing speed was 2 m min^{-1}. The drying temperature was 130 °C with a total drying time of 120 s.

4.1 Characterization

The rheology of the PEDOT:PSS and P3HT:PCBM inks was measured using an MCR-301 rheometer (Anton Paar). The alignment and dimensions of the printed layers were measured using a Smartscope OGP-250 microscope, and the layer thicknesses were measured using a Dektak profilometer (Veeco). The surface morphologies of the P3HT:PCBM, PEDOT:PSS, and silver were measured using a Veeco Dimension 3100 in tapping mode. A high quality silicon tip with a radius less than 10 nm was used to probe the sample surfaces. After R2R processing, the non-encapsulated modules were transferred to a glove box for current–voltage measurements. The modules did not undergo any light soaking or thermal treatment after R2R processing prior to electrical characterization. The current–voltage characteristics under illumination were measured with a solar simulator (Atlas Solar Cell Test 1200) calibrated to 100 mW cm^{-2} using a calibrated Si-reference cell filtered with a KG5 filter. The active area was defined by the overlap of ITO bottom and Ag top electrodes.

References

1 C. W. Tang, *Appl. Phys. Lett.*, 1986, **48**, 183.
2 G. A. Chamberlain, *Sol. Cells*, 1983, **8**, 47.
3 M. C. Scharber, D. Mühlbacher, M. Koppe, P. Denk, C. Waldauf, A. J. Heeger and C. J. Brabec, *Adv. Mater.*, 2006, **18**, 789.
4 J. You, L. Dou, K. Yoshimura, T. Kato, K. Ohya, T. Moriarty, K. Emery, C. C. Chen, J. Gao, G. Li and Y. Yang, *Nat. Commun.*, 2013, **4**, 1446.

5 N. Espinosa, R. García-Valverde, A. Urbina, F. Lenzmann, M. Manceau, D. Angmo and F. C. Krebs, *Sol. Energy Mater. Sol. Cells*, 2012, **97**, 3.

6 N. Espinosa, R. Garcia-Valverde, A. Urbina and F. C. Krebs, *Sol. Energy Mater. Sol. Cells*, 2011, **95**, 1293.

7 N. Espinosa, R. García-Valverde and F. C. Krebs, *Energy Environ. Sci.*, 2011, **4**, 1547.

8 M. Jørgensen, J. E. Carlé, R. R. Søndergaard, M. Lauritzen, N. A. Dagnæs-Hansen, S. L. Byskov, T. R. Andersen, T. T. Larsen-Olsen, A. P. L. Böttiger, B. Andreasen, L. Fu, L. Zuo, Y. Liu, E. Bundgaard, X. Zhan, H. Chen and F. C. Krebs, *Sol. Energy Mater. Sol. Cells*, 2013, **119**, 84.

9 R. R. Søndergaard, M. Hösel and F. C. Krebs, *J. Polym. Sci., Part B: Polym. Phys.*, 2013, **51**, 16.

10 S. Dongaonkar, S. Loser, E. J. Sheets, K. Zaunbrecher, R. Agrawal, T. J. Marks and M. A. Alam, *Energy Environ. Sci.*, 2013, **6**, 782.

11 R. Po, A. Bernardi, A. Calabrese, C. Carbonera, G. Corso and A. Pellegrino, *Energy Environ. Sci.*, 2014, **7**, 925.

12 S. B. Darling and F. You, *RSC Adv.*, 2013, **3**, 17633.

13 F. C. Krebs and M. Jørgensen, *Sol. Energy Mater. Sol. Cells*, 2013, **119**, 73.

14 T. P. Osedach, T. L. Andrew and V. Bulovic, *Energy Environ. Sci.*, 2013, **6**, 711.

15 R. Po, G. Bianchi, C. Carbonera and A. Pellegrino, *Macromolecules*, 2015, **48**, 453.

16 W. Chen, T. Xu, F. He, W. Wang, C. Wang, J. Strzalka, Y. Liu, J. Wen, D. J. Miller, J. Chen, K. Hong, L. Yu and S. B. Darling, *Nano Lett.*, 2011, **11**, 3707.

17 B. A. Collins, J. R. Tumbleston and H. Ade, *J. Phys. Chem. Lett*, 2011, **2**, 3135.

18 C. Koidis, S. Logothetidis, A. Ioakeimidis, A. Laskarakis and C. Kapnopoulos, *Org. Electron.*, 2013, **14**, 1744.

19 C. Koidis, S. Logothetidis, S. Kassavetis, C. Kapnopoulos, P. G. Karagiannidis, D. Georgiou and A. Laskarakis, *Sol. Energy Mater. Sol. Cells*, 2013, **112**, 36.

20 W.-H. Baek, H. Yang, T.-S. Yoon, C. J. Kang, H. H. Lee and Y.-S. Kim Sol, *Energy Mater. Sol. Cells*, 2009, **93**, 1263.

21 R. Søndergaard, M. Hösel, D. Angmo, T. T. Larsen-Olsen and F. C. Krebs, *Mater. Today*, 2012, **15**, 36.

22 L. Blankenburg, K. Schultheis, H. Schache, S. Sensfuss and M. Schrödner, *Sol. Energy Mater. Sol. Cells*, 2009, **93**, 476.

23 F. C. Krebs, S. A. Gevorgyan and J. Alstrup, *J. Mater. Chem.*, 2009, **19**, 5442.

24 F. C. Krebs, T. Tromholt and M. Jorgensen, *Nanoscale*, 2010, **2**, 873.

25 F. C. Krebs, J. Fyenbo and M. Jorgensen, *J. Mater. Chem.*, 2010, **20**, 8994.

26 Y. Galagan, I. G. de Vries, A. P. Langen, R. Andriessen, W. J. H. Verhees, S. C. Veenstra and J. M. Kroon, *Chem. Eng. Process. Process Intensif.*, 2011, **50**, 454.

27 D. Angmo, S. A. Gevorgyan, T. T. Larsen-Olsen, R. R. Søndergaard, M. Hösel, M. Jørgensen, R. Gupta, G. U. Kulkarni and F. C. Krebs, *Org. Electron.*, 2013, **14**, 984.

28 M. Hösel, R. R. Søndergaard, M. Jørgensen and F. C. Krebs, *Energy Technol.*, 2013, **1**, 102.

29 F. C. Krebs, M. Hösel, M. Corazza, B. Roth, M. V. Madsen, S. A. Gevorgyan, R. R. Søndergaard, D. Karg and M. Jørgensen, *Energy Technol.*, 2013, **1**, 378.

30 F. C. Krebs, N. Espinosa, M. Hösel, R. R. Søndergaard and M. Jørgensen, *Adv. Mater.*, 2014, **26**, 29.

31 P. Sommer-Larsen, M. Jørgensen, R. R. Søndergaard, M. Hösel and F. C. Krebs, *Energy Technol.*, 2013, **1**, 15.

32 T. R. Andersen, H. F. Dam, M. Hösel, M. Helgesen, J. E. Carlé, T. T. Larsen-Olsen, S. A. Gevorgyan, J. W. Andreasen, J. Adams, N. Li, F. Machui, G. D. Spyropoulos, T. Ameri, N. Lemaître, M. Legros, A. Scheel, D. Gaiser, K. Kreul, S. Berny, O. R. Lozman, S. Nordman, M. Välimäki, M. Vilkman, R. R. Søndergaard, M. Jørgensen, C. J. Brabec and F. C. Krebs, *Energy Environ. Sci.*, 2014, **7**, 2925.

33 D. Angmo, J. Sweelssen, R. Andriessen, Y. Galagan and F. C. Krebs, *Adv. Energy Mater.*, 2013, **3**, 1230.

34 Y. Galagan, E. W. C. Coenen, B. Zimmermann, L. H. Slooff, W. J. H. Verhees, S. C. Veenstra, J. M. Kroon, M. Jørgensen, F. C. Krebs and R. Andriessen, *Adv. Energy Mater.*, 2014, **4**, 13.00498.

35 T. M. Eggenhuisen, Y. Galagan, A. F. K. V. Biezemans, T. M. W. L. Slaats, W. P. Voorthuijzen, S. Kommeren, S. Shanmugam, J. P. Teunissen, A. Hadipour, W. J. H. Verhees, S. C. Veenstra, M. J. J. Coenen, J. Gilot, R. Andriessen and W. A. Groen, *J. Mater. Chem. A*, 2015, **3**, 7255.

36 J. M. Ding, A. de la Fuente Vornbrock, C. Ting and V. Subramanian, *Sol. Energy Mater. Sol. Cells*, 2009, **93**, 459.

37 P. Kopola, T. Aernouts, S. Guillerez, H. Jin, M. Tuomikoski, A. Maaninen and J. Hast, *Sol. Energy Mater. Sol. Cells*, 2010, **94**, 1673.

38 P. Kopola, T. Aernouts, R. Sliz, S. Guillerez, M. Ylikunnari, D. Cheyns, M. Välimäki, M. Tuomikoski, J. Hast, G. Jabbour, R. Myllylä and A. Maaninen, *Sol. Energy Mater. Sol. Cells*, 2011, **95**, 1344.

39 M. M. Voigt, R. C. I. Mackenzie, C. P. Yau, P. Atienzar, J. Dane, P. E. Keivanidis, D. D. C. Bradley and J. Nelson, *Sol. Energy Mater. Sol. Cells*, 2011, **95**, 731.

40 M. M. Voigt, R. C. I. Mackenzie, S. P. King, C. P. Yau, P. Atienzar, J. Dane, P. E. Keivanidis, I. Zadrazil, D. D. C. Bradley and J. Nelson Sol, *Energy Mater. Sol. Cells*, 2012, **105**, 77.

41 J. Yang, D. Vak, N. Clark, J. Subbiah, W. W. H. Wong, D. J. Jones, S. E. Watkins and G. Wilson, *Sol. Energy Mater. Sol. Cells*, 2013, **109**, 47.

42 P. Apilo, J. Hiltunen, M. Välimäki, S. Heinilehto, R. Sliz and J. Hast, *Prog. Photovoltaics*, 2014, DOI: 10.1002/pip.2508.

43 A. Hübler, B. Trnovec, T. Zillger, M. Ali, N. Wetzold, M. Mingebach, A. Wagenpfahl, C. Deibel and V. Dyakonov, *Adv. Energy Mater.*, 2011, **1**, 1018.

44 R. Po, C. Carbonera, A. Bernardi, F. Tinti and N. Camaioni, *Sol. Energy Mater. Sol. Cells*, 2012, **100**, 97.

45 D. S. Hecht, L. Hu and G. Irvin, *Adv. Mater*, 2011, **23**, 1482.

46 T. R. Andersen, H. F. Dam, B. Andreasen, M. Hösel, M. V. Madsen, S. A. Gevorgyan, R. R. Søndergaard, M. Jørgensen and F. C. Krebs, *Sol. Energy Mater. Sol. Cells*, 2014, **120**, 735.

47 Y. Galagan, E. W. C. Coenen, S. Sabik, H. H. Gorter, M. Barink, S. C. Veenstra, J. M. Kroon, R. Andriessen and P. W. M. Blom, *Sol. Energy Mater. Sol. Cells*, 2012, **104**, 32.

48 J.-S. Yu, I. Kim, J.-S. Kim, J. Jo, T. T. Larsen-Olsen, R. R. Søndergaard, M. Hösel, D. Angmo, M. Jørgensen and F. C. Krebs, *Nanoscale*, 2012, **4**, 6032.

49 P. Kopola, B. Zimmermann, A. Filipovic, H.-F. Schleiermacher, J. Greulich, S. Rousu, J. Hast, R. Myllylä and U. Würfel, *Sol. Energy Mater. Sol. Cells*, 2012, **107**, 252.

50 H. J. van de Wiel, Y. Galagan, T. J. van Lammeren, J. F. J. de Riet, J. Gilot, M. G. M. Nagelkerke, R. H. C. A. T. Lelieveld, S. Shanmugam, A. Pagudala, D. Hui and W. A. Groen, *Nanotechnology*, 2013, **24**, 484014.

51 D. Kaduwal, H.-F. Schleiermacher, J. Schulz-Gericke, T. Kroyer, B. Zimmermann and U. Würfel, *Sol. Energy Mater. Sol. Cells*, 2014, **124**, 92.

52 G. A. dos Reis Benatto, B. Roth, M. V. Madsen, M. Hösel, R. R. Søndergaard, M. Jørgensen and F. C. Krebs, *Adv. Energy Mater.*, 2014, **4**, 1400732.

53 F. Guo, N. Li, V. V. Radmilović, V. R. Radmilović, M. Turbiez, E. Spiecker, K. Forberich and C. J. Brabec, *Energy Environ. Sci.*, 2015, DOI: 10.1039/c5ee00184f.

54 M. Ylikunnari, J. Hiitola-Keinänen, E. Jansson and S. Rousu, *Proc. of LOPE-C Conf. Roll-to-roll patterning of electrodes*, Munich, Germany, (6, 2012).

55 M. Vilkman, P. Apilo, M. Välimäki, M. Ylikunnari, A. Bernardi, R. Po, G. Corso and J. Hast, *Energy Technol.*, 2015, **3**, 407.

56 R. Kitsomboonloha, S. J. S. Morris, X. Rong and V. Subramanian, *Langmuir*, 2012, **28**, 16711.

57 F. C. Krebs, *Sol. Energy Mater. Sol. Cells*, 2009, **93**, 465.

58 F. J. Lim, K. Ananthanarayanan, J. Luther and G. W. Ho, *J. Mater. Chem.*, 2012, **22**, 25057.

59 S.-A. Gopalan, M.-H. Seo, G. Anantha-Iyengar, B. Han, S.-W. Lee, D.-H. Kwon, S.-H. Lee and S.-W. Kang, *J. Mater. Chem. A*, 2014, **2**, 2174.

60 F. C. Krebs, *Org. Electron.*, 2009, **10**, 761.

ARTICLE V

Aerosol jet printed grid for ITO-free inverted organic solar cells

Solar Energy Materials & Solar Cells 107:252–258.

Solar Energy Materials & Solar Cells 107 (2012) 252–258

Contents lists available at SciVerse ScienceDirect

Solar Energy Materials & Solar Cells

journal homepage: www.elsevier.com/locate/solmat

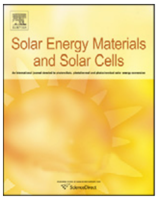

Aerosol jet printed grid for ITO-free inverted organic solar cells

Pälvi Kopola [a,b,*], Birger Zimmermann [a], Aleksander Filipovic [a], Hans-Frieder Schleiermacher [a], Johannes Greulich [a], Sanna Rousu [b], Jukka Hast [b], Risto Myllylä [c], Uli Würfel [a,d]

[a] Fraunhofer Institute for Solar Energy Systems (ISE), Heidenhofstr. 2, 79110 Freiburg, Germany
[b] VTT Technical Research Centre of Finland, Printed Functional Solutions, Kaitoväylä 1, FIN-90571 Oulu, Finland
[c] University of Oulu, Optoelectronics and Measurement Techniques Laboratory, P.O. BOX 4500, 90014 University of Oulu, Finland
[d] Freiburg Material Research Centre (FMF), Stefan-Meier-Str. 21, 79104 Freiburg, Germany

ARTICLE INFO

Article history:
Received 2 April 2012
Received in revised form
17 June 2012
Accepted 22 June 2012
Available online 20 July 2012

Keywords:
Organic solar cells
Aerosol jet printing
Indium tin oxide free
Current collecting grid
Inverted layer sequence

ABSTRACT

Aerosol jet printing is investigated as a new deposition method for a current collecting grid in indium tin oxide (ITO) free organic solar cells with an inverted layer sequence. In this device configuration, the ITO layer which usually serves as the hole contact is replaced by a transparent highly conductive poly(3,4-ethylenedioxythiophene):poly(styrenesulfonate) (PEDOT:PSS) layer in combination with a silver grid deposited by aerosol jet printing. Since the cells are illuminated from the grid side, the optimisation of the grid design is a trade-off between area coverage and conductivity of the grid lines. These factors have been controlled by the printing parameters such as chuck temperature, printing speed and the number of printing passes. In this paper, we demonstrate that continuous, conductive grid lines with a minimum line width of 58 μm can be processed on the top of the PEDOT:PSS layer. For single pass printing the area coverage varied from 5.8% to 11.9% with corresponding effective sheet resistances ranging from 8.9 Ω to 1.5 Ω. The ITO-free inverted devices with aerosol jet printed grid (an active area of 1.1 cm^2) show comparable performance to the cells with an evaporated gold grid. The effective sheet resistance can be further decreased by multiple printing passes without increasing the area coverage proportionally due to an improved aspect ratio. By increasing the conductivity and aspect ratio by multiple line printing, the cell length in the module structures can be significantly extended.

1. Introduction

Organic solar cells are an attractive complement for silicon solar cells converting solar energy to electricity due to their light weight and flexibility. Up to now the efficiency of silicon based solar cells is far ahead to the values obtained with organic solar cells. The utmost importance of organic solar cells is to use established printing and coating technologies [1–8] leading to cost-efficient production. One of the main cost driving factors is indium tin oxide (ITO) [9] which is conventionally used as a high work function transparent electrode in organic solar cells. Due to the high price and brittleness of ITO [10], solution-processed alternatives to replace the vacuum deposited ITO by other transparent conductive materials are investigated. Several approaches [11] including graphenes [12] and carbon nanotubes [13] have been developed in order to replace ITO. Also, highly conductive formulations of poly(3,4-ethylenedioxythiophene) poly(styrenesulfonate) (PEDOT:PSS) have been investigated [14]. To further decrease the resistive losses, which is essential in realising large area module structures, a metal grid can be applied. Using a metal grid in combination with a PEDOT:PSS layer in conventional organic solar cells leads to significantly reduced series resistance [15] compared to a pure PEDOT:PSS electrode. A rough optimisation of the metal grid dimensions in terms of line width and spacing considering the shadowing and resistive losses of PEDOT:PSS and grid was performed by Tvingstedt and co-workers [16]. Recently, a more detailed analysis was conducted by Galagan et al. [17]. Further progress was introduced by preparing the grid structure by inkjet printing [18]. Including a printed grid in a conventional structure is often problematic due to the fact that the thickness of the metal grid is usually in a micrometer range compared to the few hundred nanometers of the organic layers which have to be deposited on top of the metal grid. As a consequence, it is challenging to avoid shunting of the device. This problem can be circumvented in the inverted structure, because the silver grid is applied as last layer on top of all other layers. Therefore, the solvents and additives in the metal ink/paste should not harm or dissolve the underlying organic layers. To avoid possible short circuits due to mechanical damage a non-contact method is advantageous. Applying a metal grid to an inverted structure as a top electrode (hole contact) by using

---

[*] Corresponding author at: VTT Technical Research Centre of Finland, Printed Functional Solutions, Kaitoväylä 1, FIN-90571 Oulu, Finland.
Tel.: +358 20 7222046; fax: +358 20 7222320.
E-mail address: palvi.kopola@vtt.fi (P. Kopola).

0927-0248/$ - see front matter © 2012 Elsevier B.V. All rights reserved.
http://dx.doi.org/10.1016/j.solmat.2012.06.042

screen printing was already demonstrated in Ref. [19]. Recently, a solution processed silver nanowire top electrode for organic solar cells was published [20].

In this work, we implement aerosol jet printing as a new potential technique to deposit a fine line current collecting grid for ITO-free inverted solar cells. Aerosol jet printing is a non-contact printing method used successfully for the front side metallisation in silicon solar cells [21] and for active layer in polymer solar cells [22]. The work presented in this manuscript is based on the inverted cell configuration developed by Glatthaar et al [23]. In this setup the electron contact is processed first and the hole contact as the last layer. The hole contact is formed by a layer of highly conductive PEDOT:PSS in combination with an evaporated metal grid. A layer stack of chromium (Cr)/aluminium (Al)/chromium has been identified as a stable electron contact [24] for this cell architecture. Aerosol jet printing allows to use inks with large viscosity and particle size range [21] and thereby the ink properties are not tightly restricted as in ink jet printing. Also, the suitability of aerosol printing for producing narrow lines (50 μm) makes it an attractive alternative to other competitive methods such as screen printing. Here, the printed silver grid dimensions and conductivity have been controlled and optimised by the printing speed, chuck temperature and number of printing passes.

2. Experimental

The device structure of the ITO-free inverted organic solar cells studied in this work is shown in Fig. 1. As substrate 50 μm thick polyethylene terephthalate (PET) supplied by Mitsubishi Polyester Film GmbH Europe was used. The substrates were washed with 2-propanol, rinsed with deionised water, dried, attached to a glass carrier and placed in a vacuum overnight. Afterwards the electron contact of Cr (5 nm)/Al (100 nm)/Cr (5 nm) was deposited by evaporation through a shadow mask. The Cr layers were electron-beam evaporated and the Al layer thermally evaporated. Before the deposition of the photoactive layer the substrates were solvent pre-treated with ethanol. The photoactive blend solution consisted of poly(3-hexylthiophene) (P3HT, 4002-E) purchased from Rieke Metals Inc. and [6,6]-phenyl C_{61} butyric acid methyl ester ([60]PCBM, 99%) from Solenne BV which were dissolved in o-xylene with a mixing ratio of 1:0.7 by weight. The P3HT:PCBM solution was spin coated with a speed of 500 rpm for 360 s resulting in an active layer thickness of 160 nm. Before the deposition of PEDOT:PSS, solvent pre-treatment with 1-butanol was prepared. The PEDOT:PSS ink (CLEVIOS^{TM} F CPP 105 DM) supplied by H.C. Starck was spin coated with a speed of 2000 rpm for 60 s. The PEDOT:PSS and light absorbing layers were wiped outside the active area in order to clean the contact areas and to define the active area of 1.1 cm^2. The samples were annealed at 80 °C on a hotplate under nitrogen atmosphere for 15 min in order to remove the water from the PEDOT:PSS layer. Finally, the grid was either aerosol jet printed by using the fine particle silver ink CSD66 (Cabot) or for reference cells the gold grid was thermally evaporated. The grid design was composed of 22 lines with a line separation (center to center) of 1 mm. For aerosol jet printing, a Maskless Mesoscale Material Deposition (M3D) system from Optomec INC. was used. After grid preparation, the samples were thermally annealed on a hotplate under a nitrogen atmosphere at 120 °C for 10 min. The current density–voltage (JV) characteristics under illumination were measured with a solar simulator (Steuernagel SolarCelltest 575) calibrated to 100 mW cm^{-2} using a calibrated Si-reference cell filtered with a KG5 filter to reduce spectral mismatch and correcting the light intensity for the remaining spectral mismatch factor. The aerosol jet printed silver lines were characterised in terms of line width, height and profile with a LEXT OLS4000 Measuring Laser Confocal Microscope. The resistance of the silver lines on the top of a plain PET foil (RNK50) was measured with a multimeter using distances for the contact pins of 1 cm and 3 cm, respectively.

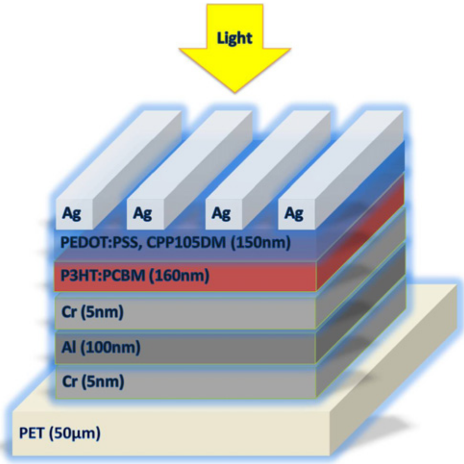

Fig. 1. Schematic illustration of the inverted solar cell structure investigated in this work. The samples are illuminated from the grid side.

3. Results and discussion

As the solar cells are illuminated from the grid side, the grid lines should cover as little area as possible to minimise the shadowing losses. However, by minimising the line width and generally also the line height, the resistive losses are increased. The optimisation of the grid design is a trade-off between shadowing losses and resistive losses. Printing parameters including printing speed, chuck temperature and number of printing passes were varied in order to optimise the grid dimensions. The chuck temperature is one of the adjustable parameters that strongly affects the uniformity of the printed line. In the preliminary printing tests prepared on top of PEDOT:PSS, different chuck temperatures ranging from 35 °C to 130 °C were examined. The chuck temperature is limited by the properties of the substrate material (PET). The results obtained with chuck temperature below 70 °C indicated that the drying of the ink is too slow leading to excessive spreading and possibly also dissolving partly the underlying PEDOT:PSS layer. The main solvent in the CSD66 aerosol jet printing ink is ethylene glycol, which has a boiling point of 197 °C. Hence, a higher chuck temperature is needed to accelerate the drying process and thus to avoid the spreading of the silver ink. Therefore, all the further experiments presented in this manuscript were carried out with higher chuck temperatures from 70 to 120 °C.

At first, single pass printing was examined. The parameter combinations in terms of chuck temperature and printing speed are shown in Table 1. The 3D microscope images of the single pass printed lines are shown in Fig. 2.

These microscope images clearly illustrate that the printing speed strongly influences the quality of the aerosol printed silver lines. With the lowest tested printing speed, 5 mm s^{-1}, these uniform conductive lines have expanded areas in random intervals as shown in Fig. 2(b). This implies that silver ink is accumulated in certain intervals forming up to 100 μm wider and thicker areas. This can also be observed from Table 2 in which the standard deviations of the line widths are presented. Increasing the printing speed to 10 mm s^{-1} leads to significant improvement in line uniformity. No expanded areas in the printed lines can be detected. The cross-sectional profiles of the single pass printed silver lines were measured and the profiles of individual measurements for each parameter combination are shown in Fig. 3. It can be seen that a higher chuck temperature leads to a slightly higher aspect ratio of

Table 1
Printing parameter combinations in terms of number of printing passes, chuck temperature and printing speed.

Number	Number of printing passes	Chuck temperature (°C)	Printing speed (mm s^{-1})
#1	1	70	5
#2	1	70	10
#3	1	70	20
#4	1	120	10
#5	2	70	10
#6	4	70	10

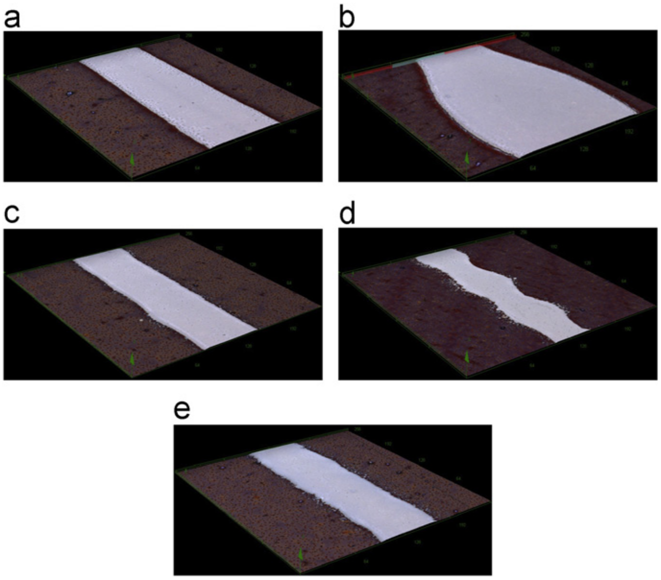

Fig. 2. 3D microscope images of aerosol jet printed lines with different printing parameter combinations in terms of chuck temperature and printing speed. The images were taken with a objective lens of 50 × magnification. (a) #1: 70 °C, 5 mm s^{-1}, (b) #1: 70 °C, 5 mm s^{-1} (expanded area), (c) #2: 70 °C, 10 mm s^{-1}, (e) #3: 70 °C, 20 mm s^{-1} and (e) #4: 120 °C, 10 mm s^{-1}.

Table 2
Mean cross-sectional area, line width, height, effective sheet resistance, resistivity and aspect ratio of the aerosol jet printed lines with different printing parameter combinations (numbers #1–#6). Standard deviation values are in brackets.

Number	Area (μm^2)	Width (μm)	Height (μm)	Effective sheet resistance (Ω)	Resistivity (Ω cm)	Aspect ratio
#1	228.0 (91.3)	119.3 (34.5)	1.6 (0.3)	1.5 (0.2)	3.4×10^{-5}	0.013
#2	75.9 (9.2)	76.6 (5.5)	1.0 (0.0)	3.2 (0.6)	2.4×10^{-5}	0.012
#3	43.8 (11.2)	58.1 (9.4)	0.8 (0.0)	8.9 (2.2)	3.9×10^{-5}	0.013
#4	70.3 (7.3)	70.0 (5.3)	1.2 (0.0)	3.0 (0.5)	2.1×10^{-5}	0.017
#5	142.2 (15.9)	93.8 (7.8)	1.7 (0.3)	1.7 (0.3)	2.5×10^{-5}	0.018
#6	307.1 (81.6)	111.8 (18.0)	3.7 (0.3)	0.7 (0.1)	2.0×10^{-5}	0.032

the silver line. With constant chuck temperature and varied printing speed, the change in the shape of the cross-sectional profile is unsubstantial. However, the printing speed affects the line width and height. Increasing the printing speed leads to narrower and thinner lines, as less material is deposited.

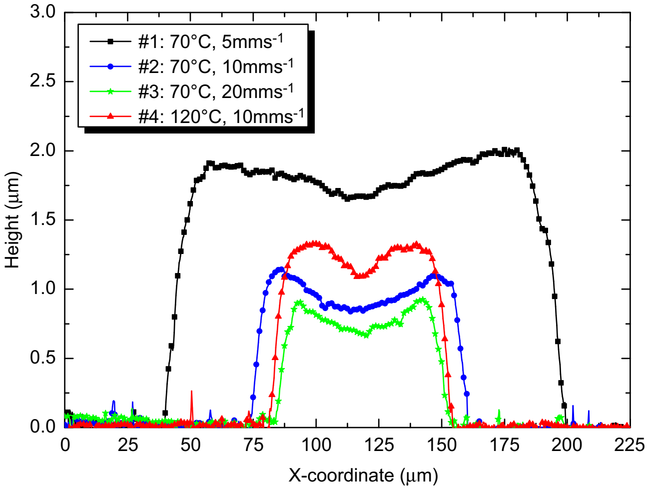

Fig. 3. Cross-sectional profiles of printed silver lines with different chuck temperatures (70 °C, 120 °C) and printing speeds 5 mm s^{-1} to 20 mm s^{-1}.

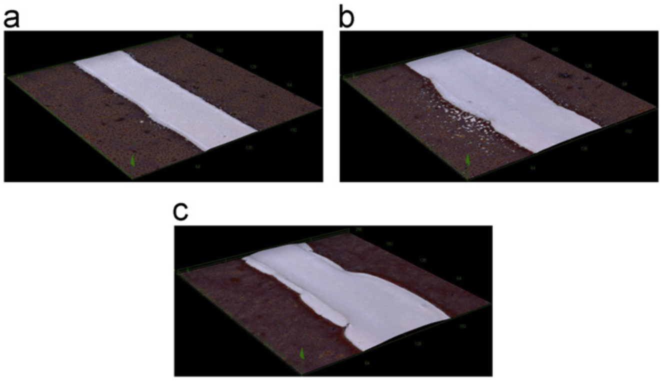

Fig. 4. 3D microscope images of aerosol jet printed lines by varying the number of printing passes. The images were taken with an objective lens of 50 × magnification. (a) #2: Single pass, 70 °C, 10 mm s^{-1}, (b) #5: Two passes, 70 °C, 10 mm s^{-1} and (c) #6: Four passes, 70 °C, 10 mm s^{-1}.

Additionally, in order to increase the conductivity of the silver lines, multiple pass printing was investigated (two to four printing passes). The 3D microscope images are shown in Fig. 4 and the corresponding cross-sectional profiles of individual measurements in Fig. 5. The line height increased linearly as a function of the number of printing passes and also the line width increased from the one-pass value, as could be expected. In comparison to single pass printing, there is a deterioration in uniformity as the thickness varies along the line. As the number of printing passes is increased, this effect becomes more pronounced.

As the conductivity of a silver line is proportional to the deposited mass and the latter is proportional to the cross-sectional area, the cross-sectional profiles were integrated. The mean and standard deviations of the integrated area, line width, height, effective sheet resistance, resistivity and aspect ratio are summarised in Table 2. The measurements have been prepared from 12 separate measurement points for each parameter combination. The widened edges in the two pass and four pass printed lines were considered. The scattered single dots were not included since they cover a negligible area of the surface. The effective sheet resistance was determined from the line resistance for a length of 1 cm by calculating the parallel circuitry of the respective number of lines per centimetre. The specific resistivity was calculated by multiplying the line resistance with the cross-sectional area divided by the length of the line. The aspect ratio is the ratio between the line height and the line width. A higher aspect ratio is advantageous for

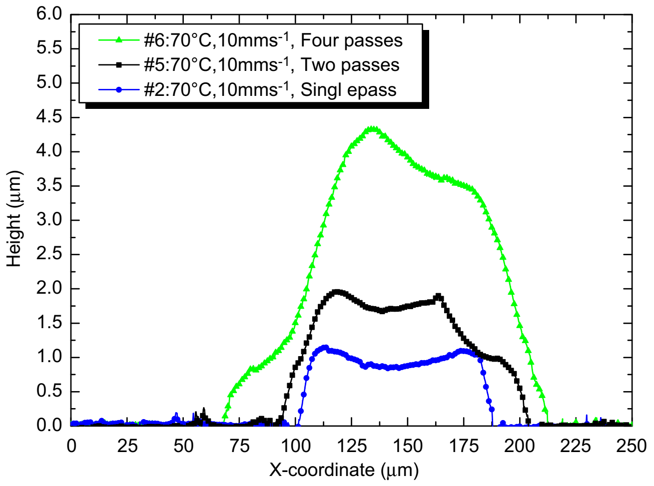

Fig. 5. Cross-sectional profiles of printed silver lines by varying the amount of printing passes (70 °C, 10 mm s^{-1}, 1–4 passes).

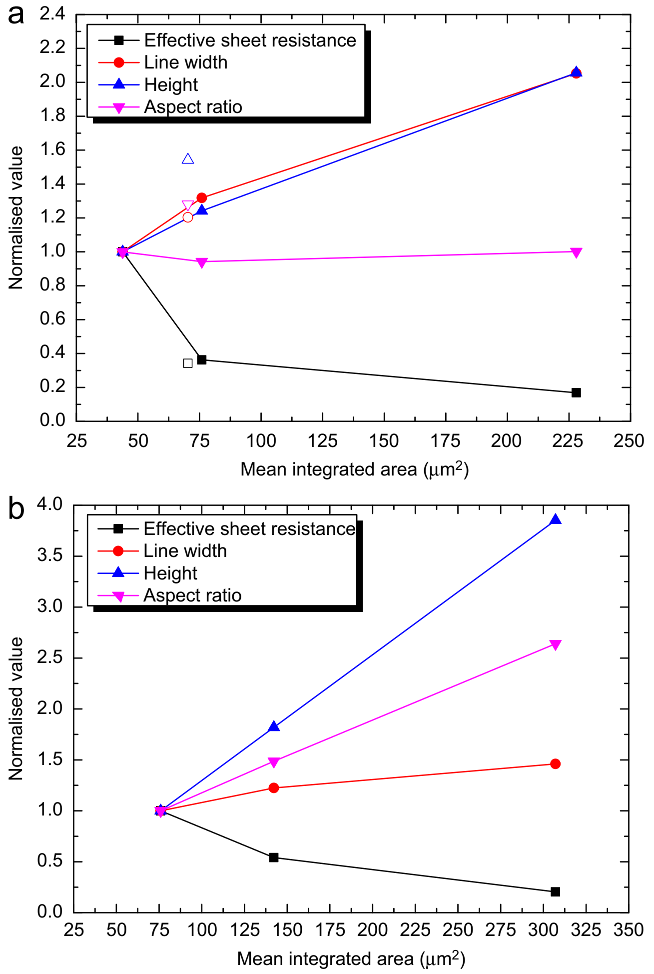

Fig. 6. Normalised effective sheet resistance, line width, height and aspect ratio as a function of the cross-sectional area which is a measure for the deposited mass. (a) Single pass printing, normalised to the values of the smallest cross-sectional area (#3). Filled symbols and lines refer to a chuck temperature of 70 °C and open symbols to 120 °C. (b) Multiple pass printing, normalised to the smallest cross-sectional area (#2, one pass printing).

electrical performance. Additionally, the normalised values of effective sheet resistance, line width, height and aspect ratio as a function of the mean cross-sectional area are depicted in Fig. 6. The values are normalised to the value of the line where the least mass was deposited which means that in Fig. 6(a) the values are normalized to #3 (70 °C, 20 mm s^{-1}) and in Fig. 6(b) to #2 (70 °C, 10 mm s^{-1}). In Fig. 6 the color filled symbols and lines refer to the values obtained with a chuck temperature of 70 °C and the open symbols to a chuck temperature of 120 °C, respectively. It is clearly visible from Table 2 and Fig. 6(a) that by increasing the printing speed in single line printing, the line height and width are decreased which correlates to a decreased deposited mass. This leads to an increase in effective sheet resistance. At a chuck temperature of 70 °C the relative increase in line width and height are equal leaving the aspect ratio unchanged. When the chuck temperature was increased to 120 °C the printed lines became thicker and slightly narrower which is depicted as open symbols in Fig. 6(a). This was due to the faster drying process of the ink. However, the amount of deposited mass remained similar compared to a chuck temperature of 70 °C. The corresponding graphs for multiple pass printed lines are shown in Fig. 6(b). It can be seen that two printing passes doubled the height of the silver line and four printing passes quadrupled it compared to a single pass printing process. The line width was slightly increased by increasing the number of printing passes. The aspect ratio was significantly improved. Correspondingly, the effective sheet resistance was decreased as a function of the number of printing passes without increasing the area coverage significantly. Fig. 7 shows a microscope image of three adjacent grid lines with a line separation of 1 mm. It can be seen that the lines which were printed with a chuck temperature of 70 °C and a printing speed of 10 mm s^{-1} can be well reproduced.

The summary of the performance parameters (J_{sc}, V_{oc}, FF, η) in terms of area coverage and electrical performance of the inverted ITO-free solar cells with the aerosol jet printed grid is provided in Table 3. The area coverage is the ratio of the area covered by the grid structure to the total designated area of the cell. In addition, the current density versus voltage characteristics of the inverted solar cells under illumination with different printing speeds are shown in Fig. 8(a) and varied number of printing passes in Fig. 8(b). The photovoltaic performance of the cells with aerosol jet printed grid were comparable with the cells comprising an evaporated gold grid. The largest variations in the electrical

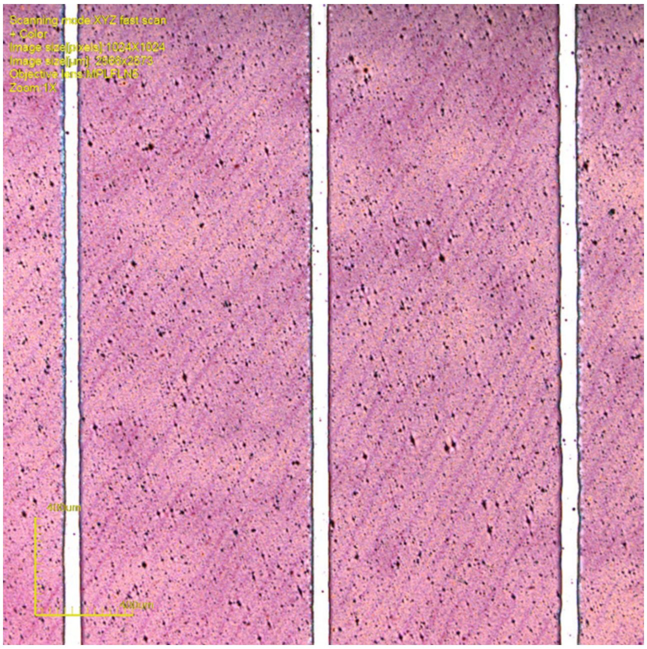

Fig. 7. Part of the grid structure in the inverted solar cells with a magnification of 5 × . In each cell, the grid is composed of 22 lines with a separation of 1 mm.

Table 3
Electrical performance of organic solar cells with aerosol jet printed grid by varying the printing parameters. Standard deviation values are in brackets.

Number	Area coverage (%)	J_{sc} (mA/cm^2)	V_{oc} (mV)	FF	η (%)
#1	11.9	7.3 (0.2)	602 (13)	0.50 (0.06)	2.18 (0.31)
#2	7.7	7.3 (0.1)	602 (3)	0.55 (0.01)	2.42 (0.04)
#3	5.8	7.7 (0.2)	606 (6)	0.56 (0.01)	2.60 (0.09)
#4	7.0	7.7 (0.1)	610 (1)	0.56 (0.01)	2.64 (0.06)
#5	9.4	7.0 (0.2)	599 (8)	0.54 (0.03)	2.27 (0.14)
#6	11.2	6.8 (0.0)	604 (4)	0.56 (0.01)	2.31 (0.06)
Reference	8.1	7.2 (0.1)	611 (5)	0.58 (0.01)	2.56 (0.12)

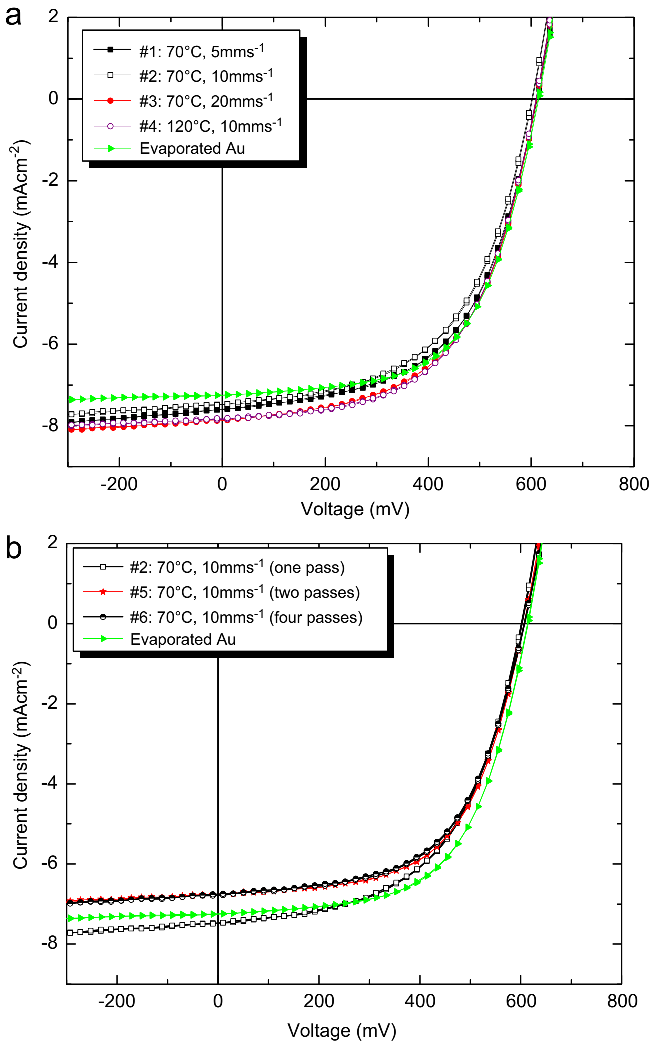

Fig. 8. Illuminated current density–voltage characteristics of inverted devices with aerosol jet printed metal grids (a) at varying printing speed and chuck temperature and (b) varying the number of printing passes.

parameters in terms of open-circuit voltage, fill factor and power conversion efficiency were detected with the printing speed of 5 mm s^{-1} and chuck temperature of 70 °C. As mentioned above, the highest variation in the line width was observed with a printing speed of 5 mm s^{-1}. The short-circuit current density was increased as the printing speed increased. This could be due to the reduced shadowing loss. The area coverage decreased from 11.9% to 5.8% as the printing speed increased from 5 mm s^{-1} to 20 mm s^{-1}. In addition, multiple pass printing was investigated in order to increase the conductivity of the printed silver lines by increasing the aspect ratio. This approach led to the lowest short-circuit current density of 7.0 mA cm^{-2} with two pass printed grid and 6.8 mA cm^{-2} with four pass printed grid. For a single cell structure, the difference in short-circuit current density was not significant when comparing single pass and multiple pass printed grid lines.

The experimental results for single cell structures carried out in this work were verified by simulations. The short-circuit current plotted as a function of area coverage in percentage is presented in Fig. 9. It should be emphasized that according to the simulations the area coverage is proportional to the loss in J_{sc}. However, with this cell design in which the active area is 1.1 cm^2, the maximum difference in short-circuit current with different grid dimensions is only 5%. The benefits of the multiple line printing with decreased effective sheet resistance and increased aspect ratio could not be observed with this specific design in which the active area is rather small. As a hypothesis, better conductivity should become more critical when the cell length would be extended in cell or module structures.

Simulations were performed in order to study the effect of the different grids (in terms of finger width and conductivity) on the cell and module performance. As input we used a numerical quasi-three dimensional model that accounts for the distributed character of the series resistance and allows for lateral variations of the junction voltage. At each point of the cell's surface the local $j(V)$ curve is modeled with the one-dimensional two-diode model (Eq. (1)) describing the z-direction.

$$j(V)=j_{01}\left(\exp\left[\frac{e_0V}{n_1k_BT}\right]-1\right)+j_{02}\left(\exp\left[\frac{e_0V}{n_2k_BT}\right]-1\right)+\frac{V}{R_p}-j_{SC}, \qquad (1)$$

in which e_0 is the elementary charge, k_B is Boltzmann's constant, n_1, n_2 represent the diode ideality factors, T is the temperature in Kelvin. The lateral variations of the junction voltage due to current through the PEDOT:PSS layer and the grid fingers are taken into account by numerically solving the relevant quasi-two-dimensional differential equations in the x- and y-direction with a 4th-order Runge–Kutta algorithm. Details can be found elsewhere [25,26]. The parameters used in the calculations were as follows: $j_{01}=10^{-6}$ mA cm^{-2}, $j_{02}=5\times10^{-4}$ mA cm^{-2}, $n_1=1.7$, $n_2=2.4$, $R_p=2000\ \Omega\ \text{cm}^2$ and $j_{sc}=10$ mA cm^{-2} and $T=300$ K. The values were chosen as they reproduce the PV parameters of a state-of-the-art P3HT:PCBM solar cell i.e. $V_{oc}=606$ mV, $J_{sc}=10$ mA cm^{-2}, FF=67.8% and PCE=4.1%.

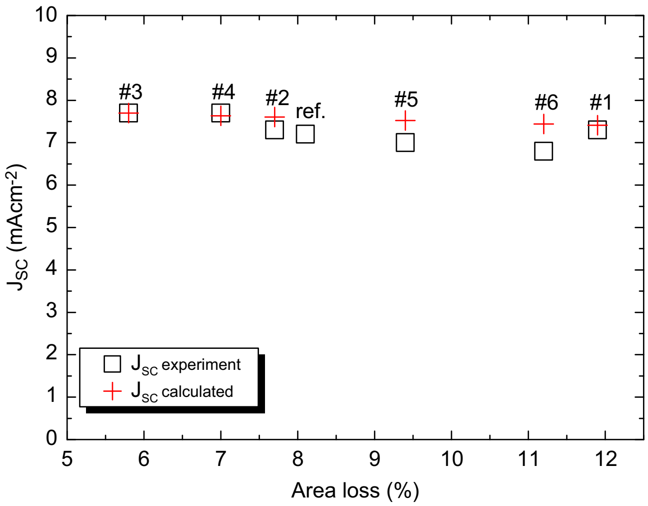

Fig. 9. Calculated vs. experimental data of the short circuit current density values with different area losses. For better comparison the calculated values are normalized to the experimental value of line #3.

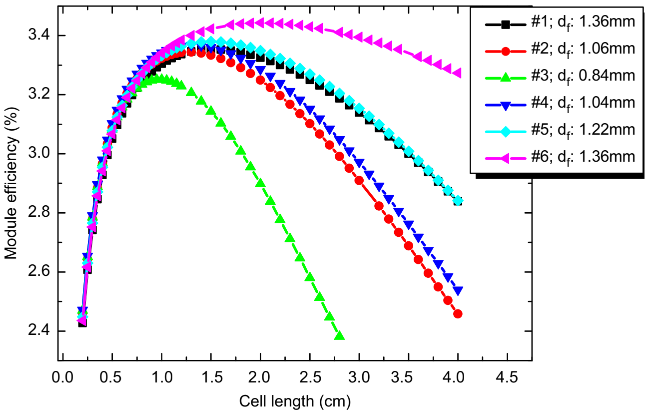

Fig. 10. Module efficiency vs. cell length for the different grid lines. For each line the individual optimum finger spacing d_f was used as indicated in the legend.

On the cell level we calculated the theoretical loss induced by the different grids for a fixed finger spacing of 1 mm. The model calculates explicitly the losses occurring due to the resistivity of both the PEDOT:PSS layer (which was assumed to have a sheet resistance of 1000 Ω) and the grid fingers as well as the shadowing effect of the grid. It should be noted that the differences for the calculated J_{sc} are smaller than the experimental scatter between different substrates. Nevertheless, the trend is reproduced as can be seen in Fig. 9.

Next, we determined the global optimum of the efficiency as a function of finger spacing and cell length for each grid parameter set. The curves in Fig. 10 show the efficiency of a module as a function of cell length when keeping the finger spacing constant at its value for the global optimum. A loss of 1 mm was taken into account for the series interconnection.

It can be clearly seen that an increased conductivity by multiple pass printing benefits the module efficiency as larger cell strips can be used, reducing the relative area loss due to the series circuitry. While on cell level line #3 allowed the highest efficiency due to the lowest shadowing, on module scale line #6 overcompensates the higher area loss with the increased conductivity. Furthermore it can be seen from Fig. 10 that for low conductivity lines the optimum finger distance at the global maximum is lower than for the high conductivity lines. This can be rationalised as by increasing the density of lines more metal is deposited, resulting in a lower effective resistivity of the parallel circuitry formed by the metal grid. This allows again larger cells strips and reduces the relative area loss due to the series circuitry which in this case (very narrow lines) overcompensates the additional area loss due to the higher number of grid fingers. This balance is a tradeoff between the area loss due to the parallel circuitry and the series circuitry, i.e. the ratio between the width of the grid lines (60 μm to 100 μm) and the width of the series circuitry (1 mm).

4. Conclusion

We have demonstrated the incorporation of aerosol jet printing technique into the fine line grid preparation (less than 60 μm) in organic solar cells. We have used an inverted configuration with a non-transparent electron contact and a partly transparent hole contact consisting of highly conductive PEDOT:PSS and a silver grid in which the illumination of the grid side is required. As the grid covers a part of the active layer, the grid properties in terms of dimensions and conductivity was shown to have a direct impact on the resistive and shadowing losses. Using a combination of solar cell experiments and simulations, it was verified that with a single cell structure (cell length 6 mm, total active area $1.1\,cm^2$), the highest current density and the best efficiency was reached with the narrowest and thinnest grid lines. The solar cells with a single pass printed grid showed a similar efficiency as the reference cells prepared with an evaporated Au grid. The results of the simulations revealed that the conductivity of the grid lines becomes critical when the cell length in the module structures was extended over 1.0 cm. The conductivity of the grid lines was increased by applying several printed lines on top of each other and hence increasing the aspect ratio and depositing more material. The results disclosed in this study let us conclude that aerosol jet printing is a versatile printing method which can be used for replacing the currently available methods, screen printing and ink jet printing, for applying the grid when targeting to finer grid lines and low material consumption. With screen printing, the properties of the screens limit the line width in the fine line grid preparation. The wide variety of the inks that can be printed with aerosol jet printing is a huge advantage over other printing technologies. Currently, the low printing speed of aerosol jet printing is a limiting factor for roll-to-roll processing and needs to be further increased by at least a factor of 10. These results can be extended in a number of applications in which the line width and conductivity of metal grid lines are critical factors.

Acknowledgements

P. K. appreciates the financial support by VTT Technical Research Centre of Finland. B. Z. would like to thank the European Comission under grant agreement number 248678 and U. W. expresses gratitude to the Federal Ministry of Education and Science (BMBF) under contract number 03SF0331.

References

[1] F.C. Krebs, Fabrication and processing of polymer solar cells: a review of printing and coating techniques, Solar Energy Materials and Solar Cells 93 (2009) 394–412.
[2] P. Kopola, T. Aernouts, R. Sliz, S. Guillerez, M. Ylikunnari, D. Cheyns, M. Välimäki, M. Tuomikoski, J. Hast, G. Jabbour, R. Myllylä, A. Maaninen, Gravure printed flexible organic photovoltaic modules, Solar Energy Materials and Solar Cells 95 (2011) 1344–1347.
[3] B. Zimmermann, H.-F. Schleiermacher, M. Niggemann, U. Würfel, ITO-free flexible inverted organic solar cell modules with high fill factor prepared by slot die coating, Solar Energy Materials and Solar Cells 95 (2011) 1587–1589.
[4] Y. Galagan, I. de Vries, A. Langen, R. Andriessen, W. Verhees, S. Veenstra, J. Kroon, Technology development for roll-to-roll production of organic photovoltaics, Chemical Engineering and Processing: Process Intensification 50 (2011) 454–461.
[5] C. Lungenschmied, G. Dennler, H. Neugebauer, S. Sariciftci, M. Glatthaar, T. Meyer, A. Meyer, Flexible, long-lived, large-area, organic solar cells, Solar Energy Materials and Solar Cells 91 (2007) 379–384.
[6] F. Krebs, M. Jørgensen, K. Norrman, O. Hagemann, J. Alstrup, T. Nielsen, J. Fyenbo, K. Larsen, J. Kristensen, A complete process for production of flexible large area polymer solar cells entirely using screen printing: first public demonstration, Solar Energy Materials and Solar Cells 93 (2009) 422–441.
[7] L. Blankenburg, K. Schultheis, H. Schache, S. Sensfuss, M. Schrödner, Reel-to-reel wet coating as an efficient up-scaling technique for the production of bulk-heterojunction polymer solar cells, Solar Energy Materials and Solar Cells 93 (2009) 476–483.
[8] P. Kopola, T. Aernouts, S. Guillerez, H. Jin, M. Tuomikoski, A. Maaninen, J. Hast, High efficient plastic solar cells fabricated with a high-throughput gravure printing method, Solar Energy Materials and Solar Cells 94 (2010) 1673–1680.
[9] C. Emmott, A. Urbina, J. Nelson, Environmental and economic assessment of ITO-free electrodes for organic solar cells, Solar Energy Materials and Solar Cells 97 (2012) 14–21.
[10] S. Park, Mechanical stability of externally deformed indium-tin-oxide films on polymer substrates, Japanese Journal of Applied Physics 42 (2003) 623–629.
[11] R. Po, C. Carbonera, A. Bernardi, F. Tinti, N. Camaioni, Polymer- and carbon-based electrodes for polymer solar cells: toward low-cost, continuous fabrication over large area, Solar Energy Materials and Solar Cells 100 (2012) 97–114.

[12] X. Wang, L. Zhi, N. Tsao, Z. Tomović, J. Li, K. Müllen, Transparent carbon films as electrodes in organic solar cells, Angewandte Chemie 120 (2008) 3032–3034.

[13] H. Ago, K. Petrisch, M. Shaffer, A. Windle, R. Friend, Composites of carbon nanotubes and conjugated polymers for photovoltaic devices, Advanced Materials 11 (1999) 1281–1285.

[14] S. Na, S.-S. Kim, J. Jo, D.-Y. Kim, Efficient and flexible ITO-free organic solar cells using highly conductive polymer anodes, Advanced Materials 20 (2008) 4061–4067.

[15] T. Aernouts, P. Vanlaeke, W. Geens, J. Poortmans, P. Heremans, S. Borghs, R. Mertens, R. Andriessen, L. Leenders, Printable anodes for flexible organic solar cell modules, Thin Solid Films 451-452 (2004) 22–25.

[16] K. Tvingstedt, O. Inganäs, Electrode grids for ITO-free organic photovoltaic devices, Advanced Materials 19 (2007) 2893–2897.

[17] Y. Galagan, B. Zimmermann, E. Coenen, M. Jørgensen, D. Tanenbaum, F. Krebs, H. Gorter, S. Sabik, L. Slooff, S. Veenstra, J. Kroon, R. Andriessen, Current collecting grids for ITO-free solar cells, Advanced Energy Materials 2 (2012) 103–110.

[18] Y. Galagan, J.-E. Rubingh, R. Andriessen, C.-C. Fan, P. Blom, S. Veenstra, J. Kroon, ITO-free flexible organic solar cells with printed current collecting grids, Solar Energy Materials and Solar Cells 95 (2011) 1339–1343.

[19] F.C. Krebs, Polymer solar cell modules prepared using roll-to-roll methods: knife-over-edge coating, slot-die coating and screen printing, Solar Energy Materials and Solar Cells 93 (2009) 465–475.

[20] W. Gaynor, J.-Y. Lee, P. Peumans, Fully solution-processed inverted polymer solar cells with laminated nanowire electrodes, ACS Nano 4 (2010) 30–34.

[21] A. Mette, P. Richter, M. Hörteis, S. Glunz, Metal aerosol jet printing for solar cell metallization, Progress in Photovoltaics: Research and Applications 15 (2007) 621–627.

[22] C. Yang, E. Zhou, S. Miyanishi, K. Hashimoto, K. Tajima, Preparation of active layers in polymer solar cells by aerosol jet printing, ACS Applied Materials and Interfaces 3 (2011) 4053–4058.

[23] M. Glatthaar, M. Niggemann, B. Zimmermann, P. Lewer, M. Riede, A. Hinsch, J. Luther, Organic solar cells using inverted layer sequence, Thin Solid Films 491 (2005) 298–300.

[24] B. Zimmermann, U. Würfel, M. Niggemann, Longterm stability of efficient inverted P3HT: PCBM solar cells, Solar Energy Materials and Solar Cells 93 (2009) 491–496.

[25] J. Greulich, M. Glatthaar, A. Krieg, G. Emanuel, S. Rein, JV characteristics of industrial silicon solar cells: influence of distributed series resistance and shockley read hall recombination, in: Proceedings of the 24th European Photovoltaic Solar Energy Conference, Hamburg, Germany, 2009, pp. 2065–2069.

[26] J. Greulich, M. Glatthaar, S. Rein, Fill factor analysis of solar cells current-voltage curves, Progress in Photovoltaics: Research and Applications 18 (2010) 511–515.

ARTICLE VI

Determining the photocurrent of individual cells within an organic solar module by LBIC and the filtering approach: Experiments and simulations

Solar Energy Materials & Solar Cells 134:157–164.

Solar Energy Materials & Solar Cells 134 (2015) 157–164

Contents lists available at ScienceDirect

Solar Energy Materials & Solar Cells

journal homepage: www.elsevier.com/locate/solmat

Determining the photocurrent of individual cells within an organic solar module by LBIC and the filtering approach: Experiments and simulations

Jens Reinhardt [a,b,*], Pälvi Apilo [c], Birger Zimmermann [a], Sanna Rousu [c], Uli Würfel [a,b]

[a] *Fraunhofer Institute for Solar Energy Systems, Heidenhofstr. 2, DE-79110 Freiburg, Germany*
[b] *Freiburger Materialforschungszentrum (FMF), Stefan-Meier-Str. 21, DE-79104 Freiburg, Germany*
[c] *VTT Technical Research Centre of Finland, Kaitoväylä 1, FIN-90571 Oulu, Finland*

ARTICLE INFO

Article history:
Received 5 September 2014
Received in revised form
10 November 2014
Accepted 15 November 2014

Keywords:
Organic solar cells
Imaging of modules
Photocurrent imaging
LBIC
DLIT
Parallel resistance
Shunts

ABSTRACT

Light beam induced current (LBIC) measurements of ITO-free organic photovoltaic modules with monolithic series connection are presented. Selective bias illumination is used to extract the light beam generated current from the module. A large variation of the photocurrent is observed among the cells which is unlikely to match the real generated photocurrent. In order to investigate this behavior, a novel approach (filtering approach) is presented in which the photocurrent of the measured cell is reduced while the remaining cells are kept under full illumination. This method enables the detection of the correct photocurrent of each cell and thus to identify the cell which limits the module current if all the cells comprise large parallel resistances. Dark lock-in thermography measurements of the module revealed several shunted cells. In this case the filtering approach overestimates the photocurrent. Numerical simulations of LBIC applied to modules using either selective bias illumination or forward bias voltage were carried out to understand the observed behavior in detail. The results reveal that a reliable detection of the photocurrent is impossible when several cells have rather low parallel resistances. Whereas for selective bias illumination the photocurrent response of the measured cell is an unambiguous function of the cell's parallel resistance this is not the case for an applied forward bias voltage.

1. Introduction

Organic photovoltaics (OPV), one of the emerging thin film PV technologies, has gained more and more interest in the last decade particularly due to the possibility for utilization of low cost production methods [1]. The intense research on high performance photoactive materials and novel device structures has led to power conversion efficiency exceeding 10% [2]. So far the record efficiencies were achieved with small-scale cells with apertures in the range of 1 cm^2. For solution-processed photoactive layers, these cells are typically processed by combining spin coating and vacuum deposition [3]. However, it was recently demonstrated that it is possible to achieve comparable results (9%) with small-scale (5 cm²) modules and single cells (10.2%) prepared in nitrogen atmosphere by using a roll-to-roll (R2R) compatible meniscus coating method [4]. On the other hand large-scale modules processed by R2R coating [1,5–9] and printing technologies [10] in air with commercial photoactive materials have shown substantially lower performances, leading to a strong discrepancy between the small-scale cell and large-scale module performances. In order to achieve comparable efficiencies several technological problems need to be investigated and resolved, e.g. shunts and non-uniformity in large area coated and printed films. Shunt prevention and detection is especially crucial for such ultra-thin solution-processed organic solar cells or light emitting diodes, since small dust particles or local dewetting can easily induce pinholes in layers with thicknesses in the order of 100 nm. Electro-optical imaging techniques such as e.g. dark lock-in thermography (DLIT), light beam induced current (LBIC), and electroluminescence (EL) have been demonstrated to be suitable characterization methods for detection of shunts, processing defects, inhomogeneity, and degradation studies in OPV structures [11–22].

Modules with cells connected in series have in general lower short-circuit currents than their individual cells. This originates from the fact that the cell with the lowest current limits the overall current of the module. Thus, comparable to series connected tandem solar cells where current matching is crucial for a good device performance, the cells in a module have to be current matched to avoid

---

[*] Corresponding author at: Fraunhofer Institute for Solar Energy Systems, Heidenhofstr. 2, DE-79110 Freiburg, Germany. Tel.: +49 7612034798.
E-mail address: jens.reinhardt@ise.fraunhofer.de (J. Reinhardt).

http://dx.doi.org/10.1016/j.solmat.2014.11.032

losses due to the series interconnection. Spatial characterization of the photocurrent generation can help to optimize the module efficiency. For single cells this is commonly done with LBIC [23]. The application of LBIC to modules is more complicated since the current of the particular cell, which is illuminated by the scanning light beam, will be blocked by the other cells of the module. This can be overcome by using bias light for all but the particular cell under investigation. This ensures that the cell illuminated with the light beam limits the current of the module.

The bias illumination method was used in the work presented here, whereas Krebs et al. [17] applied a forward bias voltage. However, in both cases the results seem not to reflect the photogenerated current. To clarify the origin of these doubtful experimental results we investigated the operating conditions of the measured cell and the remaining cells of the module during the LBIC experiment in more detail. To do so we introduce a filtering approach which gradually imitates the measurement conditions of LBIC. This leads to a much better understanding of the observed phenomena. Furthermore, numerical simulations were performed to investigate the filtering approach as well as LBIC measurements using both bias methods. Each of the series-interconnected cells of the module is represented by a one-diode model with series and parallel resistance, respectively. The relation between the obtained LBIC signal, the parasitic resistances, as well as the overall series resistance is analyzed in detail. A different approach was presented by Eisgruber and Sites [24]. They perform a frequency analysis (no lock-in amplification) of an LBIC signal by chopping the scanning light beam at different frequencies. This requires the capacity of each cell to be equal, however enables to distinguish shunt resistance from photocurrent variation. Recently, Krebs et al. presented an interesting method, in which the physical electrical connection to the contacts in a LBIC-measurement is replaced by contactless capacitive coupling [25], which may in the future enable in-line photocurrent and shunt detection.

2. Material and methods

The investigated ITO-free organic photovoltaic modules were fabricated on PET foils as described by Zimmermann et al [26]. The two-cell module used for investigation of the filtering process was fabricated by soldering two 1.1 cm² ITO-free P3HT:PCBM cells in a series connection. The cells itself were produced as published by Sapkota et al [27].

For DLIT an infrared (IR) camera with 320 × 256 pixels is used to detect the thermal radiation. The heat is introduced periodically by a square-wave pulsed voltage signal with the lock-in frequency (10 Hz). The voltage is applied to the modules in forward direction with maximum amplitude below 1 V per cell. The camera captures images with a sampling rate of 4 per lock-in period (40 Hz). The recorded lock-in signal is averaged over 3000 periods, for every pixel.

Electroluminescence imaging was conducted with a back-illuminated silicon CCD camera (1024 × 1024 pixels). Optical long-pass filters are used to filter light below 975 nm. High integration times of 20 min were necessary since only small currents (approx. 5 mA/cm^2) were used in the measurement process to avoid series resistance effects.

The light intensities in the filtering approach were reduced by 4 neutral density filter foils. The transparency of these foils was calibrated for their spectral mismatch with the used sun simulator.

LBIC mapping was performed using a commercially obtained setup (LOANA from pv-tools). The setup comprises laser beams with 6 different wavelengths; however only the data collected with the 532 nm laser were used. One cell is measured at a time, and the remaining cells are illuminated using OLED panels which are powered by a static DC source. The latter was necessary to avoid interference with the lock-in process. The resolution of the images is limited by the scanning laser spot which has approximately a diameter of 50 μm. With this resolution the scanning time was approximately 18 min cm^{-2}. This measurement time is unsuited for in-line measurements in roll-to-roll processing, however it could be greatly reduced by a factor of 6 by measuring with a single wavelength and further reduced by lowering the resolution either in one or both scanning dimensions.

3. Results and discussion

3.1. LBIC of organic solar modules

It is essential when applying LBIC to a module with cells connected in series that each but the measured cell is in forward bias conditions, otherwise the current generated by the light beam will be blocked by the remaining cells of the module. This is ensured in our case applying a bias illumination to all cells except the measured one. The investigated module has 11 equally sized cells connected in series, with a total active area of 12.1 cm^2. The specifications of the module were an open-circuit voltage of V_{OC}=5.1 V, a short-circuit current density of J_{SC}=7.7 mA cm^{-2}, a filling factor of FF=42%, and an efficiency of η=1.5% (active area). The module type is described in detail in Reference [26]. The V_{OC} of this particular module lacks roughly the voltage of 2–3 cells (each approximately 600 mV). The J_{SC} however is rather high and lacks only approximately 1–2 mA cm^{-2} compared to the short-circuit current density of a single cell. A common J_{SC} for this module type is in the range of 5–6 mA cm^{-2}.

The LBIC measurement system derives the external quantum efficiency (EQE) from the LBIC response signal. It is important to know that the system uses a modulated light beam with a weak intensity, and a lock-in amplifier to obtain the LBIC response signal. This makes sure that only the current generated by the light beam is recognized as the LBIC signal. Fig. 1(a) shows the EQE as derived from the LBIC response signal for a typical module. The values differ very strongly from cell to cell. These strong EQE variations among the individual cells were observed for all except the very best of the investigated modules. Large differences in morphology (and hence charge generation efficiency), charge carrier mobilities and absorption properties between individual cells can be ruled out as in our modules all individual cells are obviously processed together. Hence it appears very unlikely that

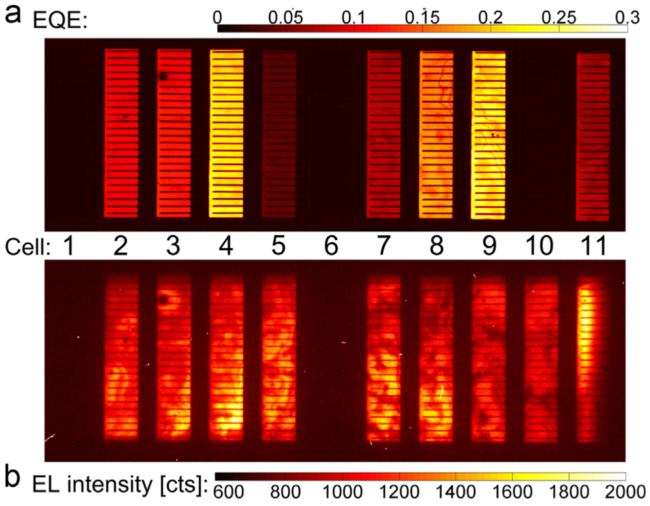

Fig. 1. (a) Spatially resolved external quantum efficiency of an organic solar cell module for an excitation wavelength of 532 nm. The image was assembled from 11 LBIC mappings with OLED bias-illumination and (b) electroluminescence measurement of the same module at low forward current densities.

the results shown in Fig. 1(a) represents the real photo-generated current in the individual cells in an accurate manner.

Additionally, an EL measurement was carried out to compare the EQE obtained by LBIC to the radiative recombination in the device. For EL a small forward current density ($4.7\ \mathrm{mA\ cm^{-2}}$) was used to minimize series resistance effects. The EL image in Fig. 1(b) shows some similar features inside the cell areas, as well as two inactive cells inside the module (cell numbers 1 and 6), which appear as well completely inactive in the LBIC results. However, no large variation between the single cell stripes or any correlation to the variation in the LBIC results can be recognized. For example cell 4 shows a relatively high EQE as well as an average EL intensity; whereas cell 9 shows the same EQE while having a lower EL signal, Cell 5 shows a very low EQE and an average EL emission, and Cell 9 and 10 differ strongly in the LBIC signal but are comparable in their EL response. A measurement artifact due to inhomogeneous bias illumination would be a possible explanation for this behavior, but since the setup uses the lock-in technique to obtain the LBIC signal this can be ruled out. In addition, the results published by Krebs et al. [17] are very similar – without the application of a bias illumination.

3.2. *The filtering approach*

LBIC was unable to measure conclusive data on the photocurrent distribution among the cells, therefore it was investigated whether the filtering approach is able to identify the current-limiting cell or measure the photocurrent of each cell. In contrast to LBIC the filtering approach does not spatially resolve the collected data. The idea of the filtering approach is that by reducing the photocurrent of one individual cell, the overall current of the module is reduced below the limiting cell current. Note that the module conditions are comparable to an LBIC measurement under bias illumination (with a low transmission filter), yet in contrast to LBIC this approach does not use lock-in amplification. While the photocurrent of one individual cell is reduced using a neutral density filter the remaining cells of the module are illuminated with approximately one sun intensity. A 'filtered module current' is measured, while keeping the module under external short-circuit conditions. The filtered current is determined by the photocurrent of the 'filtered solar cell', as long as the photocurrent of the latter is lower than the photocurrents of all the fully illuminated cells and as long as the parallel resistance R_P is infinitely large. If this is fulfilled all fully illuminated cells are then under forward bias conditions with $0 \leq V \leq V_{oc}$ and the filtered cell is under negative bias (with $V_i = -\sum_{j \neq i} V_j$, with i being the measured cell and $j \neq i$ all other cells of the module) as the whole module is still kept at 0 V. It is important to note that if a certain cell has a finite parallel resistance, i.e. $1/R_P > 0$, this negative voltage causes a leakage current which is given by $I = V/R_P$. This leads to an overestimation of the photocurrent of the filtered cell. Therefore the filtering approach will only deliver reliable results if the investigated cell shows a good blocking behavior, i.e. has a reasonable high parallel resistance and no reduced photocurrent due to poor charge carrier transport properties, i.e., very low mobilities (present e.g. in Ref. [28]). In order to still derive useful information despite possible low parallel resistances of certain cells, several filters with varying transmission values need to be used. Due to the variation of the limiting current the fully illuminated cells generate different bias voltage levels for the filtered cell. This additional information is then used to assess the reverse blocking behavior of the filtered cell. The filtering experiment was conducted with the same module as already shown in Fig. 1, thus a direct comparison with the results of the LBIC measurement can be drawn. It is important to note that for cells with an infinitely large R_P, the photocurrent is expected to be proportional to the light intensity: $J_{SC} \propto I_{\mathrm{light}}$. Provided that all other cells are illuminated with a higher intensity, any deviation of the expected behavior can be assigned to a finite parallel resistance.

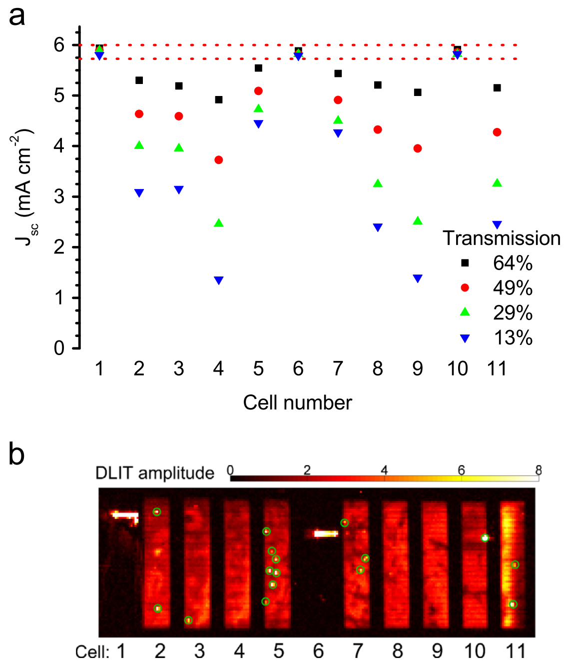

Fig. 2. (a) Filtering results using four transmission levels. The effect on the short-circuit current density of the module is shown. The two dashed lines denote the error margins of the unfiltered short-circuit current of the module. (b) DLIT amplitude image of the measured module. The green circles mark the position of the less visible hot-spots.

Fig. 2a) shows the module current density while filtering each cell subsequently with four different transmission levels. First it can be seen that cells which are insensitive to filtering are completely dark in the LBIC measurement (Fig. 1a: cell number 1, 6 and 10). Further it is found that the current of those cells which show low EQE values in the LBIC measurement is not proportional to the different transmission levels (of course the response can still be linear, but it will not be a line through origin). On the other side, the cells with the strongest response to filtering (Cells 4, 8, and 9) also show the highest EQE values in the LBIC measurement. Therefore it is evident that module LBIC measurements with selective bias illumination show a strong dependence on the parallel resistance of the cells and thus on the blocking behavior under reverse bias voltages.

To verify whether the poor blocking behavior of the modules originates from shunts, we recorded a thermographic image of the module using dark lock-in thermography (DLIT). The result is shown in Fig. 2b). The image shows several hot-spots, which are denoted by green circles. These hot-spots are indications that the module has several shunted cells. Furthermore the shunt distribution fits well to the results of both LBIC and the filtering approach. For example the cells (1, 6 and 10) which were completely insensitive to filtering show the most severe hot-spots, while the low-performing cells 5 and 7 show the highest number of small hot-spots. The three cells without visible hotspots (Cells 4, 8, and 9) show the highest degree of proportionality in the filtering approach and also the highest EQE values in the LBIC measurement. Cell 10, which shows no blocking behavior at all, broke down completely after the DLIT measurement and possibly during the filtering measurement. All other characterizations methods mentioned so far were applied before this event. In a second DLIT measurement after filtering, cell 10 showed no response from the cell area. The only remaining heat-source was the already visible hot-spot in the first thermography measurement. It is likely that the large negative bias voltages during the filtering are responsible for damaging the cell. It was reported by Steim et al. that applying negative bias voltages to cells with hot-spots further reduces their blocking behavior [18], yet Steim et al. left their cells for extended periods of time in negative bias conditions, while in the filtering approach each filter is only applied for several seconds. In general we do not expect that applying the filtering approach damages the cells, except in extreme cases where the cells are already severely shunted. Cell 10 for example already showed a quite severe hotspot in the initial DLIT measurement, and did not show any measurable EQE in the LBIC experiment.

4. Investigation of the Filtering Approach with Numerical Circuit Simulations

In order to improve our understanding of the filtering measurement we performed electrical simulations of a module consisting of two in series connected cells. To do this we implemented a numerical representation of two organic solar cells produced in our lab. Cell 1 had a J_{SC} of 8.6 mA cm^{-2}, a V_{OC} of 600 mV, a FF of 57% and an efficiency of 3.0% whereas cell 2 had a J_{SC} of 8.0 mA cm^{-2}, a V_{OC} of 610 mV, a FF of 57% and an efficiency of 2.8%. These devices were simulated by implementing a one diode model in SPICE according to the following equation (Eq. (1)).

$$J(V) = J_0\left[\exp\left(\frac{e(V - J(V)R_S)}{nkT}\right) - 1\right] - J_{SC} + \frac{V - J(V)R_S}{R_P} \qquad (1)$$

The parameters used are listed in Table 1.

It must be pointed out that the one diode model representation has limited physical meaning, it is solely meant as an electrical representation of the device.

Finally, with these SPICE devices we are able to simulate a filtering measurement and compare it to experiments with a solar module that was fabricated by connecting the cells 1 and 2 (Table 1) in series. The results of measurement and simulation are shown in Fig. 3. It can be seen that there is a good match between measured and simulated J_{SC} of the module at 1 sun intensity. The slightly higher measured value originates possibly from a further increase of extracted photocurrent under negative bias. This may either stem from high series resistances or low mobility. The latter will lead to a slightly voltage-dependent series resistance of the real cells. This would of course be ignored in such a simple model, while high series resistances on the other hand could be included. It was shown that the low mobility present in organic solar cells can have this effect [29].

Furthermore Fig. 3 shows that the measured J_{SC} of the module for the different transmission levels corresponds well to the simulated data (except for a slightly higher value for $T = 64\%$). This demonstrates that the electrical description in SPICE is sufficiently accurate. From a measurement with a filter having a transmission T_i the J_{SC} (1 sun) can be deduced according to: $J_{SC,\,i}(1\text{ sun}) = J_{SC}(T_i)/T_i$. As will be analyzed in more detail below we find in our simulations that lowering the transmission value of the filter leads to an increased negative bias voltage at the filtered cell. As a consequence, the lower the parallel resistance, the more $J_{SC,i}$ (1 sun) will be overestimated. In addition, this effect is stronger the smaller the value for T_i. Therefore the filtering approach can be used to evaluate whether the photocurrent measurement is reliable or not. If the increase, of the estimated photocurrent with lower transmission, is smaller than the measurement uncertainty the obtained photocurrent can be regarded as reliable. Yet it is not possible to exactly quantify the parallel resistance from a filtering measurement since the internal bias voltages still remain unknown.

Table 1
Electrical parameters of the two used solar cells. The cell with the highest and the lowest short-circuit current density was selected from one fabrication batch (16 cells).

	J_0 (mA/cm^2)	J_{gen} (mA/cm^2)	N	R_S (Ωcm^2)	R_P (Ωcm^2)
Cell 1	5.45×10^{-5}	8.6	2	2.8	100 k
Cell 2	5.45×10^{-5}	8.0	2	2.8	10 k

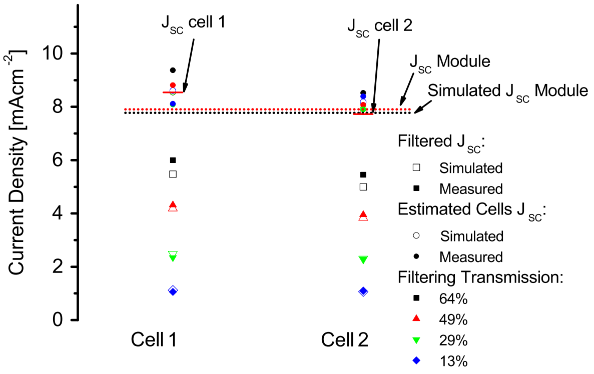

Fig. 3. Filtering results for the exemplary two-cell module. The cells J_{SC} is the measured (bars – individually using a JV measurement) or estimated (circles – using the filtering approach) short-circuit current of the single cells, while the filtered J_{SC} describes the short-circuit current of the simulated or fabricated module. The hollow data points were retrieved from the simulation, while the filled were measured.

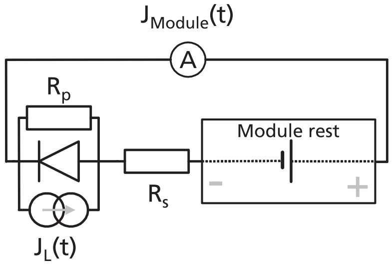

Fig. 4. Simplified equivalent circuit scheme for an LBIC measurement. JL(t) is the photocurrent density generated by the scanning light beam, RP the parallel resistance, RS the series resistance of the whole module, and Jmodule(t) the measured time-dependent current density.

4.1. *The influence of parallel resistances on the LBIC signal filtering approach*

We use some simplifications to investigate the influence of the cells parallel resistance on the LBIC measurement. The used equivalent circuit is shown in Fig. 4. The main assumption is that the current generated by the light beam is too small to alter the operating state of the remaining module; therefore it is assumed to be an ideal DC voltage source applying a negative bias to the measured cell. Further, we simplify the situation by summarizing all series resistances into one single resistance. This is a valid simplification, not an approximation, for all series connected resistances.

The current density measured by the current meter in Fig. 4 can be represented as follws:.

$$J_{Module}(V) = J_0\left[\exp\left(\frac{e(V_{bias} - J_{Module}(V)R_S)}{nkT}\right) - 1\right] - J_L(t) + \frac{V_{bias} - J_{Module}(V)R_S}{R_P} \qquad (2)$$

The bias illuminated cells ("module rest" in Fig. 4) create a negative bias voltage V_{bias} for the measured cell, while all their series resistances are summarized as R_s. $J_L(t)$ is the current density generated by the light beam. Since the light beam is much weaker (typically generating current densities in the μA cm^{-2} range) than the bias illumination (typically generating current densities in the mA cm^{-2} range) the measured cell is always under negative bias conditions. Therefore the exponential term in (Eq. (2)) is between 0 and 1. This limits the current density over the diode, i.e., the recombination current, to the dark saturation current density J_0. Since this current density is very small, the exponential term can be neglected. Using this approach, we can find the following term (Eq. (3)) for the relation of the generated to the measured current density:

$$J_{Module}(J_L(t)) = \frac{R_P}{R_P+R_S} J_L(t) + \frac{V_{bias}}{R_P+R_S} \tag{3}$$

Since the lock-in process determines the EQE from the time-dependent signal we have to subtract the time-independent part from the current-density to obtain a term for the extracted current density ('current response'), which is identical to the EQE derived from the LBIC measurement. This current response $\eta_{\mathbf{CR}}$ is derived from the following Equation (Eq. (4)), wherein $\eta_{\mathbf{CQE}}$ is the EQE of the cell in the case of an infinite parallel resistance.

$$\eta_{CR} = \frac{J_{Module}(J_L(t)) - J_{Module}(0)}{J_L(t)} = \frac{R_P}{R_P+R_S}\eta_{CQE} \tag{4}$$

This means that the current response measured by LBIC using selective bias illumination is reduced by internal currents flowing over the parallel resistance. This effect is the more pronounced the lower the parallel resistance of the cell and the higher the series resistance of the module.

In order to test the assumption that the operating state of the remaining module is not altered by the light beam and that it behaves like an ideal voltage source, we implemented a numerical model of a module (Eq. (5)). It consists of one cell with a finite parallel resistance and a non-zero series resistance connected in series with a second cell which is assumed to be ideal, as depicted in Fig. 5. It is straightforward to expand the model to include more cells or include finite parallel resistances in other cells as well. For sake of simplicity we restricted the investigations to the above mentioned case. The following equations represent each in series connected element.

$$\begin{aligned}
&\text{Cell 1}: \quad J_1\left(V_1, J_{gen,1}\right) = J_0\left(\exp\left(\frac{eV_1}{nkT}\right) - 1\right) - J_{gen,1} + \frac{V_1}{R_P}\\
&\text{Cell 2}: \quad J_2\left(V_2, J_{gen,2}\right) = J_0\left(\exp\left(\frac{eV_2}{nkT}\right) - 1\right) - J_{gen,2}\\
&\text{Series Resistance}: \quad J_3(V_3) = \frac{V_3}{R_S}
\end{aligned} \tag{5}$$

Eq. (5): Description used for the three elements in the module.

J_0 and the ideality factor n were assumed to be identical for both cells. V_1 and V_2 describe the voltages of the two solar cells, and V_3 the voltage that drops over the series resistance. Since all elements are connected in series we obtain the following set of non-linear equations (Eq. (6)):

$$\begin{aligned}
&(1) \quad J_1\left(V_1, J_{\text{lightbeam}}\right) = J_2\left(V_2, J_{biaslight}\right)\\
&(2) \quad J_1\left(V_1, J_{\text{lightbeam}}\right) = J_3(V_3)\\
&(3) \quad V_{\text{bias}} = V_1 + V_2 + V_3
\end{aligned} \tag{6}$$

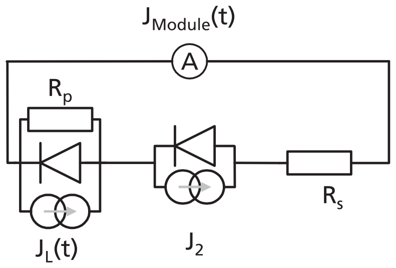

Fig. 5. Equivalent circuit scheme for implemented model. JL(t) is the photocurrent density generated by the scanning light beam, RP the parallel resistance of the investigated cell, Rs the series resistance of the whole module, J2 the current density due to bias illumination, and Jmodule(t) the measured time-dependent current density.

Eq. (6): Set of equations used to describe the 2 cell module.

These equations cannot be solved analytically because of their non-linearity. It is however possible to solve them numerically by finding the correct voltages for all the given parameters.

4.1.1. Numerical calculation of the current response under bias illumination conditions

To obtain a parameter which can be compared to the LBIC signal, we solve these equations once for the maximum amplitude of the current generated by the light beam in the LBIC measurement ($J_{\text{lb, max}} = 20\ \mu A\ \text{cm}^{-2}$ was used) and once for the minimum ($J_{\text{lb, min}} = 0$). The difference between the two results divided by $J_{\text{lb, max}}$ is the current response η_{CR} (Eq. (7)).

$$\eta_{CR} = \frac{J_1(V_1^*, J_{lb,max}) - J_1(V_1^{**}, 0)}{J_{lb,\ \max}} \tag{7}$$

The values for V_1^* (corresponding to $J_{\text{lb, max}}$) and V_1^{**} (no light beam) were obtained by solving the corresponding set of module equations (Eq. (5)), with the module under external short-circuit conditions, i.e., $V_{\text{bias}} = 0$. The bias illumination was adjusted such that $J_{\text{gen, 2}} = 0.8\ \text{mA}\ \text{cm}^{-2}$, corresponding to approximately $I_{\text{light}} = 0.1$ sun. The series resistance is $R_S = 1\ \Omega\ \text{cm}^2$, as long as not mentioned otherwise. The remaining parameters were the ones listed in Table 1.

It is true that the light beam induced change ΔV_2 on the operating state of the bias illuminated cell 2 remains quite small (below 7 mV). On the other hand it appears that the assumption to describe the remaining module as an ideal voltage source depends largely on its operating state V_2. The latter depends on the steady-state current through the module. This steady-state current is generated by the bias illumination in cell 2. However, whether this current flow through cell 1 is determined by cell 1's reverse blocking behavior. If R_P is very high V_2 will be close to V_{OC} and in this case the remaining module (represented by cell 2 in our model) behaves indeed almost like an ideal voltage source. The reason is that the current density–voltage (JV)-curve (of cell 2) is very steep near V_{OC}. Therefore a very small ΔV_2 is sufficient to allow for the (time-dependent) current $J_L(t)$ to flow through the module. In contrast, the lower the parallel resistance the more V_2 gets shifted toward short circuit conditions. As a consequence the voltage ΔV_2 required to allow $J_L(t)$ to flow is increasing strongly. Furthermore the maximum voltage shift ΔV_1 is limited by the open-circuit voltage of cell 1 (which is small due to the low intensity of the light beam). Fig. 6 shows the operating states V_2 of cell 2 for different parallel resistances of cell 1, the black line being the normal JV-curve as guide to the eyes. The inset shows the voltage shift ΔV_2 induced by the light beam for a parallel resistance of 1 kΩ cm^2.

The more the operating state of the bias illuminated cell deviates from open-circuit conditions, the larger the voltage shift required in order to let the light beam generated current flow through it. The required voltage shift $\Delta V_{20\mu A}$ is illustrated as the dashed blue (color online) curve in Fig. 7. However, the maximum voltage cell 1 can "provide" is its V_{OC} which is shown as the dotted green (color online) curve. Of course if cell 1 is under open-circuit conditions all light beam generated charge carriers will recombine but it is still helpful as an upper limit. It can clearly be seen that for $R_p < 200$–$300\ \Omega\ \text{cm}^2$ the required voltage shift is already too large to be provided by cell 1. In general it can be deduced from Fig. 7 that for low parallel resistances the generated voltage shift $\Delta V_1 = V_1{}^* - V_1{}^{**}$ is equal to the open-circuit voltage of cell 1 and for high parallel resistances it is equal to the voltage required to extract the light beam generated current. In the case of realistic series resistances, this leads to a current response which is much more sensitive to parallel resistances than expected from the approximation formula (Eq. 4).

The change in of the voltage drop over the series resistance (ΔV_3) was not mentioned so far because it is very small compared to the voltage shifts (i.e., $\Delta V_1 \approx -\Delta V_2$). Of course this changes in the case

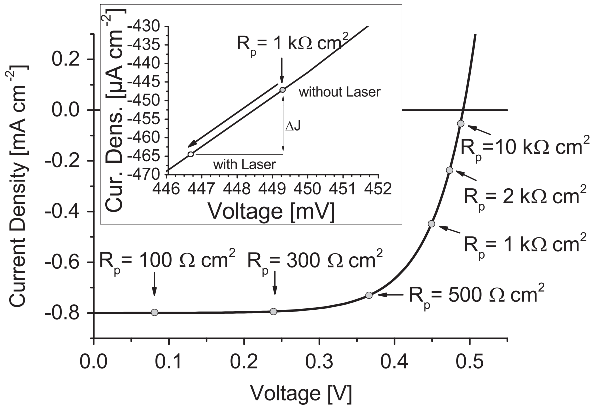

Fig. 6. Working-points of the bias-illuminated cell 2 depending on the parallel resistance in cell 1. The black curve shows the JV-curve of the bias illuminated cell 2, while the gray circles show its working points for specific parallel resistances of cell 1, without light beam applied to cell 1. The inset shows the difference between the solution with and without light beam generated current in cell 1.

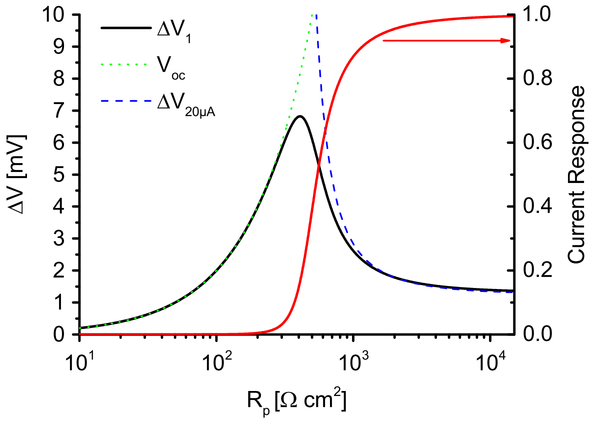

Fig. 7. Voltage differences between maximum and minimum light beam intensity. The solid black curve shows the actual voltage shift ΔV_1 of cell 1 induced by the light beam, while the solid curve associated with the right axis shows the current response of the module. The dotted line shows the V_{OC} of cell 1 illuminated by the light beam, while the dashed line shows the voltage shift required in order to let the light beam generated current flow through cell 2.

of high series resistances, as will be taken into consideration briefly. Although the general behavior of the current response is still similar with the approximation formula, the current response is already reduced by parallel resistances orders of magnitude higher than predicted. This is visualized in Fig. 8. Here, the approximation and the numerical calculation are compared for four different series resistances. It appears that the approximation formula describes the upper limit of the current response. For reasonable series resistances of $R_S \le 10\,\Omega\,\text{cm}^2$ the current response is independent of the series resistance. However for an unrealistic high series resistance of 1 kOhm the approximation formula describes the behavior sufficiently well, since the high voltage drop over the series resistance reduces the voltage shift of the bias illuminated cell 2. Note that the data was obtained using 0.1 suns ($J_{\text{gen},\,2} = 0.8$ mA cm^{-2}) and a laser intensity corresponding to $J_{\text{lb, max}} = 20\,\mu A$ cm^{-2}. These values have of course an influence on the resulting current response. Increasing the intensity of the bias illumination will shift the current response curve to lower parallel resistances until the bias illuminated cells behave like an ideal voltage source. Therefore Eq. (4) forms the upper limit for the current response, which is achieved in these calculations for bias illuminations above 100 suns. However, the intensity of the laser beam has only little influence on the current response curve as long as the intensity remains at least one order of magnitude below the bias illumination. Fig. S1 in the supplementary information (SI) shows the current response as a function of bias illumination intensity. Modules are commonly comprised of more than two cells. This can be included into the model by adding more diode elements and changing R_S accordingly. Alternatively, the additional cells can be represented by cell 2 by multiplying its ideality factor with the number of additional cells. The first approach was performed for our simulations, since it offers the freedom to manipulate the parameters of each cell individually. Modifying the ideality factor however offers a more intuitive understanding of the impact which additional cells have on the measurement. Going from a two cell to a three cell module doubles the voltage required to extract the charges generated by the light beam, which shifts the current response curve shown in Fig. 8 to higher values of R_P.

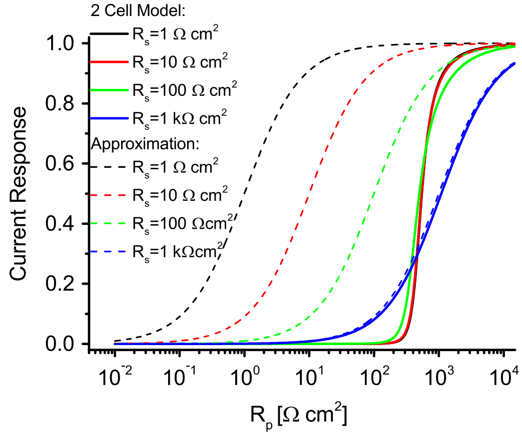

Fig. 8. Comparison of the approximated formula to the numerically obtained results. The graphs show the current response for four different series resistances. The dashed graphs correspond to the approximated formula whereas the solid lines show the current response obtained with the numerical model.

4.1.2. Numerical calculation of the current response under forward bias conditions

LBIC measurements of modules can also be conducted by applying a forward bias voltage. The results in the literature are comparable [17] to what was shown in Fig. 1(a); therefore we examined the consequences of a low parallel resistance for this bias method. In contrast to bias illumination all cells are under forward bias conditions. For low parallel resistances the measured cell is practically short-circuited, which means that the remaining cells share (almost) the full bias voltage. For higher parallel resistances the voltage of the measured cell increases, while the working points of the remaining cells are shifted to lower voltages. This leads to a decrease of the (steady-state) current in a similar manner as in the case of bias illumination. Analogously, the voltage ΔV required to extract the current generated by the light beam increases with decreasing voltage of the remaining cells. To model the case of LBIC with bias voltage we used the same two cell module as before.

Fig. 9 shows that the approximation (Eq. (4)) is in good accordance with the numerical results only for extremely low parallel resistances. With increasing values of R_P the curves first peak and then decrease again asymptotically. Decreasing the series resistance increases the peak height, shifts the peak to lower parallel resistances and increases the asymptotic value (for large R_p). In order to understand why the asymptotic value is far below unity – in contrast to the bias illumination method – it is important to consider the direction of the current.

4.1.2.1. Case of large or infinite parallel resistance. The voltage is distributed equally among the two cells, therefore both cells have a forward current according to 0.5 V_{bias}. The additional charge carriers generated in cell 1 by the scanning light beam form however, if they are extracted, a current in reverse direction and will therefore

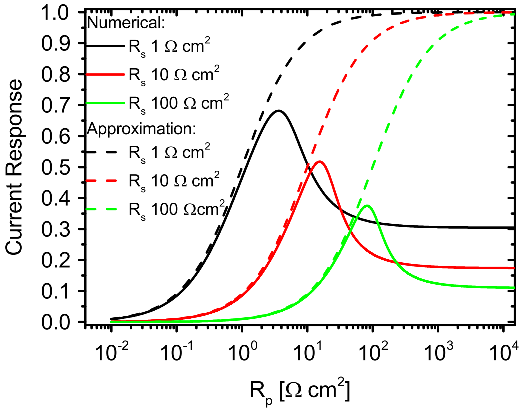

Fig. 9. Current Responses for various series resistances under forward bias conditions. The dashed lines show the result of the approximation formula, while the solid lines show the result of the numerical solution under a forward bias of 1.5 V.

reduce the overall current. As a consequence the voltage of the blocking cell V_2 needs to be lowered. Since the sum of all voltages in the module are equal to the applied bias voltage, this leads to an increase of V_1. This however increases the forward current which counteracts the effect of the generated photocurrent. Therefore it is important to state that a current response of unity cannot be achieved with this method. For $R_S > 0$ an additional voltage drop ΔV_{Rs} occurs and hence$\Delta V_1 = \Delta V_{\mathrm{R_S}} + \Delta V_2$. This leads to an even lower current response.

At first it might seem that high bias voltages could help to extract more photocurrent since the voltage change ΔV_2 required to reduce the current of the module accordingly becomes smaller as the slope of the JV-curve is larger for higher bias voltages. However, this applies as well to cell 1 which counteracts the benefits of higher bias voltages. In fact, our calculations prove that the asymptotic value of the current response indeed decreases with higher bias voltages. This is shown in Fig. S2 in the SI.

4.1.2.2. Case of low parallel resistance. Lower parallel resistances in the investigated cell reduce the voltage V_1 while increasing V_2, therefore increasing the module forward current. This effect is beneficial for the extraction of photogenerated current of cell 1. However, there is also a certain fraction of the photocurrent lost due to the low parallel resistance of cell 1. The increased steepness (of the JV-curve) of cell 2 due to the higher value of V_2 reduces the voltage shift ΔV_2 required to extract the photocurrent. Furthermore, the smaller slope of the JV-curve of cell 1 reduces the current increase due to the voltage increase ΔV_1, therefore reducing the above described counteraction. This improves the current response for a (surprisingly) large range of parallel resistances down to extremely low values where the module efficiency would already be severely limited. Of course the maximum possible voltage cell 1 can provide is still limited by its V_{OC} which will eventually drop to zero for extremely low parallel resistances. Therefore the current response then also drops to zero. The fact that the current response has a maximum leads to the problem that the same current response is obtained for two largely different parallel resistances. For example, the curve with $R_S = 1$ Ohm cm^2 has the same current response for $R_P \geq 10^3$ Ohm cm^2 (asymptotic value) and for $R_P \approx 0.5$ Ohm cm^2. Therefore it is impossible to quantitatively interpret data from an LBIC measurement with forward bias. This is not the case for the bias illumination approach.

The bias voltage has an impact on the current response curve; however the described principles apply generally for all bias voltages. The peak of the current response curve is shifted to lower parallel resistances for higher bias voltages, while the asymptotic value (for large parallel resistances) of the current response decreases. The peak value decreases as it approaches the limit set by Eq. (4). For lower bias voltages the peak broadens and shifts to higher parallel resistance until it starts to decrease for very low bias voltages (data shown in Fig. S2 in the SI).

The general conclusions deduced from the results of the numerical simulations are not altered by adding additional cells. For a given bias voltage an increasing number of cells reduce the operating voltage of each cell in the module. In principle this effect can be accounted for by increasing the applied bias voltage. However, the additional bias required depends again on the exact value of the parallel resistance.

Meusel et al. have reported on a combination of light and voltage bias for the EQE-measurements in tandem solar cells [3]. This approach turns out to be beneficial in our numerical simulations as it is found that the decrease of the current response is less steep which is plotted in Fig. S3 in the SI. The bias voltage should thereby not exceed the V_{OC} of the illuminated cells.

In LBIC measurements of single cells the series resistance of the outer circuitry is very small, and there is no blocking cell to be overcome. Therefore the approximation formula actually describes the current response that one would expect from a single cell under negative bias conditions. Yet, in a module the other cells interfere with the measurement. Under bias illumination as well as for forward bias voltage the parallel resistance determines largely the operating points of the remaining cells. In the case of bias illumination the current response is already reduced by much higher parallel resistances, making the measurement procedure highly sensitive to shunts. On the other hand, in the case of forward bias conditions the parallel resistance makes quantitative interpretations of the obtained results impossible.

5. Conclusions

Light beam induced current (LBIC) measurements using selective bias illumination were performed on organic solar modules. However, the results do not seem to represent the real photogenerated current. With dark lock-in thermography (DLIT) measurements and the filtering approach this phenomenon could be attributed to varying parallel resistances of the cells in the module. Further it was shown that electroluminescence (EL) imaging is largely insensitive to shunts, since already for small forward bias currents the parasitic current flowing through shunt pathways (being linearly dependent on voltage) becomes relatively small compared to the current flowing through well-working areas of the cell (depending exponentially on voltage). Therefore only severely shunted cells can be identified in an EL measurement.

In order to understand the observed phenomena in detail, numerical simulations of the filtering approach as well as of LBIC measurements under selective bias lighting and different forward bias conditions were performed. It was shown that filtering can reliably recognize whether parallel resistances in the module affect the measurement results. Furthermore if filtering is not affected this verifies that LBIC is able to correctly measure the local photocurrents. The impact of different parallel resistances on the current response in an LBIC measurement was demonstrated in detail. The filtering approach clearly provides a figure of merit for the amount of current lost through shunt resistances, yet so far quantitative assessments of the parallel resistances are not possible.

The parallel resistance of the measured cell has two effects on an LBIC measurement. First, it determines the operating voltage of the remaining cells in the module and secondly, it reduces the maximum possible photovoltage (due to the reduction in V_{OC}) that the measured cell can provide to drive the current through the rest of the module. Both effects determine the current response obtained from an LBIC measurement. It is important to point out that the operating voltage of the remaining cells in the module is of crucial importance since it determines the reaction of the module to the additional current generated by the light beam. In the case of selective bias illumination the current response was shown to be independent of the series resistance for realistic values of the latter. Further, the current response depends in an unambiguous manner on the parallel resistance for this bias method. However for applied forward bias voltages LBIC measurements depend critically on the series resistance and a drawback is that identical results can be obtained for very different parallel resistances. Therefore without an exact knowledge of parallel and series resistances it is impossible to quantitatively interpret LBIC measurements using forward bias voltage.

It could clearly be shown that LBIC measurements of modules with in series connected cells are highly sensitive to the parallel resistances of each individual cell. If LBIC is intended as a method to measure the photocurrent distribution within a module, it is crucial to determine whether parallel resistances do interfere. This distinction is possible with the proposed filtering approach. However, the results of LBIC with forward bias voltages applied to a module comprising high parallel resistances for each cell still depend on the series resistance value. A qualitative measurement of the photocurrent distribution is only possible if the variation of the series resistance among individual cells is small compared to the overall series resistance.

Acknowledgments

The authors acknowledge Hans-Frieder Schleiermacher and Deepak Kaduwal for their help in module preparation, Umair Ali Shah for his help in cell fabrication, and Stephen Thomas Haag for his assistance during the LBIC measurements. This work has been cofinanced by the European Union/European Regional Development Fund (ERDF) in the framework of the program “Interreg IV Upper Rhine” under project number C25, RHEIN-SOLAR.

Appendix A. Supporting information

Supplementary data associated with this article can be found in the online version at http://dx.doi.org/10.1016/j.solmat.2014.11.032.

References

[1] F.C. Krebs, N. Espinosa, M. Hösel, R.R. Søndergaard, M. Jørgensen, 25th anniversary article: rise to power – OPV-based solar parks, Adv. Mater. 26 (2014) 29–39.

[2] J. You, L. Dou, K. Yoshimura, T. Kato, K. Ohya, T. Moriarty, K. Emery, C.-C. Chen, J. Gao, G. Li, Y. Yang, A polymer tandem solar cell with 10.6% power conversion efficiency, Nat. Commun. 4 (2013) 1446.

[3] R. Søndergaard, M. Hösel, D. Angmo, T.T. Larsen-Olsen, F.C. Krebs, Roll-to-roll fabrication of polymer solar cells, Mater. Today 15 (2012) 36–49.

[4] M. Hosoya, H. Oooka, H. Nakao, S. Mori, T. Gotanda, N. Shida, R. Hayase, Y. Nakano, M. Saito, Module Development for Organic Thin-Film Photovoltaics, in: Proceedings of the EU PVSEC 2013: 28th European Photovoltaic Solar Energy Conference and Exhibition, Parc des Expositions Paris Nord Villepinte, Paris, France, WIP, München, 2013, pp. 2236–2238.

[5] Y. Galagan, d.e. Vries, G. Ike, A.P. Langen, R. Andriessen, W.J. Verhees, S. C. Veenstra, J.M. Kroon, Technology development for roll-to-roll production of organic photovoltaics, Chem. Eng. Process. 50 (2011) 454–461.

[6] F.C. Krebs, T. Tromholt, M. Jørgensen, Upscaling of polymer solar cell fabrication using full roll-to-roll processing, Nanoscale 2 (2010) 873–886.

[7] D. Angmo, S.A. Gevorgyan, T.T. Larsen-Olsen, R.R. Søndergaard, M. Hösel, M. Jørgensen, R. Gupta, G.U. Kulkarni, F.C. Krebs, Scalability and stability of very thin, roll-to-roll processed, large area, indium-tin-oxide free polymer solar cell modules, Org. Electron. 14 (2013) 984–994.

[8] M. Hösel, R.R. Søndergaard, M. Jørgensen, F.C. Krebs, Fast inline roll-to-roll printing for indium-tin-oxide-free polymer solar cells using automatic registration, Energy Technol. 1 (2013) 102–107.

[9] P. Sommer-Larsen, M. Jørgensen, R.R. Søndergaard, M. Hösel, F.C. Krebs, It is all in the pattern—high-efficiency power extraction from polymer solar cells through high-voltage serial connection, Energy Technol. 1 (2013) 15–19.

[10] P. Apilo, J. Hiltunen, M. Välimäki, S. Heinilehto, R. Sliz, J. Hast, Roll-to-roll gravure printing of organic photovoltaic modules-insulation of processing defects by an interfacial layer, Prog. Photovolt: Res. Appl. (2014) http://dx.doi.org/10.1002/pip.2508 (published online).

[11] U. Hoyer, M. Wagner, T. Swonke, J. Bachmann, R. Auer, A. Osvet, C.J. Brabec, Electroluminescence imaging of organic photovoltaic modules, Appl. Phys. Lett. 97 (2010) 233303.

[12] M. Seeland, R. Rösch, H. Hoppe, Luminescence imaging of polymer solar cells: visualization of progressing degradation, J. Appl. Phys. 109 (2011) 64513.

[13] J. Reinhardt, M. Grein, C. Bühler, M. Schubert, U. Würfel, Identifying the impact of surface recombination at electrodes in organic solar cells by means of electroluminescence and modeling, Adv. Energy Mater. 4 (2014) 1400081.

[14] U. Hoyer, L. Pinna, T. Swonke, R. Auer, C.J. Brabec, T. Stubhan, N. Li, Comparison of electroluminescence intensity and photocurrent of polymer based solar cells, Adv. Energy Mater. 1 (2011) 1097–1100.

[15] R. Rösch, D.M. Tanenbaum, M. Jørgensen, M. Seeland, M. Bärenklau, M. Hermenau, E. Voroshazi, M.T. Lloyd, Y. Galagan, B. Zimmermann, U. Würfel, M. Hösel, H.F. Dam, S.A. Gevorgyan, S. Kudret, W. Maes, L. Lutsen, D. Vanderzande, R. Andriessen, G. Teran-Escobar, M. Lira-Cantu, A. Rivaton, G. Y. Uzunoğlu, D. Germack, B. Andreasen, M.V. Madsen, K. Norrman, H. Hoppe, F. C. Krebs, Investigation of the degradation mechanisms of a variety of organic photovoltaic devices by combination of imaging techniques—the ISOS-3 interlaboratory collaboration, Energy Environ. Sci. 5 (2012) 6521.

[16] R. Rösch, F.C. Krebs, D.M. Tanenbaum, H. Hoppe, Quality control of roll-to-roll processed polymer solar modules by complementary imaging methods, Sol. Energy Mater. Sol. Cells 97 (2012) 176–180.

[17] F.C. Krebs, R. Søndergaard, M. Jørgensen, Printed metal back electrodes for R2R fabricated polymer solar cells studied using the LBIC technique, Sol. Energy Mater. Sol. Cells 95 (2011) 1348–1353.

[18] R. Steim, S.A. Choulis, P. Schilinsky, U. Lemmer, C.J. Brabec, Formation and impact of hot spots on the performance of organic photovoltaic cells, Appl. Phys. Lett. 94 (2009) 43304.

[19] H. Hoppe, J. Bachmann, B. Muhsin, K.-H. Drüe, I. Riedel, G. Gobsch, C. Buerhop-Lutz, C.J. Brabec, V. Dyakonov, Quality control of polymer solar modules by lock-in thermography, J. Appl. Phys. 107 (2010) 14505.

[20] J. Bachmann, C. Buerhop-Lutz, R. Steim, P. Schilinsky, J.A. Hauch, E. Zeira, B. Christoh J., Highly sensitive non-contact shunt detection of organic photovoltaic modules, Sol. Energy Mater. Sol. Cells 101 (2012) 176–179.

[21] J. Bachmann, C. Buerhop-Lutz, C. Deibel, I. Riedel, H. Hoppe, C.J. Brabec, V. Dyakonov, Organic solar cells characterized by dark lock-in thermography, Sol. Energy Mater. Sol. Cells 94 (2010) 642–647.

[22] P. Vorasayan, T.R. Betts, A.N. Tiwari, R. Gottschalg, Multi-laser LBIC system for thin film PV module characterisation, Sol. Energy Mater. Sol. Cells 93 (2009) 917–921.

[23] J. Carstensen, G. Popkirov, J. Bahr, H. Föll, CELLO: an advanced LBIC measurement technique for solar cell local characterization, Sol. Energy Mater. Sol. Cells 76 (2003) 599–611.

[24] I.L. Eisgruber, J.R. Sites, Extraction of individual-cell photocurrents and shunt resistances in encapsulated modules using large-scale laser scanning, Prog. Photovolt: Res. Appl. 4 (1996) 63–75.

[25] F.C. Krebs, M. Jørgensen, 2D characterization of OPV from single and tandem cells to fully roll-to-roll processed modules with and without electrical contact, Adv. Opt. Mater. 2 (2014) 465–477.

[26] B. Zimmermann, H.-F. Schleiermacher, M. Niggemann, U. Würfel, ITO-free flexible inverted organic solar cell modules with high fill factor prepared by slot die coating, Sol. Energy Mater. Sol. Cells 95 (2011) 1587–1589.

[27] S.B. Sapkota, M. Fischer, B. Zimmermann, U. Würfel, Analysis of the degradation mechanism of ITO-free organic solar cells under UV radiation, Sol. Energy Mater. Sol. Cells 121 (2014) 43–48.

[28] H. Ahme, M. Lee, C. Im, U. Würfel, Influence of the acceptor on electrical performance and charge carrier transport in bulk heterojunction solar cells with HXS-1, J. Phys. Chem. C 118 (2014) 3386–3392.

[29] J. Gilot, M.M. Wienk, Janssen, A.J. René, Measuring the external quantum efficiency of two-terminal polymer tandem solar cells, Adv. Funct. Mater. 20 (2010) 3904–3911.

Series title and number

VTT Science 101

Title	**Roll-to-roll printing of organic photovoltaic cells and modules**
Author(s)	Pälvi Apilo
Abstract	Organic photovoltaics (OPV), one of the emerging thin-film photovoltaic technologies, has gained considerable interest being flexible, light weight and transparent. OPVs can be processed by using roll-to-roll (R2R) printing and coating methods which can lead to significant manufacturing cost reduction. Gravure printing brings the advantage of layer patterning directly in the printing process. This differentiates gravure printing from coating technologies. Importantly, this increases product design freedom by enabling large-area arbitrary shape and size structures. This opens up possibility to use OPVs also as decorative elements on the surfaces of interior and exterior building spaces. Secondly, gravure printing enables high repeatability and accuracy in thin-film deposition. In this Thesis, the applicability of gravure printing was demonstrated firstly in the laboratory by using a standard OPV device configuration. The layer properties (layer thickness, uniformity) of the gravure-printed hole transport layer and photoactive layer were optimized by engineering the printability using printing master parameters, ink formulations and printing parameters. The electrical functionality of these printed layers was studied in organic solar cells using a standard measurement method. The cells were further connected to modules. After this, the outlined processing conditions for OPV modules (active area 15 cm^2) were transferred to R2R pilot production environment. Small pinholes were found to form readily in the photoactive layer in R2R gravure printing with a standard cell configuration. However, by using an ultrathin evaporated insulating interlayer electrical short-circuit could be inhibited, leading to considerably improved performance with a maximum efficiency of 1.9%. In addition, a R2R printing process for inverted OPV configuration modules was developed and demonstrated. The device structure consisted of five layers, which were either gravure or screen printed. Few hundred fully R2R printed modules with the active area ranging from 14–97 cm^2 were fabricated with excellent yield. With the 97 cm^2 sized modules an average output power of 0.17W was generated (power conversion efficiency of 1.8±0.1 %). The main achievements of this thesis are i) gravure printing based R2R thin-film deposition technology for OPV, ii) printed standard and inverted device structures, iii) R2R manufactured large-area flexible solar modules, iv) OPV process upscaling to R2R pilot level and v) investigation of characterization methods for OPV modules.
ISBN, ISSN	ISBN 978-951-38-8328-7 (Soft back ed.) ISBN 978-951-38-8329-4 (URL: http://www.vttresearch.com/impact/publications) ISSN-L 2242-119X ISSN 2242-119X (Print) ISSN 2242-1203 (Online)
Date	September 2015
Language	English, Finnish abstract
Pages	90 p. + app. 64 p.
Name of the project	
Commissioned by	
Keywords	roll-to-roll printing, gravure printing, organic photovoltaics, upscaling, monolithic modules, printed electronics, electrical imaging
Publisher	VTT Technical Research Centre of Finland Ltd P.O. Box 1000, FI-02044 VTT, Finland, Tel. 020 722 111

Julkaisun sarja ja numero

VTT Science 101

Nimeke	**Rullalta rullalle painettavat orgaaniset aurinkokennot ja -moduulit**
Tekijä(t)	Pälvi Apilo
Tiivistelmä	Orgaaninen aurinkokennoteknologia on herättänyt suurta mielenkiintoa tulevaisuuden energiantuottomenetelmänä erityisesti taipuisuutta, keveyttä ja läpinäkyvyyttä vaativissa sovelluksissa. Orgaanisia aurinkokennoja voidaan valmistaa kustannustehokkaasti rullalta rullalle paino- tai päällystysmenetelmillä. Syväpainomenetelmän merkittävimpänä etuna päällystysteknologioihin verrattuna voidaan pitää kerroksen kuviointia samanaikaisesti jo painoprosessissa ilman erillistä kuviointiprosessivaihetta. Kuviointi avaa mahdollisuuksia moduulien muodon ja koon vapaalle suunnittelulle ja toteutukselle. Tämä lisää moduulien käyttömahdollisuuksia myös dekoratiivisina elementteinä rakennusten sisä- ja ulkotiloissa. Lisäksi syväpainolla on mahdollista saavuttaa erinomainen toistettavuus ja tarkkuus ohutkalvon muodostamisessa. Tässä väitöskirjassa on kehitetty perinteiselle aurinkokennorakenteelle syväpainoon perustuva ohutkalvoprosessi sekä aukonkuljettaja- että fotoaktiiviselle kerrokselle. Optimoimalla painotelan parametreja, painovärin koostumusta ja painoparametreja voidaan ohutkalvokerroksen ominaisuuksia, kuten kerrospaksuutta ja pinnan laatua, säätää halutunlaiseksi. Painettujen kerrosten sähköinen toiminnallisuus aurinkokennoilla on karakterisoitu käyttäen standardoitua mittausmenetelmää. Edelleen kennoja sarjaankytkemällä on toteutettu moduulirakenteita. Syväpainoon perustuva rullalta rullalle valmistusprosessi perinteisen rakenteen moduuleille on siirretty laboratoriosta pilot-valmistusympäristöön. Perinteisellä rakenteella rullalta rullalle valmistetuissa moduuleissa (15 cm^2) havaittiin aktiivikerroksessa pieniä reikiä. Valmistusongelma saatiin ratkaistua käyttämällä erittäin ohutta höyrystettyä välikerrosta. Moduulien hyötysuhteeksi mitattiin maksimissaan 1,9 %. Lisäksi tässä työssä demonstroitiin ja kehitettiin rullalta rullalle prosessi käänteiselle aurinkokennorakenteelle, joka koostui kahdesta rullalta rullalle syväpainetusta ja kolmesta silkkipainetusta kerroksesta. Kyseessä olevalla prosessilla valmistettiin satoja täysin painettuja aurinkokennomoduuleja erinomaisella saannolla. Moduulien aktiivipinta-alana oli 14–97 cm^2. Suurimman pinta-alan moduuleilla pystyttiin keskimäärin tuottamaan 0,17 W teho auringonvalossa (hyötysuhde 1,8±0,1 %). Tämän väitöskirjatyön pääsaavutukset ovat i) syväpainoon perustuva orgaanisen aurinkokennon ohutkalvovalmistusteknologia, ii) painetut aurinkokennot sekä perinteisellä että käänteisellä rakenteella, iii) taipuisalle substraatille valmistetut rullalta rullalle painetut, suuren pinta-alan aurinkokennomoduulit, iv) valmistusteknologian siirto laboratoriosta pilot-valmistusympäristöön ja v) aurinkokennomoduulien rakenteiden tutkimus kuvantamismenetelmillä.
ISBN, ISSN	ISBN 978-951-38-8328-7 (nid.) ISBN 978-951-38-8329-4 (URL: http://www.vtt.fi/julkaisut) ISSN-L 2242-119X ISSN 2242-119X (Painettu) ISSN 2242-1203 (Verkkojulkaisu)
Julkaisuaika	Syyskuu 2015
Kieli	Englanti, suomenkielinen tiivistelmä
Sivumäärä	90 s. + liitt. 64 s.
Projektin nimi	
Rahoittajat	
Avainsanat	rullalta rullalle painaminen, syväpaino, orgaaniset aurinkokennot, ylösskaalaus, monoliittiset moduulit, painettava elektroniikka, sähköinen kuvantaminen
Julkaisija	Teknologian tutkimuskeskus VTT Oy PL 1000, 02044 VTT, puh. 020 722 111

VTT SCIENCE 101
Roll-to-roll printing of organic photovoltaic cells and...

Roll-to-roll printing of organic photovoltaic cells and modules

Organic photovoltaics (OPV) has gained considerable interest being flexible, light weight and transparent. OPVs can be processed by using roll-to-roll (R2R) printing and coating methods which can lead to significant manufacturing cost reduction. Gravure printing brings the advantage of layer patterning directly in the printing process. Importantly, this increases product design freedom by enabling large-area arbitrary shape and size structures.

The applicability of gravure printing was demonstrated in the laboratory by using a standard OPV device configuration. The layer properties of the gravure-printed hole transport layer and photoactive layer were optimized by engineering the printability using printing master parameters, ink formulations and printing parameters. The electrical functionality of these layers was studied in organic solar cells and modules. After this, the outlined processing conditions were transferred to R2R pilot production environment. Small pinholes were found in the photoactive layer. However, by using an ultrathin interlayer electrical short-circuit could be inhibited. In addition, a R2R printing process for inverted OPV configuration modules was developed and demonstrated. The device structure consisted of five printed layers. Few hundred fully R2R printed modules were fabricated with excellent yield. With the 97 cm^2 sized modules an average output power of 0.17W was generated (efficiency of 1.8±0.1 %).

The main achievements of this thesis are i) gravure printing based R2R thin-film deposition technology for OPV, ii) printed standard and inverted device structures, iii) R2R manufactured large-area flexible solar modules, iv) OPV process upscaling to R2R pilot level and v) investigation of characterization methods for OPV modules.

ISBN 978-951-38-8328-7 (Soft back ed.)
ISBN 978-951-38-8329-4 (URL: http://www.vttresearch.com/impact/publications)
ISSN-L 2242-119X
ISSN 2242-119X (Print)
ISSN 2242-1203 (Online)